

# Endotracheal Tube Placement with Fibre Optic Sensing

Brett J Gadsby, MSc

Thesis submitted to the University of Nottingham  
for the degree of Doctor of Philosophy  
December 2022



**University of  
Nottingham**

UK | CHINA | MALAYSIA

# Abstract

Unrecognised oesophageal intubation is often described as a ‘Never Event’; an entirely preventable and extremely serious incident. However, there is still prevalence, with severe consequences for the patient. The current gold standards of visually confirming passage through the vocal cords, observing chest movement, and end-tidal capnography all have limitations. There is an opportunity for an alternative method to determine correct endotracheal tube placement in the trachea. One such solution is described here, through the development of a compact fibre optic sensor integrated into a standard endotracheal tube. The sensor contains no electrical components inside the invasive portion of the device, and it is magnetic resonance imaging safe.

The spectral characteristics of the trachea and oesophagus are observed using a fibre optic probe, with the presence of oxyhaemoglobin being used to distinguish the tissues. A novel epoxy sensor is then designed using plastic optical fibres. A rounded top with a square base sensor shape had the least impact on the overall performance of the ETT. Furthermore, by forming the sensor with two illumination fibres, pulse oximetry can be performed. A fibre separation distance between 1.27 and 2.54 mm is optimal. However, a Monte Carlo simulation demonstrates a viable separation of 0.5 to 3 mm. Therefore, by reducing this to 0.88 mm, a more compact sensor can be produced whilst still retaining a classification rate (average correct identification of trachea and oesophagus) of >89.2% in *ex-vivo* models.

Two methods for emitting light perpendicularly to the fibre axis are explored, demonstrating that bending the fibres caused an optical power loss of 29.0%, whereas cleaving the fibres at 45° produced an 81.9% loss. The position of the sensor on the endotracheal tube is investigated, finding that integration behind the cuff is preferable. However, placement outside the main lumen of the ETT is also a viable option.

Computational methods to process spectral measurements are developed. Data for these methods was provided by two experiments on two different sensor types, providing a high tissue classification rate for both the trachea and oesophagus. The first experiment consisted of 9 *ex-vivo* porcine samples, producing a correct tissue identification of up to 100.0%. The second consisted of 10 sensors on 1 *ex-vivo* porcine sample, yielding a maximum correct tissue identification of 89.2% when a support vector machine classifier was used. Application of the sensor in an animal study, which consisted of 3 porcine subjects, generated a maximum correct tissue identification of 98.3% using principal component analysis and a support vector machine. The data were recorded over a combined time of 348 minutes, obtained during varying cuff pressures, endotracheal tube orientations, and movement.

Finally, suggested future developments to the sensor design and computational methods demonstrate a potential route to improving tissue identification rates. Changes to the experimental protocol are described to verify classification rates. Concepts for exchanging the spectrometer for photodiodes and optical filters to reduce the cost of the opto-electronic units display potential. The technology has applications in wider healthcare, with examples of integration within naso-/oro- gastric tubes and other invasive medical devices given.

## Author's research publications

Correia, R., Gadsby, B., Korposh, S., Norris, A. M., Hayes-Gill, B. R., Sinha, R., ... & Morgan, S. P. (2022). Intra-tracheal multiplexed sensing of contact pressure and perfusion. *Biomedical Optics Express*, 13(1), 48-64.

Gadsby, B., Morgan, S. P., Correia, R., Chenyang H., Hayes-Gill, B. R., Norris, A. M., Hardman, J. G., & Korposh, S. Smart endotracheal tube for identifying oesophageal intubation, *IEEE Trans. Biomed. Eng.* (draft subject to approval - Appendix D).

Gadsby, B., Correia, R., Korposh, S., Norris, A. M., Hayes-Gill, B. R., Sinha, R., ... & Morgan, S. P. (2021). iTraXS (intra-Tracheal multipleXed Sensing) - an optical fibre sensing endotracheal tube, (research poster presented at the Midlands Health and Life Science Symposium - Appendix E).

## Acknowledgements

I would like to express my gratitude for the exceptional guidance provided by my supervisors, Professor Serhiy Korposh, Professor Stephen P. Morgan, Professor Barrie Hayes-Gill, Dr Ricardo Correia, and Professor Jonathan Hardman. I look forward to continuing my academic career alongside you.

I am grateful to Dr Andrew Norris, Professor David Gardner, and Dr Caroline Bergmann. The clinical and medical advice, along with the access to facilities throughout this project has been vital to its success.

I would like to thank Chenyang He, Chong Liu, and Sandor Erdody, for excellent research on the iTraXS projects.

I would also like to thank Dr George Gordon for his role as the internal assessor on this research project.

I appreciate the expert design and manufacturing resources provided by P3 Medical and BlueFrog Design.

I would also like to thank all members of the Optics and Photonics Research Group, here at the University of Nottingham. The advice and support offered have made this experience an immensely enjoyable one.

I want to express my appreciation to the Engineering and Physical Sciences Research Council (EPSRC) for funding this project.

A special thanks to Karen, Mal, and Natasha. I owe all that I achieve to you.



# Contents

Abstract .....	1
Author's research publications.....	2
Acknowledgements .....	3
List of Acronyms and abbreviations .....	7
Chapter 1    Background .....	9
1.1    Introduction .....	9
1.2    Airway Management .....	9
1.2.1    The Airway.....	10
1.2.2    Intubation .....	13
1.2.3    Unrecognised Oesophageal Intubation (UOI).....	15
1.2.4    Clinician Questionnaire.....	15
1.3    Literature Review .....	16
1.3.1    Spectroscopy .....	16
1.3.2    Tissue Reflectance Spectroscopy .....	17
1.3.3    Pulse Oximetry .....	18
1.4    Identifying Oesophageal Intubation .....	20
1.4.1    The Tracheal Characteristic .....	23
1.5    Summary & Aims.....	26
Chapter 2    Spectral Tissue Characterisation .....	28
2.1    Introduction .....	28
2.2    Commercial Reflection Probe Measurements .....	28
2.3    Normalization .....	30
2.4    Spectral Characteristic Origin .....	31
2.5    Discussion .....	37
Chapter 3    Endotracheal Tube Sensor Integration .....	38
3.1    Introduction .....	38
3.2    Distribution of Light Around a Cleaved Fibre .....	38
3.3    Fibre Separation .....	44
3.3.1    Experimental .....	44
3.3.2    Monte Carlo Simulation .....	47
3.4    Sensor Design.....	50
3.4.1    Two-Fibre Rectangle.....	51
3.4.2    J-shape Fibres .....	54
3.4.3    Three-fibre sensor .....	62

3.5	Sensor Placement .....	63
3.6	Sensor Manufacture.....	69
3.6.1	Fabrication.....	69
3.6.2	Modifications .....	72
3.7	Discussion .....	78
Chapter 4	<i>Ex-vivo</i> measurements & Computational Methods.....	82
4.1	Introduction .....	82
4.2	Experimental Methodology .....	82
4.3	Spectral Identification .....	85
4.3.1	Spectral Ratios .....	85
4.3.2	Principal Component Analysis.....	94
4.4	Statistical Measures .....	98
4.5	Spectral Classification.....	100
4.5.1	Linear Discriminant Analysis .....	100
4.5.2	Logistic Regression Analysis.....	106
4.5.3	Support Vector Machine .....	110
4.5.4	K-Nearest Neighbour .....	113
4.6	Summary & Discussion.....	117
Chapter 5	iTraXS & The Animal Studies .....	121
5.1	Introduction .....	121
5.2	iTraXS .....	121
5.3	First Animal Study .....	122
5.3.1	Perfusion Sensor .....	122
5.3.2	Contact Pressure Sensor.....	123
5.3.3	First Animal Study .....	124
5.3.4	Discussion .....	127
5.4	Second Animal Study .....	128
5.4.1	Analysis by Subject.....	134
5.4.2	Subject 3.....	134
5.4.3	Subject 2.....	145
5.4.4	Subject 1.....	151
5.5	Combined Analysis .....	152
5.5.1	LDA, KNN & SVM.....	152
5.5.2	Full Spectrum PCA & SVM .....	157
5.6	Summary & Discussion.....	158

Chapter 6	Conclusions & Further Developments .....	162
6.1	Introduction .....	162
6.2	Further Developments .....	162
6.2.1	Experimental Design .....	162
6.2.2	Sensor Design .....	163
6.2.3	Differential Method.....	164
6.2.4	Machine Learning .....	165
6.2.5	Minimum Viable Product (MVP) .....	165
6.3	Applications in Other Areas .....	169
6.4	Conclusion.....	172
References	.....	174
List of Figures	.....	183
List of Tables	.....	192
Appendix A	.....	193
Appendix B	.....	198
Appendix C	.....	207
Appendix D	.....	211
Appendix E	.....	217
Appendix F	.....	218
Appendix G	.....	223

# List of Acronyms and abbreviations

Alternating current	AC
Analogue-to-digital converter	ADC
Arbitrary units	a.u.
Area under the curve	AUC
Artificial neural network	ANN
Ballistocardiograph	BCG
Bayonet Neil-Concelman	BNC
Beats per minute	BPM
Burn intensive care unit	BICU
Capillary refill time	CRT
Carbon dioxide	CO <sub>2</sub>
Cardiopulmonary resuscitation	CPR
Chronic obstructive pulmonary disease	COPD
Compound annual growth rate	CAGR
Computerized numerical control	CNC
Continuous positive airway pressure	CPAP
Delivery room	DR
Direct current	DC
Electromagnetic radiation	EMR
Endotracheal intubation	ETI
Endotracheal tube	ETT
End-tidal capnography	ETCO <sub>2</sub>
Far-infrared	FIR
Full width at half maximum	FWHM
General anaesthesia	GA
Heart rate	HR
Intensive Care Unit	ICU
Interquartile range	IQR
Intra-tracheal multiplex sensing	iTraXS
Isopropanol alcohol	IPA
K-nearest neighbour	KNN
Linear discriminant analysis	LDA
Logistic regression analysis	LRA

Lower oesophageal sphincter	LES
Magnetic resonance imaging	MRI
Minimum viable product	MVP
Multiple logistic regression analysis	MLRA
Nasogastric	NG
National Health Service	NHS
National Instruments	NI
Near-infrared	NIR
Newborn intensive care unit	NICU
Numerical Aperture	NA
Oesophageal intubation	OI
Orogastric	OG
Oxyhaemoglobin	OHb or HbO <sub>2</sub>
Peak inspiratory pressure	PIP
Peripheral capillary oxygen saturation	SpO <sub>2</sub>
Photodiode	PD
Photoplethysmogram	PPG
Plastic optical fibre	POF
PolymethylMethacrylate	PMMA
Polyvinylchloride	PVC
Post-intubation laryngotracheal stenosis	PILTS
Potential hydrogen	pH
Principal component analysis	PCA
Receiver operating characteristic	ROC
Sub-Miniature version A	SMA
Support vector machine	SVM
United Kingdom	UK
United States Army Institute of Surgical Research	USAISR
Universal serial bus	USB
Unrecognised oesophageal intubation	UOI
Upper oesophageal sphincter	UOS
Ventilator-associated pneumonia	VAP
World Health Organization	WHO

# Chapter 1 Background

## 1.1 Introduction

This chapter introduces the airway and its management in healthcare. Intubation is then described with a summary of its prevalence. Unrecognised oesophageal intubation (UOI) refers to the incorrect intubation of the oesophagus. This can quickly cause severe and irreparable damage to the patient; this problem is discussed in this chapter. A literature review summarises the main concept of this research which is to identify oesophageal intubation using the spectral properties of the trachea and the oesophagus via tissue reflectance spectroscopy. Finally, the aims and objectives of this research are described.

## 1.2 Airway Management

The assessments, preparations, and medical procedures required to restore and maintain an individual's breathing, or ventilation are referred to as airway management [1]. Airway management is essential in critical situations throughout emergency medicine and is necessary during respiratory distress, airway obstruction, and patient sedation [2]. The most *basic* and non-invasive management techniques include chest compressions, cardiopulmonary resuscitation (CPR), and a bag valve mask [3]. There are also more *invasive* and specialised methods such as a laryngeal mask, oro-/naso- pharyngeal tube, tracheotomy, and endotracheal intubation (ETI). Continuous positive airway pressure (CPAP) provides positive pressure via a mask worn over the mouth and nose [4]. This system can be used in place of ETI in some cases, especially for preterm babies where ETI is problematic. However, side effects can include congestion and nosebleeds. Furthermore, CPAP is generally reserved for patients with less severe respiratory distress and obstructive sleep apnea as it is a less dependable method to secure a patient's airway. ETI is preferred during severe respiratory distress or complete loss of respiratory function as during surgery or for coma patients. *Basic* methods are used for minor airway obstructions with more *invasive* methods used for severe or critical situations such as decreased levels of consciousness, airway injury, and respiratory failure. ETI remains the most ubiquitous modality for airway management.

The global market for airway management devices is estimated to be between 1.7 and 1.9 billion USD in 2022, expected to grow at a compound annual growth rate (CAGR) of ~7.6% to 2028 [5,6]. Chronic obstructive pulmonary disease (COPD) refers to a group of lung conditions which cause breathing difficulties, such as emphysema and chronic bronchitis. COPD is the patient group most commonly intubated. A 2019 World Health Organization (WHO) report found that worldwide, COPD is the third leading cause of death, and accounted for 3.23 million in 2019. Lower respiratory infections and trachea, bronchus, and lung cancers are the fourth and sixth leading causes of global deaths, respectively [7,8]. Given the standard and widespread use of airway management devices, the demand for research and development is significant, with innovation in the field still required.

## 1.2.1 The Airway

The trachea (Fig. 1.1a, [9]), commonly known as the windpipe, is a fibrocartilaginous tube that connects the larynx (throat containing the vocal cords) to the bronchi. The trachea branches off at the bottom (carina) into two primary bronchi. The branching then continues into bronchioles to exchange gases with pulmonary lobes and segments, known as the tracheobronchial tree. The average length of an adult's trachea is 10 to 13 cm [10], with a normative diameter of 13 to 27 mm in men and 10 to 21 mm in women [11]. 16 to 20 rings of c-shaped hyaline cartilage line the trachea [12]. A pseudostratified columnar epithelium and intercartilaginous membrane connect and cover the cartilage. This forms a thin mucosa and submucosa lining the internal surface of the trachea (Fig. 1.1b, [13]). Behind the posterior of the trachea and connecting it to the oesophagus is the trachealis muscle, with the distinct absence of the cartilage causing the posterior to be smoother, more flexible, and softer. Surrounding the trachea on the outside is the adventitia, a layer of connective tissue that loosely binds the trachea to the oesophagus and the musculocutaneous layer.

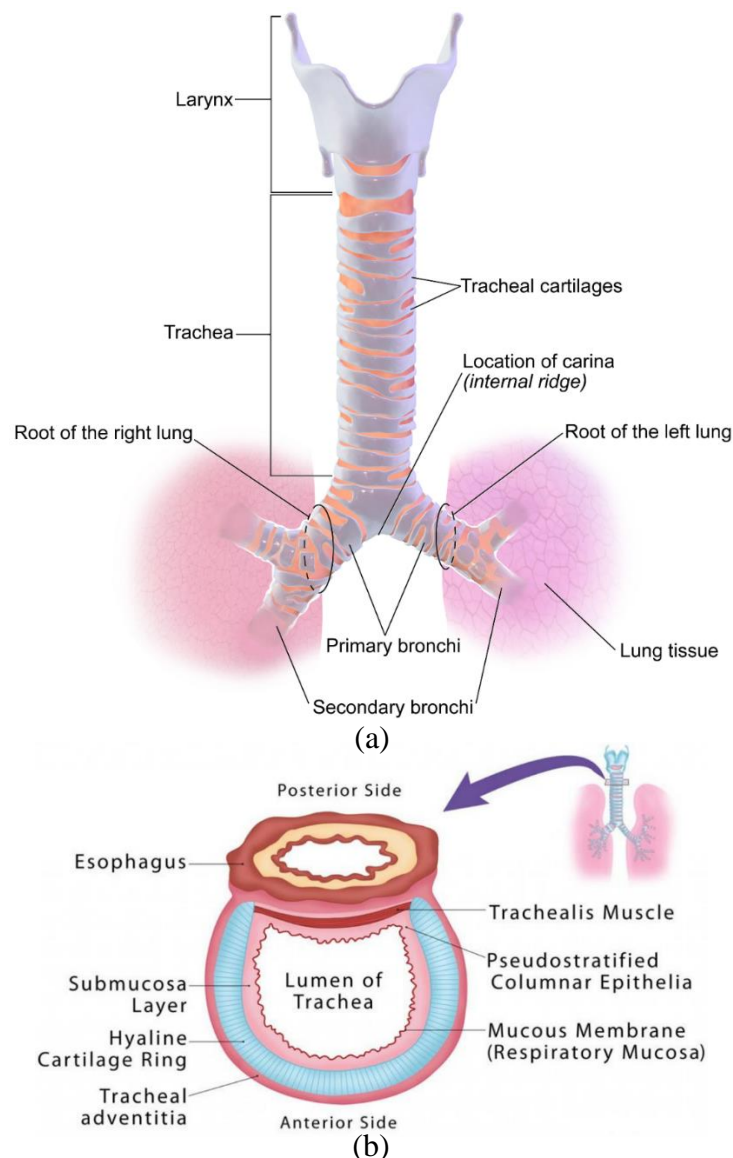


Fig. 1.1: (a) The anatomy of the trachea [9]. (b) Cross-section of the trachea and oesophagus [13]

The oesophagus is a muscular tube that connects the pharynx (upper throat) to the stomach, it is 25 to 28 cm long and approximately 20 mm in diameter [14]. The oesophagus runs behind the trachea and just in front of the spine, continuing behind the heart and then through the diaphragm and to the stomach. Its function is to deliver food and drink from the pharynx to the stomach. A bundle of muscles called the upper oesophageal sphincter (UES) is found at the very top of the oesophagus. The UES is used when breathing, eating, and vomiting to stop food and aspirations from going down the trachea. The UES is voluntarily controlled and is non-functioning during a loss of consciousness. The oesophagus has four layers, the innermost of which (lining the lumen) is the mucosa, consisting of a folded nonkeratinized stratified squamous epithelium [15], which varies from the simple columnar epithelium of the cardia (top part) of the stomach, giving an oesophageal mucosa that is paler. The lamina propria and muscularis consist of loose connective tissue, smooth muscle tissue, and elastic fibres. The submucosa comprises of elastic and collagen fibres, forming a dense connective tissue, along with veins, lymphatics, and the Meissner plexus. The third layer is the muscularis, containing longitudinal and circular muscle fibres which allow for peristalsis (waves of muscle contractions that move food through the oesophagus). The final layer is the adventitia, which surrounds the oesophagus and trachea. A histological cross-section of the oesophagus and trachea is found in Fig. 1.2a [16], and Fig. 1.2b [17], respectively.

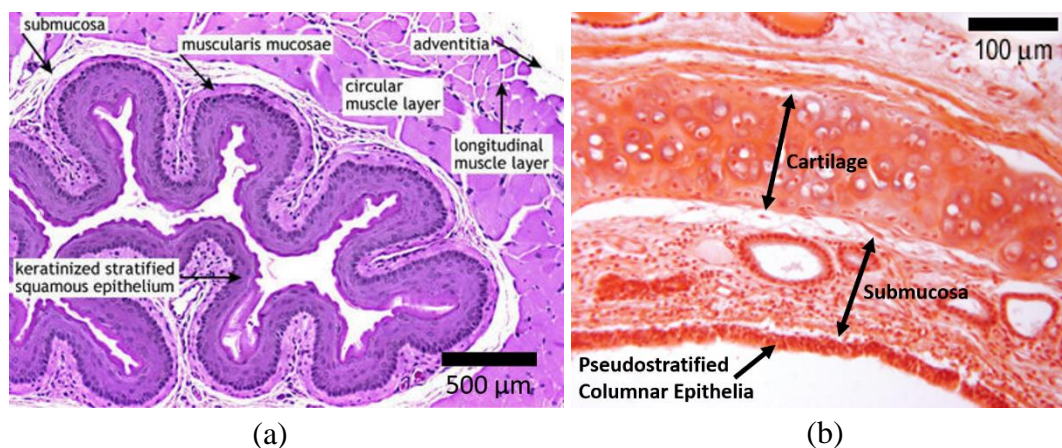


Fig. 1.2: Labelled histological cross-section of the (a) oesophagus [16], and (b) trachea [17].

As is discussed in Section 2.4, the detectability of oxygenated blood plays a key role in distinguishing between the trachea and oesophagus. Therefore, the blood flow to these organs is described in this section. Arterial blood supplies the trachea through tracheal branches of the inferior thyroid artery (Fig. 1.3). The inferior thyroid venous plexus drains the venous blood, which then empties into the brachiocephalic veins. Tracheal veins flow into larger laryngeal veins or directly into the left inferior thyroid vein, with the pulmonary plexus supplying innervation to the trachea [18]. The arteries approach the trachea branch and segment along its longitudinal axis, providing vascularisation to the tissues. Transverse intercartilaginous arteries enter the space between the tracheal rings of cartilage and then travel between the rings anteriorly or posteriorly where they terminate in the submucosal capillary plexus. The plexus provides a blood supply to the cartilaginous segments of the trachea, while secondary branches of the trachea-oesophageal arteries directly supply the membranous portions



of the trachea [19]. The oesophagus is supplied with oxygenated blood by much of the same arteries (Fig. 1.3). Primary blood flow to the oesophagus is provided by the inferior thyroid artery, with the thoracic portion taking blood flow directly from the aorta. The venous system starts at the submucosal plexus, perforates the muscular layer and empties into the azygos system [15].

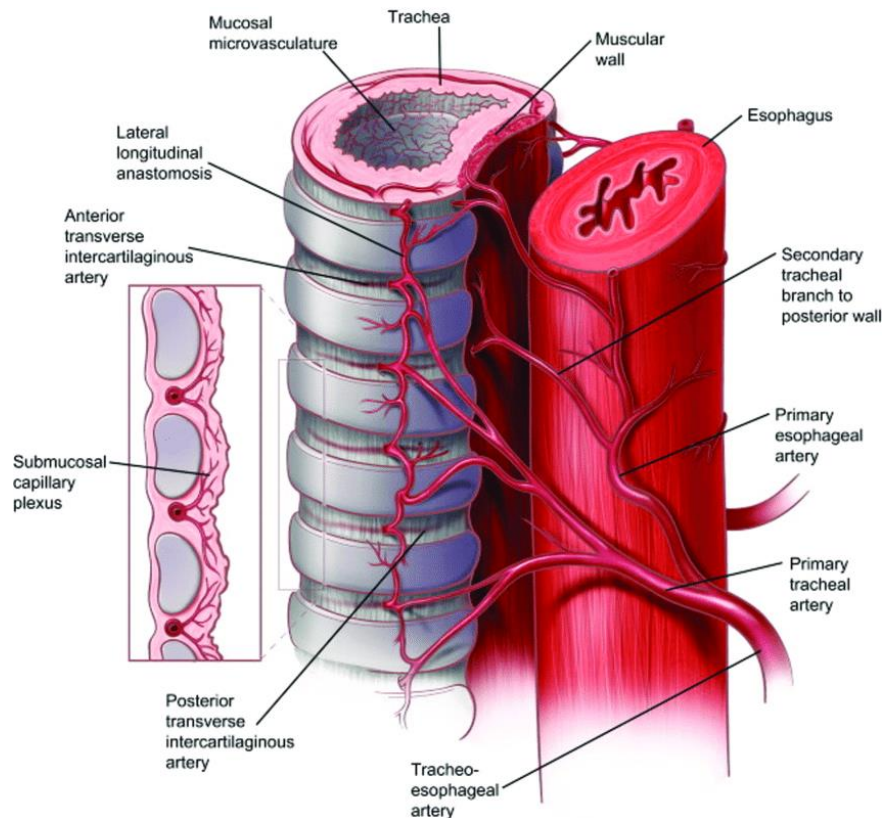


Fig. 1.3: Blood vessel network of the trachea and oesophagus [10].

The larynx (Fig. 1.4a, [20]) is a cartilaginous skeleton with muscles and ligaments that move and stabilise it, as well as a mucosa that lubricates and protects it from particles and pathogens [21]. The larynx serves three major functions: to protect the lower airway; to facilitate respiration; and to enable phonation (production of sound by the movement of the vocal cords). The skeleton of the larynx consists of nine cartilages, including the epiglottis at the top, the cricoid at the bottom, and the thyroid which surrounds and protects the middle portion of the larynx (Fig. 1.4a). The epiglottis is a leaf-shaped structure that protects the airway and prevents aspiration, during swallowing it covers the larynx to allow passage of food and drink into the oesophagus.

The vocal cords (Fig. 1.4b, [22]) consist of four folds of fibro-elastic tissues. The superior (true vocal cords) are ribbon-shaped and thin, while the inferior (false vocal cords) are wider and have a muscularis layer covering them. During intubation, one of the gold standard methods for confirming tracheal intubation is observing the ETT passing through the vocal cords into the larynx. Visualisation is made easier by the

use of a laryngoscope which widens the upper airway and helps to guide the ETT through the vocal cords. However, a short or narrow neck, obesity, bodily fluids obscuring vision, a large tongue, limited mobility, and trauma can make it difficult to observe the vocal cords. These factors contribute to a difficult airway, even when video laryngoscopy is used [23].

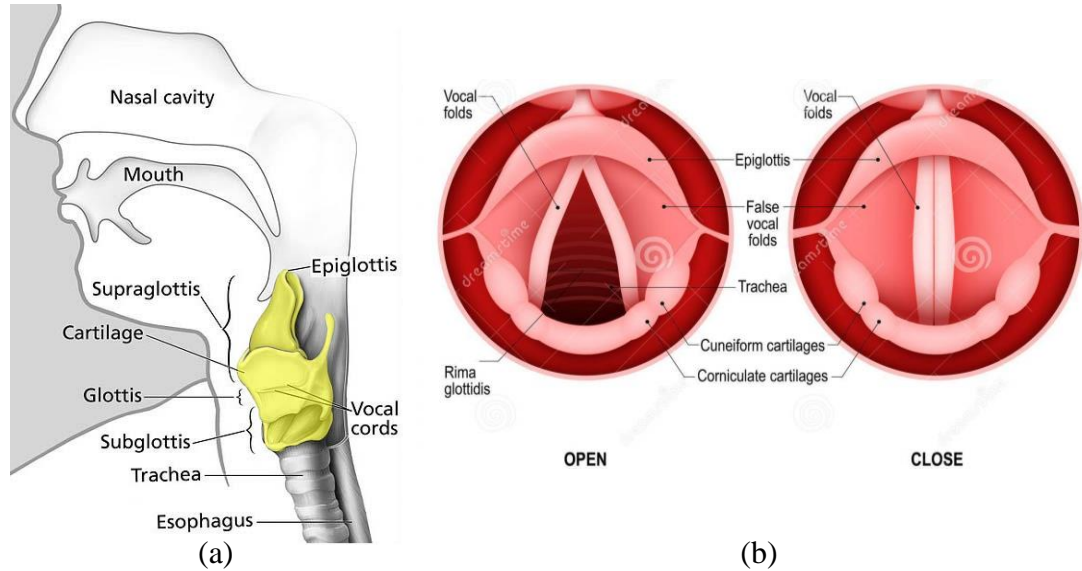


Fig. 1.4: (a) Anatomy of the larynx [20]. (b) Cross-section of the larynx showing the open and closed vocal cords [22].

## 1.2.2 Intubation

Intubation is a life-saving medical procedure performed by a healthcare professional [24]. The decision to intubate is a primary step in emergency resuscitation as a protected airway must be established to supply the necessary gases, medications, and anaesthesia. However principally, the inspiration of oxygen and the expiration of carbon dioxide ( $\text{CO}_2$ ). Therefore, if a patient's ability to sufficiently breathe on their own is compromised, they must be intubated. Intubation is required when a patient is in respiratory distress. For example, if a patient has incurred physical trauma or is suffering from anaphylaxis, smoke inhalation, or severely diminished consciousness. Intubation is also required for patients who are undergoing surgery and will be given general anaesthesia (GA), which suppresses some of the body's automatic functions that control breathing such as muscle control. For this reason, those who are in a coma must also be intubated.

The 2018 Global Surgery and Anaesthesia Statistics report [25], estimates 313 million surgical procedures performed globally per year. The same report finds that annually, in the US alone, 15 million intubations occur in the operating room and 650,000 outside the operating room, including 346,000 emergency department intubations [26,27], with the impacts of COVID likely inflating this number in still unknown ways and producing widely varying market sizes. In 2018 in the UK, over 1 million emergency and elective intubations were performed by the NHS [28].

An ETT (Fig. 1.5, [29]) consists of a flexible and hollow tube, usually made of polyvinylchloride (PVC). One end of the ETT is fitted with an adaptor which connects

to a ventilator. The other end, referred to as the distal end, is bevelled to allow for easier insertion through the mouth past the vocal cords and into the trachea. There are also typically holes (Murphy's eye) near the distal end of the ETT, providing an air passage should the hole in the distal end become obstructed by mucus or the tracheal wall. The tube is curved at a radius of  $140 \pm 20$  mm (Magill curve), as this is the natural curvature of the airway; the mouth, the throat, and the start of the trachea. This curvature makes insertion of the tube easier, as well as providing less resistance to the tissues once the tube has been inserted. This ensures the lumen of the ETT stays open and doesn't get pinched as it bends, since a straight tube may sharply bend once inserted. The tube has markings on it to determine the depth at which the ETT has been inserted, with the recommended depth of insertion to be between 21 and 23 cm for women and men, respectively. The distal end is positioned 4 cm above the tip of the carina (end of the trachea where it begins branching to the lungs) [30]. The vocal cord guide marker also helps to ensure proper depth placement as this should be in line with the vocal cords. The size of the tube is also important as it helps ensure a good fit in the trachea and is referred to by the internal diameter of the Tube. ETT sizes range from 2.0 to 12.0 mm in 0.5 mm increments, with the smaller sizes being used for neonates and paediatrics. The typical size for an average woman is 7.0 to 7.5 mm and an average man is 7.5 to 8.5 mm, although this is dependent on patient weight, height, and presence of pulmonary or airway disease.

The cuff of an ETT is a small balloon typically made from PVC, although other materials such as polyurethane, silicone, and latex can be used [31]. The cuff is inflated to secure and hold the ETT in the patient's airway. The cuff also forms a seal in the trachea so gases cannot escape around the tube, and to prevent fluids, secretions and aspirations around the cuff. The cuff is typically inflated to a pressure of 20 to 30 cmH<sub>2</sub>O (1.96 to 2.94 kPa, where cmH<sub>2</sub>O is the preferred unit clinically) inside the cuff. The exact pressure is determined by a clinician and is patient-dependent. However, an ideal pressure is one which sufficiently seals the airway and doesn't leave folds in the cuff, as well as applying the minimum pressure to the tracheal wall to avoid ischemia.

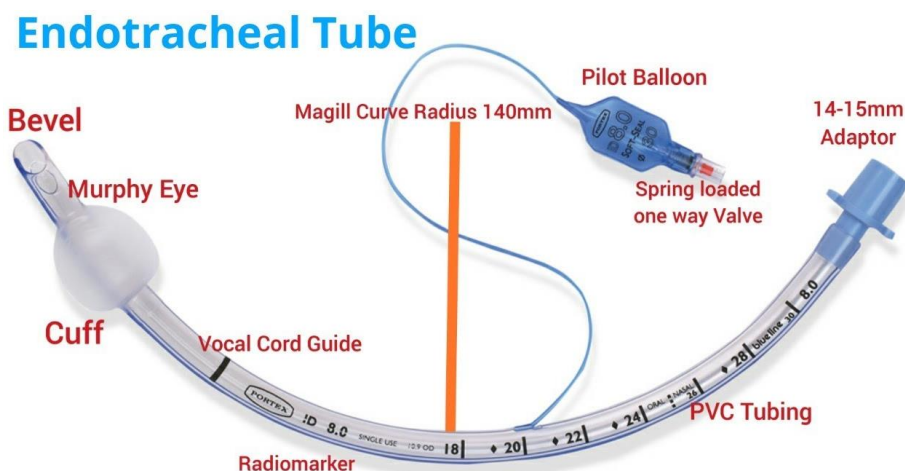


Fig. 1.5: A labelled diagram of an endotracheal tube (ETT), showing the key standard features [29].

### 1.2.3 Unrecognised Oesophageal Intubation (UOI)

Placement of the ETT incorrectly into the oesophagus leads to severe medical complications within minutes. Without the lungs being supplied with oxygen, and CO<sub>2</sub> not being removed, the patient will quickly become hypoxic due to asphyxiation. UOI leads to cardiac arrest, the development of brain damage, and ultimately death [32,33]. Recent high-profile UOI cases have arisen in the UK from UOIs. In 2016, two patients in for routine surgeries died from UOIs [34,35]. In 2020, Glenda Logsdail [36] received a UOI. The UOI caused severe brain damage and she sadly passed away 5 days later due to hypoxic-ischaemic encephalopathy. The Senior Coroner stated that “...there is a risk that future deaths could occur unless action is taken.”. The patient did not have a difficult airway and a standard Macintosh laryngoscope (to widen the upper airway and help guide the ETT) was used. Furthermore, continuous end-tidal waveform capnography was used throughout the procedure. Demonstrating that even when the current gold standard is used, UOIs can still happen.

In the 1990s, with the widespread use of end-tidal capnography, UOIs decreased from 11% to 6% [37], with an estimated further decrease to 1-2% between 1990-2013 [38, 39]. A 2019 study [40], of 10 US centres, captured data from newborn intensive care unit (NICU), and delivery room (DR) intubations (N = 2009 & 598, respectively), from 2014-2017. The study found that 11% of the NICU and DR intubations involved oesophageal intubation. Correct ETT placement success rates for junior doctors intubating neonates is less than 50%, with oesophageal intubations being common [41]. A UK study found that from 1995-2007 [42], oesophageal intubation accounted for 6% of anaesthesia-related claims. A recent international study of emergency intubations across 29 countries reported an incidence rate of 1 in 18 for the critically ill [43]. Recent publications have suggested evidence that UOI is a major concern and must be addressed [44]. Several factors may contribute to a failed intubation. A clinic’s operational environment providing a chaotic prehospital environment, or multiple severe medical emergencies occurring at the same time for a single patient increases the rates of a failed intubation [45]. Patient medical conditions such as a swollen airway, obesity, limited neck mobility and haemorrhaging can all contribute to a difficult airway [46]. In the Intensive Care Unit (ICU), difficult airways are present in 4.6 to 23% of patients, with an increase to 50% in the prehospital condition [47].

### 1.2.4 Clinician Questionnaire

A questionnaire was formed by the UoN/NUH team about the introduction of a smart ETT. The full results of the questionnaire are found in Appendix B. The questionnaire was given to 105 clinicians in 2019. 90.5% identified themselves as working in anaesthesia. 68.6% had over 10 years of experience, with 79% performing over 5 intubations per week, and 74.3% estimating they had performed over 1000 intubations. The participants were then asked what parameters they were interested in during endotracheal intubation. They were asked to rate their interest on a scale of 1-10 for the capabilities of: cuff-to-trachea contact pressure, heart rate (HR), respiration rate, peripheral capillary oxygen saturation (SpO<sub>2</sub>), blood pressure, capillary refill, pH,

CO<sub>2</sub>, tube displacement, and tracheal identification. Of the 10 parameters asked, the ones that were most important to the participants were tube displacement and tracheal identification, finding 63.5 and 60.2% ranked these parameters as 10 (most important) respectively. The third most ratings of 10 were given to CO<sub>2</sub> at 44.8%.

The participants were then asked what reduction in complications would be most important to them and then given the options: ventilator-associated pneumonia (VAP), post-intubation laryngotracheal stenosis (PILTS), sore throat, ischaemia, and oesophageal intubation (Fig. 1.6). The reduction in complications that was most important was oesophageal intubation, with 66.7% of participants rating this as a 10. The second most reduction of complication importance was ischaemia, with 39.4% of ratings of 10.

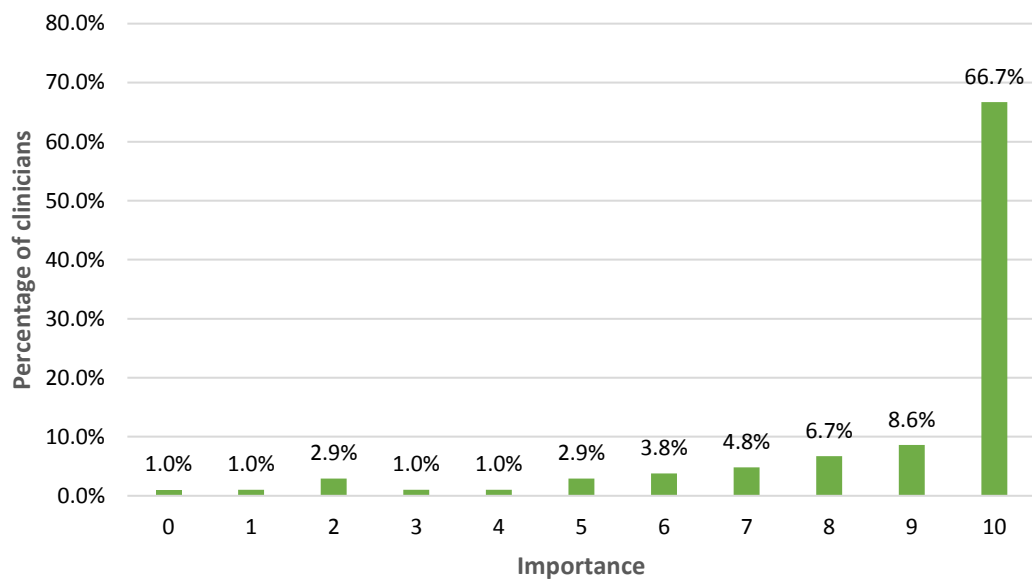


Fig. 1.6: Results of the question ‘What reduction in complications would be most important to you? Please rank them from 0 to 10, with 10 being most important for you’, for oesophageal intubation.

Finally, participants were asked if smart ETTs reduced complications from intubation would they want to use them. 87.5% responded yes, 12.5% responded maybe, and 0% responded no.

## 1.3 Literature Review

### 1.3.1 Spectroscopy

Spectroscopy is a powerful and extensive topic, with the introduction of lasers, LEDs, and optical fibres in the 60s working to widen this field further [48, 49]. Spectroscopy has helped us understand and quantify galaxies and stars, as well as molecules, cells, and atoms [50, 51]. All atoms and molecules emit, absorb, and scatter electromagnetic radiation (EMR) differently, measuring how a substance interacts with EMR is the field of spectroscopy.

Induced absorption is the process by which an atom or molecule absorbs a quantum of EMR, causing a transition from a lower energy state ( $E_1$ ), to a higher energy state ( $E_2$ ), where the absorbed energy must be related to the photon by,

$$E_2 - E_1 = \frac{hc}{\lambda} \quad (1.1)$$

where  $h$  is Planck's constant.

The emission of light can be spontaneous or induced. An atom or molecule may spontaneously emit a quantum of EMR, moving from a higher energy state to a lower energy state, described by the reverse of Eq. (1.1), where a photon carrying the energy is emitted. Induced emission occurs when a quantum of radiation causes the emission, which is the working principle for lasers,

$$E_2 + \frac{hc}{\lambda} = E_1 + 2 \frac{hc}{\lambda} \quad (1.2)$$

There are different types of spectroscopy depending on the wavelengths of EMR used, with the classical types being infrared and near-infrared [52], ultraviolet-visible [53], nuclear magnetic resonance (radio wave) [54], Raman [55], and X-ray [56]. However, there are many more specific and niche methods [57, 58]. The different energies of EMR used correspond to the transitions an atom or molecule may go through, which are rotational, vibrational, or electronic transitions. A molecule may also be ionized, or it may scatter the radiation in the Raman process. Raman spectroscopy provides detailed information on the structure of molecules by analysing their vibrational modes, detected by inelastic scattering. However, even with perfect contact with the sample, a powerful laser is required to generate low signal Raman peaks which are prone to noise. Therefore, this method is impractical for use in a clinical setting on an invasive medical device and diffuse reflectance spectroscopy is preferred.

This research study is mostly concerned with relatively low-power diffuse visible light reflectance spectroscopy, with the typical transitional process being electronic.

### 1.3.2 Tissue Reflectance Spectroscopy

A single compound in a solution has the potential to be entirely resolved by spectroscopic techniques, provided it interacts with the wavelength of light used and there is an available excited energy state. The elemental composition, atomic structure, topology, and bond types of a molecule could all be determined spectroscopically. Traditional spectroscopy is tuned to identify the wavelengths of light that interact with matter on the atomic or molecular level, revealing information about the substance. However, tissues are extremely complex structures of cells made from many different molecules. Therefore, diffuse reflectance spectroscopy is used, which primarily measures only the intensity of light that is reflected, absorbed, and transmitted, at different wavelengths on the macro scale of a sample [59].

Visible light interacts with biological tissues providing a safe and rapid spectroscopic evaluation of biochemical, structural, and physiological parameters. Infrared and visible light is most appealing and common due to low energy EMR being non-ionising and exposure to being much safer than higher energy radiation. Furthermore, electronic transitions reveal a large amount of information about the tissues, such as the macro structure, composition, and colour.



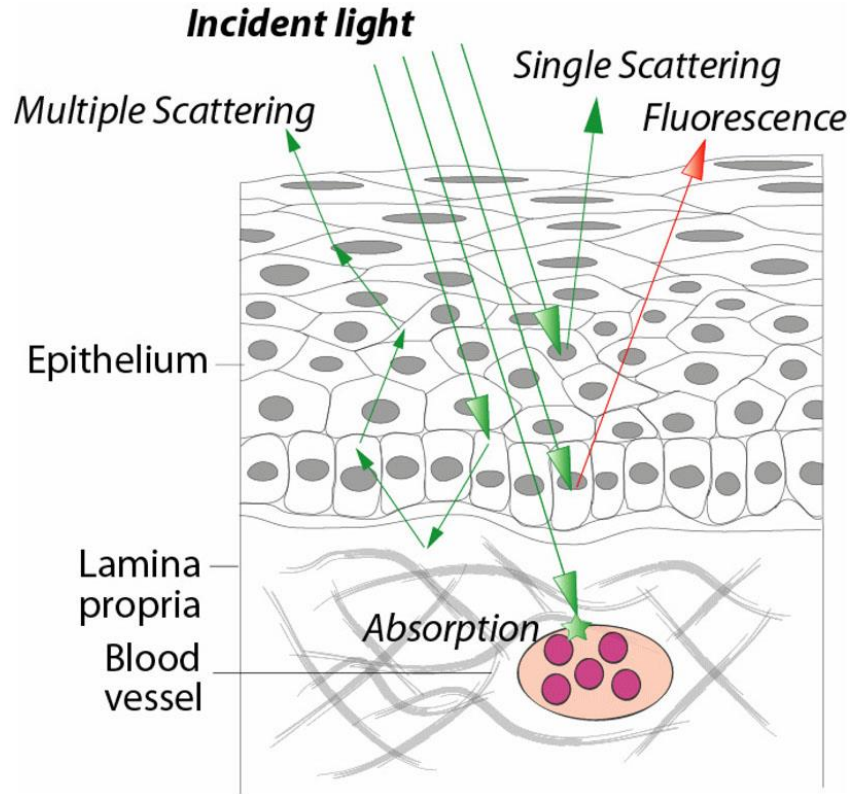


Fig. 1.7: Diagram of how incident visible light interacts with a generic tissue [60].

Incident light takes a complicated path through a tissue (Fig. 1.7, [60]), where light may be both absorbed and scattered. Absorption occurs at specific wavelengths depending on the biochemical structure of the cells. Whereas, scattering changes the trajectory of all wavelengths of light by different amounts and is the result of random variations in the refractive index caused by the microstructure of the tissue. The amount of light that is scattered and absorbed gives access to information about the tissue.

The absorption of light by tissue can be characterised by the Beer-Lambert law, which shows that absorption ( $A$ ) is proportional to the concentration ( $c$ ) of the solution,

$$A = \epsilon cl = \log\left(\frac{I_0}{I}\right) \quad (1.3)$$

where,  $\epsilon$  is the molar absorption coefficient of the solution,  $l$  is the path length the light takes,  $I_0$  is the intensity of the incident light, and  $I$  is the intensity of the transmitted light. Eq. (1.3) models the simple case of a translucent medium with constant  $\epsilon$ , held in a container of length  $l$ . Many variations of the Beer-Lambert law exist that account for the interactions outlined in Fig. 1.7, such as variable photon path lengths and multiple molar absorption coefficients [61, 62].

### 1.3.3 Pulse Oximetry

Perhaps the most common use of tissue spectral reflectance measurements is pulse oximetry [63]. Pulse oximetry is used to continuously measure the oxygen saturation of red blood cells contained in biological tissues by finding the ratio of oxyhaemoglobin (OHb) to deoxyhaemoglobin (Hb). It is a non-invasive, easy, and

painless measure of how well oxygen is being sent to the different body parts and tissues. OHb and Hb absorb light differently, with red and near-infrared (NIR) light typically being used ( $\lambda = 660$  and  $940$  nm) as absorption at these wavelengths differs greatly (Fig. 1.8, [64]). The use of at least two wavelengths is required so that a ratiometric comparison can be made between oxygenated and deoxygenated haemoglobin. Although in theory almost any two wavelengths where the relative absorptions change could be used [65]. However, these two wavelengths penetrate tissues well, whereas yellow, green, blue, and far-infrared (FIR) light is highly absorbed by tissues [66].

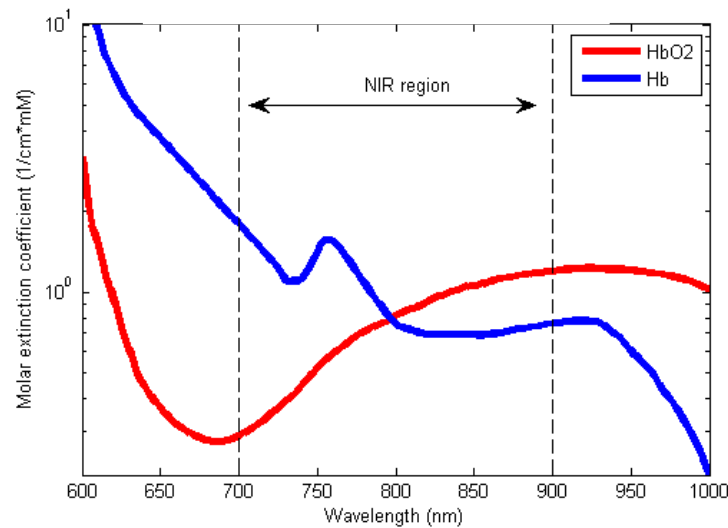


Fig. 1.8: Absorption characteristic of oxyhaemoglobin (red) and deoxyhaemoglobin (blue) [64].

Pulse oximetry can be operated in transmission mode or reflection mode. Transmission mode functions by placing a light source and detector opposite to each other, for example on the fingertip or the ear. Measurements are then made through the tissue and a large volume is detected. Transmission pulse oximetry is the most popular modality due to its accuracy and reliability. However, if the site is not peripheral, then detection cannot be made through it, as is the case with the trachea and oesophagus. Therefore, reflection mode pulse oximetry must be used. Reflection pulse oximetry functions by placing the light source and detector on the same side of the tissue. Light is reflected from the measurement site and is detected on the same side of the tissue. Pulse oximetry detects peripheral oxygen saturation ( $SpO_2$ ) as an estimate for arterial oxygen saturation  $SaO_2$ , and functions due to fluctuations in the amount of absorbed red and IR light due to the cardiac cycle. A photoplethysmogram (PPG) is obtained from a pulse oximeter and detects blood volume changes from the cardiac cycle [67]. A PPG consists of a non-pulsatile “direct current” (DC) component and a pulsatile “alternating current” (AC) component (Fig. 1.9, [68]). The DC component originates from light returned to the detector directly from the light source, the tissues, non-pulsatile venous and arterial blood, and respiratory movements. The AC component originates from changes in blood volume that occur between the systolic and diastolic phases of the cardiac cycle in the arteries and capillaries, with the fundamental frequency being the heart rate.



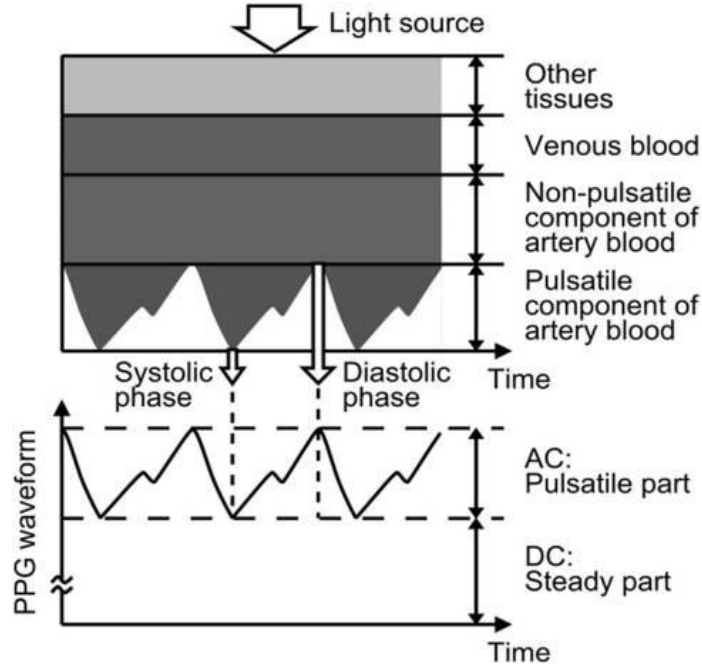


Fig. 1.9: photoplethysmogram diagram [68].

$SpO_2$  can be calculated from the PPG by finding  $R$ : the double-ratio of the pulsatile ( $AC_{red}$  and  $AC_{IR}$ ) and non-pulsatile ( $DC_{red}$  and  $DC_{IR}$ ) components of the red and IR light (Eq. (1.4)),

$$R = \frac{AC_{red}/DC_{red}}{AC_{IR}/DC_{IR}} \quad (1.4)$$

$R$  can then be related to the oxygen saturation from oxygen desaturation experiments that usually range from 100 to 70% in healthy volunteers.

## 1.4 Identifying Oesophageal Intubation

Visualizing the ETT passing through the vocal cords is the most direct method of identifying the correct placement. This is performed with a laryngoscope, which is used to move the tongue to the side and allow viewing of the glottis so that a clinician can see the ETT's movement through the larynx and between the vocal cords. The introduction of the video laryngoscope in 2001 allowed for this to be carried out more effectively [69], where a camera is mounted to the tip of a laryngoscope and displayed on a screen (Fig. 1.10, [70]). A traditional (non-video) laryngoscope is always used to aid intubation. Furthermore, there is a widespread use of videolaryngoscopy today, with UK hospitals having availability in 91% of operating theatres and 50% of intensive care units [71]. However, as stated previously, medical conditions such as a swollen airway, obesity, limited neck mobility, and haemorrhaging can all make it difficult to visualize the vocal cords, even when video laryngoscopy is used [72]. Furthermore, fluids covering the camera lens can make it difficult to clearly view the airway. Other visual cues may be chest movements during ventilation, condensation in the tube, and auscultation (listening to heart, lungs and other sounds) of bilateral breathing. However, these methods are unreliable and may not always be possible depending on the patient. Furthermore, ventilation of the stomach may cause

condensation, movement, and generate sounds similar to that of correct intubation [73]. Transtracheal ultrasound ETT placement verification is a more novel method with limited use currently. Ultrasound gives a real-time view of the trachea performed quickly and may be advantageous in neonates where other methods may fail [74,75]. However, ultrasound requires a trained operator and is expensive.

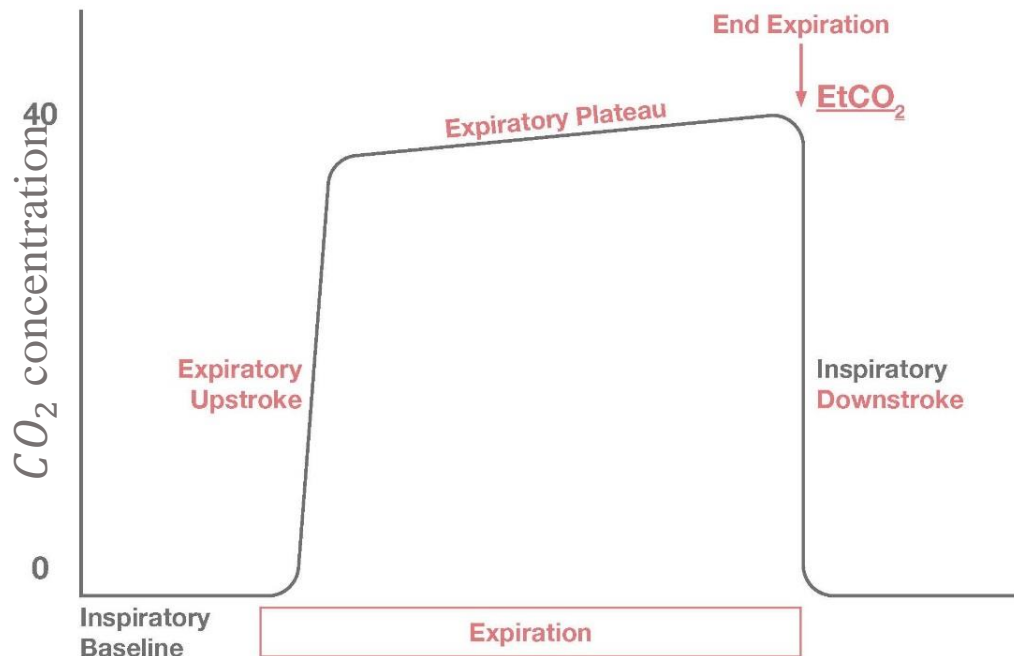


Fig. 1.10: An example of a video laryngoscope (Medcaptain, model VS-10 series) [70]

The measurement of the expiration of  $\text{CO}_2$  from the lungs indicates correct ETT placement. This can be performed with a colorimetric device that changes colour in the presence of  $\text{CO}_2$  (Fig. 1.11a, [76]). However, End-tidal capnography (ETCO<sub>2</sub>), also known as waveform capnography [77], measures the  $\text{CO}_2$  partial pressure waveform, typically as a function of time and is more quantitative (Fig. 1.11b, [78]). The colorimetric devices are inexpensive and highly portable, suitable for prehospital. However, ETCO<sub>2</sub> is more reliable as the breath-to-breath  $\text{CO}_2$  volume exhalation is tracked so the clinician can be more confident of a correct intubation.



(a)



(b)

Fig. 1.11: (a) Colorimetric device for the detection of  $\text{CO}_2$  (Nellcor, model EASYCAPII), used to assess correct ETT placement [76]. (b) Typical  $\text{ETCO}_2$  waveform for a healthy patient [78].

$\text{ETCO}_2$  is considered the gold standard of non-visual confirmation of correct ETT placement, with typical identification rates of  $> 90\%$  [79,80]. However, there are limitations, and a variety of conditions can affect  $\text{ETCO}_2$  identification rates. For example, patients in cardiac arrest, those with low tidal volumes, pulmonary disease, and mixed pathophysiology may produce erroneous readings. Furthermore, the interpretation of the waveform can be problematic and requires training [81]. These factors can reduce  $\text{ETCO}_2$  identification rates to  $64\%$  [82,83,84]

## 1.4.1 The Tracheal Characteristic

The only direct literature on the distinguishing of tracheal and oesophageal tissues using fibre optic sensing is led by the United States Army Institute of Surgical Research (USAISR). The first of the journal articles by Nawn *et al.*, titled ‘Distinguishing tracheal and esophageal tissues with hyperspectral imaging and fiber-optic sensing’ was published in 2016, [85]. Two *ex-vivo* porcine tracheas and oesophagi were dissected, and a commercial fibre optic probe was used to sample the tissues. Finally, an *in-situ* porcine experiment was performed.

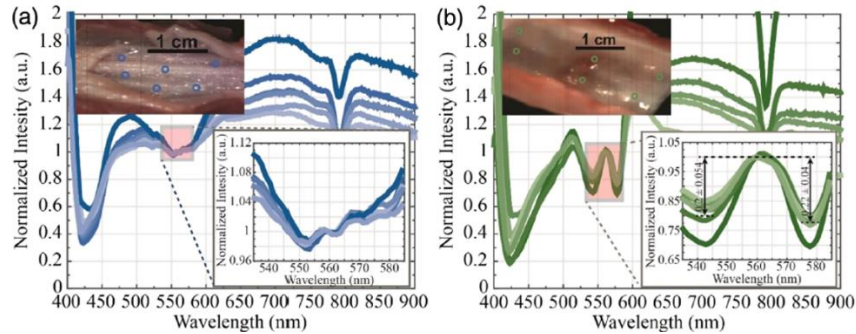


Fig. 1.12: Reflectance spectra for (a) two *ex-vivo* porcine oesophagi and (b) trachea, with photographs of the tissues, highlighting the positions sampled [85].

An interesting characteristic in the 530 - 590 nm wavelength range was observed in the trachea (Fig. 1.12). The characteristic was found to consist of a central peak at  $\lambda \approx 561$  nm, with a trough either side at 542 and 578 nm, with a significant difference in the locations of the minima between the trachea and oesophagus ( $p$  values = 0.0048 and 0.0001, respectively).

The publication offers the first known observations of spectral differences between the trachea and the oesophagus, that could potentially be used to distinguish the two tissues. However, the paper has its limitations as the first of its type. There is no convincing argument for the origin of the tracheal characteristic, only observations that there are physiological differences from the oesophagus. Furthermore, the paper utilises principal component analysis (PCA) as a possible method to classify the tissues. PCA is generally reserved for dimensionality reduction of large multivariate data sets and to highlight regions of variance in a dataset. Furthermore, the *in-situ* experiments were performed shortly after euthanasia, where the animals may be undergoing rapid physiological changes as the organs begin to shut down, which could impact the spectral properties of the tissues.

In 2019 a second journal article was published by Nawn *et al.*, titled ‘Using spectral reflectance to distinguish between tracheal and oesophageal tissue, entitled ‘applications for airway management’ [86]. This paper was a continuation of the first, containing human cadaver models, as well as more focus on classifying the tissues. The group once again utilised a commercial fibre optic probe, although this time with a prism attached at the distal end so that light is directed into the tissue, as opposed to parallel to the surface.

Finally, the characteristic was found to be present in the trachea of human cadavers (Fig. 1.13a), with its absence in the oesophagus (Fig. 1.13b). The spectral feature is more pronounced in the oesophagus of *in-vivo* porcine subjects than in *in-situ* human cadavers. Therefore demonstrating, that the ‘unique tracheal’ characteristic is partially detectable in the oesophagus. This paper also has the first mention of the feature’s similarity to the absorption characteristic of oxyhaemoglobin (OHb). However, it unmistakably originates from OHb, as is discussed in Section 2.4.

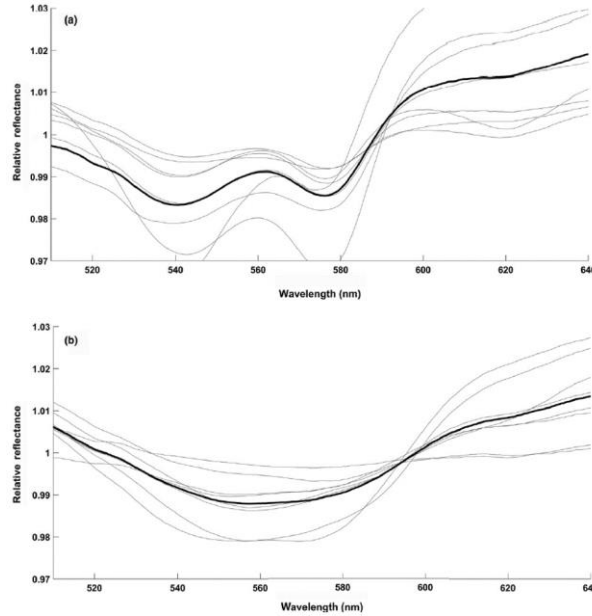


Fig. 1.13 Spectra from human cadavers, with the faint grey lines representing the averaged spectra for each cadaver, and the dark black line representing the average spectra of all human cadavers, with (a) being trachea and (b) being the oesophagus [86].

Classification of the tissues provided a sensitivity of  $\geq 65\%$  and specificity of  $\geq 85\%$ . The paper demonstrates the potential for spectral reflectance to distinguish tracheal and oesophageal tissues in humans, although it is lacking *in-vivo* human data, with the next best cadaver models being used. There is the first attempt to construct a method to classify the tissues. However, many of the same limitations persist from the first paper. A commercial fibre optic probe is used which is much too large to be useful in a clinical setting, with ventilation having to be stopped to fit the probe down the lumen of the ETT. A limited number of spectra are taken (15 measurements per tissue per porcine, and 5 spectra per tissue per human cadaver), resulting in a total of 145 captures across 7 animals and 8 human cadavers, with only the average spectra of each tissue presented in the statistical analysis. A halogen light source is also still used which produces more random variability light than alternatives, more heat, and has higher energy consumption.

A second paper in late 2019 by Blackburn *et al.*, titled ‘Testing of novel spectral device sensor in porcine model of airway obstruction’ [87], looks to develop a method to produce oxygen desaturation (hypoxia) and increased  $CO_2$  partial pressure (hypercapnia), in a porcine model. It verifies that the tracheal characteristic persists under asphyxiation, which is important as a patient requiring intubation may be hypoxic, and the ETT placement sensor must function properly in this scenario.

The paper goes on to argue that due to the presence of the unique profile in the *ex-vivo* porcine trachea, human cadavers, and hypoxic *in-vivo* porcine, it may not be attributed to the presence of OHb as previously thought. It is claimed that the profiles are intrinsic to the tissues. This is an unreasonable assumption as the samples will still be perfused with oxygenated blood long after death and during times of severe hypoxia. Furthermore, during the *ex-vivo* case, the blood remaining on and in the sample may become highly oxidised by the air. This can be seen when taking blood gas measurements as you must stop it from being exposed to the air otherwise it rapidly oxygenates giving false readings.

Another recent journal article from the USAISR, Berard *et al.*, titled ‘Spectral Reflectance can Differentiate Tracheal and Esophageal Tissue in the Presence of Bodily Fluids and Soot’ [88], looks to determine if confounding factors such as the presence of blood, soot, vomit, and saline affect the distinguishing of the tissues. The tracheal characteristic was found to remain present in all trachea samples with confounding fluids, with its absence in the oesophagus. This paper shows evidence that the characteristic is robust enough for clinical use. However, an unmentioned and clear limitation of this study is the lack of spectral measurements of the oesophagus with confounding factors, especially as it has been alluded to that the presence of the characteristic could be partially related to OHb. Therefore, a key result is whether the trachea and oesophagus can be distinguished when the oesophagus is in the presence of blood, as this may produce an oesophageal spectrum that is more closely matched to a tracheal one.

The most recent paper to date by the USAISR was published in April 2022 by Bedolla *et al.*, entitled ‘Spectral Reflectance as a Unique Tissue Identifier in Healthy Humans and Inhalation Injury Subjects’ [89]. This is the first use of living humans as a model, as well as spectral measurements in the buccal mucosa and posterior oropharynx, on healthy patients and those that have been admitted to the burn intensive care unit (BICU). However, they were unable to collect data in the oesophagus of the patients due to spectral probe size causing potential damage to the oesophagus by inserting a large commercial bifurcated probe containing 7 fibres. The tracheal characteristic is present in the healthy human subjects studied. However, due to the small margins, they claim the statistical difference is not enough for clinical relevance at this stage.

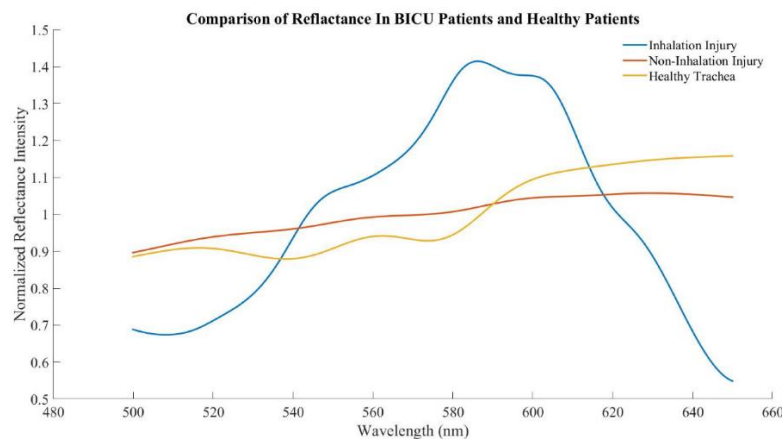


Fig. 1.14: Spectra captured (Bedolla *et al.*) in the trachea of healthy human subjects, subjects admitted to BICU with inhalation injury, and BICU patients with non-inhalation injury [89].

An interesting result from Bedola's paper is that the tracheas of BICU patients with and without injury caused by smoke inhalation did not have the tracheal profile in their spectra (Fig. 1.14). There is a clear spectral shape change between the patients although there is no statistical difference in the ratios.

Perhaps the most important finding in this Bedola paper is that the tracheal characteristic persists in living human patients, which is the first time this has been demonstrated. They also found that the spectral characteristic was absent in all the BICU patients studied. This is problematic for an ETT placement sensor as burn victims may lack the tracheal spectral profile, although they argue that they can still distinguish the tissues. It is of note that healthy patients produce a tracheal spectral shape that is different to both non-inhalation injury patients and patients with inhalation injuries. This implies that although they were not diagnosed with inhalation-related injuries, their tracheas may have been affected in some way. This could be utilised by a sensing technology for increased diagnostic capabilities. Without the complementary oesophageal data, the study is unable to determine the characteristic's ability to distinguish the tissues in living human patients. The spectral probe size was the limiting factor here, where they could not pass the probe into the oesophagus without damaging the patients. Furthermore, only three captures were taken on each tissue group

To summarise the findings across the USAISR papers, a spectral characteristic has been found in the trachea with its absence in the oesophagus. A statistical spectral difference between the tissues has been verified in *ex-vivo*, *in-situ*, and *in-vivo* porcine tissues, as well as human cadavers. The difference persists in hypoxic and hypercapnic *in-vivo* porcine models, as well as the feature persisting in the presence of blood, vomit, soot and, saline. Finally, the tracheal characteristic is present in living healthy humans.

## 1.5 Summary & Aims

Airway management is a major field in healthcare, with innovations and technologies such as video laryngoscopes and capnographical methods driving improvements to patient outcomes. However, there is an opportunity to decrease the incidents of oesophageal intubations further and provide measurements of core physiological parameters through tissue reflectance spectroscopy performed in the trachea. An alternative method of incorrect ETT placement detection is therefore described in this research, through the development of a compact sensor that can be integrated into a standard ETT.

A solid foundation has been established by the USAISR, although there are limitations across the literature. A modified commercial probe ( & Fig. 1.15) was used across all their publications, with a large, metal-coated distal end. The probe was modified by attaching a prism or redirecting mirror to the distal end, causing light emission at 90° and into the tissues. This is ideal in the experimental stage as a high proportion of light is brought to and from the tissues, as well as consistency in the manufacturing process reducing variability between measurements. However, in a clinical setting, a large probe is not useful or appropriate. Ventilation must be stopped to place the probe down the lumen of the ETT, the large metallic end may also cause damage to the throat,



trachea, and oesophagus. The procedure also requires valuable time and effort by the clinician.



Fig. 1.15: An example of one of the commercial fibre optic probes used by the USAISR during research by Gulf Fiberoptics (R200-7-UV-VIS).

There is no convincing argument for the origin of the tracheal characteristic, with conflicting arguments across the literature by USAISR. It is well documented elsewhere in literature that this feature originates from OHb, as is described in Section 2.4. Therefore, is a secondary goal of this project to establish the source of this spectral shape, as well as its limitations. A large halogen light source was used by the USAISR, which produces high-intensity light in the relevant wavelength region, although this is relatively expensive and bulky. Therefore, substituting this for an LED is beneficial. The use of a spectrometer is also beneficial during the initial experimental stage as one can precisely analyse a wide wavelength region on a single device. However, spectrometers are large and expensive, and when only a few wavelengths are needed for analysis, photodiodes are a much cheaper alternative. Finally, an algorithm to distinguish the tissues must be developed by comparing the possible candidates for the best performance.

Based on the review of the literature, the characteristic used to distinguish the trachea and oesophagus is weakly understood, with an exploration into its origin in Chapter 2. There is also an unmet need for an ETT placement sensor, which could be used seamlessly by clinicians during regular intubation procedures to indicate oesophageal intubation, this is addressed in Chapter 3. Once an ETT placement sensor has been manufactured, accompanying computational methods must be developed to classify the data and distinguish the tissues, as found in Chapter 4. A brief description of the intra-tracheal multiplexed device, known as iTraXS is described in Chapter 5, along with a description of the first animal study. The application of an ETT with integrated placement is detailed in Chapter 5 during an *in-vivo* porcine animal study. Finally, Chapter 6 demonstrates possible further development of this technology and applications to other areas, along with final conclusions.



## Chapter 2 Spectral Tissue Characterisation

### 2.1 Introduction

This chapter verifies the presence of a tracheal spectral characteristic that has been documented by the USAISR [85-89], with an exploration of its origin. The research begins with preliminary and qualitative measurements made by a diffuse reflectance probe, similar to that of Fig. 1.15. These measurements are made to verify the findings of the literature found in Chapter 1, as research into this topic is limited. Appropriate opto-electronic components are chosen, refined, and the tissue spectra are characterised. Once initial measurements provide evidence that the previously reported spectra can be replicated, research into the presence and origin of the characteristic is conducted. Finally, the optimal distance between the sensor and the tissue is explored. Ethics for this research was reviewed and approved by The University of Nottingham Faculty of Engineering Research Ethics Committee (Appendix A).

### 2.2 Commercial Reflection Probe Measurements

The opto-electronic components (Fig. 2.1) were chosen as they were all operational in the wavelength region that contains the spectral feature used to distinguish tracheal and oesophageal tissues (530 - 590 nm). A visible/near-infrared bifurcated reflection probe (Ocean Optics, model R600-7-VIS-125F), with a core diameter 600  $\mu\text{m}$  and wavelength range 400-2100 nm had its illumination port connected to a tungsten halogen broadband light source (Ocean Optics, model HL-2000). The wavelength range of the light source was 360-2400 nm, with a nominal bulb output power of 4.75 W, a 0.15% peak-to-peak optical output variation and <0.3% optical output drift per hour. The detection leg of the probe was connected to a miniature spectrometer (Ocean Optics, model USB2000+UV-VIS-ES), with a wavelength range of 200-850 nm and a resolution of 0.384 nm. The integration time of the spectrometer was varied between different experiments, to achieve around 90% of the maximum saturation of the device. Typically, this means setting an integration time between 0.1s and 1s, depending mostly on the quality of the connections in that experiment and the tissue with which the light is coupled (tissues with higher reflectance require a shorter integration time). The actual integration times deployed for the experiments are stated at the start of each section. All connections used SubMiniature version (SMA) 905 connectors and the spectrometer was connected to a computer (tower PC running windows 7) via a USB cable for data acquisition through the software OceanView (Ocean Insight, version 1.6.7). The halogen light source was chosen due to its stability and relatively high bulb power, with this translating to a typical output power when connected to an optical fibre of 4.7 mW.

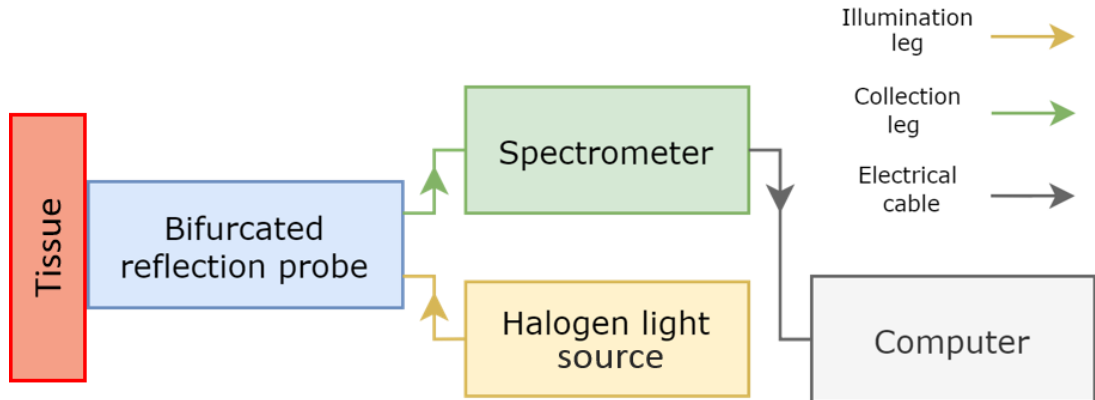


Fig. 2.1: Schematic of the opto-electronic components set-up used to make tissue reflectance measurements.

Porcine trachea and oesophagus samples were obtained from a local Sheffield abattoir and were used as *ex-vivo* samples throughout this project. Porcine samples were chosen due to their structural and physiological similarity to human organs [90,91]. The porcine samples were from Tamworth breed, reared until the ages of 6-10 months with weights ranging from 60-80 kg. The access to these samples allowed for numerous *ex-vivo* measurements during this research. The porcine samples (Fig. 2.2) consisted of an intact larynx, containing the vocal cords, glottis and epiglottis, as well as arytenoid cartilage. Attached to the larynx was the full length of the trachea, down to the carina, where the trachea branches off into bronchi which leads to the lungs. Also attached to the larynx was the oesophagus, which runs next to the trachea at the posterior.

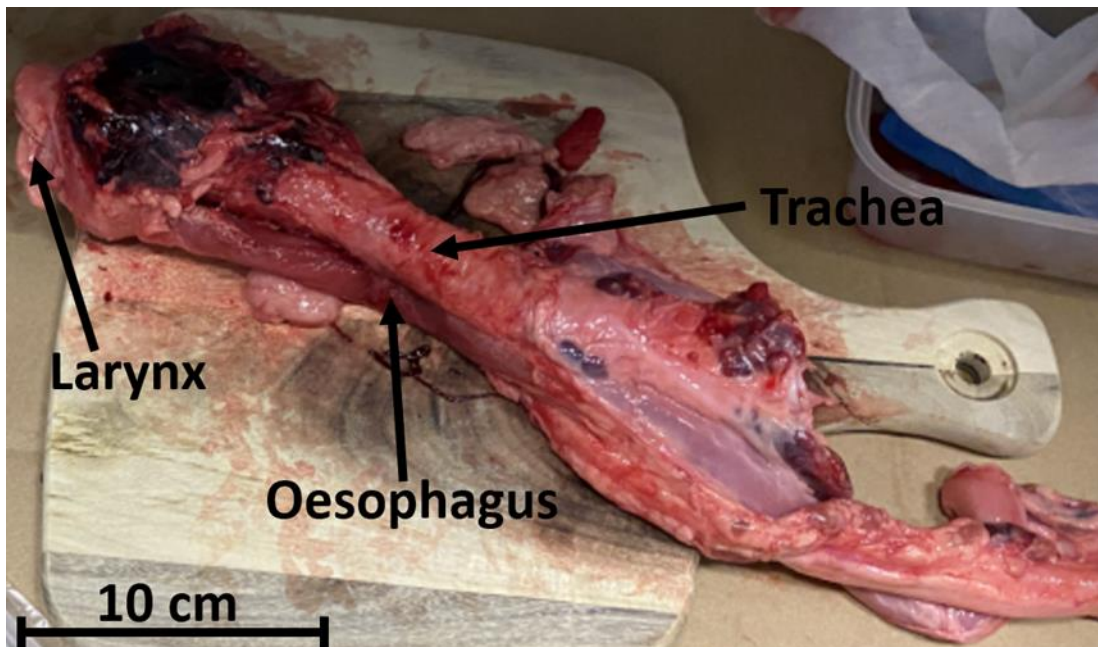


Fig. 2.2: Porcine sample used for *ex-vivo* measurements.

The sample was dissected by separating the trachea from the oesophagus, and then cutting through them lengthways from top to bottom, opening both organs to gain access for the reflection probe to measure inside the lumen. The probe was held flush

against the surface of the two tissues and the resulting spectra were measured. The spectrometer's integration time was set to 500 ms, which provided sufficient intensity (approximately 80-90% of the maximum saturation). There was no scan averaging so each spectrum was saved, giving the highest sampling rate. The boxcar width was set to 1 (no wavelength averaging) to give the maximum wavelength resolution. The spectra were acquired using OceanView spectroscopy software (Ocean Insight, version 1.6.7), and later exported into Matlab (MathWorks, version 2018) for processing.

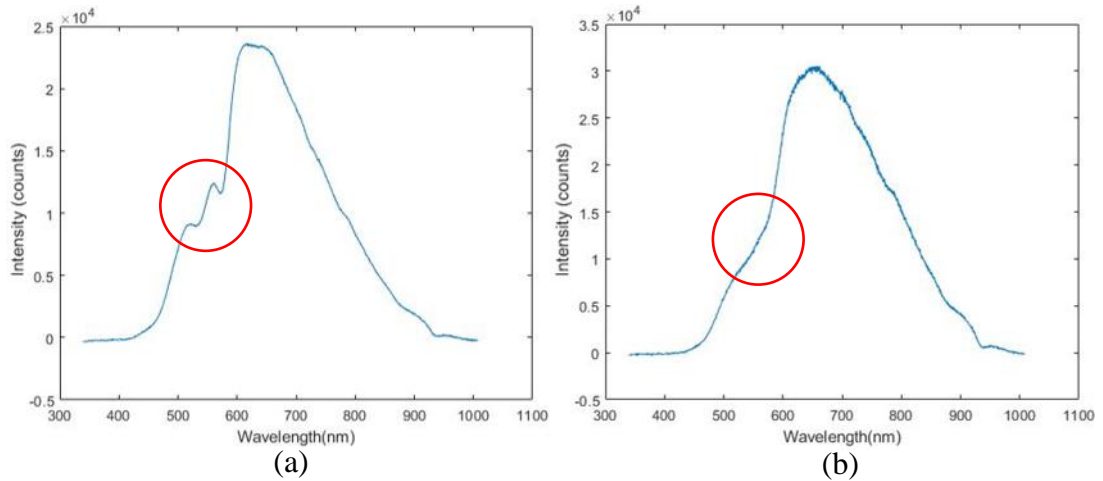


Fig. 2.3: Spectra from a porcine trachea (a), and oesophagus (b). – note the different response at the 530 – 590 nm wavelength region

A distinct characteristic in the 530 - 590 nm wavelength region, consisting of troughs at ~543 and 578 nm, as well as a peak at 561 nm can be seen on the tracheal spectrum (Fig. 2.3a), with its absence in the oesophageal spectrum (Fig. 2.3b) – see red circle. This provides the first measurements made in this research highlighting the spectral difference between these two tissues and is observationally consistent with the findings of the USAISR [85-88].

## 2.3 Normalization

For spectra to be compared the signals must be normalized appropriately. The spectrometer outputs data in terms of arbitrary unit counts, this is due to it having a wavelength-dependent quantum efficiency and this is not the true number of photons detected at each respective wavelength bin. Therefore, the optical power detected at each wavelength, or the total optical power cannot be found from intensity counts without calibration from an appropriate blackbody. However, the counts relative to each other at each wavelength are comparable and therefore ratios of intensities can be used to characterise the spectra reliably.

For a given spectral measurement, there will be a DC (direct current) offset due to thermal and shot noise. The thermal noise originates from the rate at which thermal electrons are generated [92]. The shot noise is from the event of a photon generating an electron, described by Poisson statistics [93]. These two components contribute to the dark current (or dark noise), with each pixel having a different amount of dark current and this effect being temperature-dependent. Even when ratios of intensities are taken this variation persists. Take two spectral intensity measurements ( $I_1, I_2$ ) at

two different wavelengths, even assuming a consistent dark noise effect ( $I_{Dark}$ ) on each pixel, there are variations in the ratio ( $R_1$ ) of intensities (Eq. (2.1)).

$$R_1 = \frac{I_1}{I_2} \neq \frac{I_1 + I_{Dark}}{I_2 + I_{Dark}} \quad (2.1)$$

The dark noise offset affects larger intensities proportionally less, producing varying ratios. Therefore, this was always accounted for and was achieved by turning off the light, covering the sensor and recording the dark reference, which was subtracted from the spectra. This also accounted for any background light detected, for example, by coupling to the core directly through the jacket and cladding of a plastic optical fibre (POF).

There will also be inherent variability in the light source, the sensor, fibres and connections, which will be wavelength specific. Therefore, a white reference must also be taken so that the spectral profile of the LED connected to the opto-electronic units can be obtained. In diffuse reflectance spectroscopy, this is typically performed by turning on the light source and then placing the sensor on a white reference standard and then storing the spectra. However, both the distance and angle between the sensor and target affect the reflectance values measured by a spectrometer. These two parameters will vary across the measurement phase as the medical device is moved, or bodily functions such as breathing change the position of the sensor relative to the tissue, either away from or into it. Therefore, calibration on a white reference standard may not yield accurate absolute reflectance values. This effect can be partially compensated by taking ratios of reflectance values, under the assumption that the DC light level change ( $DC_{shift}$ ) scales the intensities by the same amount (Eq. (2.2)).

$$R_1 = \frac{I_1 \times DC_{shift}}{I_2 \times DC_{shift}} = \frac{I_1}{I_2} \quad (2.2)$$

Therefore, the use of a white reference standard is less important for measurements of this nature, although it is still the gold standard of calibration. Examples of alternative normalization methods are found in Appendix C. However, normalization with a white reference standard is the preferred method and the gold standard. Therefore, a dark reference will always be taken by turning off the light source and covering the sensor with a black felt. Normalization with a white reference standard will always be implemented throughout the research presented here unless stated otherwise.

## 2.4 Spectral Characteristic Origin

The spectral characteristic present in the 530 – 590 nm wavelength region has been postulated to be unique to the trachea and originating from its tissue makeup [85]. However, its resemblance to the absorption characteristics of OHb has also been recognised [86-89]. The exact origin of this characteristic is therefore unclear, with evidence appearing contradictory. However, the feature is not uniquely inherent to the tissue of the trachea and it is well-documented that the feature originates from OHb. Although, if it derives from oxygenated blood then it is reasonable to assume that it is seen in the oesophagus, and other tissue, with the relative absorption of OHb being

dependent upon the structures, vascularisation and interstitium of the tissues, which causes variability between the tissues.

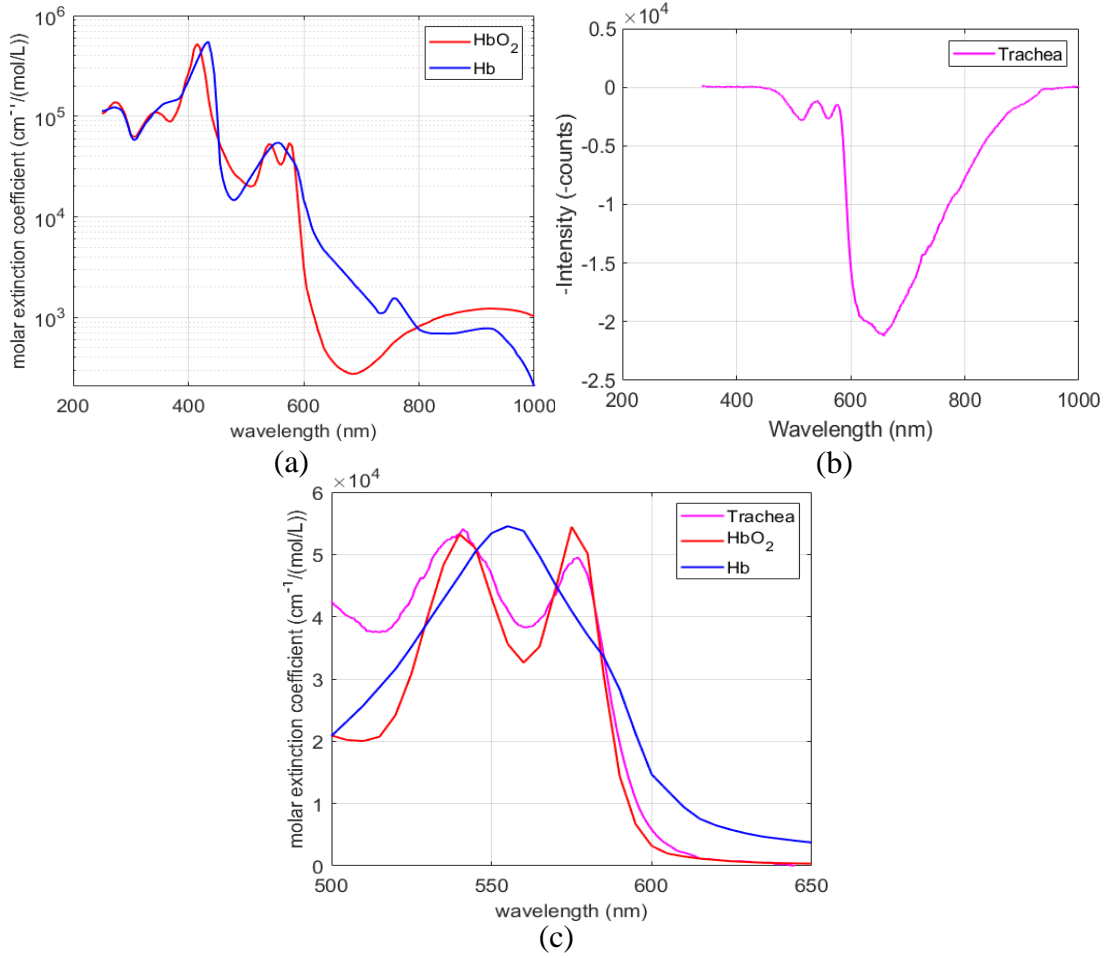


Fig. 2.4: (a) Absorption spectrum of oxyhaemoglobin ( $\text{HbO}_2$  red) and deoxyhaemoglobin (Hb blue). (b) The log of the reciprocal of reflectance spectrum (negative log) of a porcine tracheal sample (pink). (c) All three spectra with the negative log of the tracheal spectrum translated so that the first peak of the tracheal characteristic is equal to the first peak of the  $\text{HbO}_2$  characteristic.

The similarities between the spectra from the trachea and  $\text{HbO}_2$  (OHb) are highlighted in Fig. 2.4. The values used to generate the OHb and Hb absorption spectra were compiled with data from open-access online sources [94,95]. The absorption characteristics are also well documented elsewhere [96,97]. Since the reflectance spectrum of the trachea was measured, and we wish to compare it with the absorbance of OHb, Fig. 2.4b was generated by taking the log of the reciprocal of the reflectance spectrum, thus the peaks and troughs are inverted. The absorbance of OHb and Hb are represented in terms of the molar extinction coefficient ( $\epsilon$ ) i.e. how strongly a substance absorbs light, in units of  $\text{cm}^{-1}/(\text{mol/L})$ , given by the Beer-Lambert law (Eq. (1.3)). Therefore, the absorbance could be found from the concentration of the species in the medium and the length of the light path. However, we are only interested in the shape of the spectra and the wavelength positions of the peaks. Consequently, Fig. 2.4c was formed by taking the -log of the tracheal reflectance spectra and then multiplying it by a scaling factor ( $\sim 1.9 \times 10^4$ ) such that the peaks at 540 nm align with those of  $\text{HbO}_2$ . This enabled a qualitative comparison between the spectra, which



highlights the similarity in the relevant region. For a quantitative comparison, the molar absorption coefficient or absorbance of both species would have to be found, which is highly challenging given the complex nature of the tissues being studied and is unnecessary for this illustrative step.

To further understand the spectral characteristic a dissection of a porcine trachea and oesophagus was performed. Another sample was obtained, similar to Fig. 2.2, and was dissected. All photos throughout this section (and document) were captured on an iPhone camera (iPhone 13, 12-megapixel camera, standard contrast and exposure).

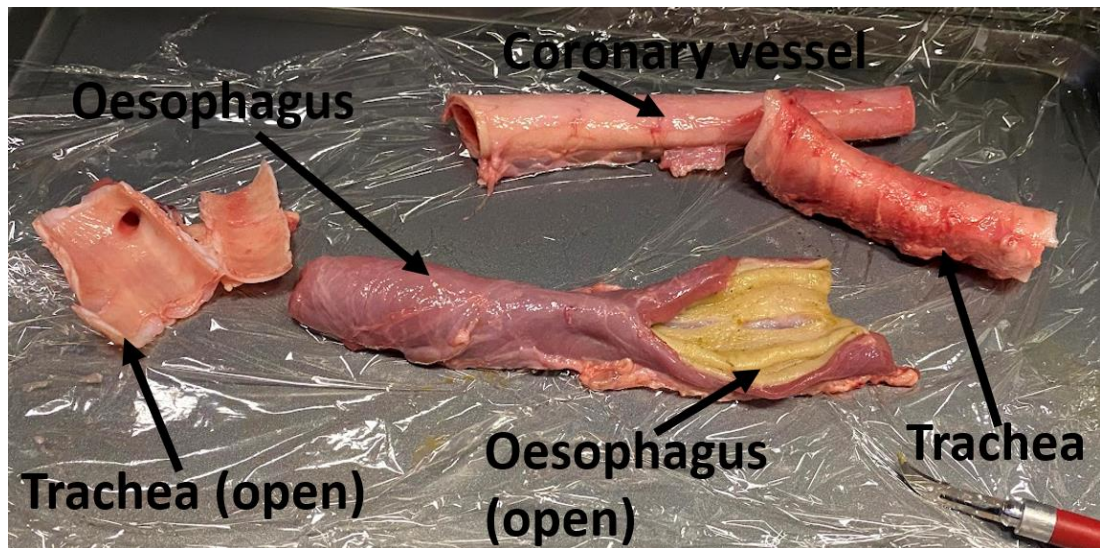
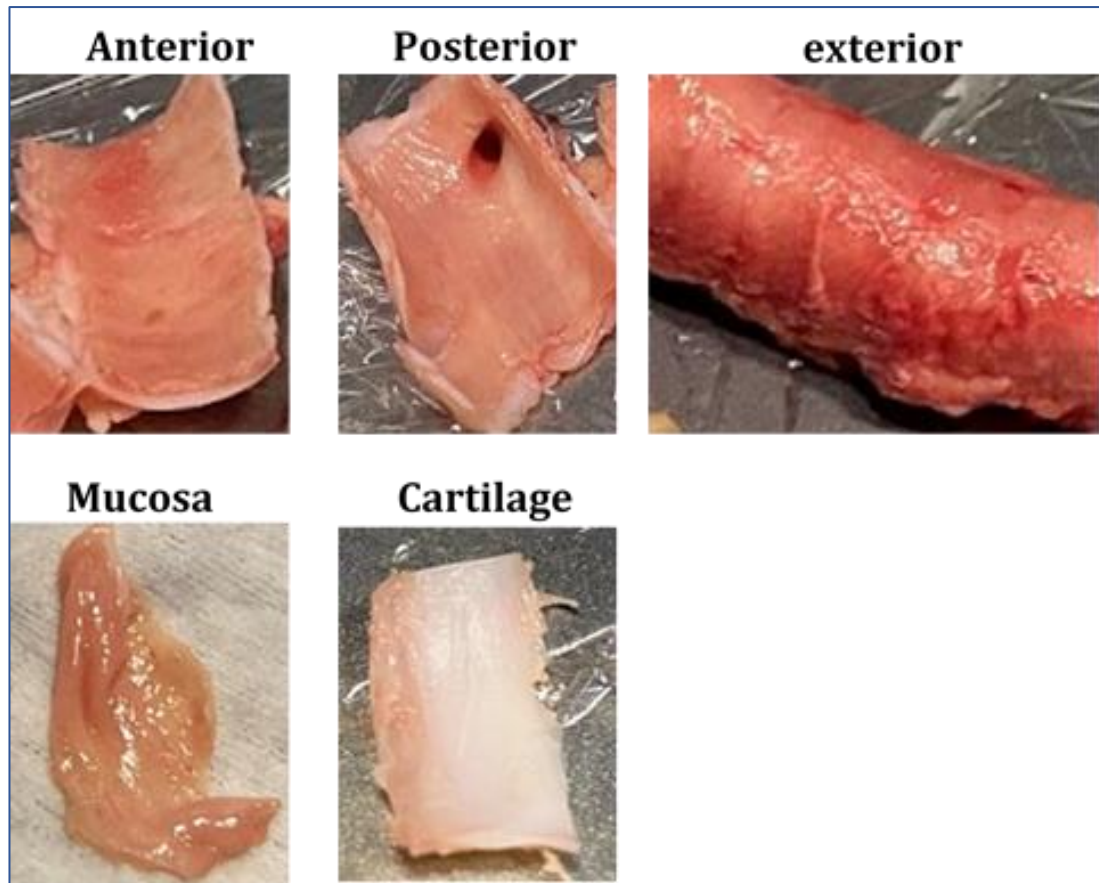


Fig. 2.5: Dissected trachea and oesophagus *ex-vivo* samples.

The trachea and oesophagus were first separated from the larynx by cutting below the subglottis and were separated from each other by cutting behind the posterior of the trachea (between the two organs) with a scalpel, leaving an intact trachea and oesophagus. They were then sliced lengthways to reveal the interior (Fig. 2.5). A coronary vessel (most likely the aorta) is also imaged in Fig. 2.5, which came with the sample, this was not used for measurements but was left in the image due to its resemblance in colour to the trachea, which may be of interest when applying this technology to other tissues.



(a)



(b)

Fig. 2.6: (a) Porcine trachea showing the inside lumen (anterior and posterior), exterior, mucosa only, and cartilage only. (b) Porcine oesophagus, showing the inside lumen (interior mucosa), the exterior (exterior muscle), and the interior with the mucosa having been cut through (interior w/o mucosa).

The trachea and oesophagus were then further dissected. The trachea was separated into the posterior (back muscle side closest to the oesophagus) and anterior (front side containing cartilages) as well as the exterior (outside of the trachea), photographed in Fig. 2.6 . The mucosa was then detached from the cartilage and annular ligaments. A piece of cartilage was then isolated. The mucosa of the oesophagus was also cut through to reveal the submucosa and the start of the exterior muscle surrounding the oesophagus. A visual difference can be seen between the internal mucosa of the trachea and the oesophagus (Fig. 2.5). The tracheal mucosa of this sample has a beige colour with a pink hue, whilst the oesophageal mucosa is more yellow. The oesophageal mucosa is also thicker and less transparent. Typically, oesophageal

mucosa is pale pink, characteristic of squamous epithelium [98, 99]. The discolouration is attributed partially to the pigs' diets of cereal grains and corn. No known treatment was applied to the samples at the abattoir, although often in the industry the post-mortem carcass is heated to kill bacteria and limit the decay, which could alter the spectroscopic characteristics. However, the same yellowing was not seen in the trachea, which would be expected if this was the cause and the full carcass was heated. Future studies should acquire samples where the absence of treatment can be guaranteed, and the animals are fed a more varied diet. The exterior of the two organs also have different colours, the trachea has a light red hue, typical of oxygenated blood, whilst the muscle surrounding the oesophagus has a dark red hue, typical of the high levels of myoglobin in muscle. It should also be noted that although only a single sample is imaged, this is typical for all porcine samples studied, as can be seen in images of the porcine samples throughout this document.

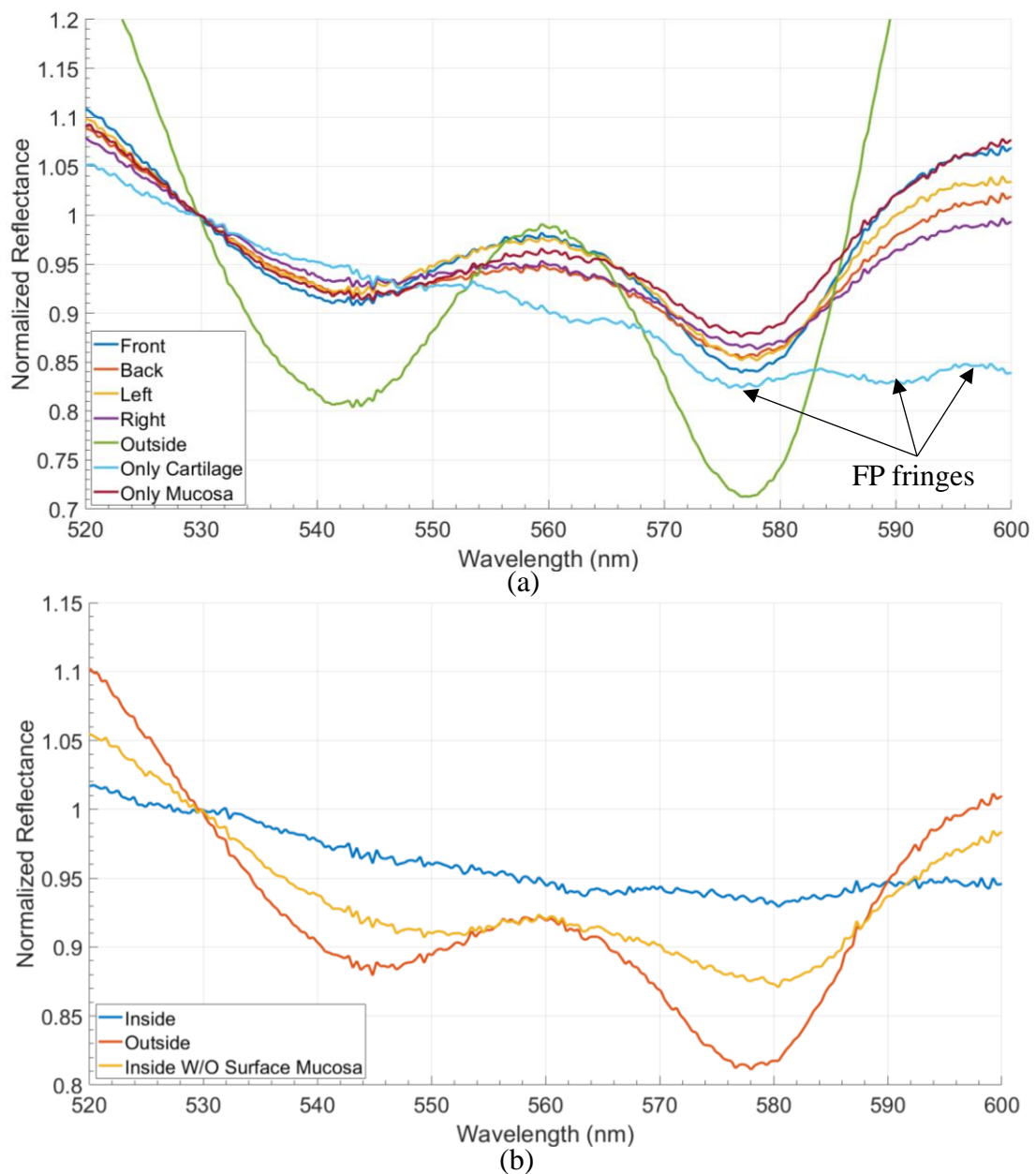


Fig. 2.7: Spectra produced from the dissected porcine sample (Fig. 2.6), for the trachea (a) and the oesophagus (b). FP fringes = Fabry-Pérot fringes.



A white reference was obtained from a reference standard (Spectralon diffuse reflectance targets, Labsphere, model SRT-99-180). The probe was then placed on the surface of each of the tissues shown in Fig. 2.6, resulting in the spectra shown in Fig. 2.7. Measurements were repeated 5 times at different locations on the same tissue type. The scans were averaged producing a single spectrum for each tissue. The averaged spectra were then normalized by a single wavelength such that the reflectance at 530 nm equalled 1.

The spectral characteristic can be observed in all the usual tracheal positions (Fig. 2.7a), back (posterior), front (anterior), left lateral and right lateral. It is also present on the outside, as well as in the mucosa alone. Interestingly, the reflection is lower (absorption higher) for the external tracheal measurements. The measurements on the cartilage produce interesting results as well, here the characteristic is mostly absent with the reflectance decreasing as the wavelength increases. There is also the presence of an oscillating feature, which may originate from the multi-layered high reflectance structure of the cartilage producing Fabry-Perot interference fringes [100,101,102]. The characteristic is mostly absent inside the oesophagus, as has been demonstrated previously. However, it is present outside the oesophagus when the probe is placed on the muscle, as well as inside the oesophagus when the mucosa has been cut through and the probe placed in the opening (Fig. 2.7b).

In summary, the spectral ‘tracheal characteristic’, consisting of a trough-peak-trough in the 530 – 590 nm wavelength region originates from OHb, which is well documented throughout literature in a variety of tissues. A 2001 publication by Strattonnikov *et al.*, titled ‘Evaluation of blood oxygen saturation in-vivo from diffuse reflectance spectra’ [103] used diffuse reflectance spectroscopy on the surface of the skin to measure oxygen saturation. Especially in recent years, there has been an influx of the use of the spectral properties of tissues to make physiological measurements. A 2021 research paper by Bachir *et al.* [104], again uses diffuse reflectance spectroscopy to estimate tissue oxygen saturation (StO<sub>2</sub>). A 2020 paper by Fanjul *et al.* [105], uses this technique to characterize skin, fat, muscle, bone and nerve tissues. Therefore, this characteristic is not unique to the trachea and is present in numerous tissues, although the oesophageal mucosa may have reduced presence of the OHb absorption feature in this wavelength range, which can be used to distinguish the two tissues. The characteristic also appears to vary enough to distinguish tissues that possess it by leveraging smaller variations in the dominant OHb absorption characteristics caused by the optical properties of surrounding tissues. Therefore, it is the distinct spectral properties of the oesophagus that allows for successful classification, as the tissue is not as well perfused with oxygenated blood that the light can interact with. The thicker and less transparent structure of the oesophagus epithelium, formed from keratinised squamous cells, reflects and attenuates the light more than the pseudostratified columnar epithelium of the trachea. The characteristic persists and tracheal detection can be made during airway obstruction reducing oxygen saturation down to 50%, as shown by Nawn *et al.* [87], as well as persisting in *ex-vivo* samples. Therefore, we can conclude that OHb is present in large enough quantities in the trachea during hypoxic periods and even post-mortem to distinguish the two tissues. Furthermore, this opens new opportunities to use this technology to distinguish other tissues, such as shown

by Fanjul *et al.* [105], or to estimate levels of tracheal hypoxia as shown by Bachir *et al.* [104].

OHb is present in most physiological tissues, with smaller variations caused by the surrounding tissues [106,107]. Preliminary measurements indicate its presence in a variety of human body parts (Appendix F), although these results require a broader more representative sample of the human population [108,109], and are therefore not presented here. Furthermore, ETCO<sub>2</sub> is imperfect and can have failure rates as high as 10% [78,79].

The double trough absorption characteristic of OHb in the 530 - 590 nm wavelength region, measured from the surface of the skin, may differ between individuals, particularly due to the amount of melanin [110,111]. Furthermore, probe pressure can also affect the shape of the diffuse reflectance characteristic [112,113], by blanching as blood is occluded. However, detecting blood occlusion in the trachea may be a useful benefit to clinicians as it indicates that cuff pressure may be too high and could lead to ischemia [114,115]. Therefore, this could also be an added benefit of this technology, although may lead to erroneous results if the blanching in the trachea partially removes the feature by which it is characterised. This may be avoided by a sensor placed on the main lumen of the ETT as opposed to inside the cuff (Section 3.5).

## 2.5 Discussion

The tracheal spectral feature in the 530 - 590 nm wavelength range, first documented by the USAISR [85], has been observed using a similar experimental set-up of a commercial reflection probe in an *ex-vivo* porcine model. Normalization accounts for shape changes in the spectra from deviations in the manufacturing of the sensor, the light source, and connections. However, this is most applicable to absolute reflectance measurements, where if relative reflection values are used and a proportional change in light intensity across all wavelengths is assumed, a simpler alternative method could be used by accounting for the general shape of the light source. However, a white reference standard is the gold standard and is used to facilitate normalization in this research as it offers a more consistent option during research. However, future designs could be consistent enough so that normalization without a white reference standard for each sensor is possible.

The origin of the spectral feature in the trachea is OHb. This has been well documented in other tissues throughout researched literature [105,106,107]. The feature is mostly absent from measurements made from inside the oesophagus. This is caused by the oesophageal mucosa not presenting the feature, whereas the muscular tissue surrounding the oesophagus does present it. Therefore, it is believed that the thicker and less transparent oesophageal mucosa attenuates the light so that only a small amount interacts with OHb (so that the feature can sometimes be weakly visible). The thinner and more transparent tracheal mucosa allows interaction with the capillary network and transverse intercartilaginous arteries. Furthermore, the reflective cartilage may help to return the light to the detection fibre.

## Chapter 3 Endotracheal Tube Sensor Integration

### 3.1 Introduction

This chapter considers the development of an ETT placement sensor, i.e. the sensor head (the invasive portion of the device, excluding opto-electronic components) and different methods of integration within an ETT. Therefore, the sensor used for ETT placement detection must fit several criteria, determined from discussions with manufacturers and clinicians. These are:

- The sensor must produce enough light and be in close enough proximity to the tissues that the OHb absorption characteristic is visible during tracheal intubation.
- The sensor must be small enough to be integrated into an ETT.
- The ETT must retain its shape so it can function normally without an increased likelihood of damaging the patient.
- The sensor must adhere to biological safety standards and be made from biocompatible materials.
- The sensor fabrication must be simple and repeatable.

One option is to attach LEDs and photodiodes (PDs) directly to the ETT. This eliminates the need to have fibres transport light to and from the trachea, and its operation is similar to the working principle of most reflection mode pulse oximeters [116]. Kyriacou *et al.* explore an advance in this approach by wrapping a flat flexible opto-electronic patch around an ETT to detect a PPG in the trachea and oesophagus [117, 118], reporting reliable oxygen saturation measurements. However, this solution produces a large sensor patch that's embedded into the ETT as the LED(s), PD(s) and electronics need to be incorporated. This also increases the likelihood of damage to the trachea and creates biocompatibility concerns. Furthermore, electrical wires providing power to the components must be brought into the body, which may cause further issues, especially when requiring a safe magnetic resonance imaging (MRI) ETT [119]. The single-use disposable ETT would also be more expensive to manufacture than the proposed fibre alternative in this research. For these reasons, a more desirable option is to produce a sensor that consists of optical fibres embedded in a patch, that brings light into and out of the body to the high-quality opto-electronic units. This resolves many of the problems of a typical 'pulse oximeter style' sensor. The fibre-only sensor could be smaller, cheaper, biocompatible, and MRI-safe. Therefore, sensor designs have been explored to determine acceptable fibre diameters and spacing, the shape of the fibre tip, sensor size, and sensor shape. Furthermore, techniques for moulding the fibres into an epoxy patch are explored. These are all introduced in this chapter.

### 3.2 Distribution of Light Around a Cleaved Fibre

One of the major difficulties when producing a fibre optic ETT placement sensor is that traditionally fibres have their tips cleaved at 90° causing light emission from the tip which travels radially outwards. Therefore, to maximise the light intensity

interacting with the tissue the fibres must be embedded perpendicular to the sensor, causing a bulkier sensor (Fig. 3.1).

### Light emission

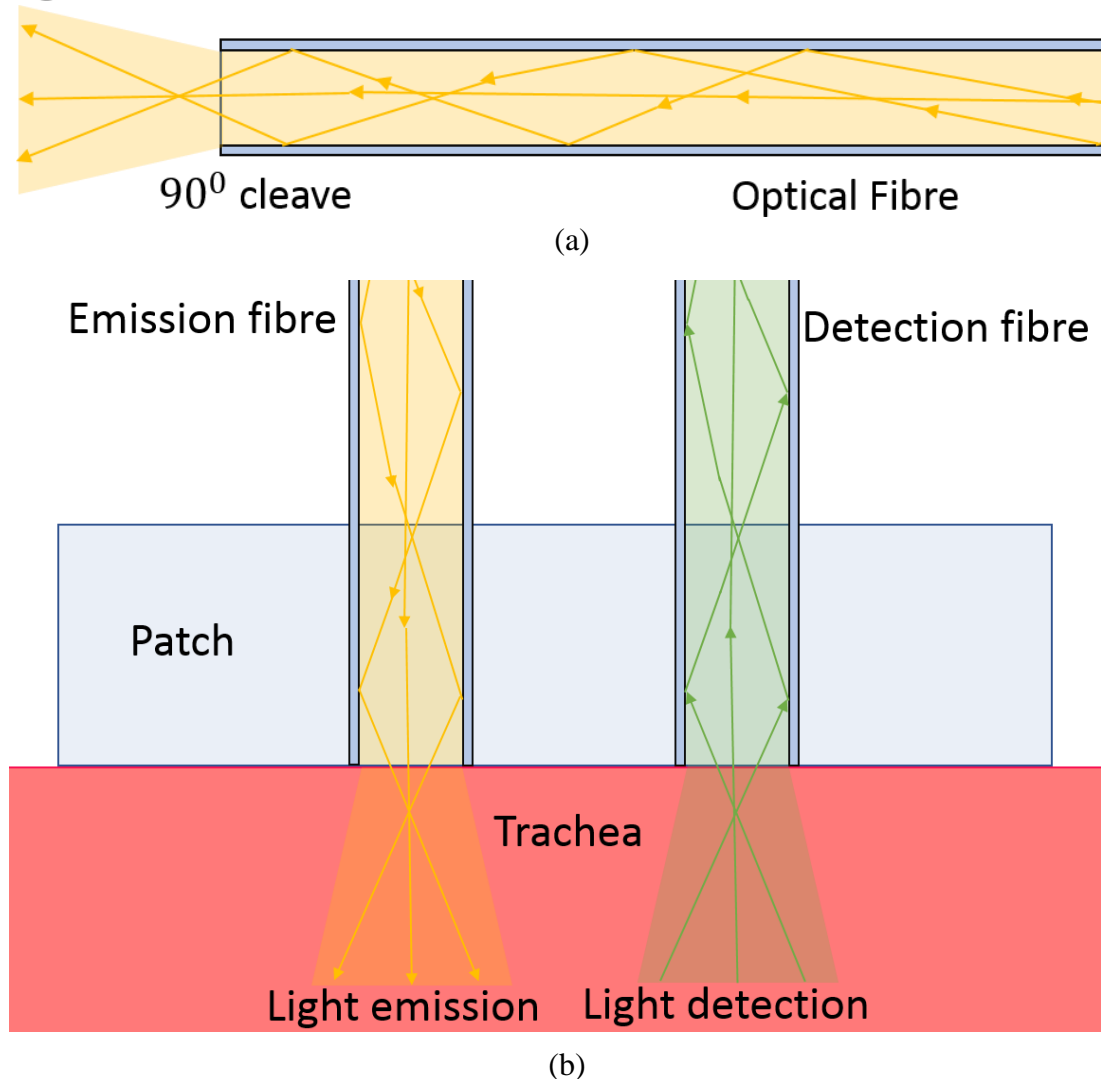


Fig. 3.1: Concept design for a fibre optic sensor containing fibres cleaved at  $90^\circ$  for the (a) emission fibre and (b) resultant patch design to maximise light intensity.

The design of Fig. 3.1 is not ideally suited for integration within an ETT, the patch is bulky to accommodate fibres coming out of the top where it is mounted to the ETT. A solution to this was first explored, by cleaving the fibres at  $45^\circ$  so that some of the light reflects at the fibre tip and travels perpendicular to the length of the fibre.

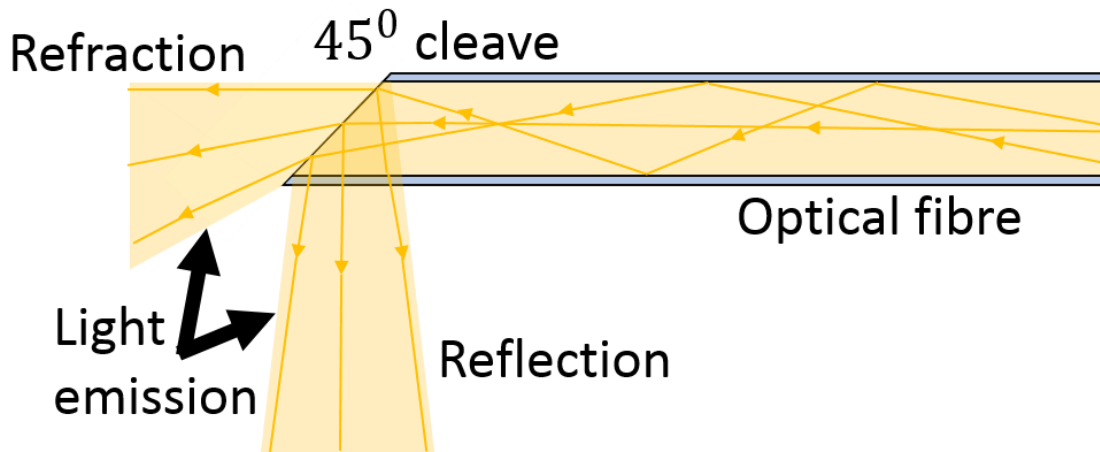
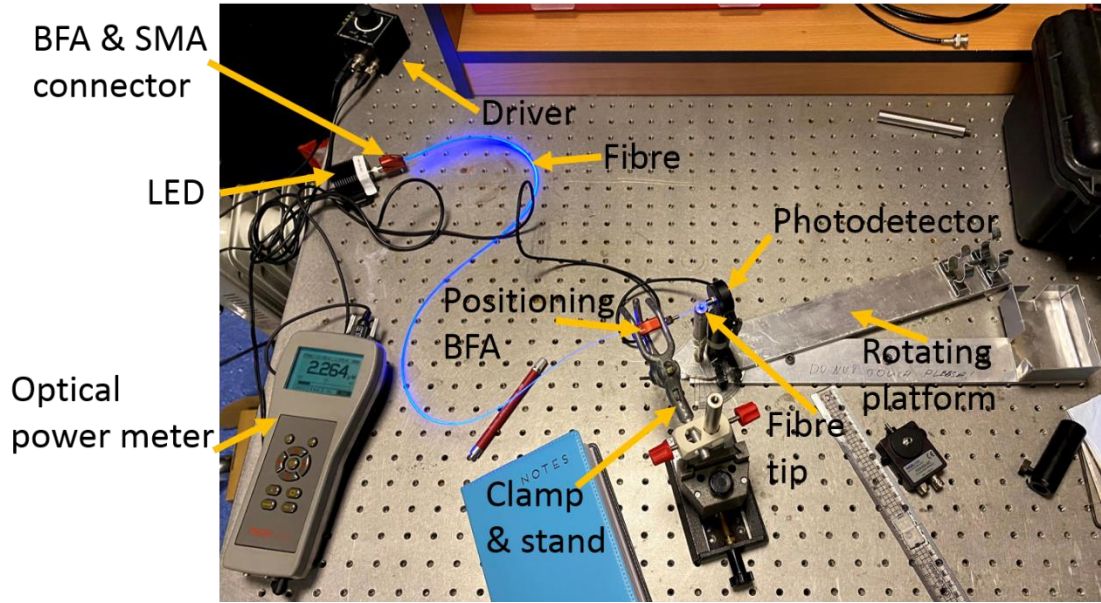


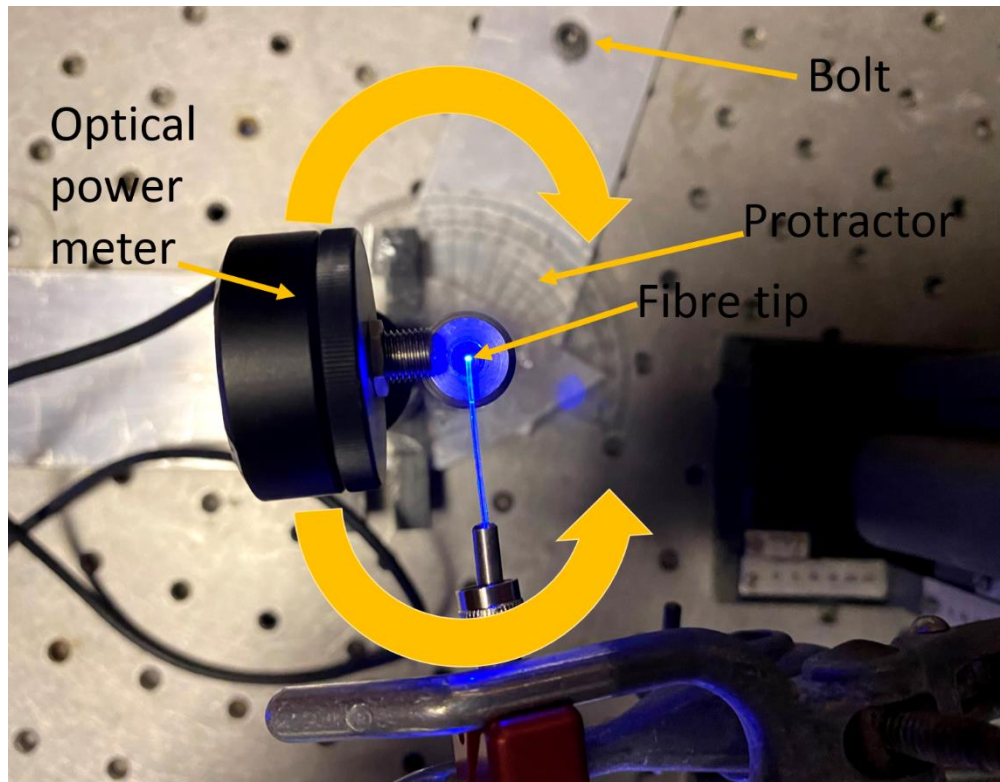
Fig. 3.2: Optical fibre cleaved at 45° showing how light is reflected and refracted.

A fibre cleaved at 45° has some light emitted perpendicular to the fibre axis due to the cleave acting like a mirror and reflecting light at the boundary (Fig. 3.2), with some light emitted approximately parallel to the fibre due to refraction. The arrangement allows for a more compact sensor than that shown in Fig. 3.1.

A custom set-up was designed to investigate the light transmitted in this 45° configuration (Fig. 3.4). A photodetector was rotated around a fibre tip and the optical power was measured. An optical fibre (commercial grade PolymethylMethacrylate (PMMA), Asahi, model DB-500) was used, with a core refractive index of 1.49 and diameter of 500  $\mu\text{m}$ . PMMA fibres were used throughout the research described here as they are inexpensive and more suitable for a single-use ETT. The fibre was fixed at the centre of a rotating platform and held by a bare fibre terminator (Thorlabs, model BFT1) and a 510  $\mu\text{m}$  SMA connector (Thorlabs, model B10510A). The photodetector was mounted to a metal bar so that it could rotate freely around the fibre with a 3 mm gap between the fibre tip and the front of the photodetector. A protractor was mounted at the centre of rotation to measure the angle between the photodetector and the fibre. The photodetector was connected to an optical power meter and optical power was read from the display. The optical fibre was connected to a blue LED (Fibre-Coupled LED, Thorlabs, model M490F3) emitting at a central wavelength of 490 nm with a full width half of maximum (FWHM) of 26 nm. There is a wavelength dependency on the percentage of reflected and refracted light at a boundary. However, this is caused only by the effective refractive index change of a medium due to the propagation of the wavelength of light in that medium, which for air and PMMA can be neglected. Therefore, a blue LED is assumed to be representative [121,122]. The fibres were cleaved at 90° and 45° degrees using a hot scalpel and a piece of paper marked by a protractor. A cleave angle of 45° was used so that light was reflected at 90° to the fibre axis. However, it may be possible to increase the intensity of light reflected at the boundary by implementing a cleave angle close to the critical angle of a PMMA fibre core and air boundary (found to be 42.2°). However, this would cause light to be reflected away from the detection fibre and may reduce the detected light intensity.



(a)



(b)

Fig. 3.3: Experimental set-up used to measure the distribution of light around a fibre tip. (a) Photograph of the equipment. (b) Close-up showing how the photodetector rotates around the fibre tip (detector at  $90^\circ$  to fibre axis).

The photodetector was rotated around the fibres in increments of  $5 \pm 1^\circ$  from an angle of  $0^\circ$  (along the fibre axis) to  $120^\circ$ , this was repeated 7 times for  $45^\circ$  and  $90^\circ$  cleaves by returning the photodetector to the  $0^\circ$  angle position.



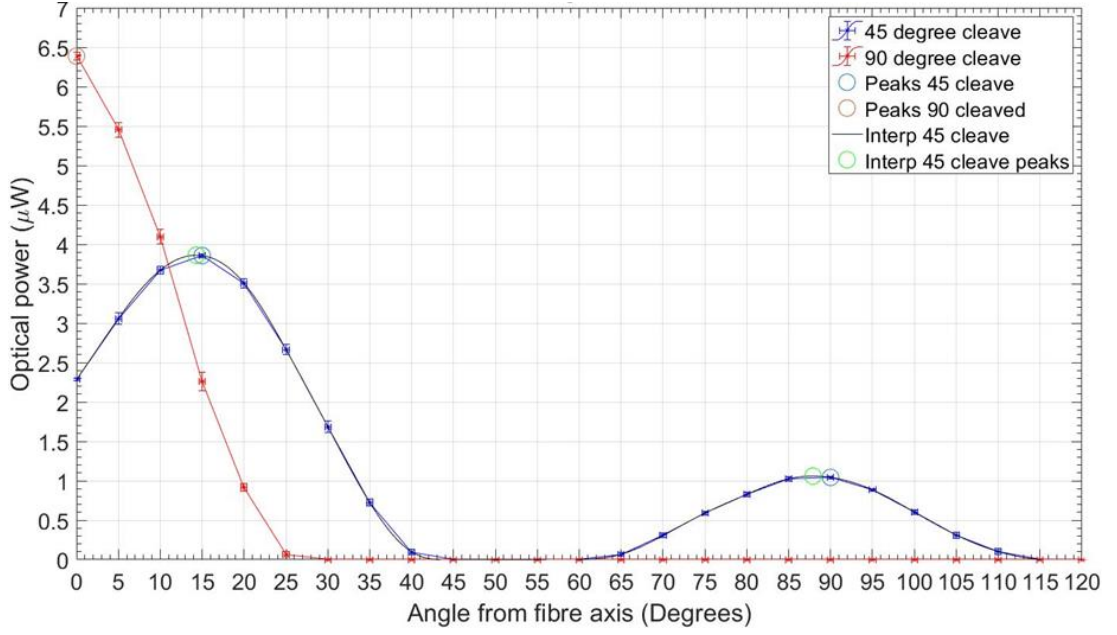


Fig. 3.4: The optical power distribution of light around the tip of a 90° (red) and 45° (blue) cleaved optical fibres, with the interpolated 45° plot (black) with peaks (green circles),

In Fig. 3.4 measurements began along the fibre axis (0°) due to a bolt on the lower leg (Fig. 3.3b) of the rotating platform limiting the maximum rotation. Therefore, light emitted at angles < 0° was not measured, although this may have been resolved by offsetting the angle of the fibre axis from the start position of the rotating platform such that there was room for it to rotate ‘backwards’. However, this can be accounted for computationally by assuming the distribution of light around the 0° axis is symmetrical.

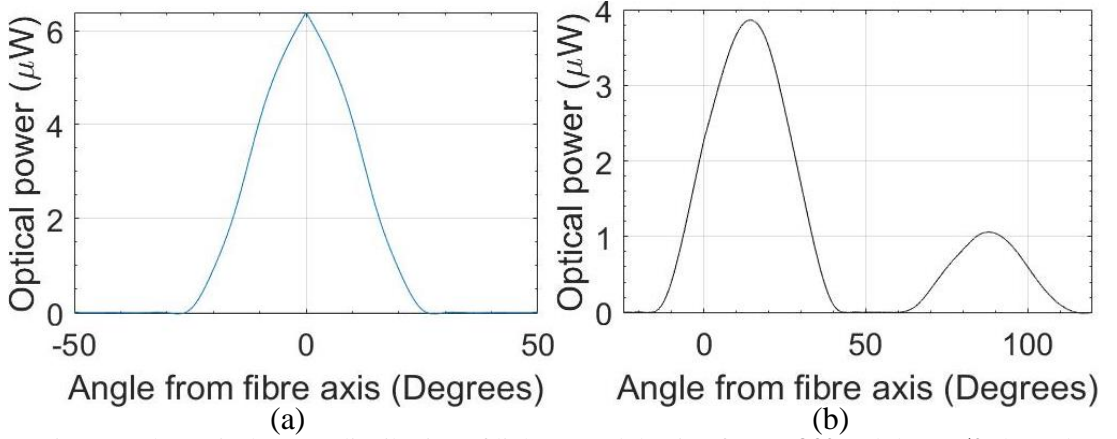


Fig. 3.5: The optical power distribution of light around the tip of, (a) a 90° and (b) a 45° cleaved optical fibres, with the distribution < 0° found by mirroring the measured distribution.

The angular shift ( $\theta_{shift}$ ) of the light refracted from a fibre that has been cleaved at an angle ( $\theta_{cleave}$ ) can be derived (Eq. (3.2)) from Snell’s law (Eq. (3.1), [120]) which describes the relationship between the angle of incidence ( $\theta_1$ ) and refraction ( $\theta_2$ ) as light travels from one medium of refractive index ( $n_1$ ) to another ( $n_2$ ).

$$n_1 \sin(\theta_1) = n_2 \sin(\theta_2) \quad (3.1)$$



$$\theta_{shift} = \sin^{-1} \left( \frac{n_2}{n_1} \sin(-\theta_{cleave}) \right) + \theta_{cleave} \quad (3.2)$$

Therefore, theoretically the angular shift  $\theta_{shift}$  ( $\theta_1 - \theta_2$ ) was calculated from Eq. (3.2) using the fibre properties with an angle of cleave of  $45^\circ$  and taking the refractive index of air as 1.0003, giving an angular shift of  $16.66^\circ$  from the fibre axis. Experimentally this was found from Fig. 3.4 from the larger first peak of the  $45^\circ$  cleaved fibre to be at  $14.4 \pm 0.4^\circ$ , with variations from the theoretical being attributed to the actual cleave angle not being exactly  $45^\circ$  and variations in the refractive index of the fibre core and the air.

For a perfect  $45^\circ$  fibre cleave the second smaller peak power on Fig. 3.4 should be at  $90^\circ$  to the fibre axis. However, this was found at  $87.9 \pm 0.5^\circ$ , which translates to a cleave angle of  $46.0 \pm 0.3^\circ$ , as every  $1^\circ$  change in the cleave angle creates a  $2^\circ$  change in the angle of the reflected light. An accurate cleave angle must be achieved for light emission perpendicular to the fibre, although an error of a few degrees will still cause most of the light to be transmitted into the tissue.

The reflectivity of the fibre tip at the air/fibre boundary can be calculated by a Fresnel equation (Eq. (3.3), [120]),

$$R_{eff} = \frac{1}{2} (R_s + R_p) = \frac{1}{2} \left( \left| \frac{n_1 \cos(\theta_1) - n_2 \cos(\theta_2)}{n_1 \cos(\theta_1) + n_2 \cos(\theta_2)} \right|^2 + \left| \frac{n_1 \cos(\theta_2) - n_2 \cos(\theta_1)}{n_1 \cos(\theta_2) + n_2 \cos(\theta_1)} \right|^2 \right) \quad (3.3)$$

where  $R_{eff}$  is the effective reflectivity,  $R_s$  is the perpendicularly polarized light reflectivity, and  $R_p$  is the parallel polarized light reflectivity. The numerical aperture (NA) of the fibre is described on the data sheet as 0.5, which gives a minimum acceptance angle of  $30.0^\circ$  and a maximum of  $60.0^\circ$ , giving ranges of effective reflectivity found from Eq. (3.3) between 4.7 and 100%, respectively, with angles of incidence above  $43.2^\circ$  always giving 100% reflectance as this is above the critical angle.

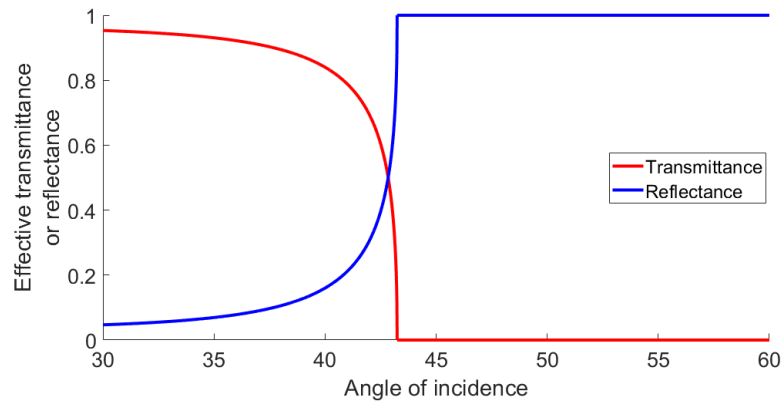


Fig. 3.6: Modelled effective transmittance and reflectance at the boundary of a  $45^\circ$  cleaved fibre.

The average transmitted light was found computationally using Eq. (3.3) (Fig. 3.6) and integrating over all angles of incidence between 30 and 60°, where theoretically the reflected light was 61.9% of the total light across all allowed incident angles. Experimentally, the approximate optical power for both cleaved fibres can be found by integrating the area under the curves of Fig. 3.5a-b. The total optical power for the 90° and 45° cleaved fibres was 159 and 145  $\mu W$ , giving a loss of optical power of 9%, which is likely due to an imperfect and vertically angled surface scattering some of the light away from the detector. The amount of light that was scattered perpendicular to the 45° cleaved fibre was 28.8  $\mu W$ , which is 18.1% of the total power. The reflected light accounts for significantly less than the theoretical (61.9%), which is likely caused by a poor-quality cleaved surface scattering the light out of the front of the fibre as opposed to reflecting on a perfect surface. This effect is possibly due to the scalpel used to cleave the fibre not being sharp enough and causing the fibre to pinch together. It may also be possible that the fibre ‘rolled over’ whilst in the holder, causing the light that is reflected to move up and down in the y-plane and not be in line with the detector.

Only the emissions from the illumination fibre were explored here. The light must also be detected by the detection fibre by following the reverse light path, entering through the side and reflecting off the cleave. Assuming an equivalent performance of the detection fibre, 18.1% of the incident light is transmitted back to the spectrometer for the 45° cleaved fibre when compared to the 90° cleaved fibre. It is also practically challenging to orientate the 45° cleaved fibre correctly so that the light is directed into the tissue. Only measurements using blue light (490 nm) were made, with a single broadband LED or multiple narrowband LEDs being required to detect ETT placement. The use of a blue LED is believed to sufficiently describe a system with a broader LED [121,122]. Although not presented, the light being reflected perpendicular to the sensor patch and detected by the other cleaved fibre was enough to distinguish the tissues based on simple tests with an appropriate high-powered broadband LED on *ex-vivo* samples and a finger.

### 3.3 Fibre Separation

An ETT placement sensor could have several fibres and fibre arrangements. Therefore, it is important to understand how the separation between the illumination fibre and the detection fibre will affect the results. Typical separations for pulse oximetry range between 3 and 6 mm [123], with smaller separations giving a higher optical power detected and larger distances penetrating the tissue deeper and coupling with more blood. Therefore, a balance between these two factors is required to achieve a high signal-to-noise ratio.

#### 3.3.1 Experimental

To determine the range of appropriate separations an experiment was designed where 6 optical fibres (commercial grade PolymethylMethacrylate (PMMA), Asahi, model DB-500) with a core refractive index of 1.49 and diameter 500  $\mu m$  were cleaved at 45°, as described in Section 3.2, and placed into a hollowed out ribbon cable (Fig. 3.7). The ribbon cable provided consistent increments in separation whilst protecting

most of the length of the fibre from direct DC shunting. However, the tip of the fibre must be exposed for the length of the cleave to ensure that light is not attenuated by the ribbon cable jacket.

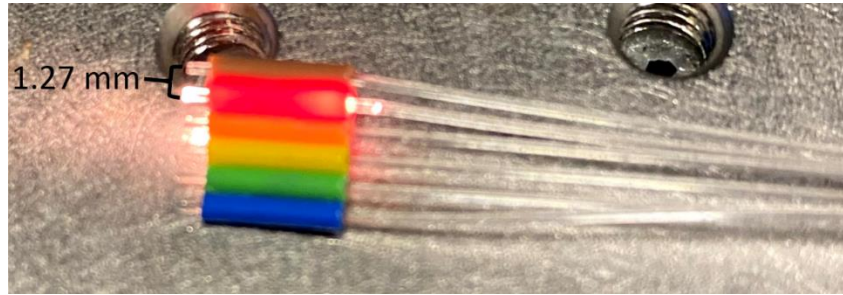


Fig. 3.7: Cleaved optical fibres placed into a hollowed-out ribbon cable.

Each fibre was separated by 1.27 mm from the next, with the first (brown jacket) acting as the detection fibre which was connected to the spectrometer. Each fibre (red, orange, yellow, green, and blue) was then sequentially connected to the halogen light source. The sensor was then placed into an *ex-vivo* porcine trachea 10 times for each separation distance. Dark and white references were obtained by covering the sensor with a dark felt and turning off the light source and then turning the light source back on and placing the sensor against a white diffuse reflectance standard (two-part epoxy, Permabond, model ET5143). The referencing with a white standard was performed during pre-processing by the OceanView software, giving a reflectance percentage.

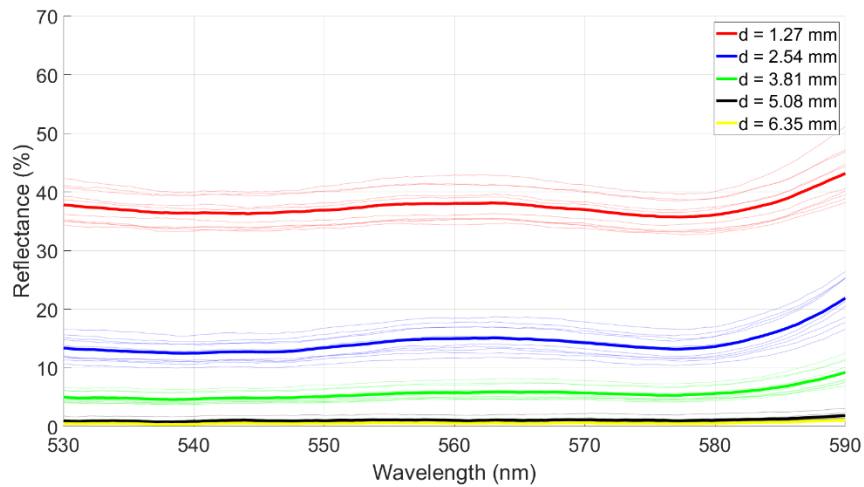


Fig. 3.8: Measured reflectance spectra for 45° cleaved fibres in the 530 - 590 nm wavelength region with varying illumination and detection fibre distance ( $d$ ). The individual repeats are shown as faint lines with the average of each 10 repeats shown as thicker lines.

As the separation between the illumination and detection fibres is reduced (fibres brought closer together) a higher optical power is received after interaction with the tissues. However, increasing the separation causes light that has penetrated deeper into the tissues to be detected [123, 124], with this also being a wavelength-dependent effect [125], as lower energy (longer wavelength) photons can penetrate the tissue further. Therefore, it is important to understand how the wavelength region containing the absorption feature of OHb (530 - 590 nm) interacts with tissues and varying separation distances. At an integration time of 500 ms, approximately 40% of the light

is detected by the detection fibre at a separation of 1.27 mm when compared to the white reference standard, with this reducing to 14, 4, 1, and 0.5% for increasing separation (2.54, 3.81, 5.08, and 6.35mm, respectively).

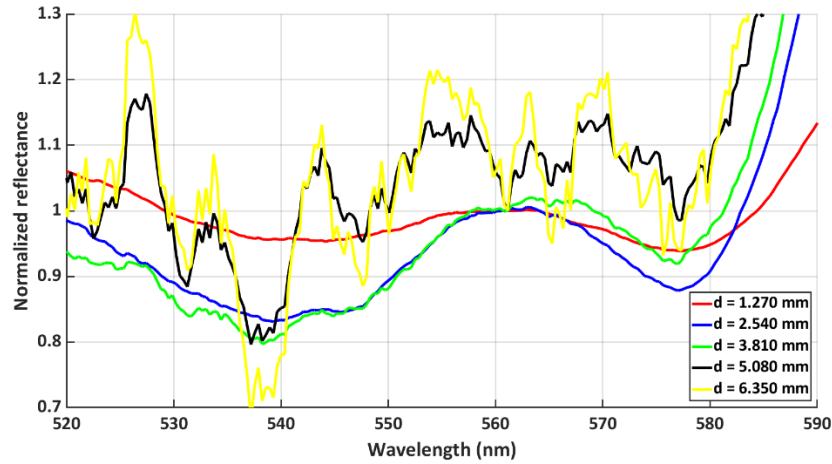


Fig. 3.9: Normalized reflectance spectra for 45° cleaved fibres in the 530 - 590 nm wavelength region with varying illumination and detection fibre separation - d.

By normalizing each of the spectra at the central peak of the OHb absorption characteristic (561 nm), a direct comparison can be made (Fig. 3.9). Observationally, the characteristic spectral features can be recognised in the first three separations (1.27, 2.54, and 3.81 mm), with the light levels being too low in the last two measurements (5.08 and 6.35 mm), resulting in a signal dominated by noise. Furthermore, the separation of 1.27 mm produces the smallest amount of relative OHb absorption at the characteristic wavelengths (543 and 578 nm), implying that the penetration depth of the light is such that it interacts with less OHb.

Table 3.1: Normalized reflectance variation at the characteristic wavelength of OHb with varying illumination and detection fibre separation, with errors on the normalized reflectance originating from the standard deviation on repeats.

Separation (mm)	Wavelength (nm)	Normalized reflectance
1.27	543	$0.954 \pm 0.008$
2.54	543	$0.85 \pm 0.03$
3.81	543	$0.844 \pm 0.001$
1.27	578	$0.941 \pm 0.008$
2.54	578	$0.88 \pm 0.05$
3.81	578	$0.94 \pm 0.02$

A smaller normalized reflectance (more absorption) at the characteristic wavelengths (543 and 578 nm) results in data that will be better distinguished from its oesophageal counterparts (Table 3.1). Therefore, fibre separations between 1.27 and 3.81 mm result in tracheal spectra with enough OHb absorption so that the feature can be recognised. However, the use of a light source with a higher optical power in the relevant region, increasing the integration time, a more sensitive spectrometer, and a superior sensor design allows more light to be directed into the tissue and detected, which may increase this range. Furthermore, due to the limited separations measured, the actual

range will extend lower than 1.27 mm and higher than 3.81 mm, with a smaller separation explored in Section 3.6, as this allows for a more compact sensor.

### 3.3.2 Monte Carlo Simulation

A simulation using MCmatlab [126] was used to model light propagation through the tissues of the trachea and oesophagus at varying fibre separations. A 3D voxel space was generated for both organs (Fig. 3.10)

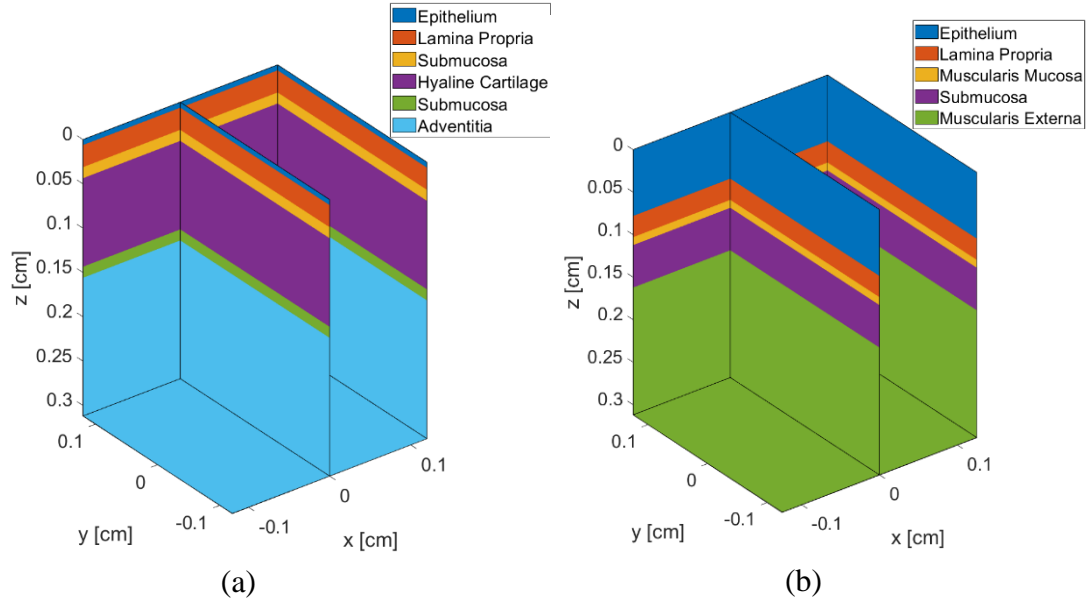


Fig. 3.10: 3D model of the (a) trachea and (b) oesophagus.

The optical properties [127, 128, 129, 130, 131, 132] and thicknesses [133, 134, 135, 136] of the tissue layers in Table 3.2 were collated from a variety of references. The individual optical properties of the layers of the mucosa could not be found at relevant wavelengths. Therefore, the average optical properties of mucosal tissue were applied over all mucosal layers for both organs.

Table 3.2: Optical properties and thicknesses of the tissue layers of the trachea and oesophagus.

Tissue		Layer Thickness ( $\mu\text{m}$ )	Absorption coefficient $\mu_a$ ( $\text{cm}^{-1}$ )	Scattering coefficient $\mu_s$ ( $\text{cm}^{-1}$ )	g-factor
Trachea	Epithelium	50	3.4	381	0.8
	Lamina Propria	270	3.4	381	0.8
	Submucosa	120	2.4	290	0.9
	Hyaline Cartilage	1000	1.1	453	0.9
	Submucosa	120	2.4	290	0.8
	Adventitia	1570	2.2	330	0.9
Oesophagu	Epithelium	780	3.4	381	0.8
	Lamina Propria	270	3.4	381	0.8
	Muscularis Mucosa	78	3.4	381	0.8
	Submucosa	500	2.4	290	0.9
	Muscularis Externa	1680	1.1	111	0.9

Excitation light at 560 nm was modelled from an illumination fibre. This was then simulated to enter the tissues from their surfaces. The light was then received by a detection fibre in the same x and z position, whilst varying the position of the y-axis (changing only fibre separation). Light emission was from an ideal 250  $\mu\text{m}$  optical fibre, whilst detection was from an ideal 500  $\mu\text{m}$  optical fibre with an NA of 0.5. The total number of photons used in each Monte Carlo simulation was  $5 \times 10^8$  (Fig. 3.11).

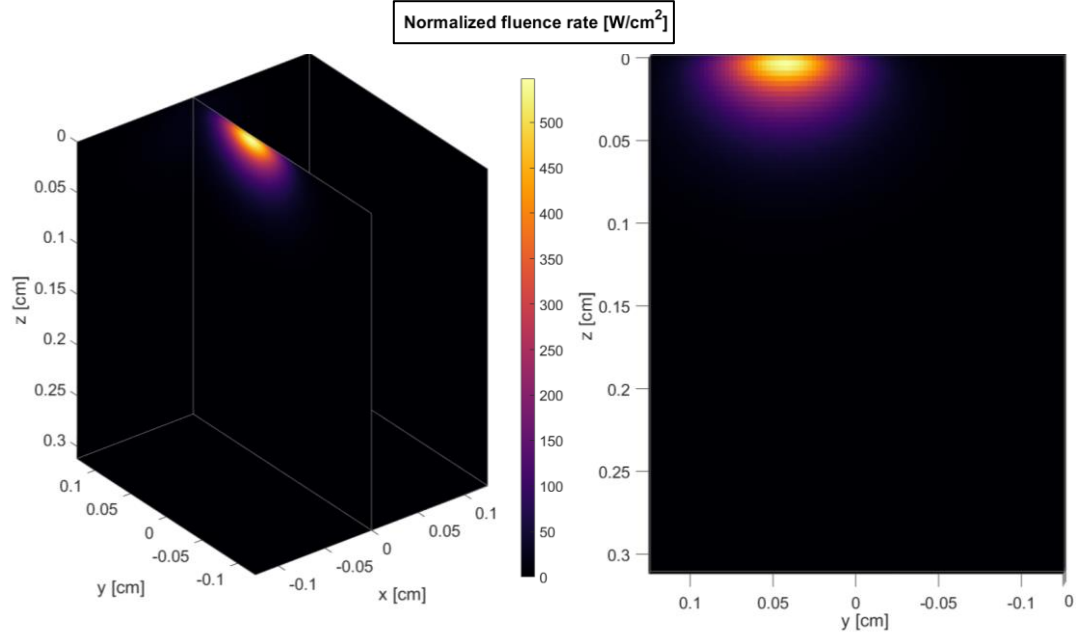


Fig. 3.11: Fluence rate of all simulated photons propagated from the tip of an optical fibre into an oesophagus.

To determine the average penetration depth of the detectable photons, only the photons that were collected by the detection fibre were used to calculate a mean depth of penetration for both the trachea and oesophagus (Fig. 3.12). The simulation was repeated 5 times and the means and standard deviations were recorded.

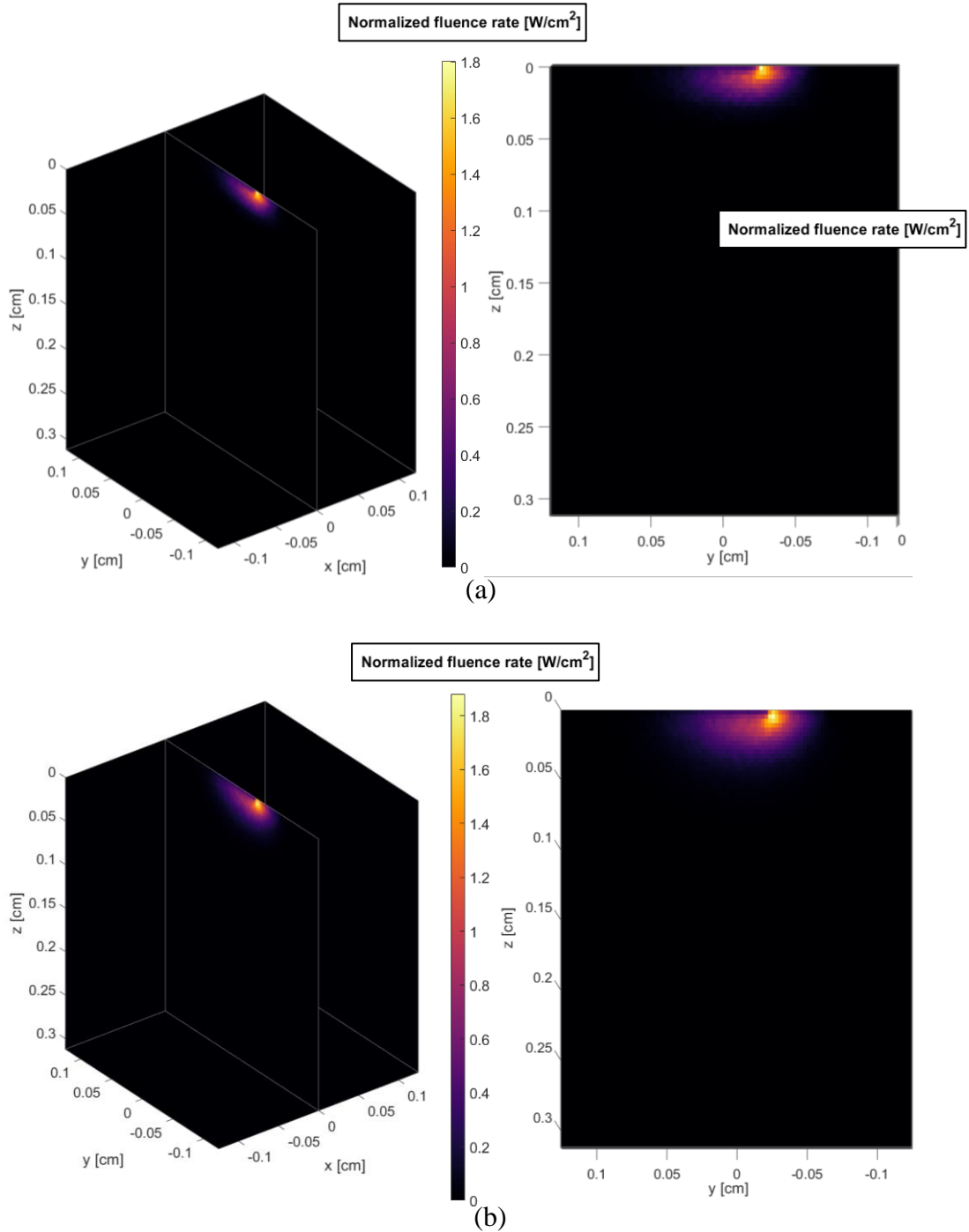


Fig. 3.12: (a) Trachea (b) Oesophagus. Fluence rate of only the photons collected by the detection fibre at a separation distance from the emission fibre of 0.875 mm.

The simulation does not model all of the optical properties or shapes of the tissues. For example, the partially keratinised squamous epithelium of the oesophagus, along with its folded shape makes it more difficult for light to penetrate the tissue. Furthermore, the complex structures of the various physiological features, such as the cell wall composition, glands and ducts are not modelled, which will play a significant role in how light is propagated through the tissues. Therefore, average absorption and scattering coefficients were used in place and formed a more ‘generic’ tissue.



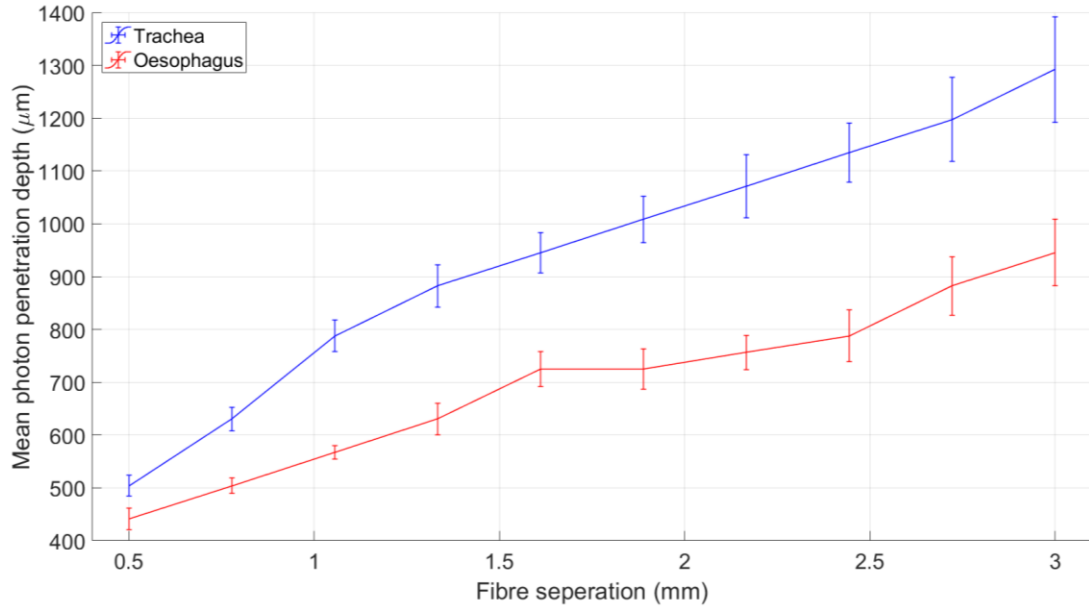


Fig. 3.13: Mean penetration depth of the simulated photons that were collected by a detection fibre in a trachea (blue) and oesophagus (red) model. The error bars in the penetration depth are from the standard deviation on 5 repeat simulations. There error bars on the fibre separations are from the number of pixels used in the 3D voxel models.

This simulation suggests that it is the proximity of the submucosa to the surface of the tissue that is the dominant effect in detecting the OHb absorption feature in the tracheal spectra. The highly reflective cartilage may also work to scatter and reflect more of the light through the upper submucosa of the trachea, whereas the light is mostly absorbed by the mucosa in the oesophagus. The mucosa is less vascularised than the submucosa and contains smaller blood vessels carrying less oxygenated blood. The penetration depth of the trachea is consistently higher than the penetration depth of the oesophagus (Fig. 3.13). This is believed to originate from the highly scattering cartilage layer causing photons to be reflected through the submucosa, but also to penetrate deeper.

The minimum mean penetration depth of the collected photons in the trachea was found to be  $500 \pm 20 \mu\text{m}$  at a fibre separation of 0.5 mm. The maximum penetration for the oesophagus was found to be  $950 \pm 60 \mu\text{m}$  at a 3 mm separation. All simulated fibre separations tested (0.5 to 3 mm) allow detection of photons that have penetrated the submucosa of the trachea, but not the oesophagus. Therefore, a fibre separation should be chosen within this range to minimise total sensor size.

### 3.4 Sensor Design

Several sensor designs were conceptualised with some of these being manufactured through 3D printing and then tested. Initially, a simple two-fibre design is described with this progressing into three-fibres. The manufacturing capabilities of Bluefrog Design (Leicester, UK) were then enlisted to manufacture a metal mould to improve the consistency and ease of production of the sensors. Finally, smaller changes to the design to produce a biocompatible sensor with improved performance were made, with an introduction to the use of ‘J-shape’ fibres to increase the optical output of the sensor. The following sections focus on the design aspect of the sensors.

### 3.4.1 Two-Fibre Rectangle

A sensor was designed that utilised the property of a 45° cleaved fibre to reflect light perpendicularly to the fibre axis (Section 3.2). The fibres are behind each other in Fig. 3.14a and Fig. 3.14b. The detection fibre functions in a similar fashion to the emission fibre, where light follows the reverse path; entering through the side and reflecting off the cleave into the fibre core.

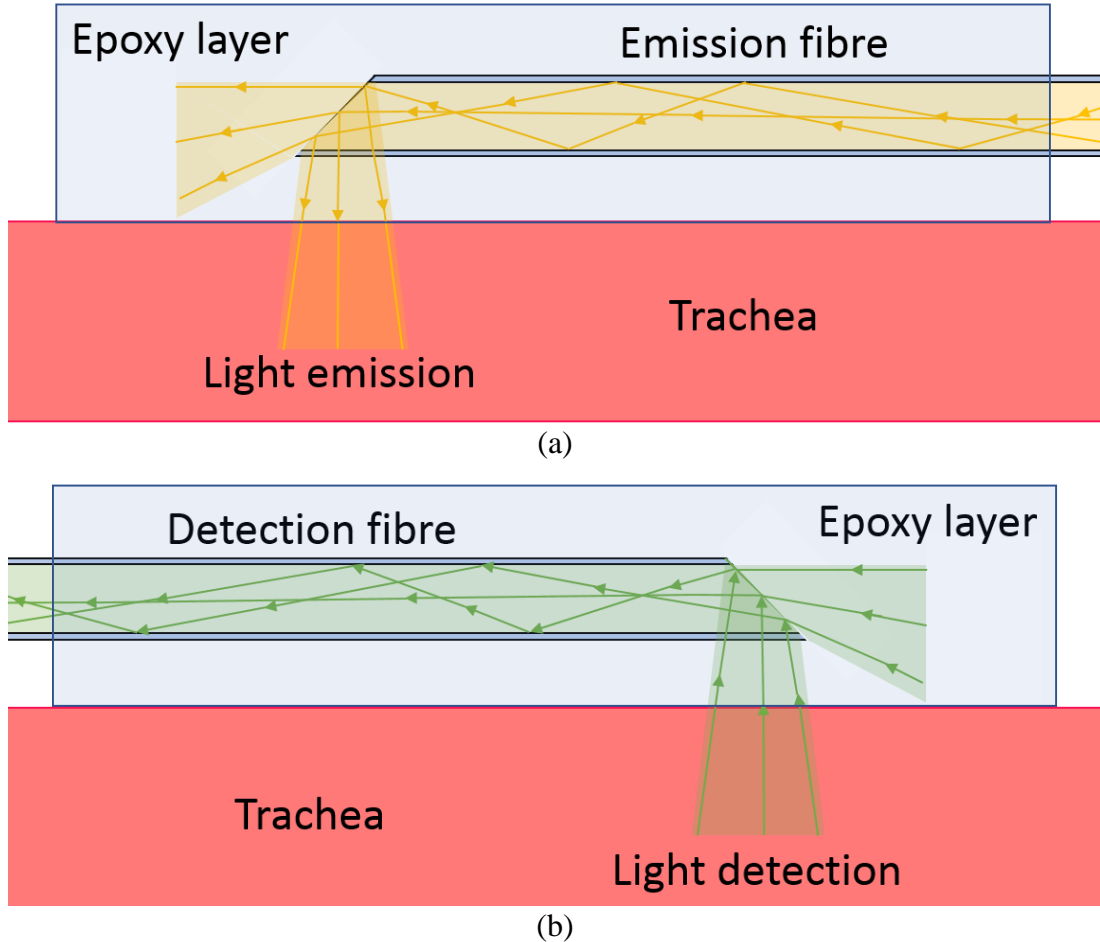
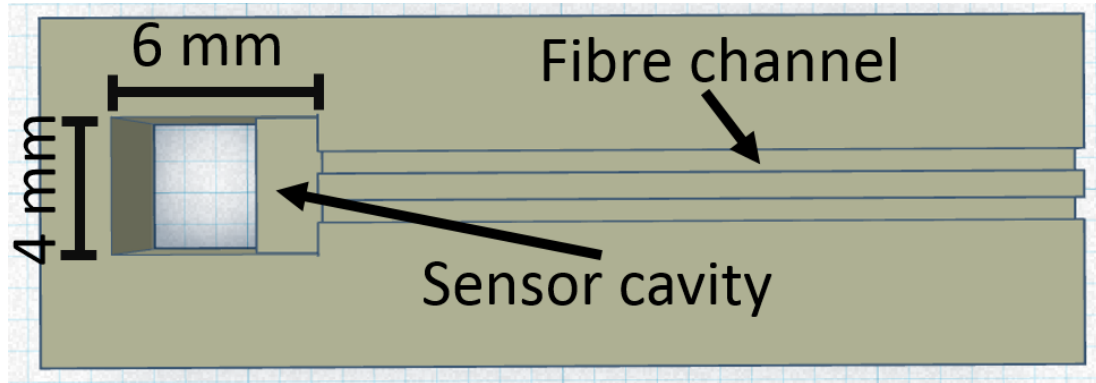


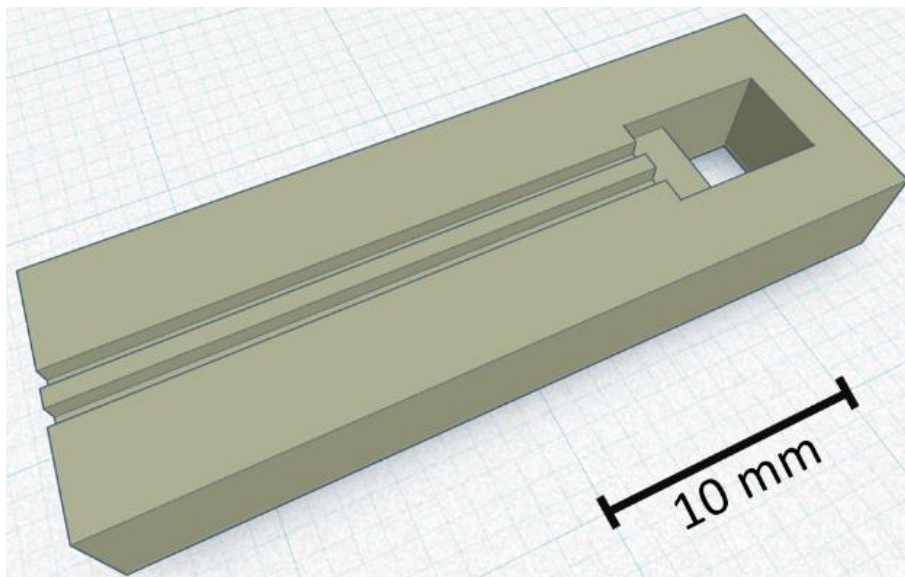
Fig. 3.14: A 45° cleaved fibre in a patch showing how light is emitted perpendicular to the fibre axis and the patch face (sensor dimension  $6 \times 4 \times 1$  mm). (a) Front view. (b) Back view.

This two-fibre sensor mould was designed on TinkerCad ([tinkercad.com](http://tinkercad.com)), a web app for 3D design (Fig. 3.15). The sensor mould dimensions were  $6 \times 4 \times 1$  mm with two long channels for the length of the fibre to sit in during casting ( $22 \times 0.7 \times 0.7$  mm). A cavity behind the sensor head ( $4 \times 4 \times 4$  mm) is designed to be filled with a soft malleable material such as Blu-Tack® to aid in the demoulding process. The separation between the fibres was 1.5 mm, which is on the lower end of the optimal separation described in Section 3.3 but produces a compact sensor, with the option to increase or decrease this separation depending on the depth of the absorption features of OHb in the 530 – 590 nm wavelength region. The mould dimensions could be decreased further as the tips of the fibres were placed approximately halfway into the sensor cavity, with a gap remaining on either side of the fibres. However, the size was chosen for the stability of the sensor at this stage and could be reduced in future

iterations. Furthermore, the choice of epoxy will affect the coupling efficiency in the 45° sensor design as light propagates from the side of the fibre through the epoxy.



(a)



(b)

Fig. 3.15: 3D model of a mould used to form a two-fibre patch (sensor dimension  $6 \times 4 \times 1$  mm).

The mould was produced using a 3D printer (Creality, model Ender-3 Pro) with a quoted printing precision of  $\pm 0.1$  mm. The plastic mould formed was of the correct shape and dimensions with the resolution being sufficient to print a sensor of this size (Fig. 3.16a). However, the channels where the fibres were to be laid occasionally had the joint covered with plastic due to their small size. Therefore, the channels had to be cleared using a metal file. The mould was sprayed with two coats of PTFE mould release spray (Rocol, aerosol mould release 400ml) to aid in demoulding. The fibres were placed into the channels such that their tips were approximately halfway into the sensor mould cavity. The positions of the cleaved fibres were verified with a compound microscope to ensure the cleave was orientated so the light reflects from the tip of the fibre and out of the front of the sensor (Fig. 3.14). The fibres were held in place using Blu-Tack® so that they didn't move or rotate during the filling of the mould. Blu-Tack® was also used to fill the void behind the sensor so that it could be easily demoulded by removing the Blu-Tack® and then pushing on the back of the sensor. Two drops of UV curable epoxy (Panacol, model Vitalit 1655) were pipetted into the mould (Fig. 3.16b) and then cured with a UV torch (Tattu, model UV395-

U1S), emitting a power of 5W with a central wavelength of 395 nm for approximately 20 minutes.

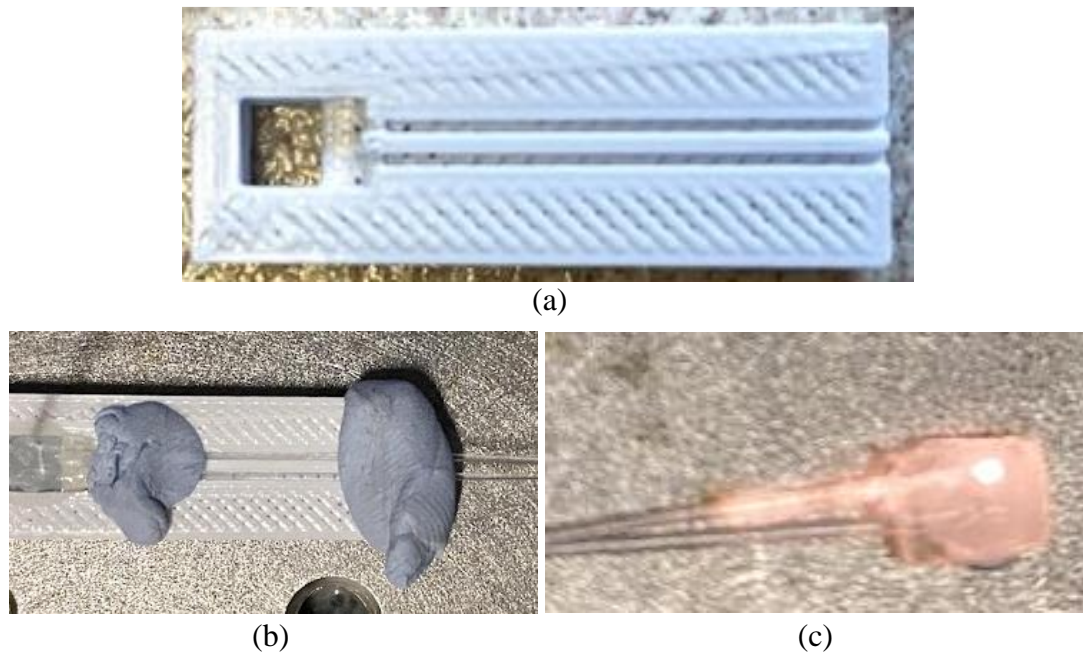


Fig. 3.16: Photographs of the (a) 3D printed mould, (b) epoxy casting using the mould, (c) resulting sensor with optical fibres embedded in the epoxy (sensor dimension  $6 \times 4 \times 1$  mm).

The resulting mould produced an approximately  $6 \times 4 \times 1$  mm sensor once the excess epoxy was removed with a handheld electric rotary tool (see Fig. 3.16c). After demoulding, the sensor was not of the correct dimensions and had an irregular shape due to the epoxy overflowing and causing bulging. Filing and polishing helped to refine the overall shape of the sensor. However, there was still some misshape to the sensor caused by the epoxy overflowing into the fibre channels during curing. In future fabrications with this mould, Blu-Tack® was pushed into the fibre channel where it connects to the sensor head. Filling the channels with Blu-Tack® made it so the epoxy could not flow into them, as the epoxy on the fibres was difficult to remove during the polishing stage.

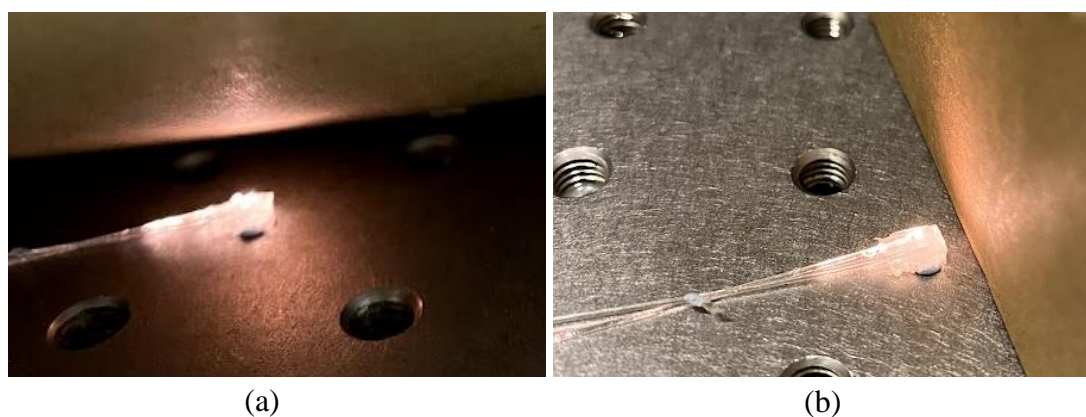


Fig. 3.17: Epoxy sensor highlighting the directionality of the emitted light, (a) parallel and (b) perpendicular (sensor dimension  $6 \times 4 \times 1$  mm).

The sensor succeeded in emitting some of the light perpendicularly to its face (Fig. 3.17a). However, a large amount of light was also emitted in parallel (Fig. 3.17b). It

should be noted that the ambient light levels of Fig. 3.17b are lower due to the shadowing caused by the surface used to demonstrate the directionality of the light emitted from the sensor.

### 3.4.2 J-shape Fibres

A large percentage of light is lost due to emissions parallel to the surface of the 45° cleaved fibre sensor (Sections 3.2 and 3.4.1). Furthermore, by cleaving the fibres to a sharp point, if the fibres become loose from the surrounding epoxy layer, they pose an increased likelihood of damage to the patient's airway. Furthermore, they may damage the ETT if the sensor is integrated into the cuff, as this is made of a thin material which must remain inflated to function properly. Furthermore, producing a precision cleaved fibre is problematic without custom equipment, with the quality of the cleave and the angle of the cleave affecting the performance of the sensor. Therefore, a new method for launching light perpendicularly to the sensor face and into the tissues was explored.

A possible solution for increasing the perpendicular emission of light is to coat the 45° cleaved fibre in a reflective material by sputtering, functioning as a mirror and increasing the amount of light reflected by the tip [137]. However, only the cleaved surface must be coated in the material so that the light can still emit from the side of the fibre, requiring some precision in the coating process. A simpler method is to bend a standard fibre (90° cleaved) so that the tip is pointing out of the sensor face, producing a 'J-shape' fibre tip (schematically shown later, see Fig. 3.24). However, bending the fibres at sharp angles will incur bend losses as light from the core modes couple to cladding modes [138,139]. Once a certain critical bend radius for the fibre is achieved these bending losses increase rapidly. Furthermore, bend losses increase more rapidly for longer wavelengths of light, introducing a wavelength dependency on the bend radius.

The minimum bend radius for the optical fibres used (commercial grade PolymethylMethacrylate (PMMA), Asahi, model DB-500) is described on the data sheet as 10 mm to give a  $\geq 90\%$  transmission rate. However, exceeding the 10 mm bend limit may still yield enough optical power, particularly at shorter wavelengths such as those used to distinguish the tracheal and oesophageal tissues. A simplified bend loss coefficient ( $\alpha$ ) at the bend of a multimode optical fibre can be found theoretically from the properties of the fibre [140], as shown in Eq. (3.4),

$$\alpha = \frac{4\pi n_1(\theta_c - \theta^2)}{\gamma} \exp\left(-\frac{4n_1 r}{3\gamma} \left(\theta_c^2 - \theta^2 - \frac{2a}{r}\right)\right) \quad (3.4)$$

Where  $n_1$  is the refractive index of the fibre core,  $\theta_c$  is the critical angle,  $\theta$  is the angle of propagation of the light relative to the fibre axis, and is on average equal to 0 for a large diameter multimode fibre,  $\gamma$  is the wavelength of the light,  $r$  is the bend radius of the fibre, and  $a$  is the fibre core radius.

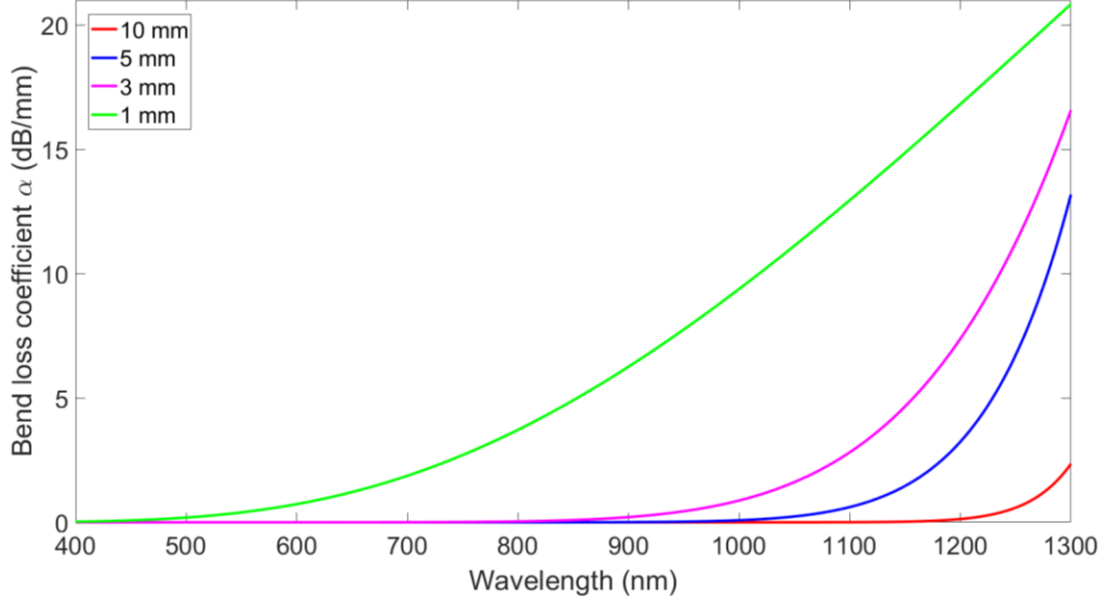


Fig. 3.18: Bend loss coefficient of a PMMA multimode optical fibre with a NA of 0.5 at varying bend radius.

The light is heavily attenuated at long wavelengths with decreasing bend radius (Fig. 3.18). For a 1 mm thick sensor patch, the bend radius required for the ‘J-shape’ fibres is approximately 3 mm, estimated by bending the fibres into the shape and then measuring the radius. The bend loss coefficient is expressed in units of dB/mm, with losses occurring over an estimated 5 mm of bending. A 3 mm bend radius follows the pink line in Fig. 3.18, producing losses of less than  $1 \times 10^{-4}$  dB/mm over the wavelength region of interest (530 – 590 nm). A sharper bend could be used if required, theoretically down to  $> 1$  mm, as the bend loss coefficient in the relevant wavelength region for the fibre is below 0.7 dB/mm (green line on Fig. 3.18), which translates to a loss of less than 3.25 dB over an estimated effective bend length of 5 mm ( $0.65 \text{ dB/mm} \times 5 \text{ mm}$ ). The light lost at the bend is emitted parallel to the fibre axis and perpendicular to the tissue surface and therefore doesn’t contribute to the measurement of tissue reflectance. Therefore, the attenuation of light at the wavelength region of interest is acceptable, with only longer wavelengths being significantly affected ( $> 1200 \text{ nm}$ ). However, Eq. (3.4) is a simplified version which does not account for effects such as: the effective refractive index change of the core and cladding due to stresses induced by the bend; interference from reflected light between any core and cladding modes; and it also assumes a perfect circular bend where a less sharp oval type bend could be used experimentally. Furthermore, only the bend loss coefficient is calculated here, where the proportion of optical power loss ( $P_{loss}$ ) caused by the bend can be found from optical power that reaches the bend ( $P_0$ ), which is given by the optical power of the light source, properties of the fibre, and coupling of the light with the fibre (Eq. (3.5)) [140],

$$P_{loss} = \frac{\left[ \int_0^{\theta_c} P_0(\theta) d\theta - \int_0^{\theta_f} P_0(\theta) \exp(-\alpha l) d\theta \right]}{\int_0^{\theta_c} P_0(\theta) d\theta} \quad (3.5)$$



$$\theta_f = \theta_c \left( 1 - \frac{2a}{R\theta_c^2} \right) \quad (3.6)$$

where  $\theta_f$  is the angle at which all modes are effectively lost at the bend (Eq.(3.6)). All variables are the same as in Eq. (3.4), and  $l$  is the distance of propagation around the bend.

There is approximately zero bending loss for a bend radius of 3 mm or more, whereas the theoretical limit for the cleaved fibres was 38.1% loss (61.9% transmission, Section 3.2). Therefore, bending the fibre so that light emits perpendicular to the face of the patch will theoretically produce a higher optical power output. A bend radius of 1 mm gives a loss of 3.25 dB (47.3% loss).

To investigate experimentally how varying the bend radius of a plastic optical fibre (POF) varies the optical power lost (Fig. 3.19), 500  $\mu\text{m}$  diameter fibres were bent in increments of  $1 \pm 0.25$  mm from 10 mm to 1 mm. One end of the fibre (commercial grade PolymethylMethacrylate (PMMA), Asahi, model DB-500) was connected to a broadband LED (Fiber-Coupled LED, Thorlabs, model MBB1F1), which was connected to an LED driver (T-Cube LED Driver, Thorlabs, model LEDD1B). The other end of the fibre was connected to a spectrometer (Ocean Optics, model USB2000+UV-VIS-ES). The integration time was set to 1 ms, which is considerably lower than for diffuse measurements as the fibre was directly coupled from the LED to the spectrometer and delivered a high optical power.

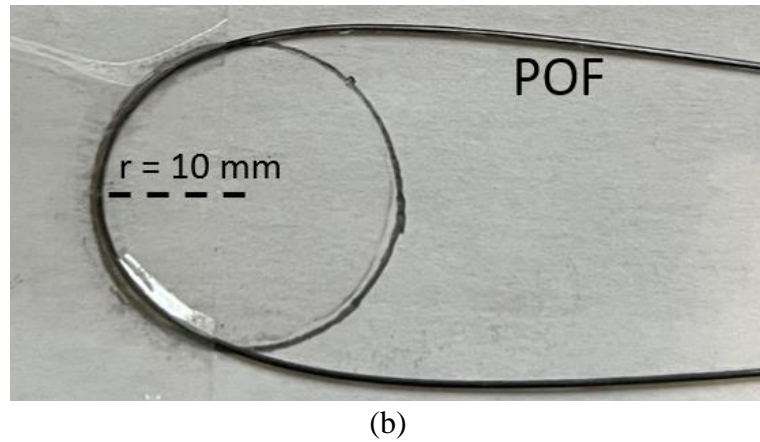
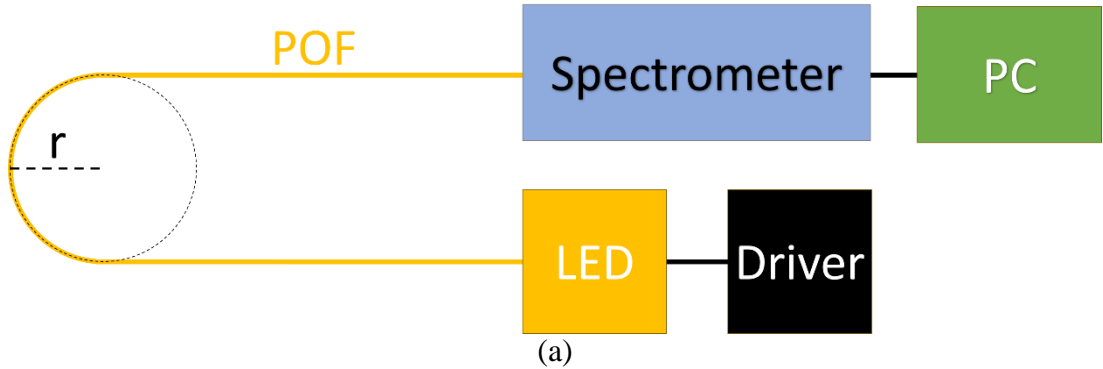


Fig. 3.19: Design of an experiment to investigate how varying fibre bend radius ( $r$ ) optical power loss at the bend. (a) Schematic. (b) Photograph of fibre at a bend radius  $r = 10$  mm.



The fibre was bent by drawing a circle of radius  $r$  onto paper (Fig. 3.19b) and then gently heating the fibre with a heat gun and bending it to the desired radius. The POF travelled around half the circumference ( $180^\circ$ ) of the circle, causing it to leave the bend in the same direction it entered (back towards the opto-electronic equipment). The fibre was bent whilst it was connected to the opto-electronic equipment. For each increment, the fibre stayed connected to the equipment to minimise the variation in losses at the connections. Three POFs were bent through the full range of increments and 100 spectra were recorded for each bend radius.

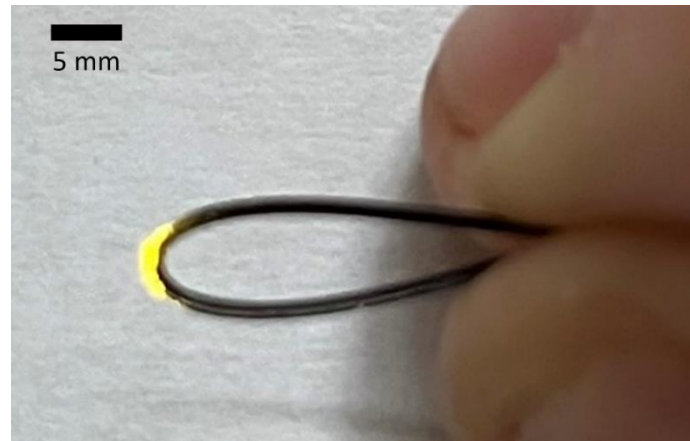


Fig. 3.20: POF bent into a J-shape. The fibres would be cut at the bend for use in a sensor. The loss of optical power is seen as yellow light at the bend.

Three more fibres were then bent into a J-shape without cutting them at the bend (Fig. 3.20), and then both fibre ends were connected to the equipment so that the power loss for a J-shape fibre could be compared to the varying bend radius. By leaving the J-shape fibre uncut, an upper limit on the bend losses is found, as light is lost coming into and out of the bend in this experiment, whereas in the sensor the light leaves the tip of the fibre halfway through the bend and couples with the tissue.

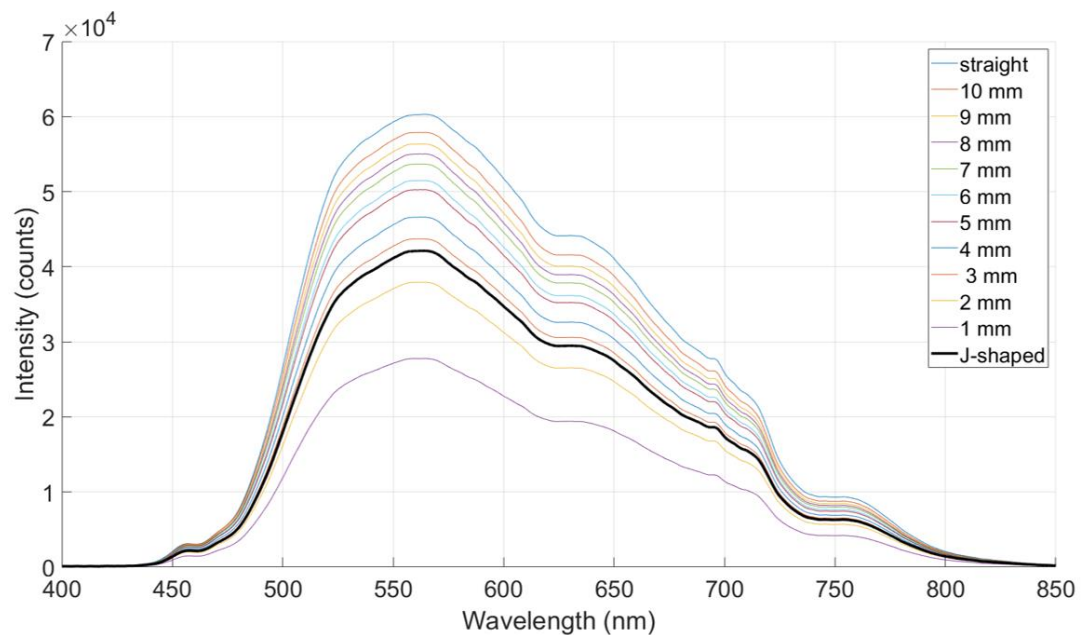


Fig. 3.21: Average intensity spectra for the first POF with varying bend radius from a straight fibre to a radius of 1 mm.

Fig. 3.21 shows the mean of the 100 spectra measured at each bend radius for the first fibre. The peak light intensity decreases with decreasing bend radius. The straight fibre gave the highest peak intensity and each subsequent bend radius gave a lower intensity, with the bend radius  $r = 1$  mm giving the lowest. The J-shape fibre (black line in Fig. 3.21) gave a peak intensity that is closest to a bend radius of 3 mm.

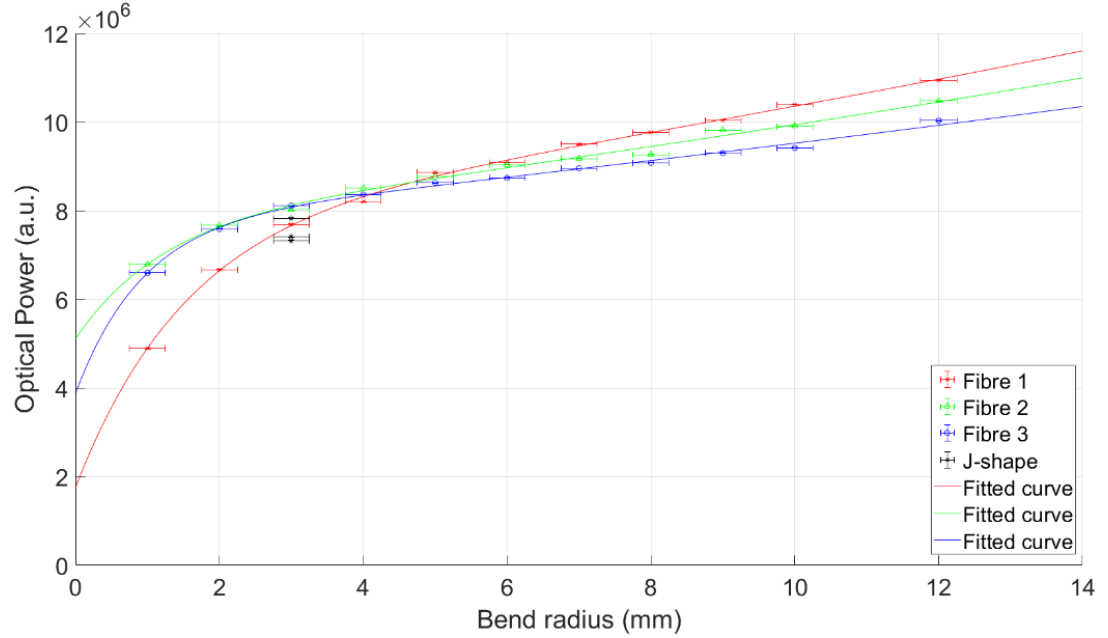


Fig. 3.22: Area under the curve of the mean spectra for three fibres at each bend radius. The fitted curves are of an exponential form.

The area under the average spectra for each bend radius (found from Fig. 3.21) was obtained, giving Fig. 3.22. The error on the bend radius was from instrument precisions and estimated at 0.5 mm from using a protractor and callipers. The error in the optical power was found from the standard deviation of the area of the 100 spectra measured at each bend radius and is too small to be seen in Fig. 3.22. The spectrometer has a varying quantum efficiency with wavelength and so the absolute optical power could not be acquired without calibration by an appropriate black body light source. Instead, the optical power in arbitrary units (a.u.) is used, allowing for comparisons between bend radii. A bend radius of 10 mm was when losses were first observed, and measurements began. However, since the straight fibre's optical powers are consistently above the fitted curve at 11 mm, there were likely losses at bend radii higher than 10 mm. Therefore, the losses of a straight fibre are equivalent to those of a larger bend radius, with 12 mm having been chosen to illustrate the straight fibre as it best matches the fitted curve. An exponential curve was found to model the data well, with all three fitted curves having an R-squared of above 99%.

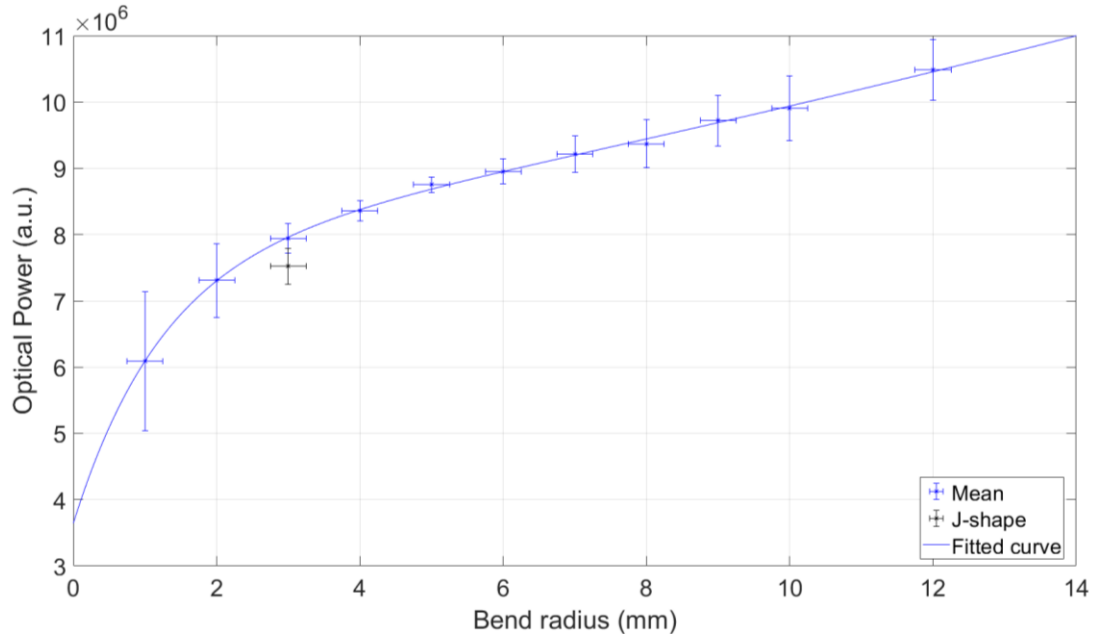


Fig. 3.23: mean area under the curve of the spectra for three fibres at each bend radius from the mean of the repeats in Fig. 3.22. The fitted curve is of an exponential form.

The mean of the three repeat fibres was then calculated and is shown in Fig. 3.23. The error in the optical power was found from the standard deviation of the three repeats. Notably, the error on the smallest bend radius (1 mm) is larger than the others as variations in bend radius for small radii affect the optical power more. The average optical power of the three J-shape fibres is also shown in

Fig. 3.23 (Black data point). A two-term exponential (Eq. (3.7)), where  $P$  is the optical power and  $r$  is the bend radius in mm, gives an R-squared percentage of 99.9%. Interestingly, a two-term exponential function better models the experimental data, whereas a one-term exponential is used theoretically (Eq. (3.4)) giving an R-squared of 88%. This is likely due to this equation being a simplified one where strains induced in the fibre are not accounted for and require a second term.

$$P = 7.7 \exp(0.025r) - 4.1 \exp(-0.80r) \quad (3.7)$$

Comparing the optical power of the straight fibre ( $1.05 \pm 0.05 \times 10^7$ ) to the J-shaped fibre ( $0.75 \pm 0.03 \times 10^7$ ) shows a power loss at the bend of  $29 \pm 2\%$ .

A sensor that incorporates J-shape fibres is preferred to one that incorporates  $45^\circ$  cleaved fibres. Observationally, the light produced by those sensors was much brighter. Furthermore, the theoretical limits for the losses of a J-shape fibre are lower than those of the cleaved fibres (limit of zero loss compared to 38.1%, respectively). Experimentally, the J-shaped fibres produced a loss of 29% compared to 81.9% for the cleaved fibres. Furthermore, the bend loss was measured for fibres bent through  $180^\circ$ , whereas in the sensor they are bent through  $90^\circ$ , decreasing the bend length by half and decreasing losses to a projected  $\sim 15\%$ . However, it should be noted that the bend losses increase exponentially with bend radius (Eq. (3.7)), and small changes to the bend radius below 2 mm may drastically decrease the performance of a sensor due to bend losses.

A sensor that incorporates the J-shape fibres is superior to one that uses a  $45^\circ$  above approximately 1 mm bend radius. The sensor design is conceptualised in (Fig. 3.24), with the detection fibre being behind the emission fibre.

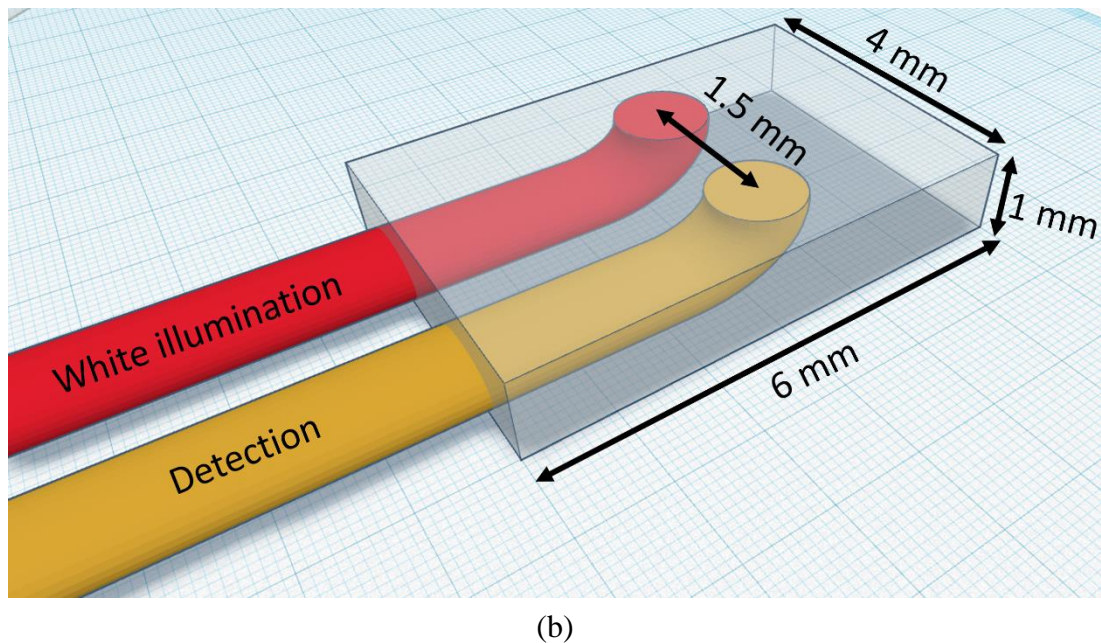
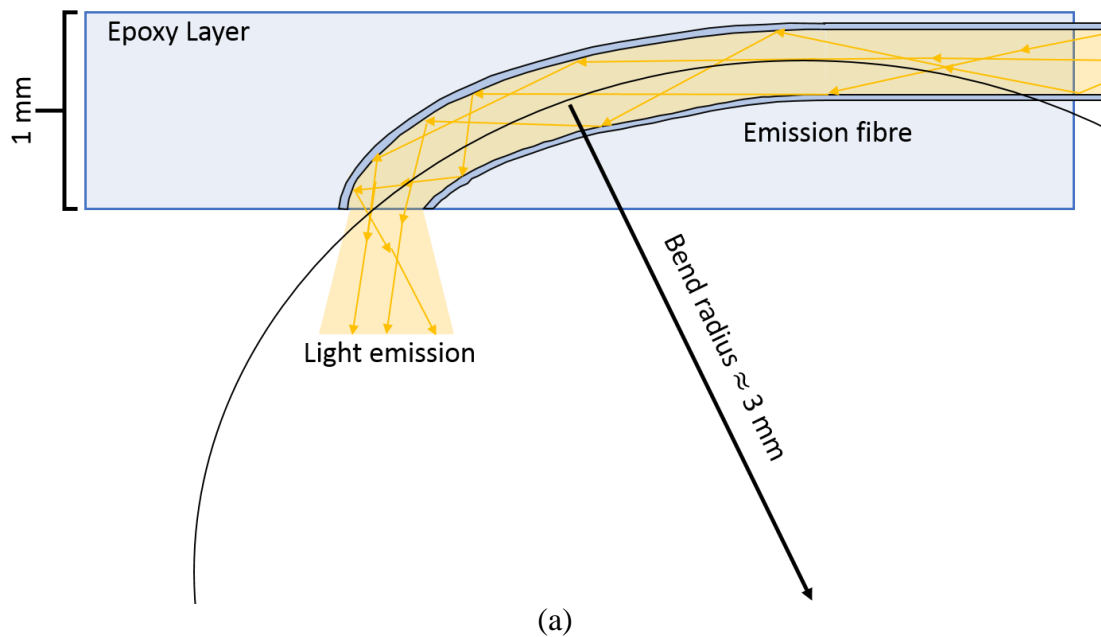


Fig. 3.24: (a) J-shape bent emission fibre in an epoxy layer. (b) 3D rendering of the J-shape fibres in an epoxy layer.

A fibre with the maximum bend radius should be used to minimise losses. Therefore, the fibres were bent to maximise the space inside the epoxy layer forming a J-shape. To achieve this, the fibres were bent under moderate heating from a heat gun so that they became more malleable. Initially, this was performed by hand using a piece of paper that had been marked with the bend shape. Performing this step by hand introduced some variations between sensors, with future mould designs accounting for this. Furthermore, the variations are less impactful than a  $45^\circ$  cleaved fibre that is off by a few degrees.



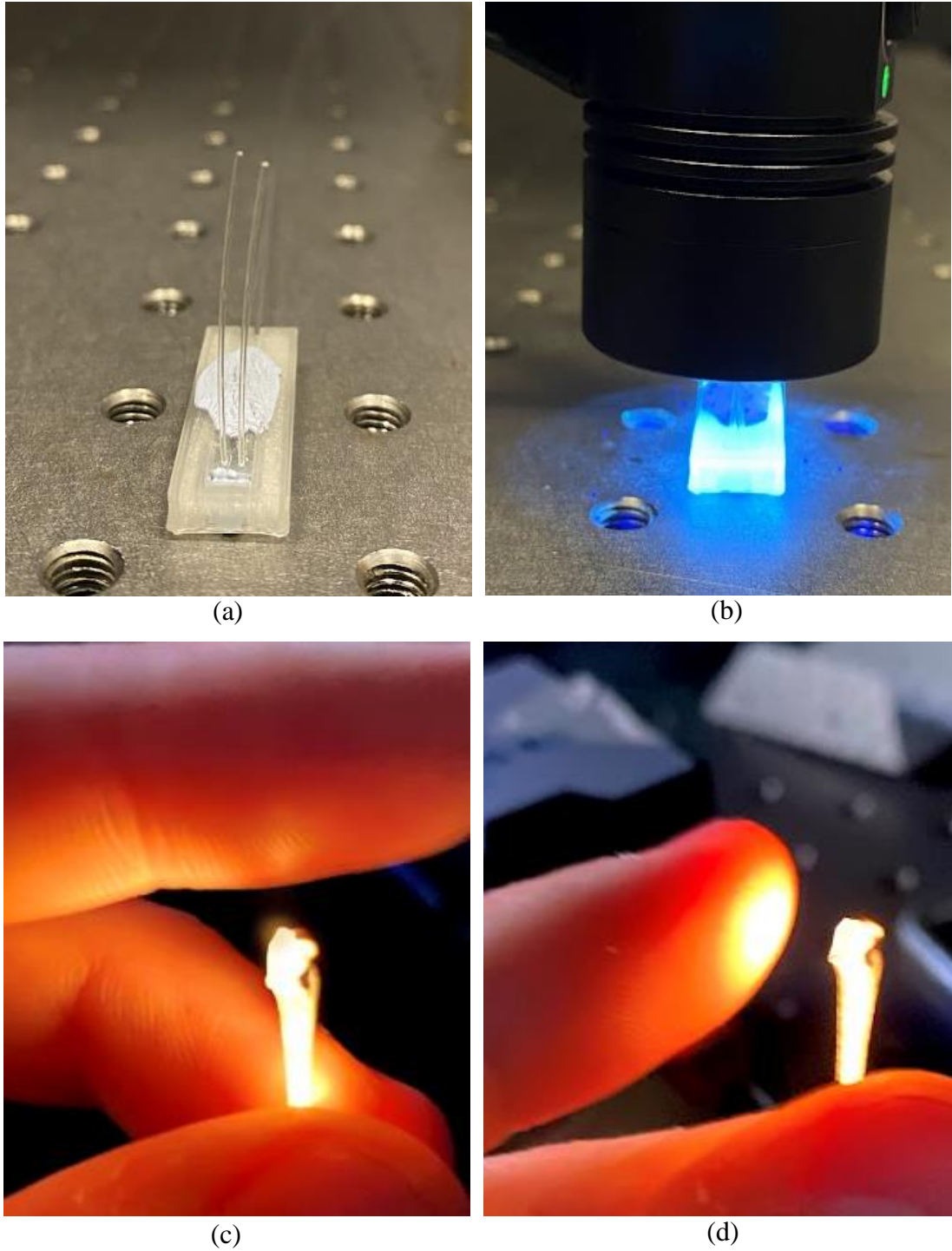


Fig. 3.25: (a) Photograph of J-shape fibre sensor being cast, (b) sensor curing with a UV torch, (c) and (d) showing the directionality of the light emitted is mostly perpendicular to the sensor face.

The sensor was produced using the same mould and the same general process as Section 3.4.1, with the bend of the fibres now being located centrally in the sensor mould (Fig. 3.25a-b). It was easier to leave excess fibre after the bend that can be removed during the final shaping and polishing of the fibre, as opposed to bending the end of a fibre. The sensor produced visibly more light perpendicular to the sensor face when compared to its 45° cleaved counterpart (Fig. 3.25c-d).

### 3.4.3 Three-fibre sensor

The capabilities of a ‘smart’ ETT, one with integrated optical fibres to make physiological measurements could detect more than ETT placement. With little modification to the sensor, oxygen saturation could be measured at the tracheal level, as discussed in Section 5.3.1. Typically, oxygen saturation measurements (Section 1.3.3) are made with red and infra-red light (660 and 940 nm) with few available light sources producing sufficient optical power in both these regions. It is also possible to use only 2 fibres and multiplex measurements. However, this may reduce the optical power due to coupling losses. Furthermore, the three-fibre design was deemed less complicated to implement at this stage. Therefore, a sensor was designed to incorporate two illumination fibres so that light could be coupled to the tissues from a light source in the visible region (white light) and the infrared region. A sensor design with two illumination fibres can therefore make both ETT placement detection and oxygen saturation measurements. The illumination fibre diameters were also reduced to compensate for the increase in the number of fibres. Decreasing the fibre diameters kept the sensor size to a minimum, as well as reducing the space the fibres take up running down the lumen of the ETT. Therefore, the illumination fibres’ diameters were changed from 500 to 250  $\mu\text{m}$  (commercial grade PolymethylMethacrylate (PMMA), Asahi, model DB-250) and a three-fibre sensor was designed. A smaller fibre diameter may also contribute to less optical power loss at the bend as it has a larger inner bend radius.

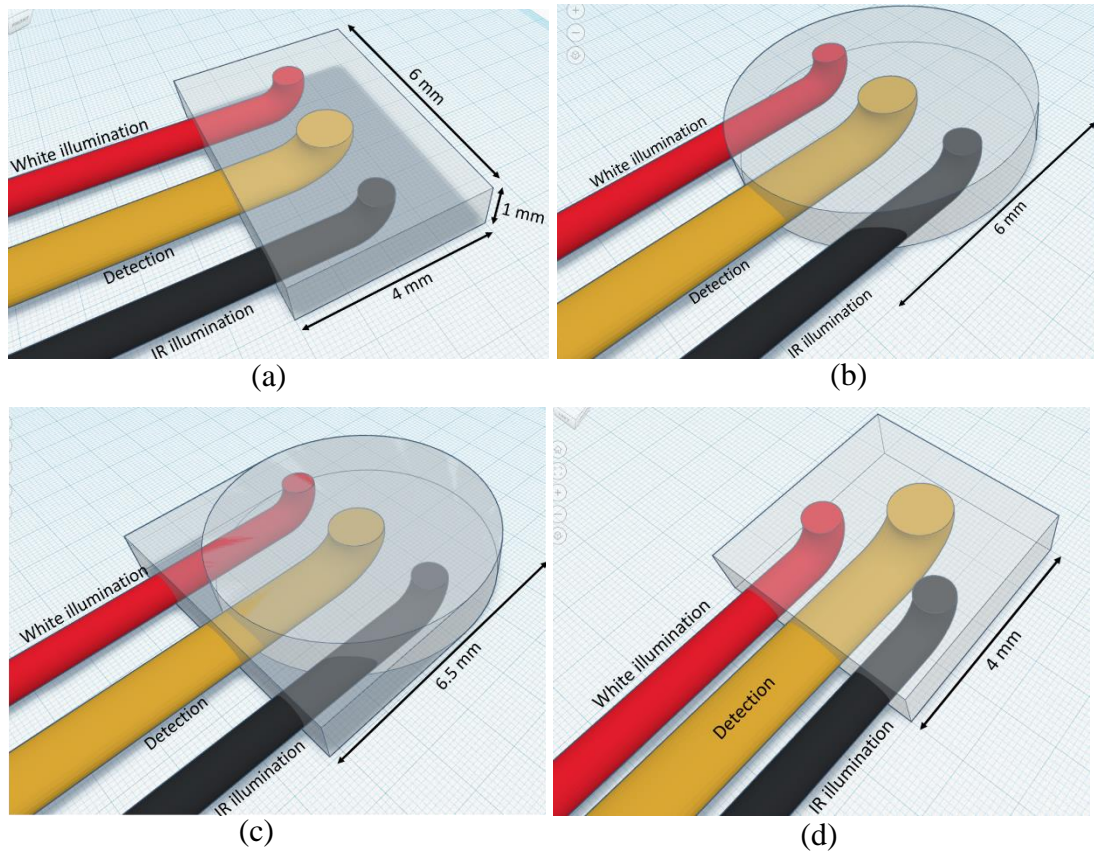


Fig. 3.26: Concept designs for different three-fibre sensors. (a) Three-fibre rectangle sensor; (b) Three-fibre circular sensor. (c) Three-fibre circular sensor with a rectangular base. (d) Square patch that reduces overall patch dimension by reducing the length of the rectangular patch from 6 to 4 mm.

The sensors were designed with the criteria of being compact and easily integrated into the ETT as described in Section 3.1. A sensor with the dimensions (6×4×1 mm) was conceptualised that could incorporate one J-shape 500  $\mu\text{m}$  diameter detection fibre and two J-shape 250  $\mu\text{m}$  diameter illumination fibres for the white (broadband) and infrared (IR) light (Fig. 3.26a). A circular sensor was also designed to utilise more of the space inside the sensor by removing the sharp edges of a rectangle (Fig. 3.26b). Further modifications to the design were implemented to improve the stability by increasing the surface area of the fibre in the epoxy. Furthermore, it was discovered that two separate castings were beneficial to achieving a consistent bend and stability, as visually the fibres were better aligned and more durable. Therefore, a sensor design consisting of a circular head with a rectangular base was conceptualised. Throughout the sensor designing process, multiple versions were formed and refined through 3D printed moulds with small modifications to improve the casting process and overall performance of the sensor, with all of them not being shown here. An example of one of these smaller modifications is shown in Fig. 3.26d, where the patch is made square to reduce its length by 2 mm and the fibres are moved away from the central axis to increase the separation between the detection and illumination fibres. A ‘triangular’ arrangement of fibres saves space and could result in a more compact sensor. However, arranging the fibres side-by-side was easier to manufacture at this stage.

### 3.5 Sensor Placement

There are three suitable places the sensor can be positioned on the ETT (Fig. 3.27), each with its advantages and disadvantages. Preliminary measurements suggest that diffuse reflectance can be performed from a range of distances from the surface of the tissue (Appendix G). Therefore, viable placements are investigated. Integrating the sensor inside the lumen of the ETT gives the sensor and patient the most protection. A thick ETT lumen separates the sensor from the tissue and provides a barrier during normal operation. However, if the sensor is damaged some of the materials could fall through the ETT lumen and be inhaled by the patient. The sensor is also separated from the tissue by a few millimetres depending on the exact type of ETT used [141], as there is an air gap between the ETT and the tissue. Furthermore, the light must travel through the relatively thick lumen, which attenuates it.

The sensor's placement outside the lumen of the ETT means it is brought closer to the tissue and the light doesn't have to travel through the relatively thick lumen. However, there is still a few millimetres gap between the sensor and the tissue at times. At other times, the sensor may press directly into the tissue which necessitates stricter biocompatibility standards.

The third option is initially the most appealing, by integrating the sensor behind the cuff of the endotracheal tube the sensor and tissues are protected by the cuff. The light then only has to penetrate the thin material of the cuff. Furthermore, the sensor is brought into intimate contact with the tissue as the cuff is pressed directly into it. Furthermore, if the sensor was damaged and broke apart, it would remain in the cuff. the other capabilities of the iTraXS ETT, as discussed in Section 5.2, greatly benefit from integration into the cuff, especially the contact pressure sensor which would not be able to function in any other position. Therefore, integration into the cuff gives two



means of protection from inhaling the sensor: the sensor must break; and the cuff must break as well. However, sealing the sensor inside the cuff is the most challenging integration method as the fibres need to run out of it. Furthermore, the sensor must be small enough to not significantly alter the shape of the cuff or to apply uneven pressure to the trachea. It may cause harm to the patient if there is too much pressure on the trachea where the sensor is located, or not enough pressure to form a good seal. Therefore, an experiment was designed to compare the sensor positions.

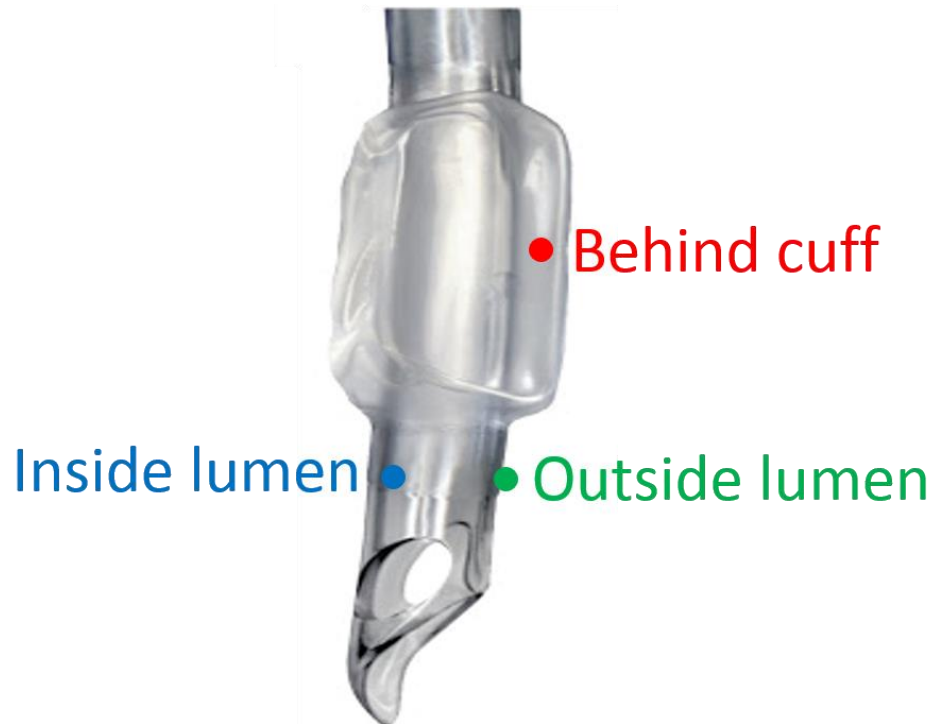


Fig. 3.27: Possible sensor locations for the ETT placement sensor.

A size 8 Mallinckrodt ETT (Covidien, model 107-80) with a high volume, low pressure (HVLP) cuff made from polyvinylchloride (PVC) was used. Sensor placement was determined before the metal moulds were manufactured. Therefore, a two-fibre rectangle sensor containing J-shape fibres was fabricated using a 3D printed mould (Section 3.4.1). A 3D-printed mould was used for convenience at this stage. Two PMMA fibres with a  $500\ \mu\text{m}$  diameter and a separation of 1.5 mm were used. The epoxy layer was made from UV-curable epoxy (Panacol, model Vitralit 1655). The sensor was attached in three positions and swapped sequentially after measurements: inside the ETT lumen; outside the ETT lumen; and behind the ETT cuff. The sensor was attached to the ETT, each time using a drop of UV curable epoxy (Fig. 3.28). The cuff was resealed using insulation tape so that it could maintain pressure. The tube was also covered with a transparent medical sensor sleeve (Pegasus Surgi Safe Tubing Sleeve small (18"×" 1.75"), Dental Sky, model 50-137) so that the sleeve could be replaced between measurements. This ensured the sensor and ETT remained clean from fluids that could affect different measurements. A new light source is used here, selected for its high optical output in the 530 - 590 nm wavelength region and fibre coupling capabilities. The light source used was a broadband LED with a wavelength range of 470 - 850 nm (Fiber-Coupled LED, Thorlabs, model MBB1F1). The LED driver was set to deliver a drive current of 500 mA with a current

ripple of 8 mA (T-Cube LED Driver, Thorlabs, model LEDD1B). The detection fibre was coupled to the same UV-visible spectrometer as used previously (Ocean Optics, model USB2000+UV-VIS-ES).

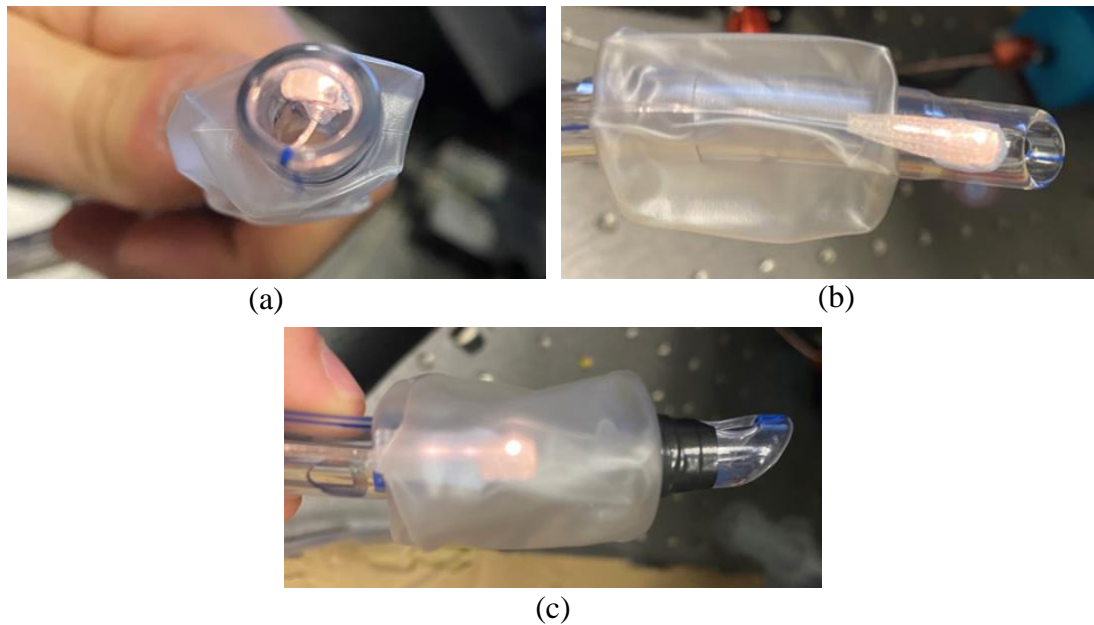


Fig. 3.28: Two-fibre sensor integrated into the (a) inside lumen (b) outside lumen, and (c) behind cuff of an ETT.

The ETT with integrated sensor (Fig. 3.28) was covered by a transparent sensor sleeve and then light and dark references were taken before measurements began. The ETT with the integrated sensor was then placed through the larynx of an *ex-vivo* porcine sample and into the top of the trachea (Fig. 3.29). The sensor was repositioned in the trachea 20 times by moving the ETT deeper into the trachea and rotating it in a spiralling motion, ensuring that different depths in the sample and different orientations were measured. The ETT was then removed from the sample, the sleeve replaced, and the tube moved into the oesophagus. The same motion of a downward spiral was used in the oesophagus to obtain 20 more spectra. The sensor was then moved to the next position on the ETT and measurements were repeated. There were two sets of measurements when the sensor was in the cuff of the ETT. One set was made when the cuff was fully deflated, as the cuff is during intubation ( $0.0 \pm 0.1$  cmH<sub>2</sub>O). The second set was when the cuff had been inflated to a typical cuff pressure, as if during normal ventilation ( $25.0 \pm 0.1$  cmH<sub>2</sub>O). The pressure was measured by an inline manometer. A total of 40 measurements for each sensor position were made (20 for the trachea and 20 for the oesophagus).

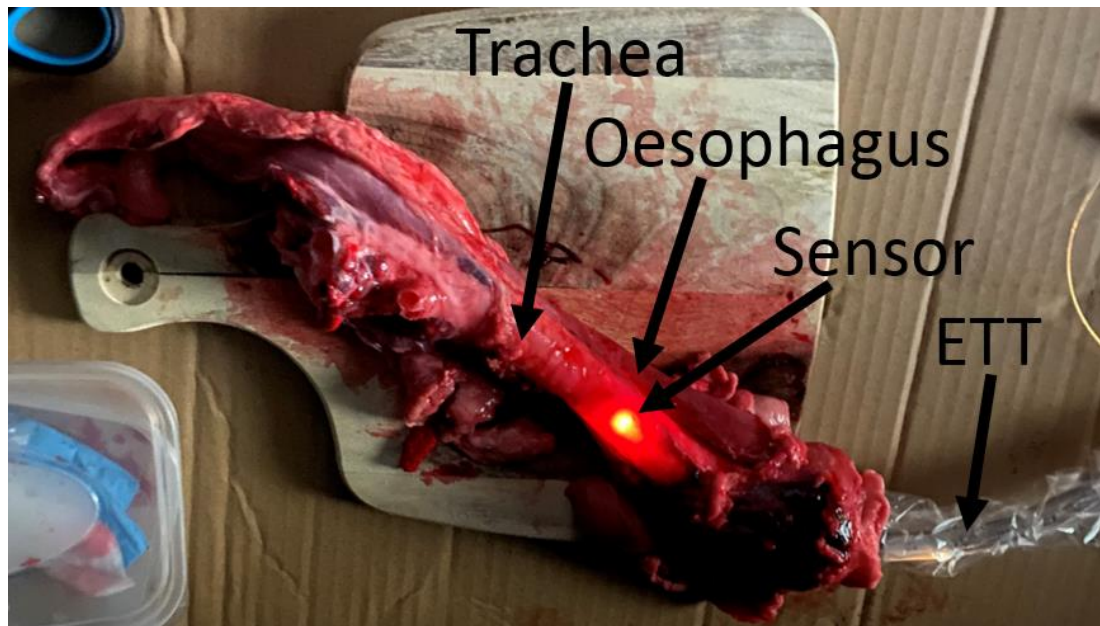


Fig. 3.29: Porcine sample with the ETT placement sensor integrated into the cuff of the ETT and then placed into the trachea.

The spectra were normalized at a single wavelength of 530 nm. The spectra when the ETT placement sensor was at different ETT locations can be seen in Fig. 3.30. Qualitatively, the tracheal spectra when the sensor was positioned in the lumen (Fig. 3.30a) do not provide a strong trough-peak-trough reflectance typical of the OHb absorption characteristic when taking measurements in the trachea. Furthermore, the signal contains more noise than the other measurements. This noise is caused by the distance from the tissue as well as the lumen material attenuating the signal such that less light is detected by the detection fibre giving a smaller signal-to-noise ratio (SNR). The tracheal spectra when the sensor was outside the lumen and behind the cuff for both the inflated and deflated measurements (Fig. 3.30b-d) all give spectra where the characteristic is visible. Interestingly, the oesophageal spectra contain some absorption in the second trough position (578 nm), which is more pronounced when the sensor is behind the inflated cuff. This implies some OHb is being accessed when the sensor is behind the cuff and pressed into the tissue slightly when it is inflated in the oesophagus, although much less than for the trachea.

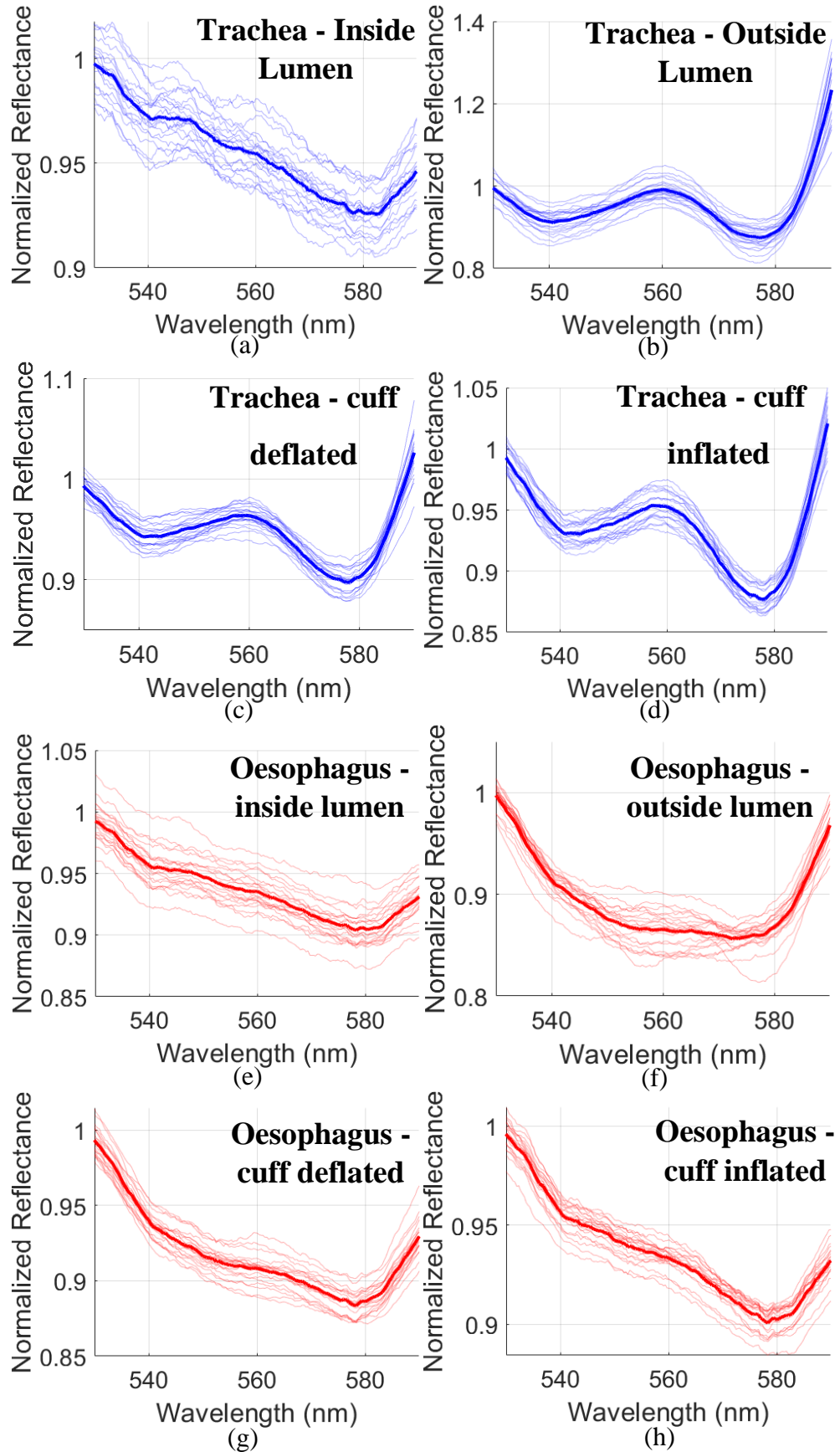


Fig. 3.30: Normalized reflectance spectra for an *ex-vivo* porcine trachea (blue) and oesophagus (red) when the ETT placement sensor is integrated (a,e) inside the ETT lumen, (b,f) outside the ETT lumen, (c,g) behind a deflated cuff, and (d,h) behind an inflated cuff. The thinner lines on each figure are the individual measurements and the thicker line is the average of the repeats.

The relative depth of the troughs in the absorption characteristic can be expressed by taking a ratio between the reflectance at 543 nm ( $R_{543}$ ) and the central peak at 561 nm ( $R_{561}$ ) giving the first ratio ( $R_1$ ), whereas the second ratio  $R_2$  includes the second trough at 578 nm ( $R_{578}$ ).

$$R_1 = \frac{R_{543}}{R_{561}} \quad (3.8)$$

$$R_2 = \frac{R_{578}}{R_{561}} \quad (3.9)$$

Therefore, a comparison can be performed by comparing the relative depth of each of the troughs expressed in the ratios  $R_1$  and  $R_2$  (Fig. 3.31).

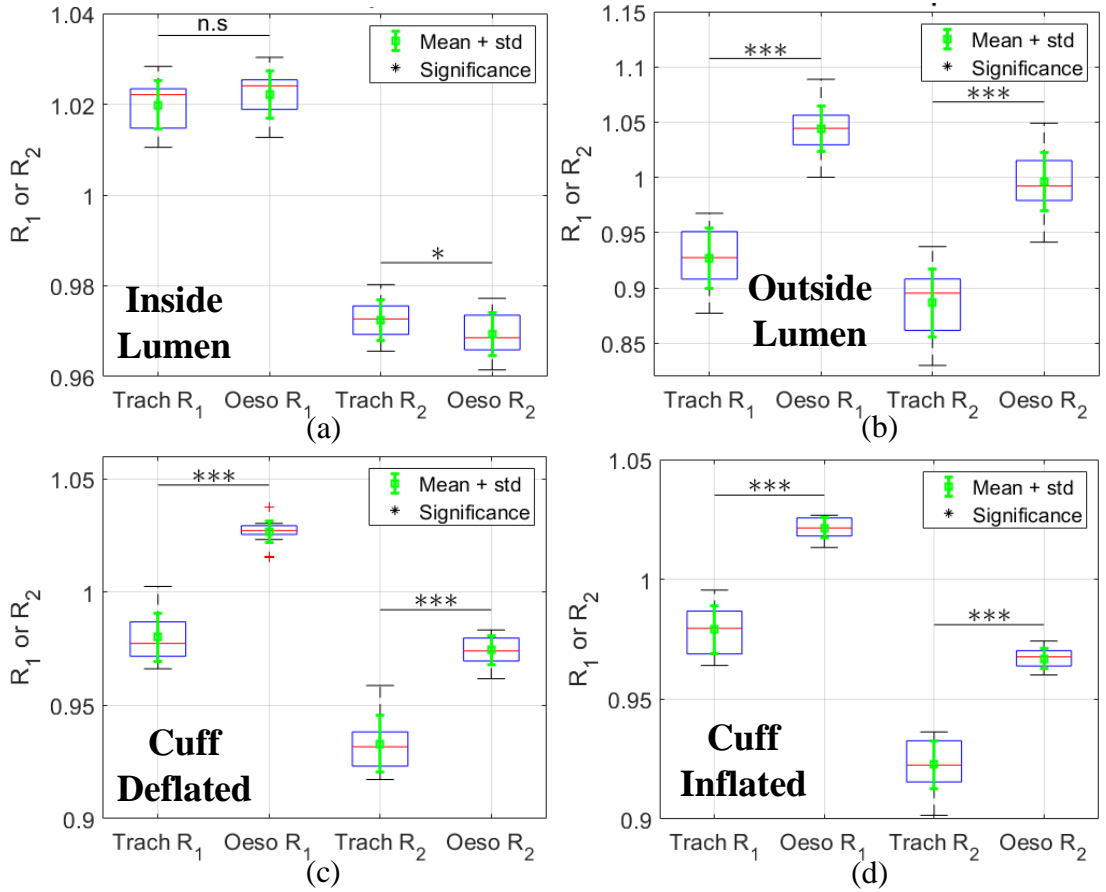


Fig. 3.31: Boxplots of the ratios  $R_1$  (Eq. (3.8)) and  $R_2$  (Eq. (3.9)) for the ETT placement sensor in an *ex-vivo* porcine trachea (Trach) and oesophagus (Oeso), when the sensor is positioned (a) inside the lumen, (b) outside the lumen, (c) behind a deflated cuff, and (d), behind an inflated cuff. The statistical significance of a t-test is denoted by an asterisk, with n.s denoting the results not being statistically significant, \* symbolises  $p < 0.05$ , and \*\*\* represents  $p < 0.001$ .

The ratios  $R_1$  and  $R_2$  compare the depth of the troughs relative to the central peak. Therefore, a value of 1 in Fig. 3.31 corresponds to reflectance at a wavelength of 543 or 578 nm which is equal to that of 561 nm. A value greater than 1 corresponds to an increase in reflectance (reflectance is above the central peak) and a value less than 1 corresponds to a decrease in reflectance (reflectance is below the central peak). The

inside lumen poorly differentiates the trachea and oesophagus as the two ratios are not different (Fig. 3.31a). All other sensor positions (Fig. 3.31b-d) produce ratios that have different values when considering the median and interquartile range. The inflated and deflated cuff gave the largest separation in reflectance ratios between the two tissues. Therefore, the sensor can perform well if it's located outside the lumen of the ETT but is unlikely to function as intended with a similar system if it was located inside the lumen. The best performance is achieved when the sensor is behind the cuff of the ETT, with this becoming more appealing due to the cuff protecting the tissue and sensor from each other by providing a protective barrier. The sensor performing well in the cuff is unsurprising as it is brought into intimate contact with the tissue, with only a thin transparent cuff to attenuate the light. Therefore, integrating the sensor behind the cuff will be the preferred method.

## 3.6 Sensor Manufacture

### 3.6.1 Fabrication

To produce a sensor that is easier to manufacture and more consistent, a collaboration with Bluefrog Design (Leicester) was formed. Their expertise in manufacturing and design solutions allowed the production of high-quality metal sensor moulds from design specifications based on the three-fibre circular sensor with a rectangular base (Section 3.4.3). The mould was manufactured with a precision computerized numerical control (CNC) machine and the dimensions were reduced to  $4.5 \times 4 \times 1$  mm. A flowchart giving an overview of the sensor fabrication process is found in Fig. 3.32, with a detailed description of each step in Fig. 3.33 - Fig. 3.35.



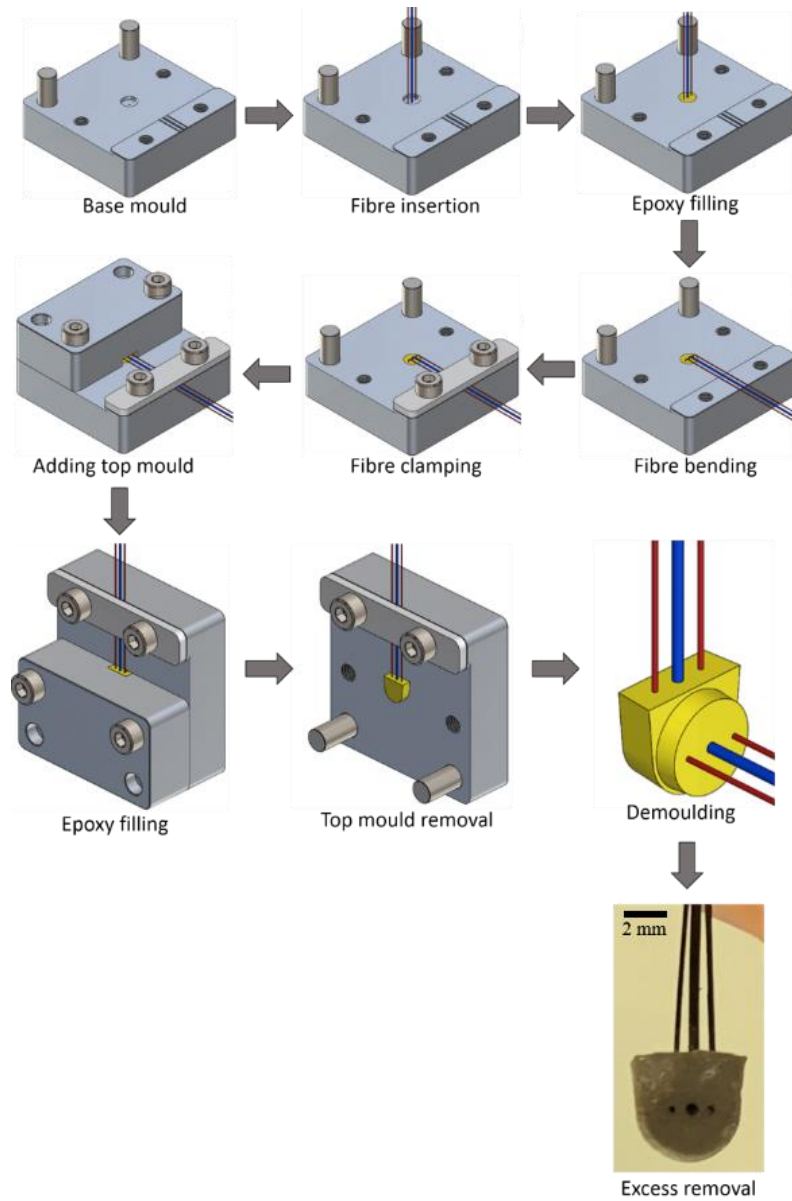


Fig. 3.32: 3D rendering of step-by-step sensor formation made by Bluefrog Design with a photograph of the finished sensor.

The base mould (Fig. 3.33) was first sprayed with two coats of PTFE mould release to aid in demoulding. A  $500\ \mu\text{m}$  diameter fibre was placed through the central channel in the base mould (Fig. 3.33). A  $250\ \mu\text{m}$  diameter fibre was placed either side of the central fibre and separated by  $1.75\ \text{mm}$  from each other ( $0.875\ \text{mm}$  from the detection fibre). A separation of  $0.875\ \text{mm}$  is lower than those explored in Section 3.3. However, preliminary measurements demonstrated the presence of the OHb characteristic spectral feature with a broadband LED, whilst minimising the size of the sensor and decreasing the impact to the normal function of an ETT. The circular mould cavity was  $4\ \text{mm}$  in diameter and  $1\ \text{mm}$  in depth. The base mould also had channels for each of the fibres to lay in after they had been bent (top of the mould on Fig. 3.33). The fibres were coated in a black pigment. The base mould had M4 threaded bolt holes to attach subsequent mould parts to the base and 4 risen guides that matched a negative shape in the top mould for more precise alignment.



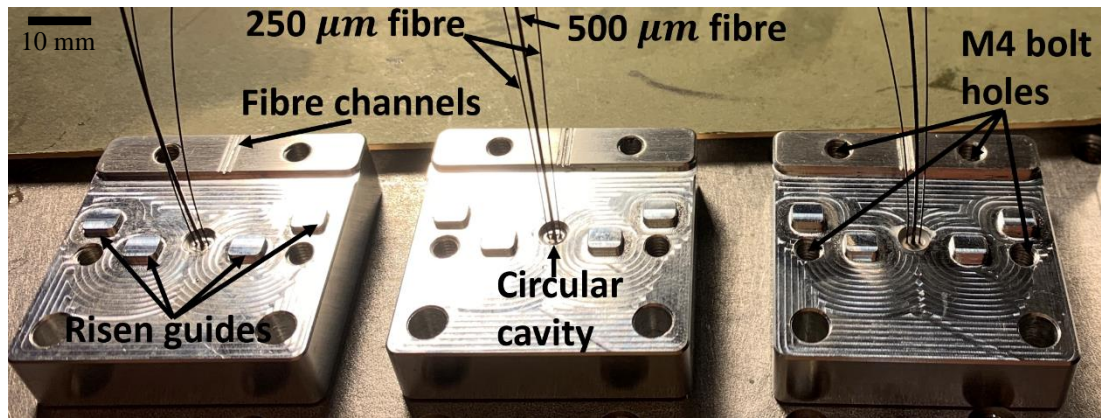
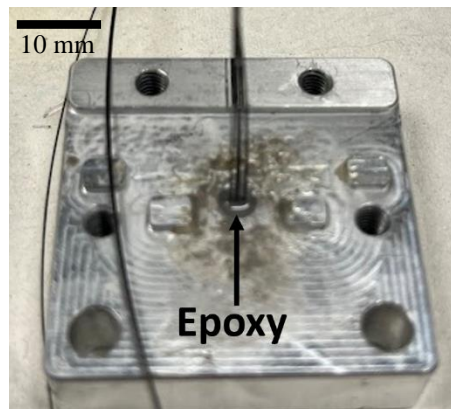
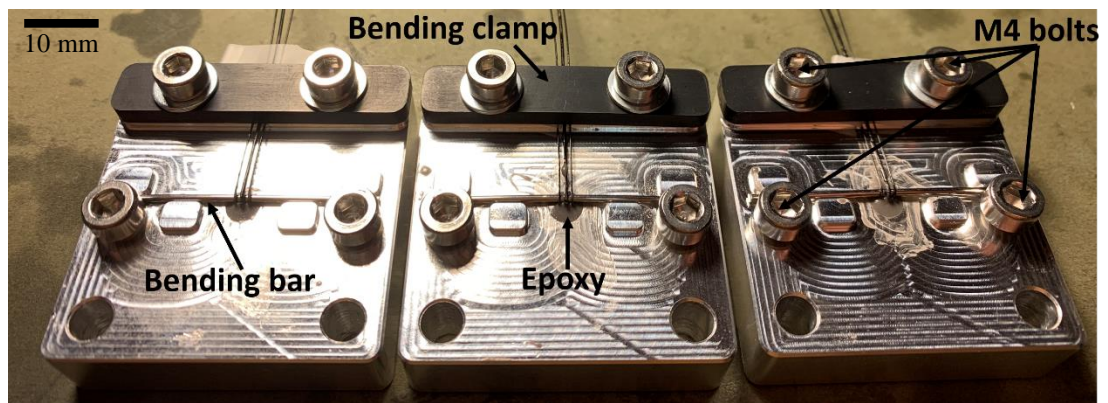


Fig. 3.33: Base mould for positioning the fibres in a circular cavity.

The epoxy was then pipetted into the mould cavity and the circular sensor was left to cure (Fig. 3.34a). By curing the mould in two parts the fibres did not move during the bending process, resulting in more consistent sensors. The bending bar was then placed behind the fibres and secured with M4 bolts (Fig. 3.34b). The fibres were then bent under moderate heating provided by a heat gun, with the bending bar providing a more consistent bend. The fibres were then placed into the fibre channels and held in place with the bending clamp.



(a)



(b)

Fig. 3.34: Base sensor mould with (a) epoxy-filled cavity and (b) fibres bent and then clamped into position.

The top mould (Fig. 3.35a) had a cavity with a circular top and rectangular base and was also filled with epoxy. The top mould was then placed onto the bottom mould

using the guide holes and then secured using M4 bolts. The epoxy was cured with the mould on its side so that the epoxy settled into the mould and didn't flow out. Once the epoxy was cured the top mould was removed from the base and then the sensor was demoulded by gently leveraging it out. The excess fibres were then trimmed, and the sensor filed to give its final shape. The sensor face was then polished using fibre optic polishing paper in decreasing coarseness. The final sensor dimensions were  $4.5 \times 4 \times 1$  mm (Fig. 3.32).

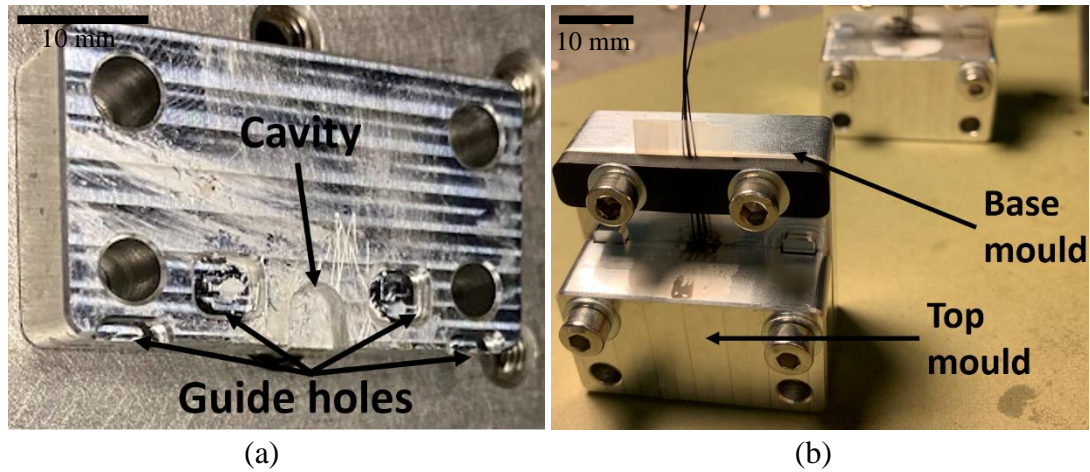


Fig. 3.35: (a) Top sensor mould and (b) combined moulds.

### 3.6.2 Modifications

To determine the final fibre separations, three metal moulds were fabricated by Bluefrog Design (Section 3.5) with a separation between an illumination fibre and the detection fibre of 1.375, 1.125, and 0.875 mm (centre-to-centre of fibre). Each of the sensors was connected to the broadband LED, IR LED and spectrometer (Ocean Optics, model OCEAN-HDX-XR) set to an integration time of 30 ms and then placed on the fingertip of a volunteer (Fig. 3.36).

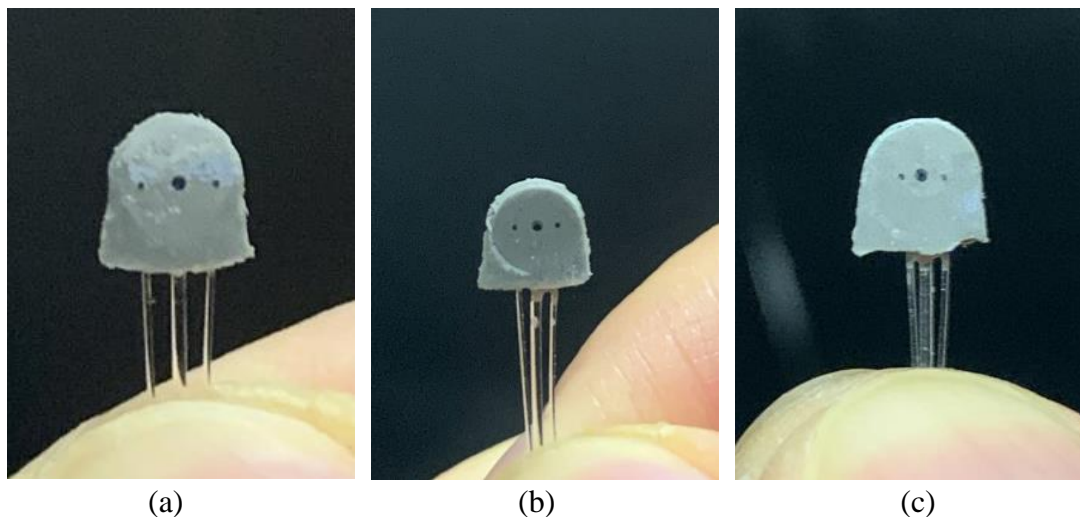


Fig. 3.36: Three sensors manufactured with metal moulds using a fibre separation of (a) 1.375 mm, (b) 1.125 mm, and (c) 0.875 mm.

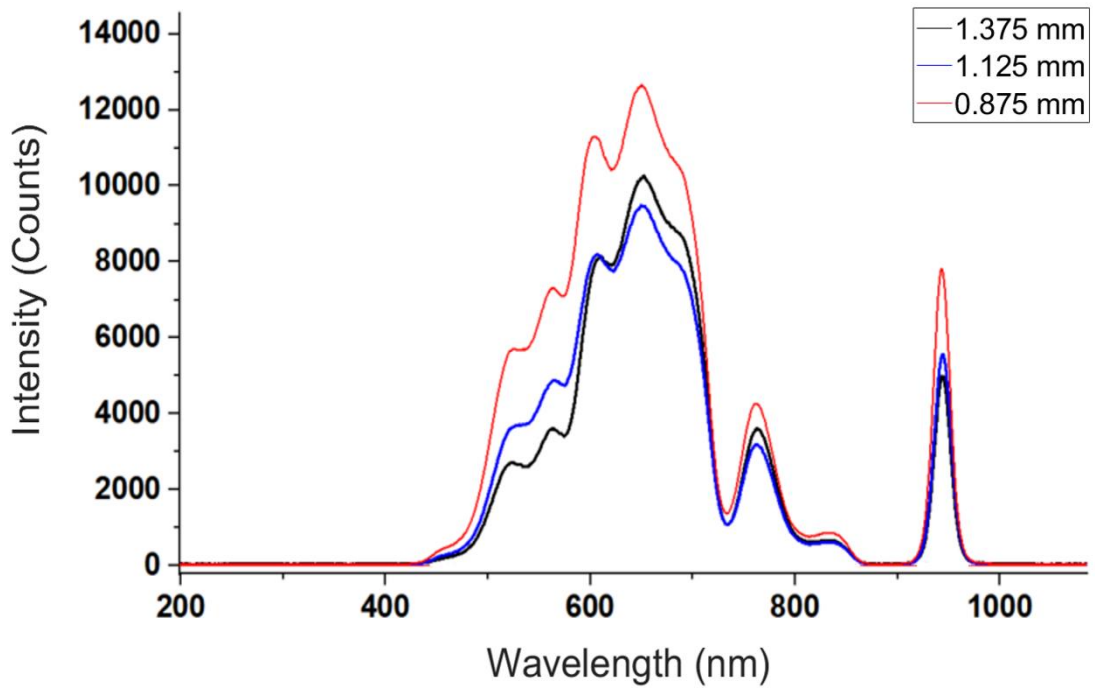


Fig. 3.37: Intensity of light detected by the detection fibre from the two illumination fibres at separations of 1.375 mm (black), 1.125 mm (blue), and 0.875 mm (red).

Only a small change in the optical power for three separations can be seen in Fig. 3.37. Furthermore, the absorption characteristic features in the 530 - 590 nm wavelength range are present for all three separations. Therefore, these preliminary data suggest that a separation of 0.875 mm (centre-to-centre of fibres) is acceptable and will be used for future fabrications as this was the most compact sensor. Preliminary measurements on an oesophageal sample showed a similar presence of the OHb absorption feature on the range of separations measured.

Another area for improvement in the design is the choice of epoxy in which the fibres are embedded. A transparent epoxy allows more light to couple directly between the illumination and detection fibre. This DC light suppresses the absorption features being measured. Some of the light will be absorbed by the black pigment coating whilst some will still make it directly into the detection fibre. Previously, a UV-curable optical epoxy (Panacol, model Vitralit 1655) was used. A transparent epoxy was only beneficial with the 45° cleaved fibres (Section 3.4.1), as the light couples through the epoxy layer due to the side of the fibre not being perfectly in line with the face. Polishing the face of the sensor so that the side of the fibre is in line with it is impractical as removing too much material could damage the cladding of the fibre. Furthermore, the side of the fibre must be exposed to give the maximum optical power output. However, using J-shape fibres (Section 3.4.2) means that the fibre tip is perpendicular to the face of the sensor and the light does not have to travel through the epoxy layer. Therefore, the sensor can be filed and polished with the core of the fibre always being in line with the sensor face, so the epoxy can be non-transparent. Therefore, a non-transparent food grade (FDA compliant) epoxy was chosen (two-part epoxy, Permabond, model ET5143). Although this epoxy is temperature cured (approximately 3 hrs at 55°C) and takes significantly longer than the UV-curable



epoxy (30 minutes with a UV torch), its biocompatibility, opaqueness, and strength, make it the epoxy of choice (Fig. 3.38).

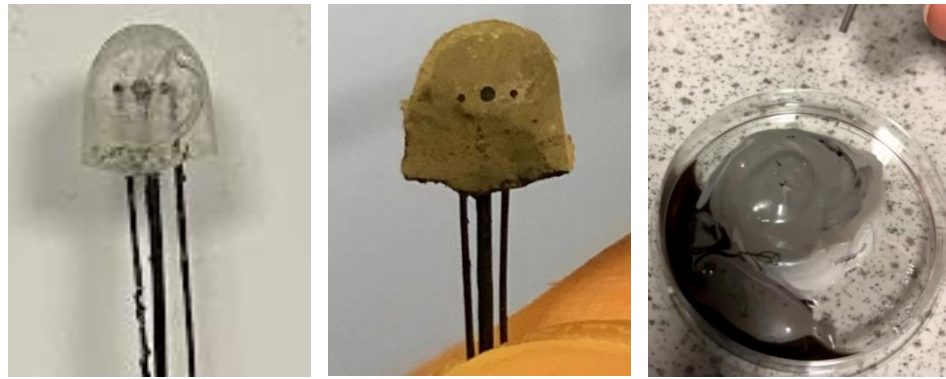


Fig. 3.38: Photographs of a sensor made with (a) a transparent UV curable epoxy (Panacol, model Vitalit 1655), (b) a non-transparent temperature curable epoxy (two-part epoxy, Permabond, model ET5143). (c) shows the non-transparent epoxy being mixed for use.

Fig. 3.39 was provided from research performed in parallel by Chenyang He [142], a collaborator on the iTraXS project and a member of the Optics and Photonics research group at The University of Nottingham. They compared the use of an epoxy layer made from a transparent and non-transparent epoxy used to fabricate the sensor described in Section 3.6.1. The sensor was placed between the cuffs of a double-cuff ETT and then a finger was placed on the sensor.

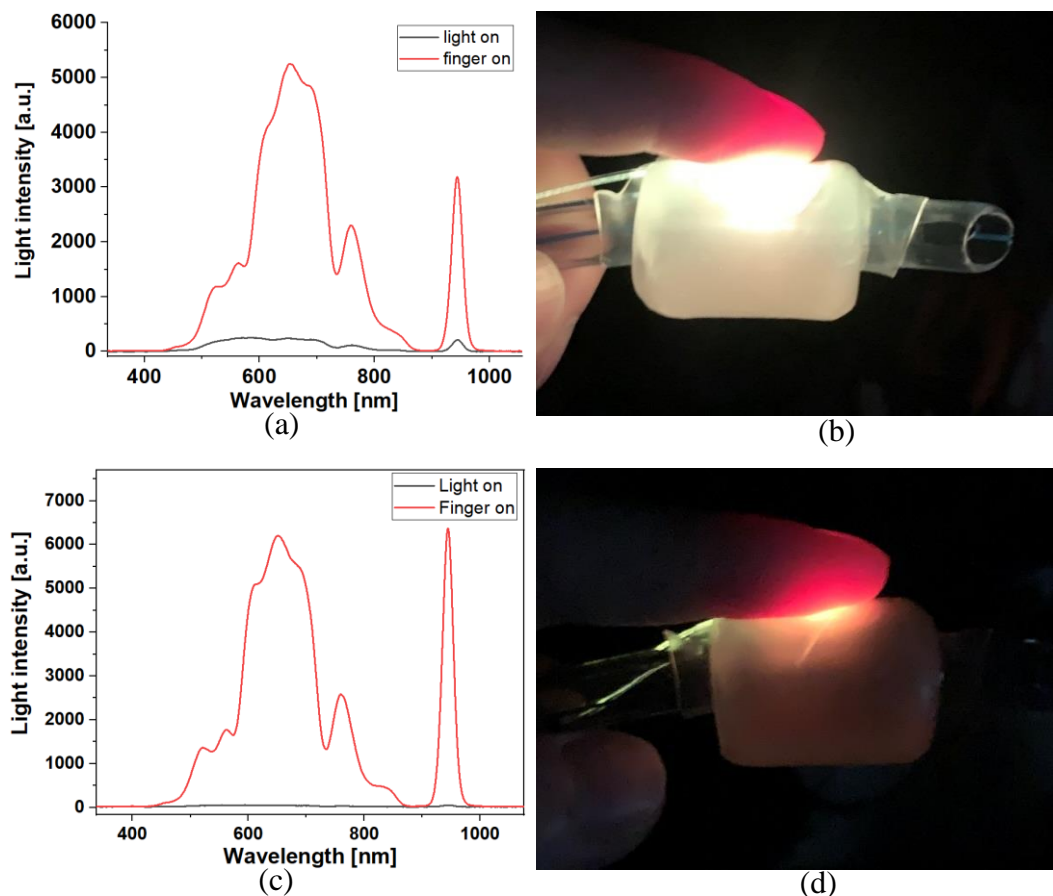


Fig. 3.39: Comparison of a sensor manufactured with (a), (b) transparent epoxy, and (c), (d) non-transparent epoxy.

Close to zero light intensity can be seen in Fig. 3.39c when a non-transparent epoxy is used in the manufacturing process and the finger is off the sensor (black line). There is a higher light intensity (approximately 300 counts at the peak) when a transparent epoxy is used (black line Fig. 3.39a). Furthermore, there is a higher light intensity when the finger is on the sensor when comparing the non-transparent epoxy to the transparent epoxy (approximately 6200 compared to 5250 peak intensity counts). Therefore, it was concluded that the non-transparent epoxy better shields the detection fibre from the illumination fibres and makes the light more directional so that a higher optical power can interact with the tissue instead of being dispersed. This is highlighted further by comparing Fig. 3.39b and Fig. 3.39d, where the non-transparent epoxy causes the ETT cuff to glow as the light is scattered more by the cuff material.

A flexible fibre is crucial for a sensor that is robust enough to handle being integrated into an ETT and used for intubation where bending and strains are unavoidable. Therefore, a plastic optical fibre (POF) is advantageous over a silica optical fibre due to having high elastic strain limits, bending flexibility, and fracture resistance [143]. Furthermore, the POFs can simply be bent in a J-shape to launch light perpendicularly to the sensor face and into the tissue where a silica fibre would break. However, one of the major downsides of POFs is their high signal attenuation and dispersion when compared to silica. For example, a 500  $\mu\text{m}$  diameter POF (commercial grade PolymethylMethacrylate (PMMA), Asahi, model DB-500) has a quoted attenuation of 160 dB/km at 650 nm, whereas a comparable silica optical fibre may have an attenuation of a few dB/km [144,145]. This can be seen by POFs ‘glowing’ as light propagates (Fig. 3.40). This difference is normally not of great concern as the lengths of optical fibres used are no greater than 2 m, giving a maximum nominal attenuation of 0.32 dB. However, if light escapes through the cladding of the optical fibre then the light will also be able to enter through the cladding by following the reverse path. With very small optical powers, especially like those travelling through the detection leg of the opto-electronic units, ambient light from places such as a well-lit hospital room could interfere with measurements. There is also coupling between the fibres throughout their lengths. A relatively large amount of DC ambient light could suppress the features in the reflectance spectra. Varying light levels could also result in DC shifts in the spectra during measurements which confounds them. One solution is to use commercial POFs with a jacket, but appropriate solutions are scarce and expensive. A black pigment coating of the POFs was chosen as a preferable solution as it is much thinner than a commercial jacket, allowing the fibres to be more flexible and to be coated up to their tips, whereas a jacketed fibre has to be stripped near the tip to achieve the J-shape bend. The black pigment used was an aqueous-based ink containing acrylic resins (sprayable black backing, LCR Hallcrest, model SPBB), chosen for its thin consistency, adhesion to the fibres, and non-transparent qualities.

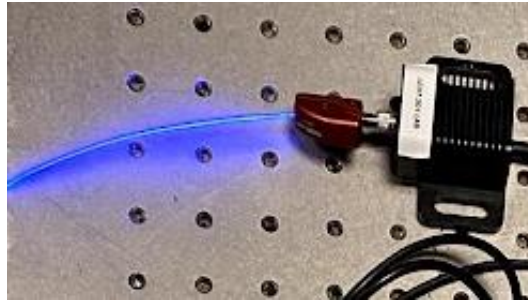
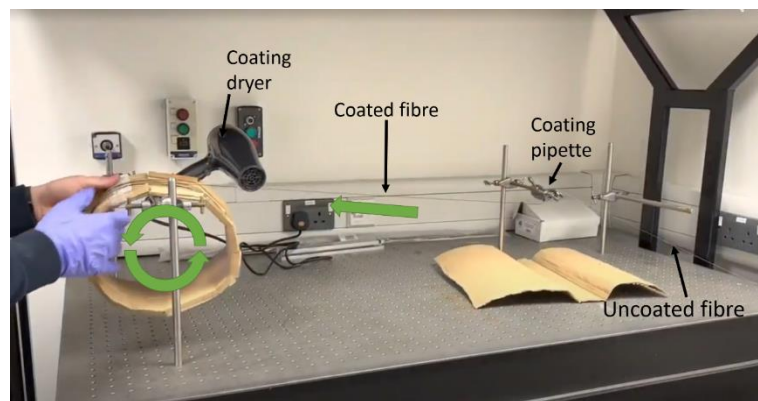
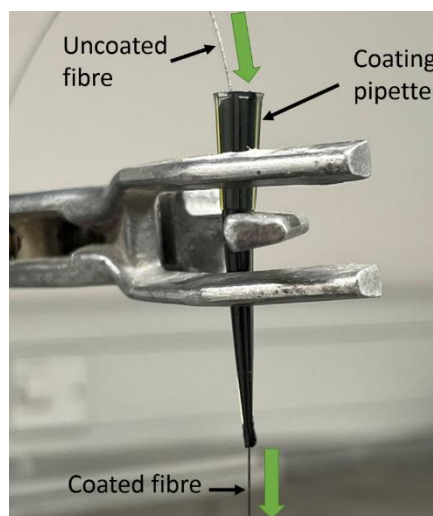


Fig. 3.40: Example of ‘glowing’ optical fibre as light from an LED is coupled to it, demonstrating a high loss of optical power through the cladding of plastic optical fibres.

Initially, the pigment was deposited on the fibre by using a gloved hand to coat it, which proved time-consuming and inconsistent. Therefore a ‘production line’ was built to aid in the coating (Fig. 3.41a). The uncoated fibre is pulled through a coating pipette where a thin layer of pigment is deposited onto it. The drying process is then sped up as it passes by a coating dryer which blows warm air over it, before being wound on a cardboard tube for later use. The coating pipette (Fig. 3.41b) is the tip of an electronic pipette that has been filled with the black pigment and then had its end cut so that it is slightly bigger than the diameter of the fibre so that a thin coating is deposited on the fibre.



(a)



(b)

Fig. 3.41: (a) ‘production line’ for consistently coating large lengths of optical fibre, and (b) close-up of coating pipette used to coat fibres.

The fibres can then be cut to the desired length when needed (Fig. 3.42), with the pigment on the tips removed easily with isopropanol alcohol (IPA) solution if an uncoated end is required to fit inside any opto-electronic units and connectors. The consistency of the coating process along the length of the fibre was verified by shining light through the fibre and observing if any light could escape.



Fig. 3.42: Black pigment-coated optical fibres fabricated using the “production line” process of Fig. 3.41.

Fig. 3.43 was again provided by Chenyang He and performed in parallel to this research. The experiment compared a sensor manufactured by the process described in Section 3.6.1, with uncoated fibres and fibres coated in the black pigment. Measurements were made when a volunteer’s finger was on and off the sensor.



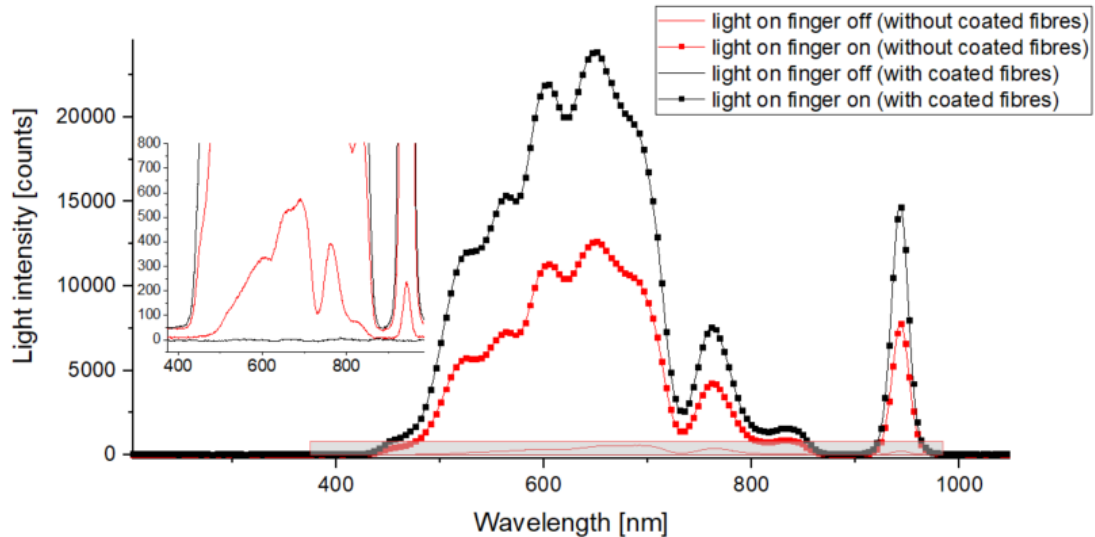


Fig. 3.43: Spectra comparing coated (red lines) and uncoated (black lines) sensors when a finger is on (squares) and off (no squares inside inset plot) the sensor.

The coated fibres when the finger is off the sensor (black line on Fig. 3.43) show close to zero light intensity, whereas the uncoated fibres (red line) show a light intensity with a peak at approximately 550 counts. Interestingly, the light intensity when the finger is on the sensor for the coated fibres (black line with squares) is higher than the uncoated fibres (red line with squares). This may be caused by the black pigment reflecting some of the light back into the fibre through the cladding when it would otherwise be dispersed. This is beneficial as a higher optical power is emitted from the tip and interacts with the tissue. Although the pigment is black and absorbs visible light it may still be possible as it reflects a small amount of optical power. A white coating would reflect the light better than a black coating and may contribute to increased transmitted optical power. However, a suitable non-transparent pigment could not be found, so ambient light could still affect measurements. However, there could also be other factors affecting the DC light levels such as the quality of the fibre tip surface and connections. Chenyang He found significant improvements in the quality of the perfusion measurements with coated fibres compared to uncoated fibres in his research. Therefore, it was concluded that coating the fibres produces less direct light coupling between the fibres and shields them from ambient light conditions and is used as part of the fabrication process moving forward.

### 3.7 Discussion

An ETT placement sensor (Fig. 3.44) has been designed with the criteria described in Section 3.4 and from the knowledge gained from the first animal study (Section 5.3.3). A summary table of the final sensor design at this stage can be seen in Table 3.3, with a photograph of the chosen optimised sensor design in Fig. 3.44.

Table 3.3: Summary of the ETT placement sensor specifications with the chosen design shown in green and the tested and unchosen design in red.

	Design specification	Advantages	Disadvantages
Position on ETT	Between cuffs	<ul style="list-style-type: none"> <li>Protected</li> <li>Intimate contact with tissue</li> </ul>	<ul style="list-style-type: none"> <li>Varying pressure</li> <li>Difficult to manufacture</li> </ul>
	Inside Lumen	<ul style="list-style-type: none"> <li>Protected</li> </ul>	<ul style="list-style-type: none"> <li>Non-intimate contact with tissue</li> </ul>
	Outside Lumen	<ul style="list-style-type: none"> <li>Proximal to tissue</li> </ul>	<ul style="list-style-type: none"> <li>Unprotected</li> </ul>
Number of sensors	3	<ul style="list-style-type: none"> <li>More measurement positions</li> </ul>	<ul style="list-style-type: none"> <li>Higher cost</li> </ul>
	2	<ul style="list-style-type: none"> <li>Lower cost</li> </ul>	<ul style="list-style-type: none"> <li>Limited measurement positions</li> </ul>
	1		
Sensor shape	Circular with a rectangular base ( $4.5 \times 4 \times 1$ mm)	<ul style="list-style-type: none"> <li>Compact</li> <li>Softer edges</li> <li>Large contact area with fibre</li> </ul>	<ul style="list-style-type: none"> <li>Small fibre separation</li> </ul>
	Larger/square/rectangular	<ul style="list-style-type: none"> <li>Larger fibre separation</li> </ul>	<ul style="list-style-type: none"> <li>Pronounced edges</li> </ul>
Fibre type	PMMA	<ul style="list-style-type: none"> <li>Cheap</li> <li>Flexible</li> </ul>	<ul style="list-style-type: none"> <li>High attenuations</li> </ul>
Fibre diameter	$1 \times 500 \mu\text{m}$ $2 \times 250 \mu\text{m}$	<ul style="list-style-type: none"> <li>Smaller fibre bundle</li> <li>Pulse oximetry capable</li> </ul>	<ul style="list-style-type: none"> <li>Lower optical power output</li> </ul>
	$3 \times 500 \mu\text{m}$	<ul style="list-style-type: none"> <li>More optical power</li> </ul>	<ul style="list-style-type: none"> <li>Larger fibre bundle</li> </ul>
Fibre tip	J-shape	<ul style="list-style-type: none"> <li>Higher optical power</li> <li>More repeatable</li> </ul>	<ul style="list-style-type: none"> <li>Thicker sensor</li> <li>Difficult to manufacture</li> </ul>
	45° cleaved	<ul style="list-style-type: none"> <li>Thinner sensor</li> </ul>	<ul style="list-style-type: none"> <li>Less optical power</li> </ul>
Fibre separation	0.875 mm	<ul style="list-style-type: none"> <li>Compact sensor</li> </ul>	<ul style="list-style-type: none"> <li>Below optimal spacing</li> </ul>
	1.125 mm	<ul style="list-style-type: none"> <li>Closer to optimal spacing</li> </ul>	<ul style="list-style-type: none"> <li>Less compact sensor</li> </ul>
	1.375 mm		
Number of fibres	3	<ul style="list-style-type: none"> <li>2 LEDs can perform pulse oximetry</li> </ul>	<ul style="list-style-type: none"> <li>More fibres</li> </ul>
	2	<ul style="list-style-type: none"> <li>Less fibre</li> </ul>	<ul style="list-style-type: none"> <li>Difficult to perform pulse oximetry</li> </ul>
Epoxy type	Non-transparent	<ul style="list-style-type: none"> <li>Less DC shunting</li> </ul>	<ul style="list-style-type: none"> <li>Requires J-shape fibres</li> </ul>
	Transparent	<ul style="list-style-type: none"> <li>Can use 45° fibres</li> </ul>	<ul style="list-style-type: none"> <li>DC shunting</li> </ul>
Coated fibres	Coated	<ul style="list-style-type: none"> <li>Less DC shunting</li> </ul>	<ul style="list-style-type: none"> <li>Extra manufacturing cost</li> </ul>
	Uncoated	<ul style="list-style-type: none"> <li>Lower manufacturing cost</li> </ul>	<ul style="list-style-type: none"> <li>DC shunting</li> </ul>

The optimal placement for the sensor is in the cuff of the ETT. Attaching the sensor to the outside of the lumen of ETT is a viable alternative as it produces spectra with the OHb absorption characteristic present. However, more intimate contact is achieved by placing the sensors in the cuff, outperforming the other positions. The protection provided to the patient and the sensor makes this option preferable. Furthermore, the contact pressure sensing capabilities of iTraXS rely upon the sensor being in the cuff. However, a varying cuff pressure could introduce a varying spectrum.

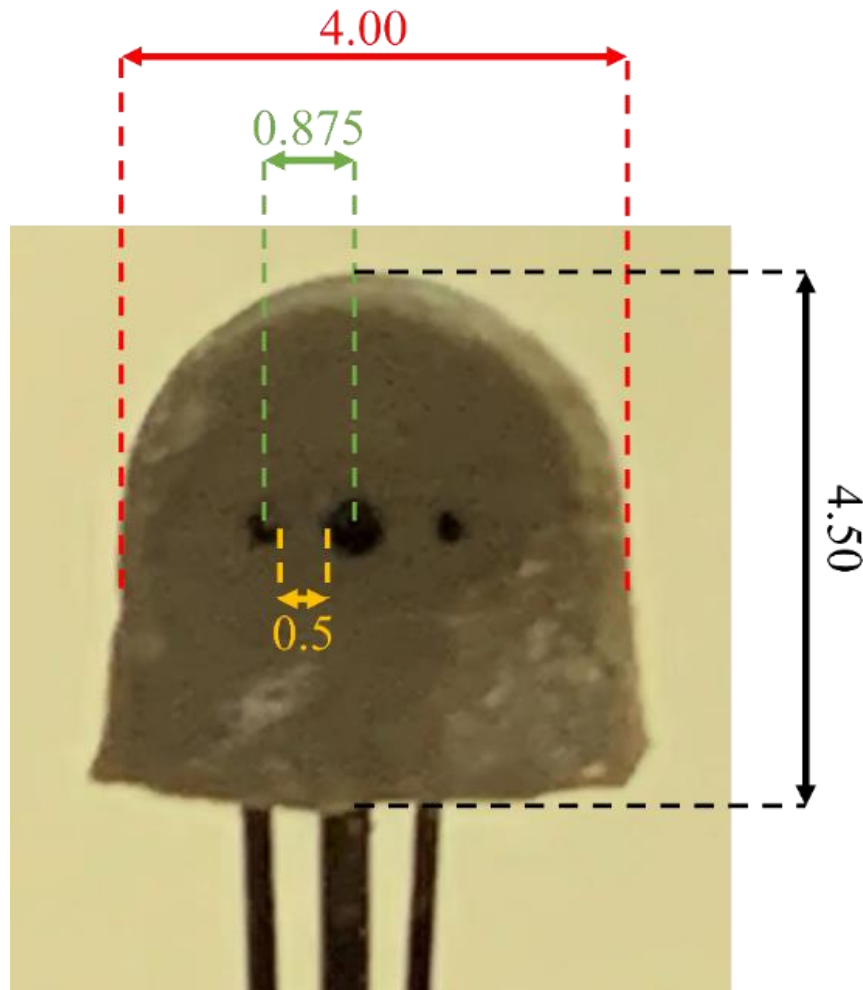


Fig. 3.44: Final sensor design with dimensions in mm.

The best performance was with the mid-range detection-illumination fibre separation (2.54 mm, Section 3.3), although the OHb absorption characteristic was still present at the minimum separation measured of 1.27 mm. However, to produce a more compact sensor this was reduced further to 0.875 mm. A larger separation would be preferable, although this compromise was made because of concerns over the size of the sensor in the cuff. This separation still produced tracheal spectra where the spectral characteristic features were present. Furthermore, a simulation demonstrated a range of acceptable separations of 0.5 to 3 mm. This allows for an extremely compact sensor ( $4.5 \times 4 \times 1$  mm).

The chosen method for directing light in and out of the front of the sensor is bending the fibres into a J-shape. A viable alternative method is to cleave them at 45°. Observationally, the sensor made from bent fibres had more light coming out from the front and was a clear choice. Bending the fibres is also easier to perform repeatably, with the cleave angle being more difficult to control during manufacturing. Achieving a good cleave surface also proved more difficult with POFs, as inspection under a microscope often revealed an uneven surface. Angle polishing is an alternative method for achieving a cleaved surface, although PMMA fibres can melt and deform from the heat generated by polishing. Theoretically, there is zero light loss in the 530 – 590 nm wavelength region when a bend angle above 3 mm is used, with bend angles above approximately 1 mm being comparable to the theoretical limit of the cleaved fibres (Sections 3.2 and 3.4.2). However, experimentally, it was found that bending the fibres also produced a light loss. This is likely caused by stress-induced damage to the bend site, not accounted for by the model used (Eq. (3.4)). Furthermore, during initial fabrications by hand, and the fibres being somewhat elastic (PMMA has a Young's modulus of 2.9 GPa), they may have been 'over bent' so they relaxed to the correct bend radius to fit inside epoxy. This overbending could have potentially damaged the fibres, with later sensor mould versions accounting for this by implementing a bending rod during sensor manufacture, which allowed consistent bending to the required bend radius.

Due to the fibres being made from PMMA, they have an attenuation of 160 dB/km, as discussed in Section 3.6. Therefore, a significant amount of light can escape and enter the fibres. Research performed in parallel revealed that a transparent epoxy allows more light to directly couple between the tips of the fibres. By choosing a non-transparent epoxy this effect was reduced. Furthermore, by coating the fibres in a black pigment, ambient light from the room and direct coupling between the fibres throughout their length was reduced. The use of silica optical fibres reduces both concerns, although they could not be bent into a J-shape and pose an increased likelihood of puncturing the cuff if they were to break.

To conclude, this chapter has presented a detailed design and manufacturing process of the epoxy sensor having been placed inside the cuff and is ready for further trials in subsequent chapters.

## Chapter 4 *Ex-vivo* measurements & Computational Methods

### 4.1 Introduction

The sensor's design was chosen and refined in Chapter 3, producing an ETT with an integrated fibre optic sensor. However, once the raw diffuse reflectance data are acquired from the tissue they must be identified and classified into being tracheal or oesophageal, which is the subject of this chapter.

A flow chart (Fig. 4.1) describes the relationship between the methods explored in this chapter. Firstly, two experiments are described which provide spectral data from 9 *ex-vivo* porcine trachea and oesophagus samples and then 10 sensors. A different sensor design was implemented between these two experiments. A set of computational methods is then developed to numerically study the spectra. A wide array of tools are available, with spectral ratios (Section 4.3.1) and principal component analysis (Section 4.3.2) being used to identify the difference between the spectra. Three statistical measures (mean, skewness, and kurtosis) are then used to summarise the characteristics of the tissue data sets (Section 4.4). The tissues are then classified using four different algorithms (Sections 4.5.1 - 4.5.4). Finally, the results are compared and discussed to summarise the strengths of each method (Section 4.6).

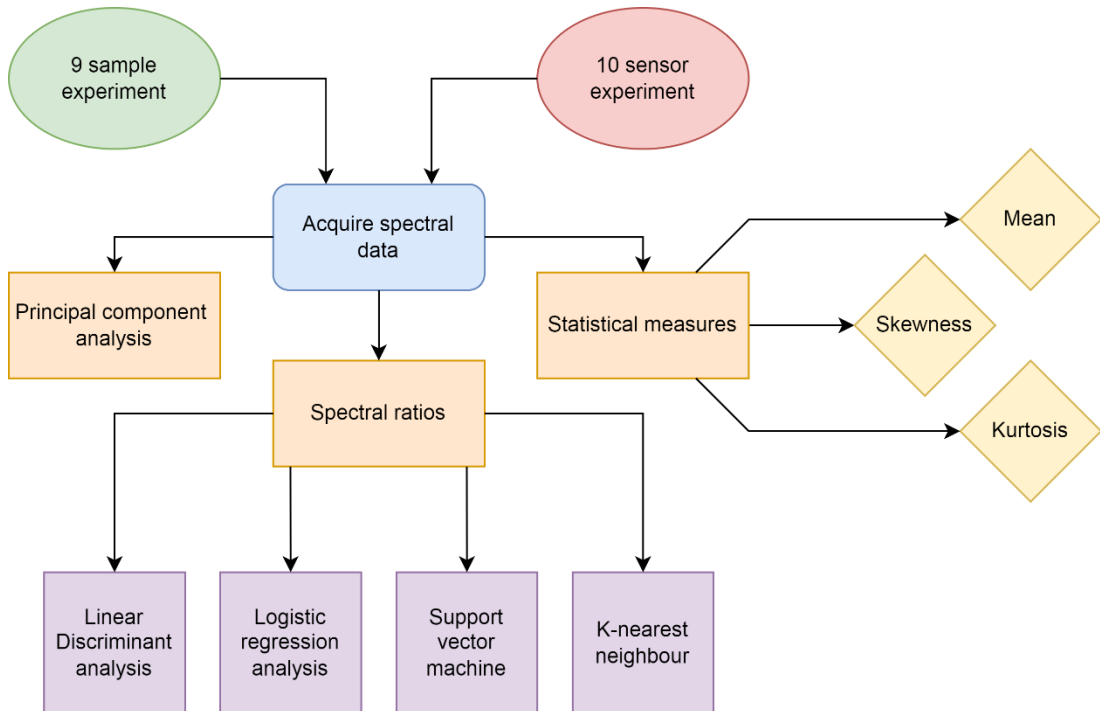


Fig. 4.1: Flow chart of the computational methods used in this chapter to analyse data from experimentation.

### 4.2 Experimental Methodology

The computational methods explored and compared in this chapter use data from two experiments. The first experiment was designed to generate a large data set to apply the computational methods and to verify the reliability of the sensor across multiple

samples. Measurements were made on 9 porcine trachea and oesophagi, acquired from an abattoir (Tamworth breed, 6-10 months age, weights from 60 to 80 kg). The sensor used in the first experiment was the two-fibre rectangle (Section 3.4.1) with J-shape fibres (Section 3.4.2), fabricated using a 3D printed mould. The resulting sensor was  $6 \times 4 \times 1$  mm (Fig. 4.2) made from an epoxy layer (Panacol, model Vitralit 1655), and two J-shape  $500 \mu\text{m}$  POFs (commercial grade PolymethylMethacrylate (PMMA), Asahi, model DB-500) with a detection-illumination fibre separation of 1.5 mm.

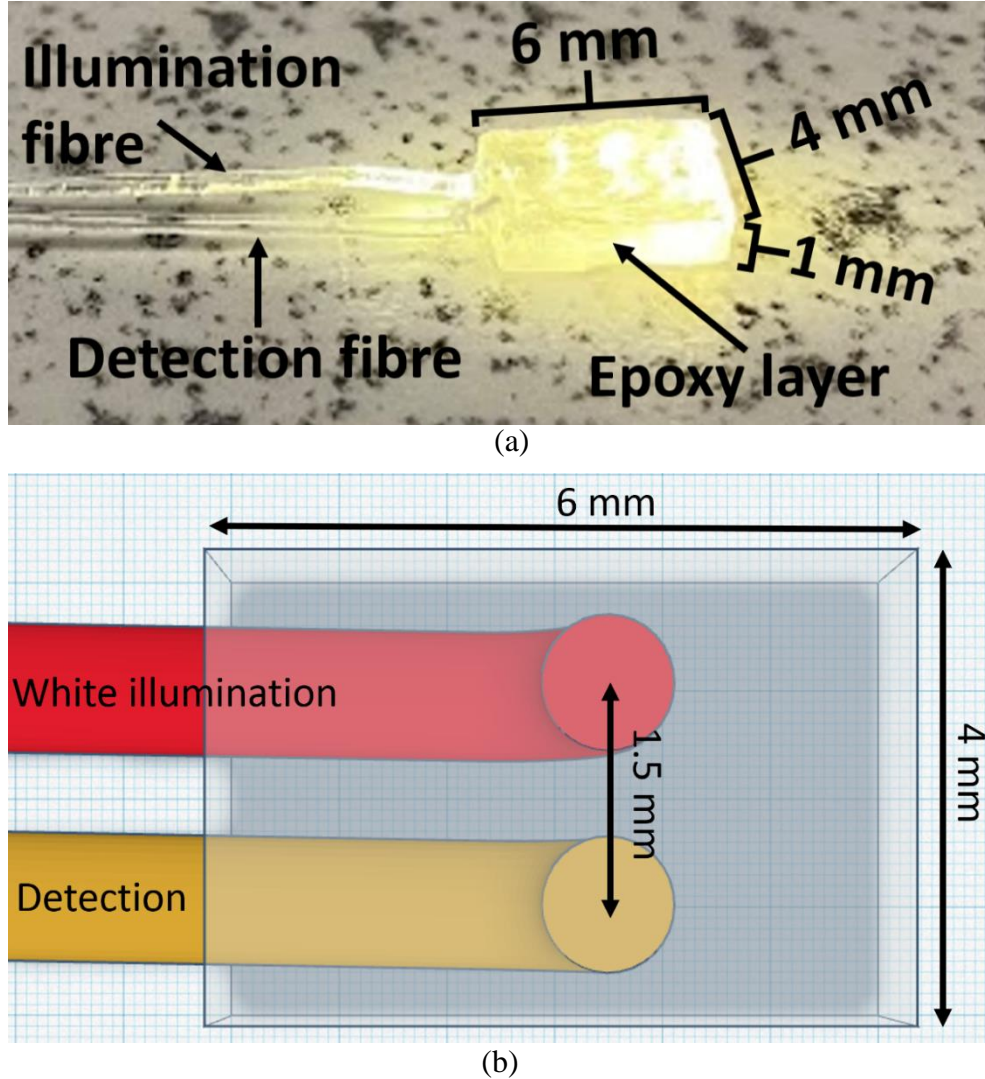


Fig. 4.2: (a) Photograph of the two-fibre rectangular sensor with J-shape fibres. (b) 3D rendering of the sensor.

The sensor was integrated into the cuff of a size 8 Mallinckrodt ETT (Covidien, model 107-80) with a high volume, low pressure (HVLP) cuff made from polyvinylchloride (PVC). A “double-cuff” arrangement was used to facilitate this [147], where the sensor was attached to the outside of a standard ETT cuff, referred to as the inner cuff, using a drop of epoxy. A second cuff, referred to as the outer cuff, from the same model of ETT was then stretched over the inner cuff, resulting in the sensor lying between the inner and outer cuffs (Fig. 4.3). The outer cuff was then sealed at the top and bottom using tape. The inner cuff expansion brings the sensor into intimate contact with the tissues, and the outer cuff protects the sensor and the tissue from each other. The fibres



running out of the sensor exited between the inner and outer cuffs and were taped to the length of the tube.

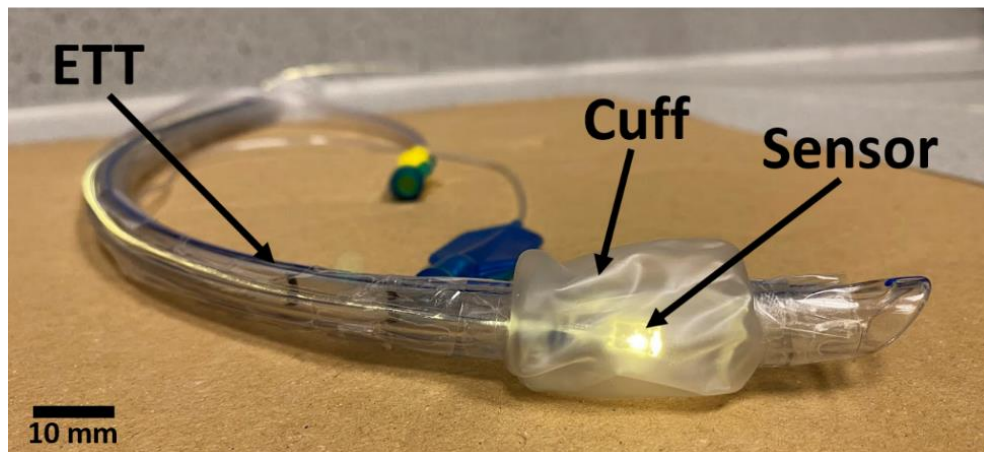


Fig. 4.3: Photograph of the tube placement Sensor integrated between a double-cuff ETT

The detection fibre is situated behind the emission fibre in Fig. 4.3b. Due to the sensor's small size which was refined in Chapter 3, a visual inspection by an expert anaesthetist [148] confirmed there was minimal impact on the shape and performance of the cuff once inflated. The ETT was then covered with a medical sensor sleeve (Pegasus Surgi Safe Tubing Sleeve small (18"×" 1.75"), Dental Sky, model 50-137) to protect the tube from fluids so it did not have to be thoroughly cleaned or replaced between measurements and the sleeve could simply be swapped for a new one.

The opto-electronic components are shown in Fig. 4.4. Consisting of an illumination leg with a broadband white LED (Fiber-Coupled LED, Thorlabs, model MBB1F1), LED driver (T-Cube LED Driver, Thorlabs, model LEDD1B), and a detection leg with a UV-visible spectrometer (Ocean Optics, model USB2000+UV-VIS-ES).

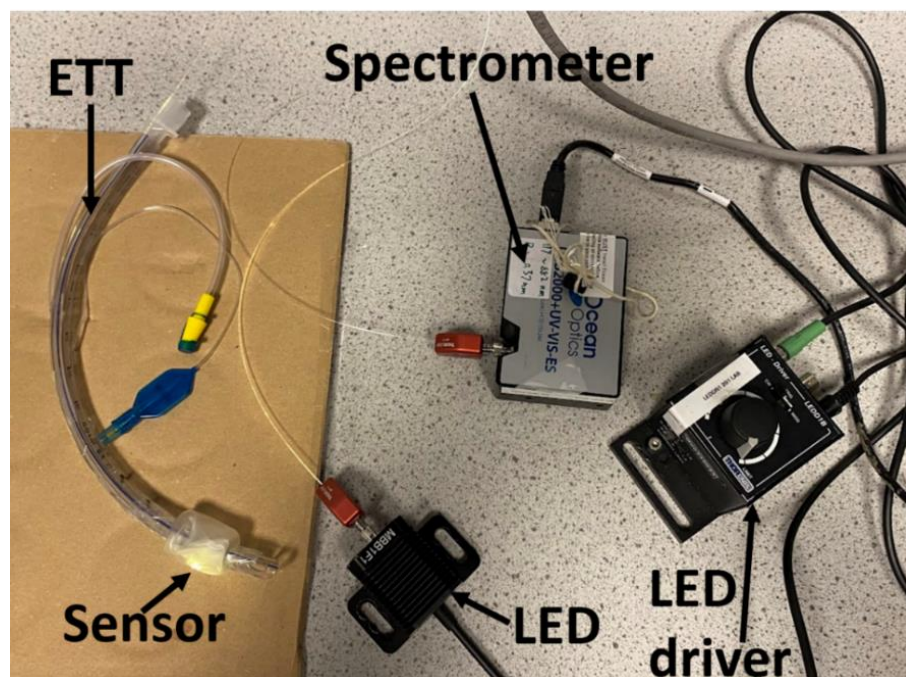


Fig. 4.4: Experimental set-up used for ETT placement measurements with a sensor-integrated ETT.

9 *ex-vivo* porcine trachea and oesophagi were measured generating 900 spectra across 18 total samples (9 samples of each organ with 450 spectra each). The ETT with the sensor between the cuffs was placed into the trachea where measurements began once the sensor passed the vocal cords. The ETT was then rotated and pushed further into the trachea whilst storing measurements until a total of 50 spectra had been obtained for each tissue. The ETT was then removed, the sleeve replaced and then 50 measurements were made in the oesophagus where the same downward spiralling motion was used. This was then repeated for a total of 9 *ex-vivo* porcine trachea and 9 oesophagi.

The second experiment follows a similar protocol as the first, although a different sensor design is used. The aim is to acquire a large data set to which to apply the computational methods. However, the focus was on whether a batch of sensors with repeatable performance could be manufactured. Therefore, 10 sensors with nominally the same configuration were manufactured and verified on a single porcine trachea and oesophagus. The sensors (Fig. 4.5a) were fabricated using the three-fibre design made using the metal mould (Section 3.5). Consisting of a 500  $\mu\text{m}$  diameter central detection fibre (commercial grade PolymethylMethacrylate (PMMA), Asahi, model DB-500) and a 250  $\mu\text{m}$  diameter illumination fibre either side (commercial grade PolymethylMethacrylate (PMMA), Asahi, model DB-500), with a fibre separation of 0.875 mm between the illumination and detection fibre. The fibres were coated in a black pigment (sprayable black backing, LCR Hallcrest, model SPBB) to reduce the effects of ambient light, as described in Section 3.6.2. However, the epoxy used was still transparent (Panacol, Vitralit, 1655, US). The same opto-electronic configuration was also used, as described previously in this section, with the same downward spiral motion used when acquiring 50 spectra in the trachea and 50 spectra in the oesophagus (Fig. 4.5b) for all 10 sensors, generating 1000 spectra across 10-sensors (100 spectra per trachea and oesophagus sample).

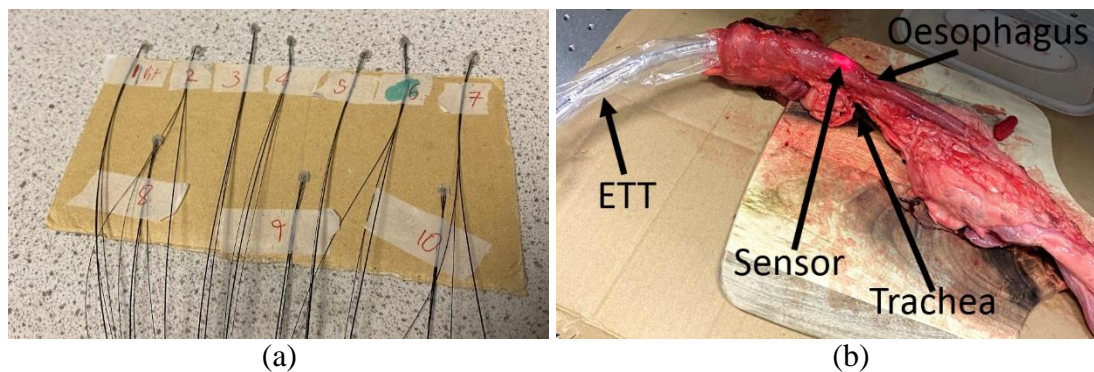


Fig. 4.5: (a) 10 ETT placement sensors fabricated using the metal mould. (b) ETT placement sensor integrated ETT inside the oesophagus of an *ex-vivo* porcine oesophagus.

## 4.3 Spectral Identification

### 4.3.1 Spectral Ratios

The measurement of absolute reflectance is challenging. Small variations in ambient light, sensor design, light source, distance to the tissue, and connections, can all contribute to a variable absolute reflectance. This can be partially accounted for by

removing the dark noise and comparing the diffuse reflectance to a known white reflector by performing dark and light referencing, as is explored in Section 2.3. However, particularly with physiological measurements, the condition of the sensor is difficult to control. Movement of the sensor relative to the tissue can generate a varying spectrum due to changes in the source-detector separation and angle. Furthermore, temperature and humidity can elicit a physiological response that can change the absolute reflectance values. Therefore, taking a ratio between two reflectance values gives more robust results as proportional DC shifts are accounted for. Taking a ratio between diffuse reflectance values is common practice, particularly during physiological measurements and other difficult-to-control environments [149,150]. Since it is the absorption features of OHb being used to characterise the tissues, two absorption troughs and a central peak are used to provide the ratios  $R_1 = R_{543}/R_{561}$  (Eq. (3.8)), and  $R_2 = R_{578}/R_{561}$  (Eq. (3.9)). These ratios are preferred over the reciprocals as it allows for a single wavelength normalization at the central peak ( $R_{561}$ ) to generate spectra where the ratios  $R_1$  and  $R_2$  can be read directly from the spectra. An example spectrum taken from a tracheal measurement is used to demonstrate the pre-processing that was performed before the computational methods were applied.

The dark reference was recorded by turning off any ambient light sources, turning off the light source, and covering the sensor with a non-transparent black felt. This is either stored as a separate measurement or performed by the OceanView software's 'dark reference feature', both methods result in the same dark referenced signal. The raw spectrum was then measured and recorded. The dark reference was then subtracted from the raw spectrum, producing the dark referenced spectrum, where the dark noise DC offset has been removed.

The sensor was then placed on a white reference standard (Spectralon diffuse reflectance targets, Labsphere, model SRT-99-180) and a white reference was stored. Again, this could also be performed by the OceanView software, generating the same referenced spectra. If the referencing is performed manually (not by OceanView), then the white reference must also have the dark reference subtracted.

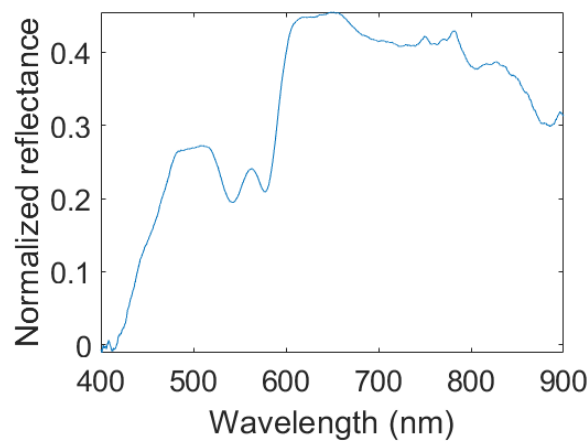


Fig. 4.6: (a) Normalized reflectance spectrum with the dark and white references in the 400-900 nm wavelength region.

The dark referenced tissue spectrum as then divided by the white reference, giving a normalized reflectance (Fig. 4.6). As there is low optical power emitted at short and long wavelengths by this light source (approximately  $< 400$  nm and  $> 900$  nm). The signal is dominated by noise in this wavelength range. However, outside this wavelength range, the normalized reflectance with the dark and white references accounted for, can be seen in Fig. 4.6. Therefore, the normalized reflectance spectrum ( $S_{Norm}$ ) was found from Eq. (4.1).

$$S_{Norm} = \frac{S_{raw} - S_{Dark}}{S_{white} - S_{Dark}} \quad (4.1)$$

where,  $S_{raw}$  is the raw spectrum,  $S_{white}$  is the white reference spectrum, and  $S_{dark}$  is the dark reference spectrum.

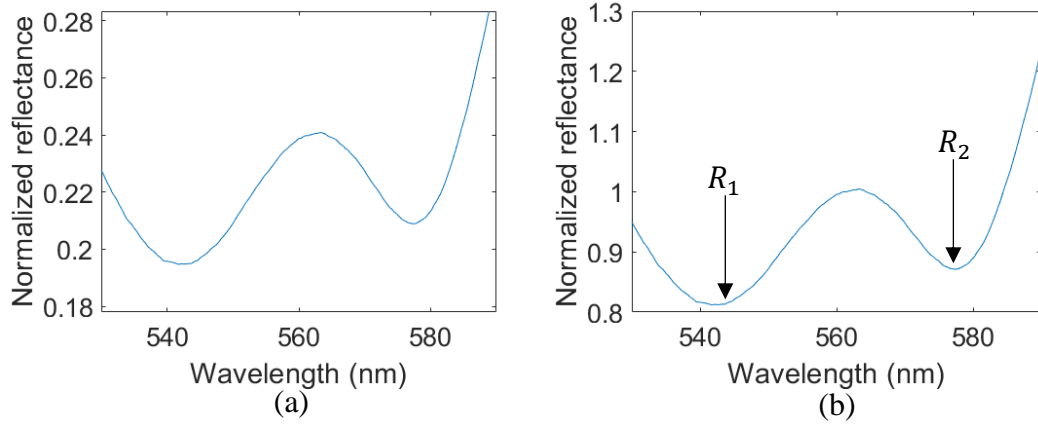
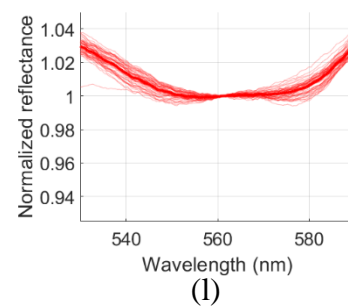
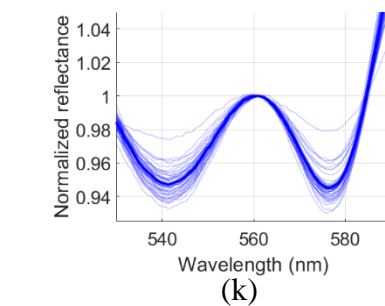
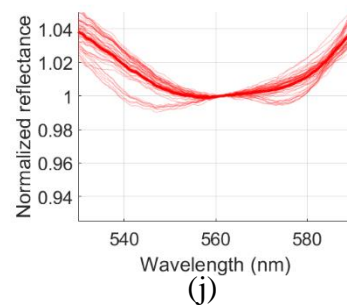
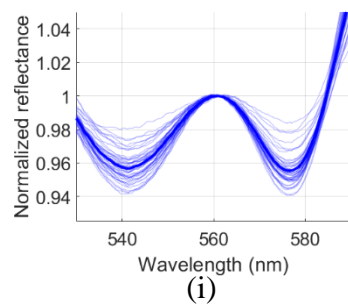
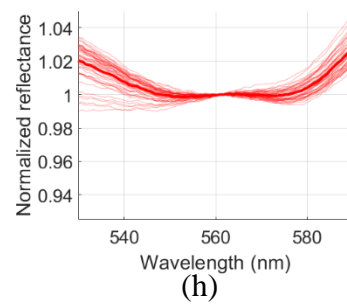
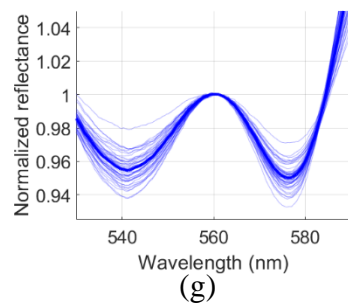
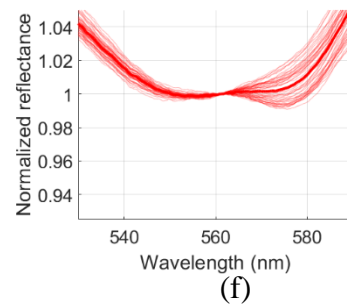
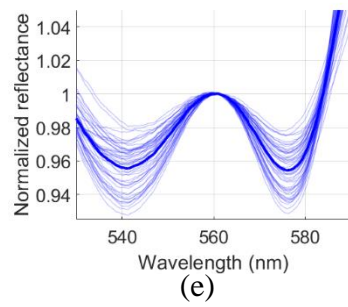
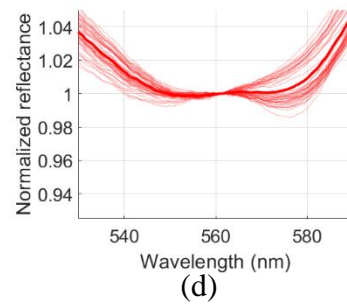
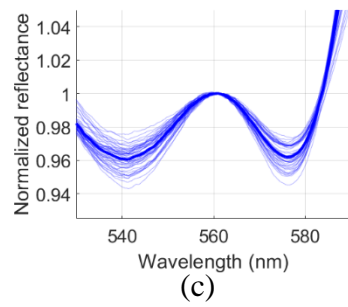
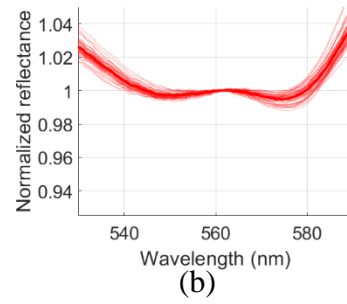
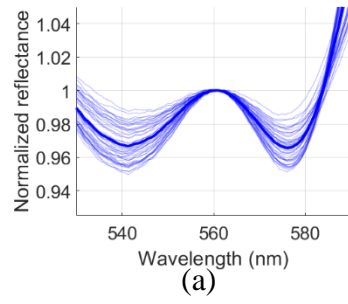


Fig. 4.7: (a) Normalized reflectance spectrum in the 530 – 590 nm region. (b) Normalized reflectance spectrum with another single wavelength normalization performed at 561 nm.

The result is that the characteristic region has been normalized appropriately with the dark and white references, and ratios are ready to be taken (Fig. 4.7a). However, since we will often be taking ratios between the central peak and the troughs on either side, it is simpler to perform a single wavelength normalization at the central peak (561 nm). Therefore the ratios  $R_1$  and  $R_2$  (Eq. (3.8) and Eq. (3.9), respectively) can be found graphically by reading the normalized reflectance values at 543 and 578 nm (Fig. 4.7b), with minima having been found computationally. Furthermore, these ratios make sense as they directly relate to the depth of these troughs, the smaller the number the deeper the trough. A number larger than 1 demonstrates an increase in the normalized reflectance when compared to the central peak. For the spectrum in Fig. 4.7b, the ratios are approximately  $R_1 = 0.81$  and  $R_2 = 0.87$ .





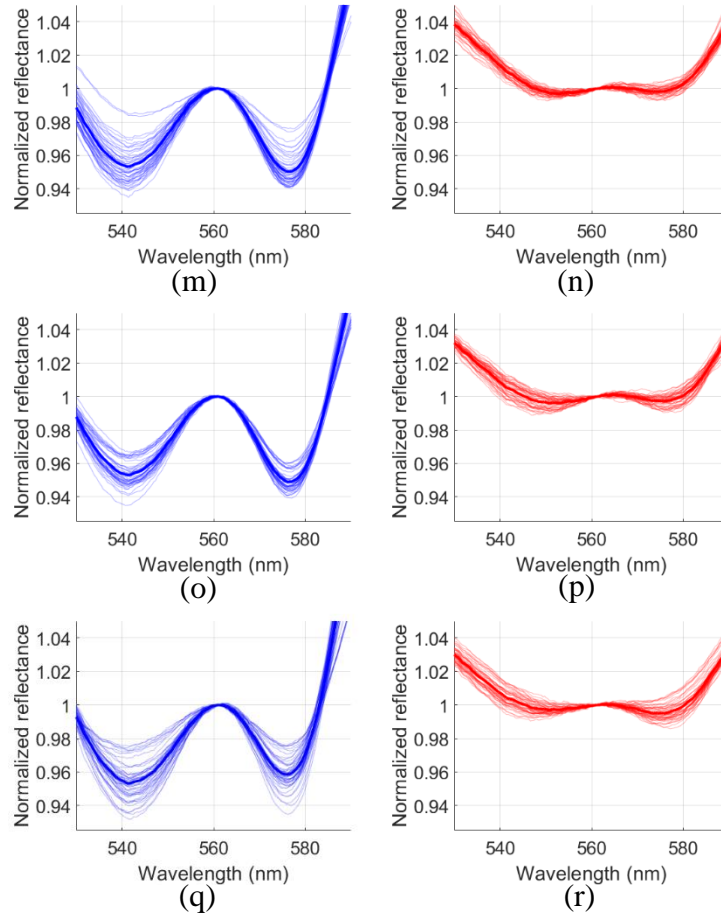


Fig. 4.8: Normalised spectra from 9 different porcine tracheal and oesophageal *ex-vivo* samples. (a) and (b) are from sample 1, (c) and (d) are from sample 2 etc., up to (q) and (r) being from sample 9.

The blue spectra, which are the left-side figures (a), (c), (e), ... , (q) are tracheal. The red spectra, which are the right-side figures (b), (d), (f), ... , (r) are oesophageal. The individual spectra are shown with faint colours, with the thicker line showing the average for all 50 measurements.

The OHb characteristic was more pronounced in the tracheal spectra when compared to the oesophageal across all samples (Fig. 4.8). The scale on the y-axis was kept the same to highlight this difference and a quantitative comparison can be made by comparing the ratios directly. The data is grouped according to tissue type and ratio ( $R_1$  and  $R_2$ ), forming four data sets across all 9-samples, which are the trachea  $R_1$ , oesophagus  $R_1$ , trachea  $R_2$ , and oesophagus  $R_2$ ). A one-sample Kolmogorov-Smirnov test [151] was used with the null hypothesis that the data comes from a standard normal distribution. The null hypothesis was rejected at a 5% significance for all four data sets and we can conclude that the data is not from a standard normal distribution and a median and IQR are preferred. However, the skewness values for the trachea and oesophagus  $R_1$  and  $R_2$  are 0.32, 0.05, 0.40, and 0.80, respectively. Therefore, all the distributions are moderately positively skewed or close to symmetrical (all skewness's between 0 and 1) [152] and a mean and standard deviation is also an appropriate statistical measure.



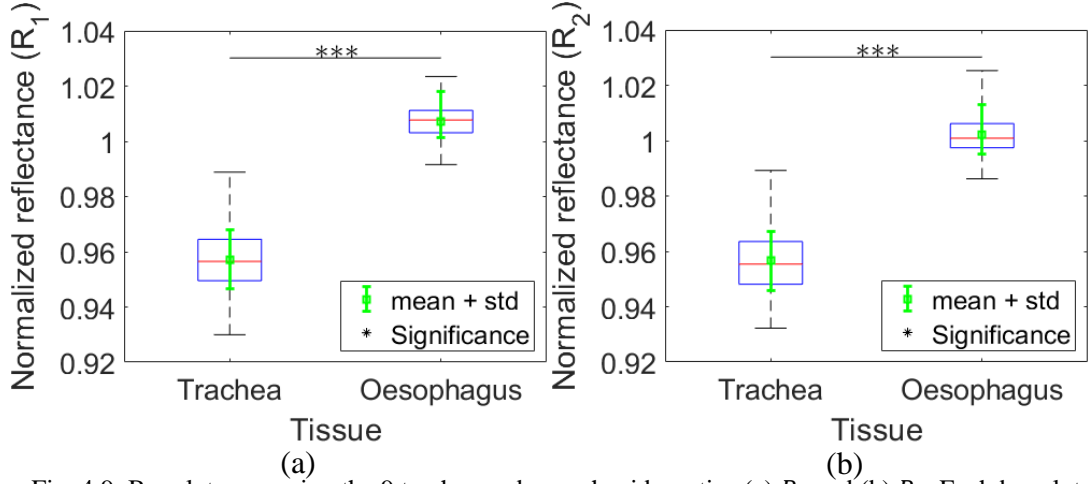
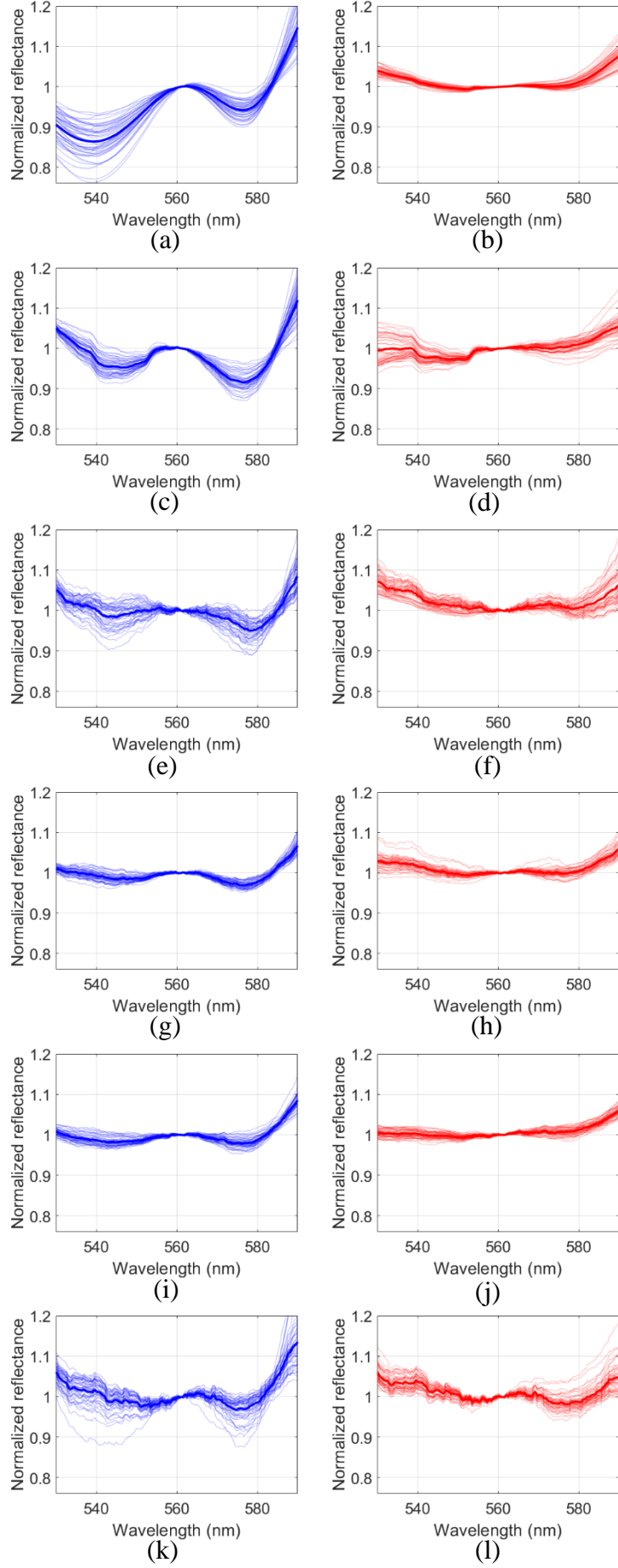


Fig. 4.9: Boxplot comparing the 9 trachea and oesophagi by ratios (a)  $R_1$  and (b)  $R_2$ . Each boxplot contains 450 spectra per tissue, leading to 450  $R_1$  and 450  $R_2$  data points (900 total). The statistical significance of a t-test is denoted by an asterisk, with \*\*\* representing  $p < 0.001$ .

The median and IQR for the trachea  $R_1$  values across all 9-samples (Fig. 4.9a) was  $0.96 \pm 0.02$  ( $n = 450$ ), where the oesophagus gave  $1.008 \pm 0.008$  ( $n = 450$ ). Furthermore, the trachea and oesophagus  $R_2$  values (Fig. 4.9b) were  $0.96 \pm 0.02$  ( $n = 450$  spectra) and  $1.001 \pm 0.009$  ( $n = 450$  spectra), respectively. The t-test is robust enough to handle data that is moderately skewed [153], as is the case here. Performing a two-sample (independent) t-test with the null hypothesis that the trachea and oesophagus  $R_1$  come from independent random samples with equal means yielded  $z = 87.2$ ,  $p < 0.001$ . Performing the test for  $R_2$  yielded,  $z = 75.3$ ,  $p < 0.001$ . Therefore, the null hypothesis was rejected and the means of the two tissues are significantly different for both  $R_1$  and  $R_2$  values. By use of appropriate thresholds an unknown tissue spectrum could be classified into being tracheal or oesophageal. An  $R_1$  threshold of 0.99 correctly identifies all tissues in this 9-sample experiment with 100% sensitivity and specificity. An  $R_2$  threshold of 0.98 correctly classifies 100% of the oesophageal data and 99.6% of the tracheal data giving a 100% sensitivity and a 99.8% specificity, with oesophageal placement identification considered as the positive rate. However, these thresholds are close to the group's extreme values and in practice, a threshold range should be used where if an unknown tissue falls into this range it is classified as 'unknown' or 'undetermined', decreasing the likelihood of the most dangerous outcome of a false negative (ETT is in the oesophagus whereas the algorithm determines it's in the trachea), at the cost of sensitivity. The same methodology was then used to analyse the 10-sensor experiment. The sensors were fabricated using the same protocol over a week. All the sensors were calibrated with a dark and white reference individually before each experiment.



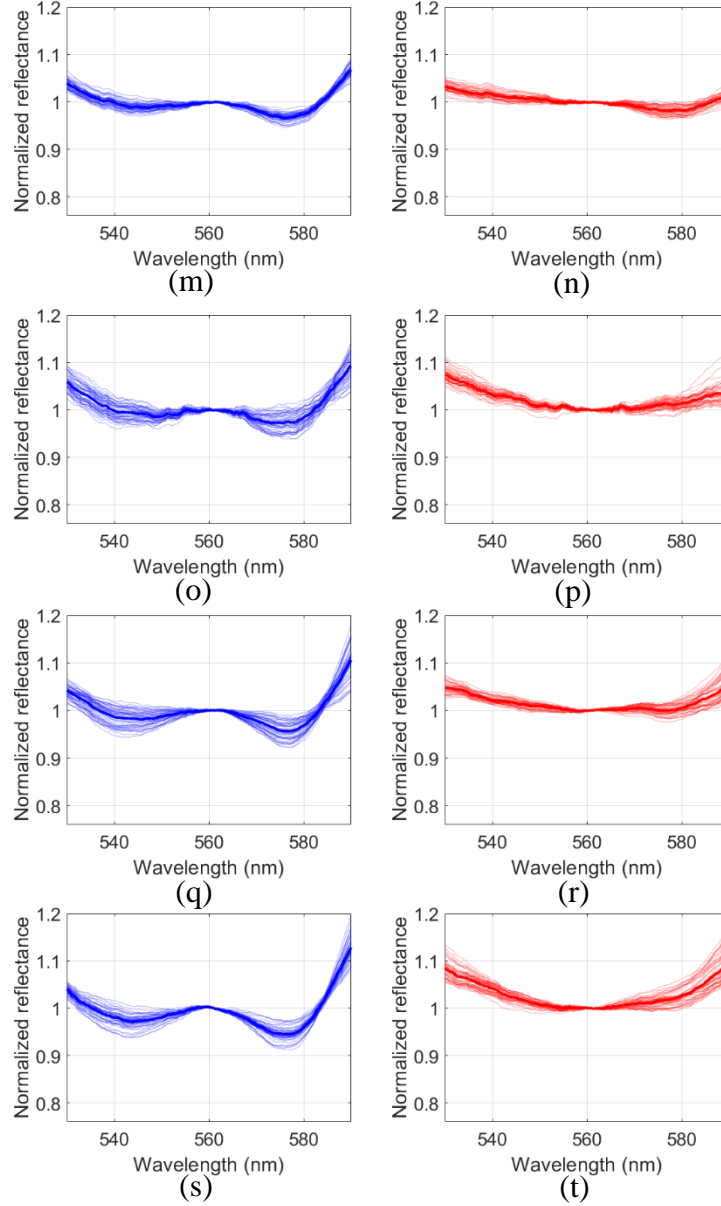


Fig. 4.10: Spectra from 10 ETT placement sensors measured in a single tracheal and oesophageal *ex-vivo* sample. (a) and (b) are from sensor 1, (c) and (d) are from sensor 2 etc., up to (s) and (t) being from sensor 10. The blue spectra, which are the left-side figures (a), (c), (e), ... , (s) are tracheal. The red spectra, which are the right-side figures (b), (d), (f), ... , (t) are oesophageal. The individual spectra are shown with faint colours, with the thicker line showing the average for all 50 measurements.

The spectra of the 10 different sensors on a single *ex-vivo* sample can be seen in Fig. 4.10. Again, most sensors produce a strong trough-peak-trough spectral characteristic in the trachea with near absence in the oesophagus. However, there are some differences in the quality of the spectra. Sensor 6 (Fig. 4.10k-l) performed particularly poorly as can be seen by the noisy signal. This likely originates from a poor-quality sensor that was improperly filed and polished. However, the fibres may have been overbent, producing significant bend loss due to damage.

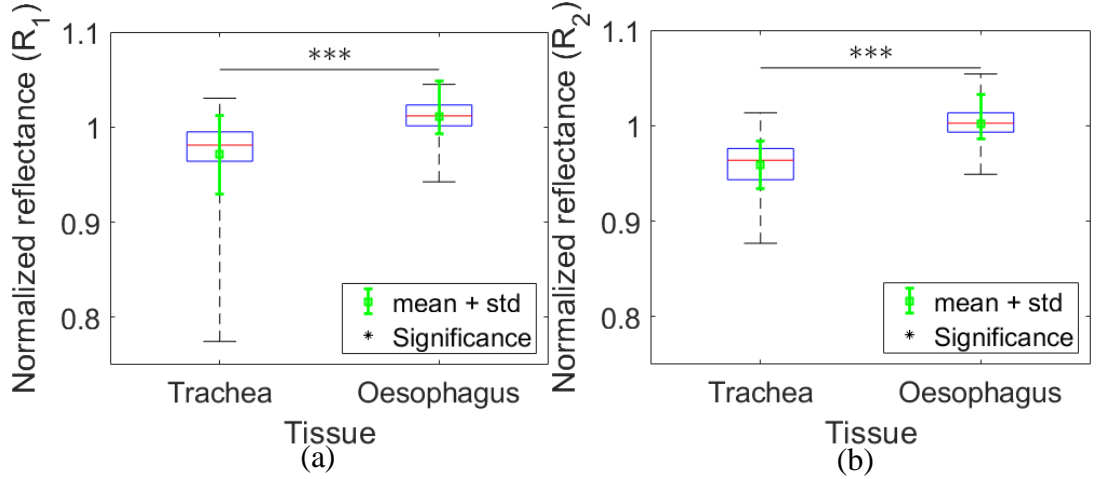


Fig. 4.11: Boxplot comparing the 10 sensors in a single trachea and oesophagus by ratios (a)  $R_1$  and (b)  $R_2$ . Each boxplot contains 500 spectra per tissue, leading to 500  $R_1$  and 500  $R_2$  data points (1000 total). The statistical significance of a t-test is denoted by an asterisk, with \*\*\* representing  $p < 0.001$ .

The median and IQR for the trachea  $R_1$ , oesophagus  $R_1$ , trachea  $R_2$ , and oesophagus  $R_2$  values were  $0.98 \pm 0.03$ ,  $1.01 \pm 0.02$ ,  $0.96 \pm 0.03$ , and  $1.00 \pm 0.02$  ( $n = 500$  spectra for all). There are overlaps in the IQRs' when comparing the trachea and oesophagus for both ratios, as can be seen in Fig. 4.11. A one-sample Kolmogorov-Smirnov test concluded that the trachea  $R_1$ , oesophagus  $R_1$ , trachea  $R_2$ , and oesophagus  $R_2$  values were not from a standard normal distribution, with skewness's of -1.97, -0.72, -0.59 and -0.24, respectively. All the distributions are moderately negatively skewed or close to normally distributed, except for the trachea  $R_1$  values (-1.97). Most of the skewness in the trachea  $R_1$  values come from a single sensor (sensor 1), accounting for 10% of the data (50/500) with the skewness reducing to -0.97 when the values from sensor 1 are neglected. Therefore, the results from the t-test are still valid and representative due to the sample size being large enough. However, a Mann-Whitney test [154] is preferred when comparing the  $R_1$  values under the null hypothesis that the trachea and oesophagus values are from distributions with equal medians. The Mann-Whitney test for the  $R_1$  values indicates a significant difference,  $z = 20.46$ ,  $p < 0.001$ . A t-test was performed on the  $R_2$  values and indicated a significant difference between them,  $z = 32.39$ ,  $p < 0.001$ .

The tissue ratios overlap more in the 10-sensor experiment, with the ratio thresholds chosen to produce 100% sensitivity (correct oesophageal identification) and being unable to produce a 100% specificity as well, as can be seen in the overlapping tails of Fig. 4.11. A good compromise is using the lower IQR of the oesophagus as the ratio threshold. Therefore, an  $R_1$  threshold of 0.99 (oesophagus  $R_1$  median minus the IQR) gives a sensitivity of 90.2% and a specificity of 66.8%. An  $R_2$  threshold of 0.98 (oesophagus  $R_2$  median minus the IQR) gives a sensitivity of 87.6% and a specificity of 82.2%. However, once again, a threshold range is more practical to decrease the likelihood of incorrect tracheal identifications. It is useful to produce a receiver operating characteristic (ROC) curve which compares the true positive rate to the false positive rate (Fig. 4.12). A compromise can be chosen from the ROC depending on the desired outcome.

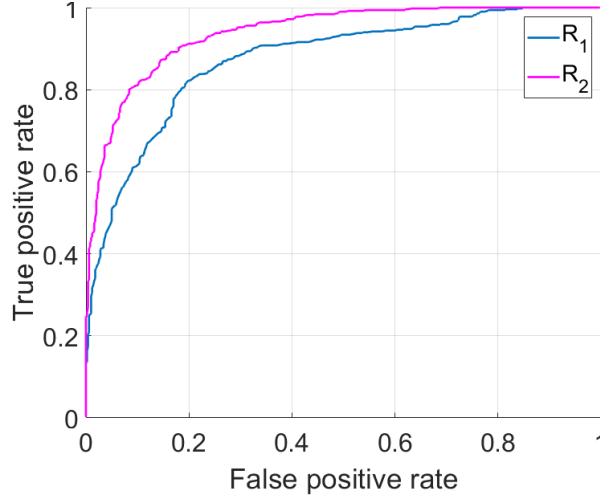


Fig. 4.12: ROC curve for the 10-sensors using  $R_1$  and  $R_2$ , the true positive rate refers to a correct identification of oesophageal tissue, whereas the false positive rate is for the incorrect identification of oesophageal tissue.

The area under the curves (AUCs) for the  $R_1$  and  $R_2$  ROCs (Fig. 4.12) are 0.87 and 0.94, respectively, demonstrating that the ratio values identify the tissues well. However, further computational processing can improve sensitivity and specificity as is described in the remainder of this chapter. Furthermore, what constitutes a true positive is open for choice, where it can either be identifying tracheal placement or oesophageal placement. Oesophageal intubation is chosen as the true positive as this is what is being studied here, although identifying the tube is correctly placed in the trachea as the true positive may be more useful in clinical practice.

In conclusion, there is a significant difference when comparing the  $R_1$  and  $R_2$  values measured in the trachea and oesophagus of *ex-vivo* porcine samples when 9 different samples are used ( $N = 900$  spectra) and when 10 sensors are used ( $N = 1000$  spectra). Therefore, these ratios can be used to significantly distinguish and identify the two tissue types given their spectra. A single sensor measured across multiple porcine models performs well, correctly identifying 99.9% of the tissues. However, the use of multiple sensors produces a weaker identification, with  $R_2$  outperforming  $R_1$  and giving an average correct tissue identification of 84.9% if the median and IQR are used as the threshold. Therefore, individual calibration of the sensors may be required, or more consistent fabrication. However, by combining the two ratios and using further computational methods, a stronger classification of the unknown tissue types can be performed. This is explored throughout the remainder of this chapter, closing with a comparison between the methods.

### 4.3.2 Principal Component Analysis

Large datasets containing many variables can be problematic to interpret. An optical spectrometer measures the properties of light and typically has a few thousand pixels [155]. The miniature spectrometer used here (Ocean Optics, model USB2000+UV-VIS-ES) has 2048 pixels with a wavelength interval of 0.384 nm. To compare spectra involves comparing thousands of wavelengths, which can be difficult to visualise and interpret. However, the spectra may only differentiate from each other at a few wavelengths. Therefore, dimensionality reduction [156] can be useful to reduce the

size of the dataset whilst still retaining most of the meaningful properties. Principal component analysis (PCA) [157] is a popular form of dimensionality reduction and is often utilised in spectrometry [158,159,160]. PCA creates a new set of uncorrelated variables known as principal components, these new variables maximise variance and retain the maximum amount of information. The USAISR utilised this technique when first determining the tracheal and oesophageal spectral differences [85]. However, the spectral wavelength range most of interest has been determined to be between 530 - 590 nm, and dimensionality reduction is less impactful as a narrower wavelength range is utilised.

PCA was performed on the data from the 9-sample experiment and computed on a large matrix containing all tracheal and oesophageal data using Matlab (MathWorks, version 2018). Therefore, each spectrum represented an observation and each wavelength a variable. Therefore, by performing PCA, the dimensionality of this matrix was reduced into two principal components (PCs). The PCs were then normalized at a wavelength of 561.1 nm (after standard white reference normalization) so that they could be compared to the mean tracheal and oesophageal spectra across all 9 samples (Fig. 4.13).

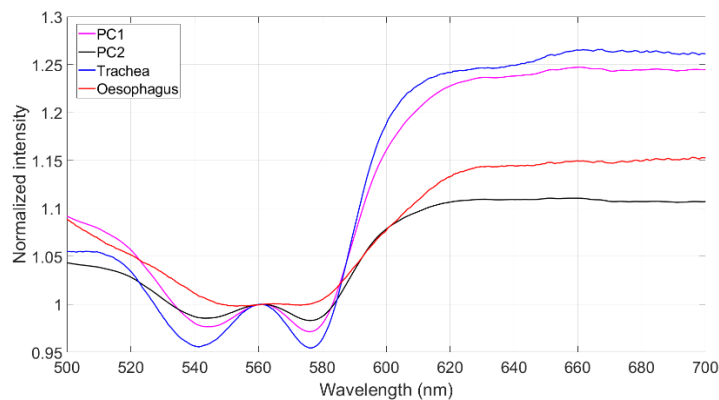


Fig. 4.13: Average *ex vivo* porcine tracheal and oesophageal spectra highlighting the similarity between the first principal component (PC1) and second principal component (PC2).

The first principal component (PC1) had a correlation coefficient with the mean trachea and oesophagus spectra of 0.9959,  $p = 0.01$ , and 0.9868,  $p = 0.01$ , respectively. The second principal component (PC2) gave a correlation coefficient of the mean trachea and oesophagus spectra of 0.9945,  $p = 0.01$ , and 0.9807,  $p = 0.01$ , respectively. These results contrast those of Nawn *et al* [85], as they found a high positive correlation coefficient between the tracheal mean and PC2, and the oesophageal mean and PC1. Perhaps the reason for this difference is in the larger number of datasets with which the PCA was applied during the analysis performed here (111 spectra compared with 900 spectra in this thesis). PCA applied in this manner, where the wavelengths are the variables, functions as a type of averaging, where the components in a dataset with the most variance are maximised. The larger dataset, documented here, gives access to more variance and is expressed more in higher-order principal components. Furthermore, the less pronounced spectral characteristic in the oesophageal data (Fig. 4.14) may contribute to the second principal component expressing this shape and therefore giving both PC's a high correlation with the tracheal and oesophageal mean spectra.



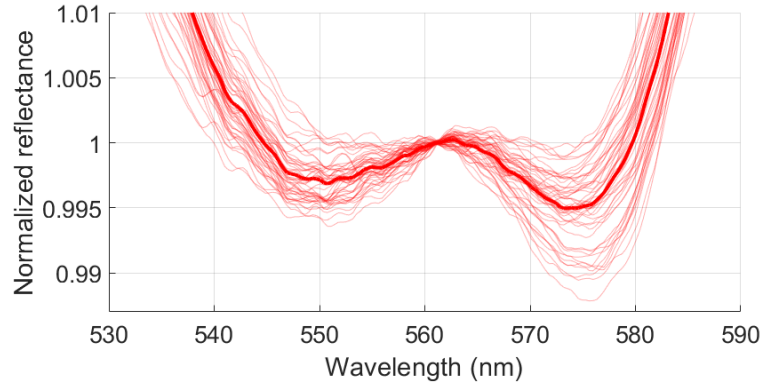


Fig. 4.14: Sample 1 oesophageal spectra from the 9-sample experiment.

The tissues can be distinguished by performing PCA over the characteristic wavelength range (530 - 590 nm) and then comparing the first and second principal components (Fig. 4.15). Instead of using PCA as a type of averaging (Fig. 4.13) over multiple spectra, where many spectra are used to generate 2 spectra containing the maximum amount of variance (PC1 and PC2), each spectrum is reduced into two variables PC1 and PC2. This process reduces all the information contained over the characteristic range into two variables with the maximum amount of variance.

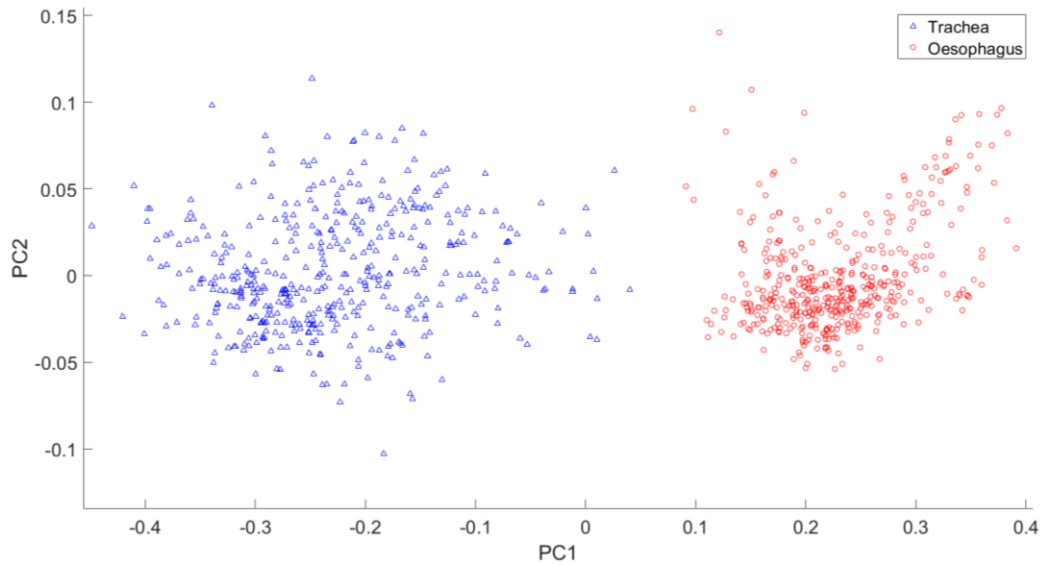


Fig. 4.15: 9-sample experiment comparing the first two principal components (PC1 and PC2) found from performing PCA over the characteristic range (530 – 590 nm) (N = 900 spectra).

A separation forms between the two tissue types when comparing the first two principal components. A clear separation can be seen (Fig. 4.15) between PC1 for the trachea and the oesophagus. By utilising the information available over the characteristic range and then reducing it into two variables PC1 can perfectly separate the 9-sample data (100% sensitivity and specificity), given a threshold of 0.0657, found from the midpoint between the maximum tracheal and minimum oesophageal value.

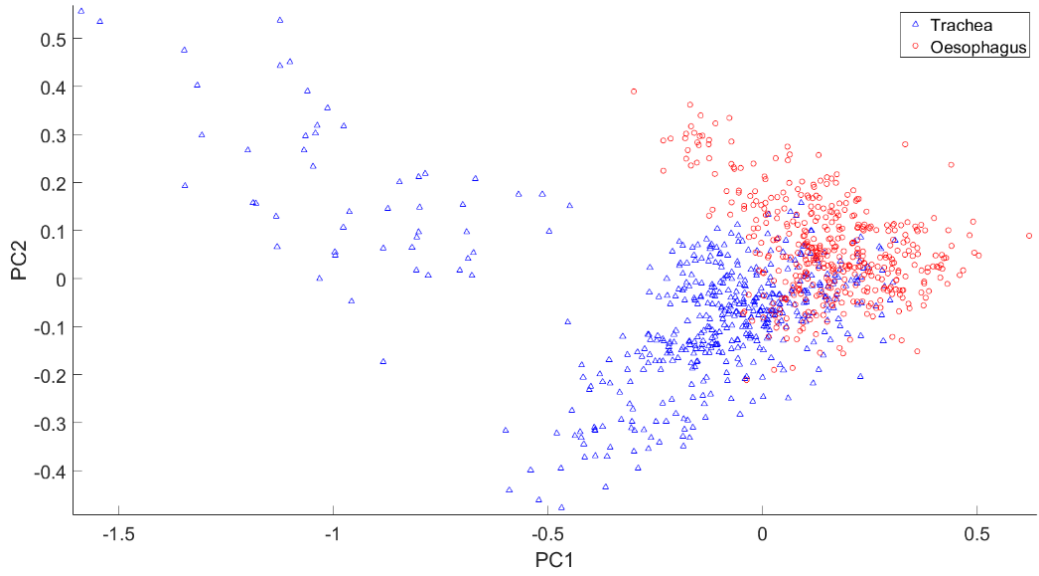


Fig. 4.16: 10-sensor experiment comparing the first two principal components (PC1 and PC2) found from performing PCA over the characteristic range (530 – 590 nm) (N = 1000).

A similar approach using PCA can be made for the 10-sensor data (Fig. 4.16). However, here the tissues are less distinguished when comparing the 10-sensor PCA (Fig. 4.16) to the 9-sample PCA (Fig. 4.15), as we have seen previously in this chapter. This is likely attributed to batch variation caused by a handmade custom sensor. A separation can be seen between the two tissue types, although the boundary is less defined, particularly if the PCs are viewed separately. However, by utilising both principal components a boundary can be formed to better separate the tissue types.

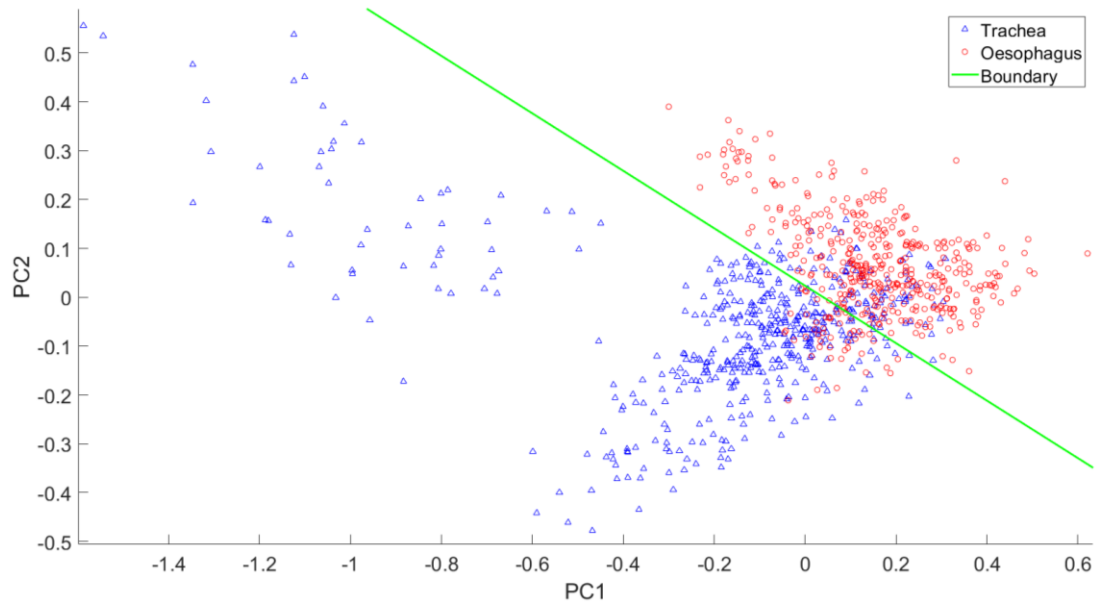


Fig. 4.17: 10-sensor experiment processed with PCA and a boundary drawn between the two.

A boundary was formed through trial and error to classify the two tissue types (Fig. 4.17), with an equation  $f(x) = -0.5882x + 0.02353$ . Using the boundary, a sensitivity of 90.4% (correct oesophageal identification) and a specificity of 83.6% (correct tracheal identification), giving total correct tissue identifications as 87%. This boundary could be formed and optimised in multiple ways, as described in Section

4.5. However, the boundary was placed by hand as an example and could likely be optimised to give a better performance if this method is utilised further.

## 4.4 Statistical Measures

The overall characteristic shape changes in the 530 – 590 nm wavelength range between the trachea and oesophagus can be quantified using statistical measures. Although statistical measures are typically used to summarise the characteristics of a data set, these differences could be used to differentiate that data. Therefore, the mean, skewness, and kurtosis of the spectra in the 9-sample and 10-sensor experiments were used as measures of spectral shape to differentiate the tissues.

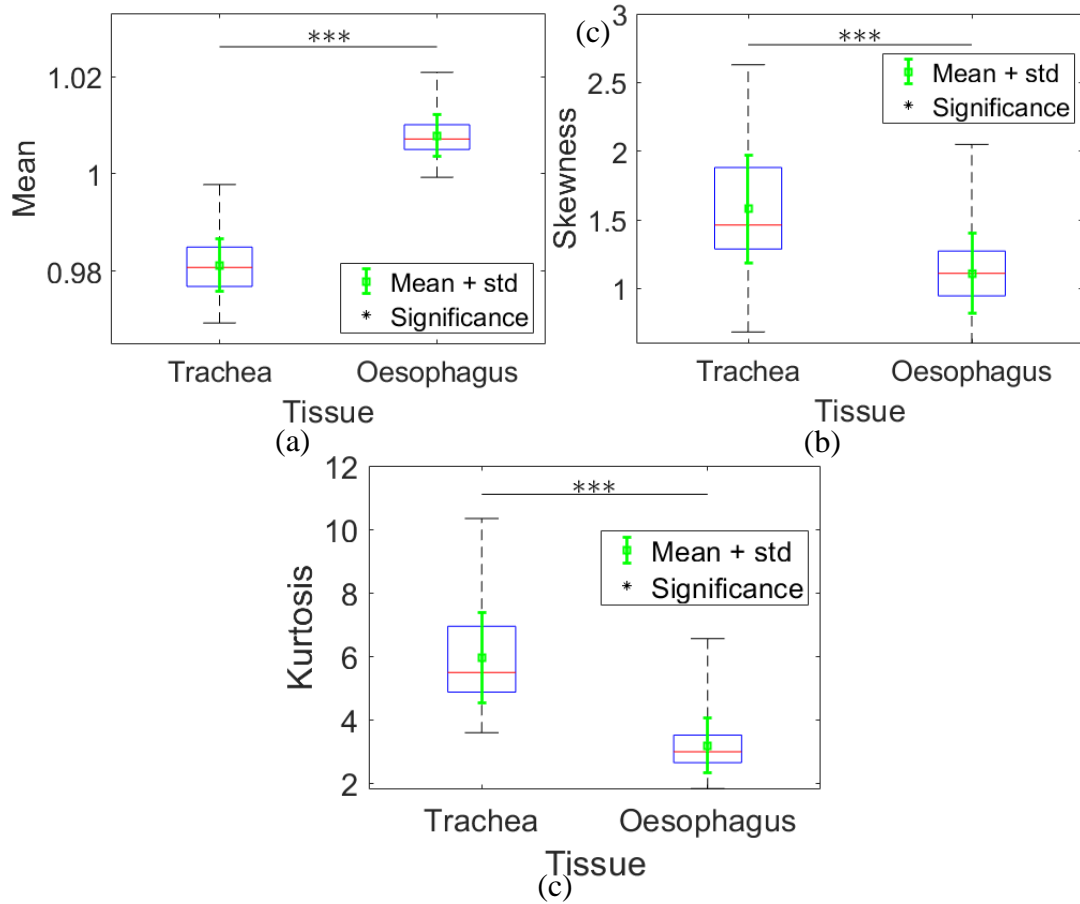


Fig. 4.18: (a) Mean, (b) skewness, and (c) kurtosis for the 9 porcine sample experiment, where the statistical measures are calculated over the characteristic range (530 – 590 nm) for each spectrum and then separated into trachea and oesophagus. The statistical significance of a t-test is denoted by an asterisk, with \*\*\* representing  $p < 0.001$ .

The tissues can be separated as indicated above using mean, skewness and kurtosis (Fig. 4.18). These statistical measures offer another way to distinguish the tissues. A summary of their performance is described at the end of this section.

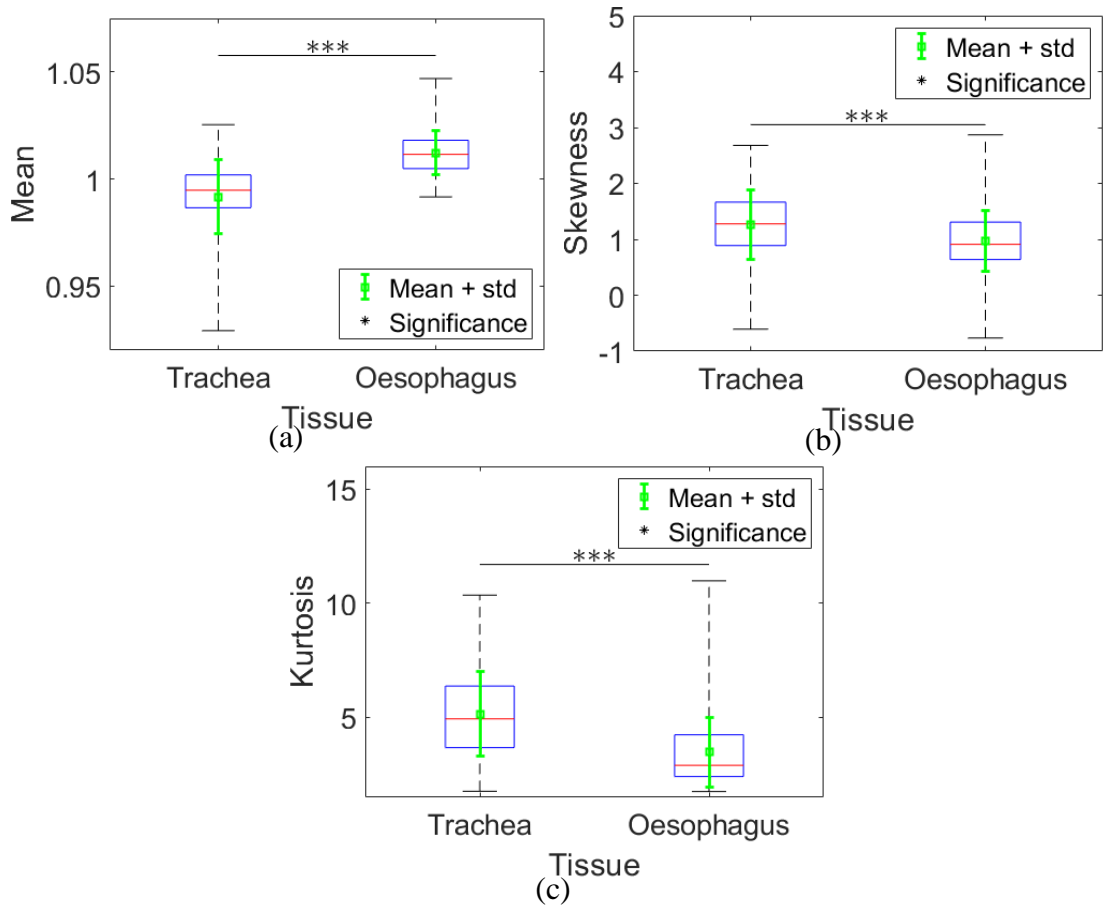


Fig. 4.19: (a) Mean, (b) skewness, and (c) kurtosis for the 10-sensor experiment, where the statistical measures are calculated over the characteristic range (530 – 590 nm) for each spectrum and then separated into trachea and oesophagus.

The data from the 10-sensor experiment form a worse separation between the trachea and oesophageal data when using mean, skewness, and kurtosis (see Fig. 4.19). This data is more difficult to separate as seen in Section 4.3.1, although using these statistical measures produces a particularly poor result. The likely cause is that changing between sensors produces a change in the characteristic range which is enough to significantly change the shape of the characteristic. A summary of the statistical measures is given in Table 4.1.

Table 4.1: Comparison of the performance of using the mean, skewness, and kurtosis of each spectrum over the characteristic range (530 – 590 nm) to distinguish the tissues.

		Method		
		Mean	Skewness	Kurtosis
Performance	9-sample sensitivity (%)	100.0	76.9	93.9
	9-sample specificity (%)	100.0	74.9	74.9
	9-sample correct tissue identification (%)	100.0	75.9	84.4
	10-sensor sensitivity (%)	82.8	75.0	75.0
	10-sensor specificity (%)	75.0	48.0	63.0
	10-sensor correct tissue identification (%)	78.9	61.5	69.0

In Table 4.1 the threshold value between whether a spectrum was identified as tracheal or oesophageal was the 75<sup>th</sup> percentile of the tissue which gave the highest sensitivity, where the sensitivity is the percentage of correct oesophageal identifications. Therefore, most of the sensitivity and specificity pairs contain a value which is ~75%, except for the mean method for the 9-sample experiment, where a perfect separation could be achieved by choosing a value in between the maximum tracheal and minimum oesophageal values. Once again, a balance between sensitivity and specificity can be achieved in multiple ways. However, the chosen method was used to prioritize sensitivity as it is the most important aspect. The use of ROC analysis (Section 4.3.1), or other appropriate methods, could refine the threshold depending on the required outcome. The mean normalized reflectance intensity across the characteristic range performs best for both the 9-sample and 10-sensor experiments, with 100.0 and 78.9% correct tissue identification, respectively. However, overall, these 3 statistical methods perform worse than both PCA and the spectral ratios  $R_1$  and  $R_2$  method.

## 4.5 Spectral Classification

Identification of known tracheal and oesophageal features can be achieved using: individual spectral ratios; PCA; or statistical measures. However, the intention is to classify unknown tissues into tracheal and oesophageal. Previously, this has been investigated by forming thresholds using IQRs and boundaries formed using trial and error, with these methods performing well when the data is highly separable, such as is the case with the *ex-vivo* 9-sample data with the same sensor. However, the use of a single *ex-vivo* sample with 10 different sensors already produces data that is more difficult to separate, with PCA being able to correctly identify 87% of the tissues using trial and error to form the boundary. Furthermore, *in-vivo* data is likely more complicated with the boundaries between the tissues less obvious and perfect separations unlikely. Therefore, three algorithms are used next to provide a more reliable method to classify the tissues. Furthermore, it is illustrated that by utilising both spectral ratios  $R_1$  and  $R_2$ , instead of viewing them separately, a stronger classification can be performed. The statistical significance of a t-test is denoted by an asterisk, with \*\*\* representing  $p < 0.001$ .

### 4.5.1 Linear Discriminant Analysis

We have seen that PCA can distinguish the data by taking the characteristic range (530 – 590 nm) and reducing it into the first two principal components (Fig. 4.15 and Fig. 4.16). However, most of the variance is expressed in the ratios  $R_1$  and  $R_2$ . Therefore, by using the two ratios together the aim is to better distinguish the data without having to use the full characteristic range and PCA.

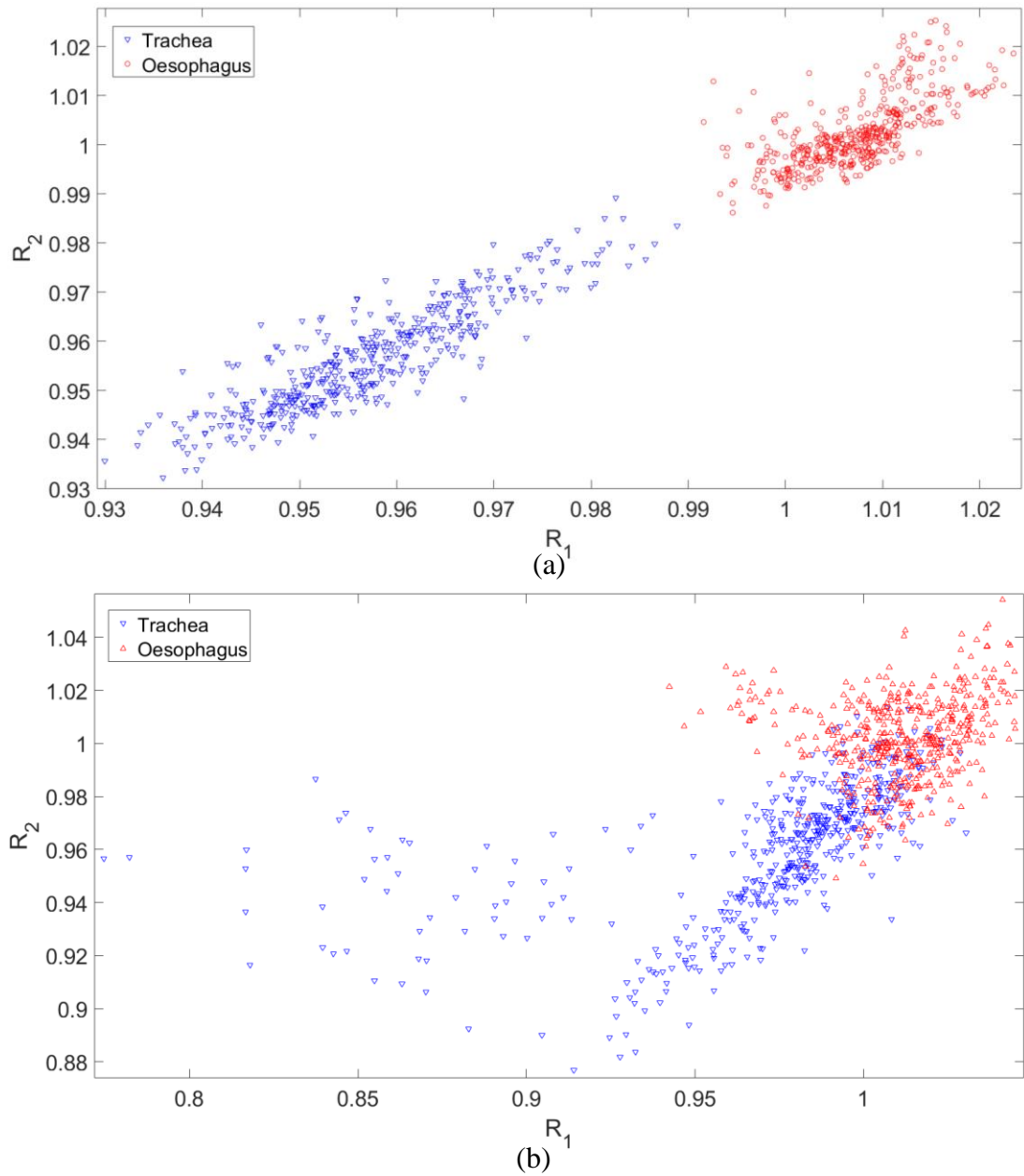


Fig. 4.20: Comparison of the ratios  $R_1$  and  $R_2$  for the (a) 9 *ex-vivo* samples with the same sensor and (b) 10 different sensors with the same single sample experiments.

There are similarities in the distributions when comparing PC1 and PC2 to  $R_1$  and  $R_2$  for the 9-sample and 10-sensor experiments (comparing Fig. 4.20a with Fig. 4.16, and comparing Fig. 4.20b with Fig. 4.17), indicating that PCA is extracting most of the same features that are described by using the variables  $R_1$  and  $R_2$ . Therefore, it is not necessary to use PCA during classification of the tissues as  $R_1$  and  $R_2$  can produce a similar identification performance. However, PCA has been a useful tool in finding these ratios by which to distinguish the tissues. Furthermore, as stated previously, if more variables are measured (temperature, perfusion, oxygen saturation, pressure, and  $\text{CO}_2$ ) then it may once again become useful.



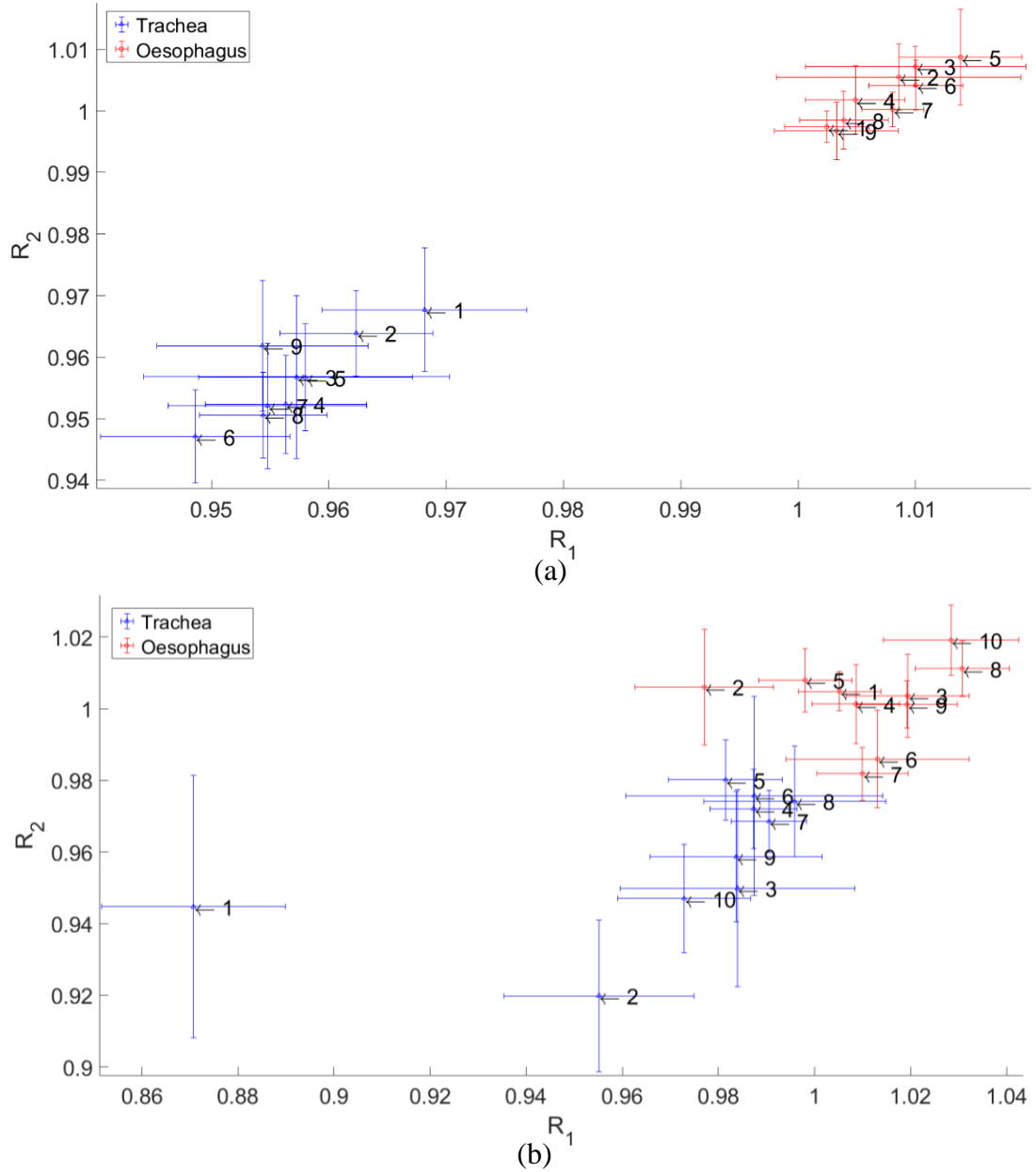


Fig. 4.21: Comparison of the means of ratios  $R_1$  and  $R_2$  for the (a) 9-sample and (b) 10-sensor experiments. The error bars refer to the standard deviation.

The mean  $R_1$  and  $R_2$  values for each (a) sample and (b) sensor can be seen in Fig. 4.21, with their standard deviations expressed by the error bars. By separating the data into individual samples and sensors, the variance in each class can be seen. Furthermore, this reiterates sensor 1 (Fig. 4.21b) has a mean  $R_1$  which is an outlier from the other sensors.

Linear discriminant analysis (LDA) is commonly used as a form of dimensionality reduction and as a classifier. It is closely related to PCA as they both find linear combinations of variables to better explain the data. LDA maximises the variance between classes and can explicitly be used as a tool to classify a group [161,162], by forming a boundary. LDA is an a priori classifier and functions by first using a training data set to generate a model which can classify a test data set. 2 variable LDA first

calculates the variance between the classes ( $S_b$ ) defined as the distance between the means of each class (Eq. (4.2)).

$$S_b = \sum_{i=1}^n N_i (\bar{x}_i - \bar{x})(\bar{x}_i - \bar{x})^T \quad (4.2)$$

where,  $N_i$  is the sample size of each class,  $\bar{x}_i$  is the mean of each class,  $\bar{x}$  is the overall mean, and T is the threshold, typically 0.5 for two classes, although lowering this improves sensitivity. The variance within each class ( $S_w$ ) is then found (Eq. (4.3)) as follows:

$$S_w = \sum_{i=1}^n (N_i - 1) S_i = \sum_{i=1}^n \sum_{j=1}^{N_i} (x_{i,j} - \bar{x}_i)(x_{i,j} - \bar{x}_i)^T \quad (4.3)$$

An argument is then constructed (Eq. (4.4)) that maximises the variance between classes ( $S_b$ , Eq. (4.2)) and minimises the variance within classes (i.e.  $S_w$ , Eq. (4.3)) using Fisher's criterion.

$$P_{lda} = \arg \max (P) \frac{|P^T S_b P|}{|P^T S_w P|} \quad (4.4)$$

where, P is the space projection in a lower dimension, and  $P_{lda}$  is the LDA space projection.

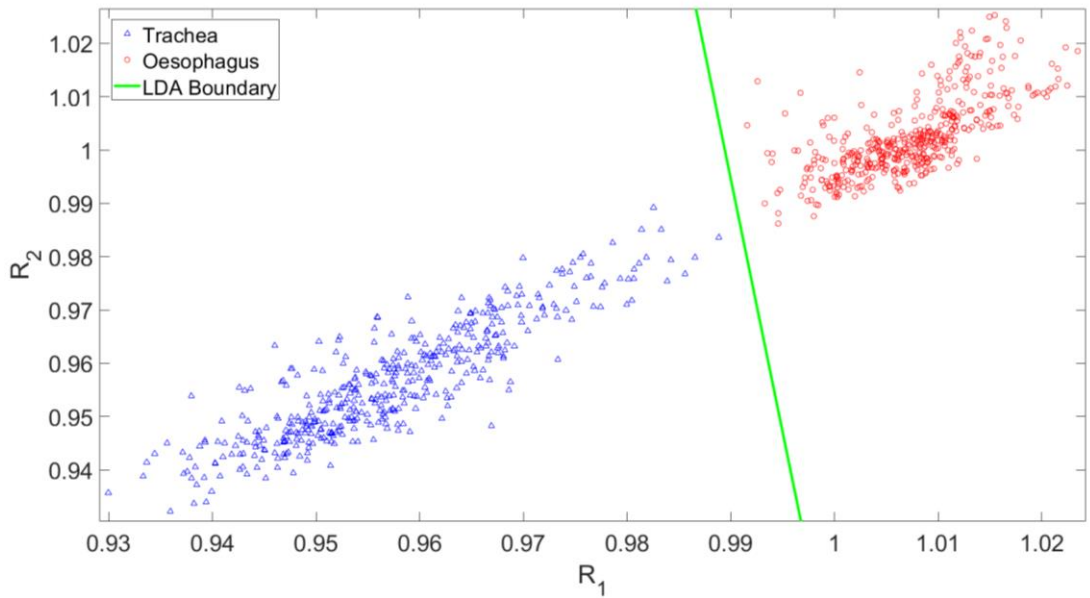


Fig. 4.22: LDA boundary formation for the 9-sample experiment.

A boundary between the two classes was formed using LDA for the 9-sample experiment (Fig. 4.22) when all 900 data points are used for training data. The groups are already well separated, and the boundary placement can be determined without the use of LDA. However, automating this step may become useful when the data is less

well separated. Furthermore, the boundary can be easily updated when introducing more training data. The performance of the LDA can be tested by using the data such that all but one data point is used as the training data (899 training data points) and the remaining one is used as the test data (1 test data point) and then permuted through so that the next point becomes the test until each data point has been the test data (900 iterations). LDA could perfectly separate the data (100% sensitivity and specificity) through all 900 iterations. However, once again, this is unsurprising given the high separability of the trachea and oesophagus in the 9-sample experiment.

A confidence level in tissue identification helps better inform the user of how well an identification can be trusted. This can be performed with LDA by calculating the distance between the data point and the boundary. Distances further from the line have higher confidence and are more ‘tracheal’ or ‘oesophageal’, whereas those closer to the line have a lower confidence.

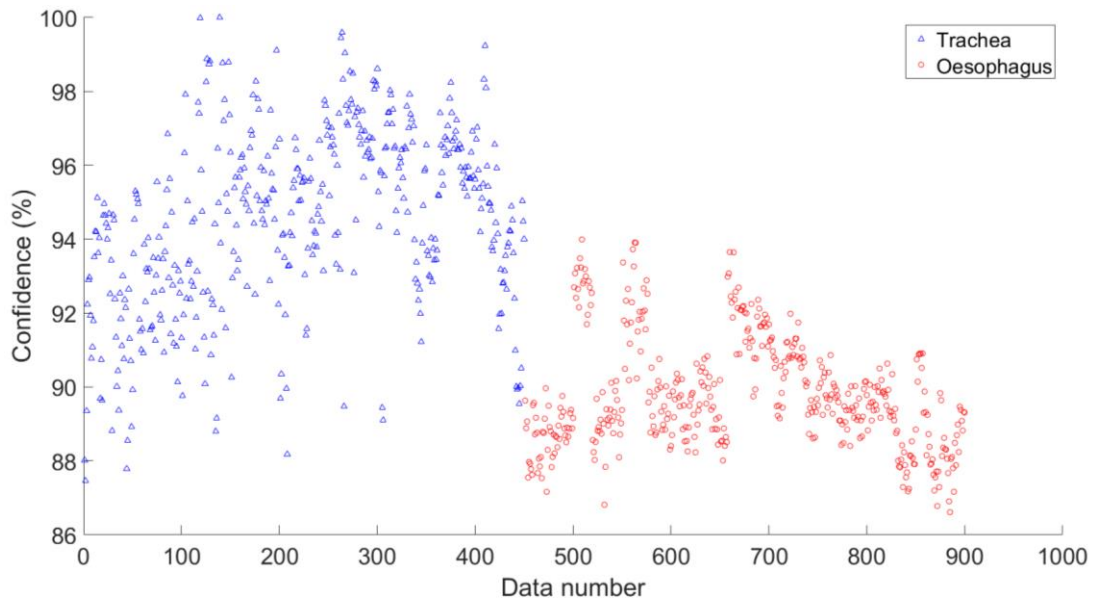


Fig. 4.23: Confidence estimate on the LDA tissue identification method for the 9-sample experiment.

The confidences were found by calculating the shortest distance to the LDA boundary. The data point furthest away from the LDA boundary was then assigned a confidence of 100% in Fig. 4.23, with distances closer to the line having proportionally less confidence. However, the scale for generating confidence is arbitrary as there is not enough context to sufficiently determine “realistic” confidence, and they could be artificially scaled to give higher or lower mean confidence. The same LDA boundary formation and confidences were then found for the 10-sensor experiment (Fig. 4.24).

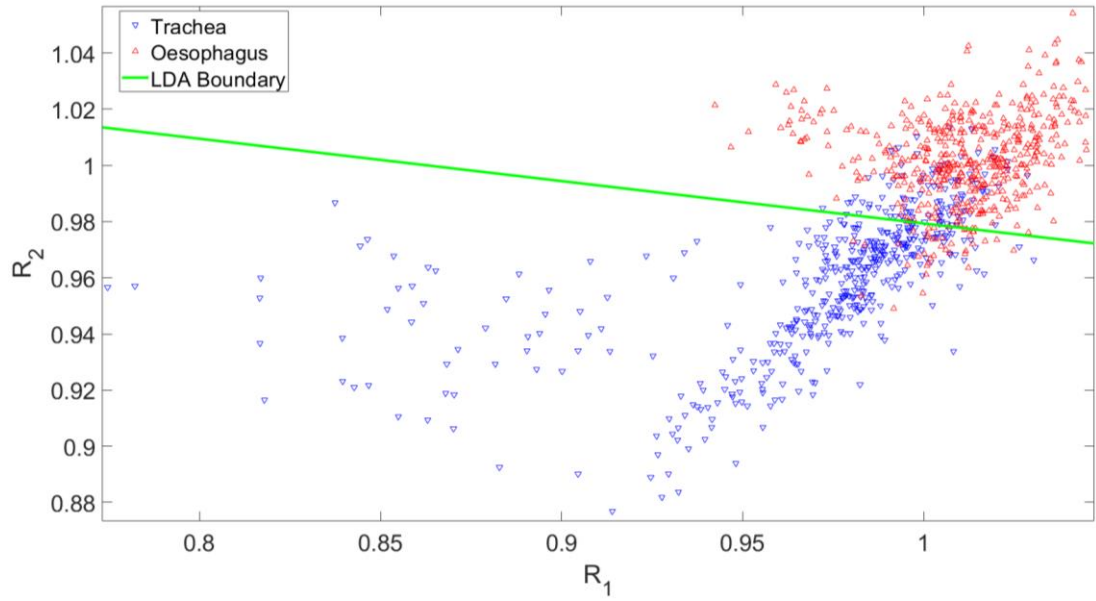


Fig. 4.24: LDA boundary formation for the 10-sensor experiment.

A permutation through the data where one data point is used as the test data and the remaining 999 data points were used as the training data gave on average a 92.6% sensitivity and 80.2% specificity (86.4% correct tissue identification). This is comparable to the PCA method which gave 87% correct tissue identification without the need to store the full characteristic range.

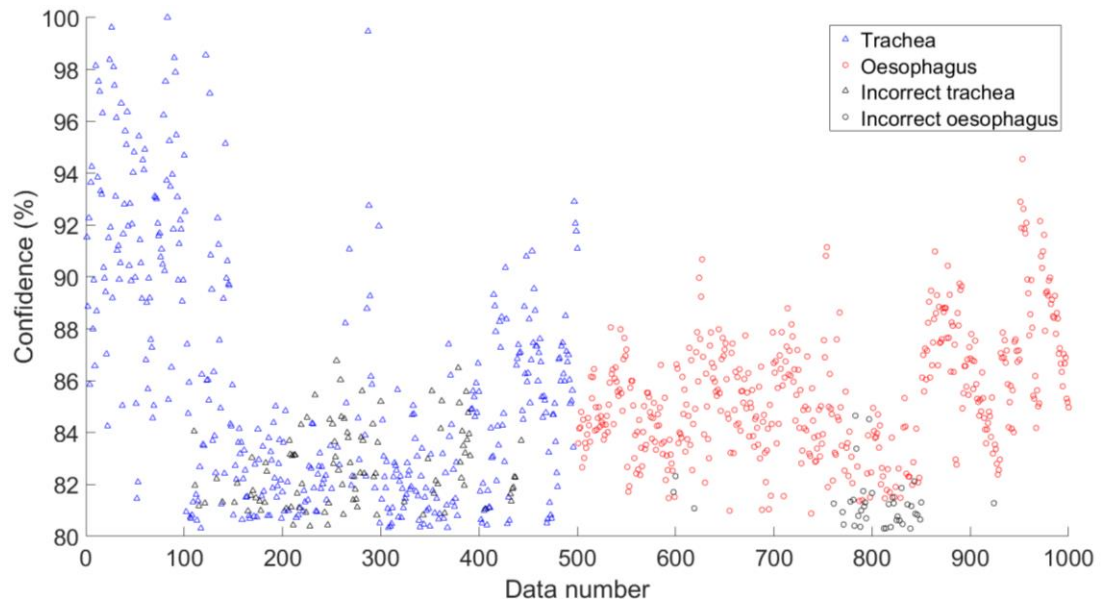


Fig. 4.25: Confidence estimate on the LDA tissue identification method for the 10-sensor experiment. The black data points refer to incorrect tissue identifications.

The confidences (Fig. 4.25) for the 10-sensor experiment were generated using the same method as the 9-sample experiment, where the data point furthest from the line was given a confidence of 100%. The data points that are on the wrong side of the LDA boundary (causing an incorrect tissue identification) are highlighted by black triangles (trachea) and black circles (oesophagus) in Fig. 4.25. A benefit of this method is that data points on the wrong side of the boundary tend to be close to the boundary

and therefore tend to give low confidence. However, the confidences can be scaled differently such that data points close to the line give much lower values which increases sensitivity and decreases specificity, as this may be more appropriate in practice.

## 4.5.2 Logistic Regression Analysis

Logistic regression analysis (LRA) [163,164] is a predictive statistical classifier used when a result is binary, such as predicting oesophageal intubation (tube is or isn't in the oesophagus). Therefore, assigning the oesophageal data a value of 1 and non-oesophageal data (tracheal data) a value of 0 allows for identification through LRA.

The equation for a straight line  $f(x)$  in linear regression is given by Eq. (4.5).

$$f(x) = mx + c \rightarrow P_L = \beta_0 + \beta_1 x \quad (4.5)$$

Where the straight-line function equals the LDA probability function  $f(x) = P_L$ , the gradient is a constant  $m = \beta_1$ , and the y-intercept is a different constant  $m = \beta_0$ . To form a probability between 0 and 1 we divide the probability by  $1 - P_L$  and then increase the restricted range by taking the log, giving Eq. (4.6).

$$\ln\left(\frac{P_L}{1 - P_L}\right) = \beta_0 + \beta_1 x \quad (4.6)$$

Solving Eq. (4.6) for  $P_L$  gives the logistic function (Eq. (4.7)) and describes the exponential growth of a population ( $P_L$ ).

$$P_L = \frac{1}{1 + e^{-(\beta_0 + \beta_1 x)}} \quad (4.7)$$

LRA was performed for the ratio values  $R_1$  and  $R_2$  separately as this produces a two-dimensional logistic regression curve and is easier to conceptualise. This further investigates the performance of each ratio separately as a predictor for oesophageal tissue identification.

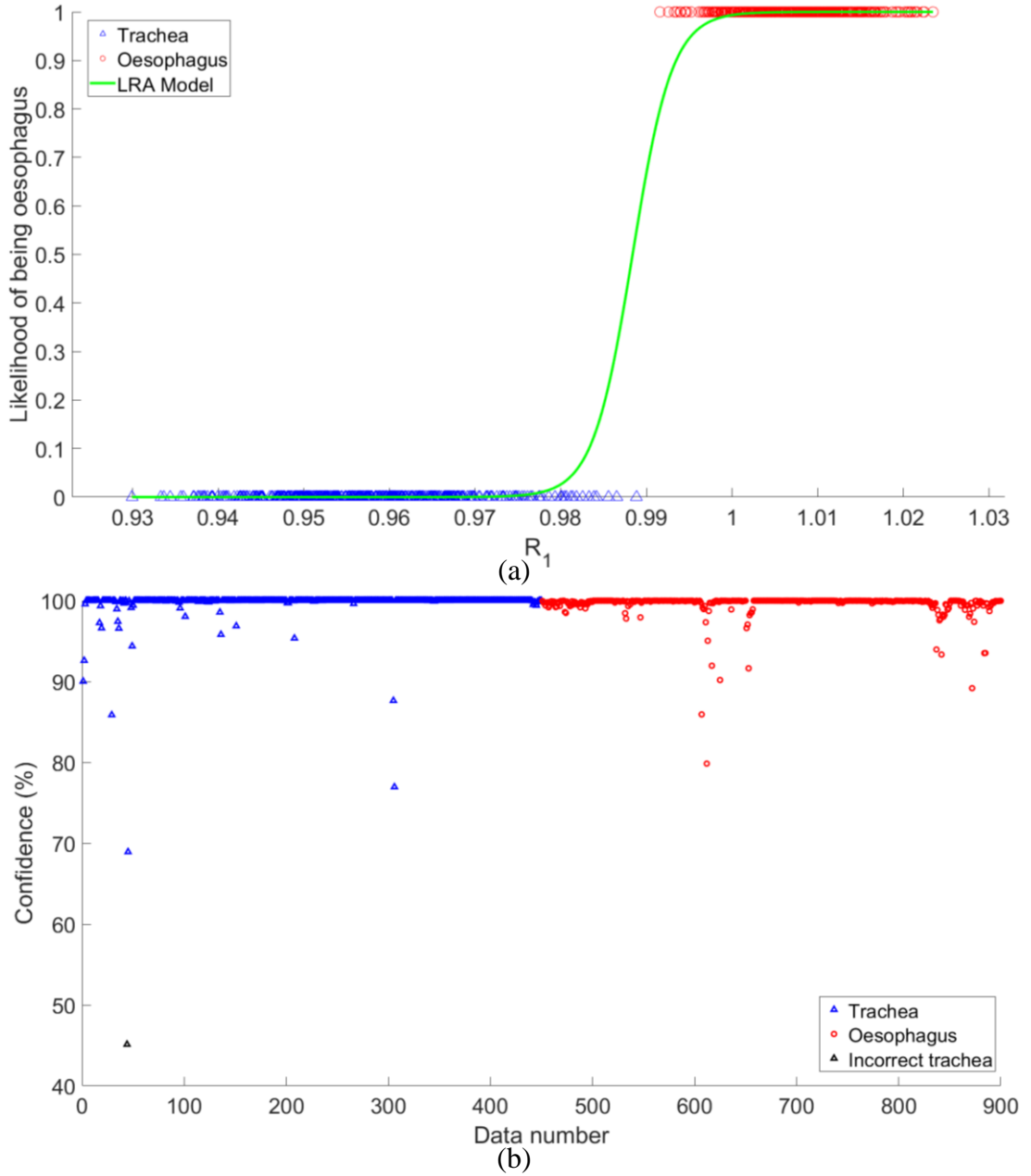


Fig. 4.26: (a) LRA model and (b) confidences for the 9-sample experiment using  $R_1$ .

Using the LRA model with  $R_1$  gives a sensitivity of 100% and a specificity of 99.8 % (1 wrong tracheal identification). However, where this method excels is in the confidence (Fig. 4.26b). The regression model predicts the likelihood a data point has a specific outcome, with the data's likelihood of being oesophagus described by the y-axis of (Fig. 4.26a). Therefore, a more obvious way to assign confidence arises, one that follows the regression curve. This gives a steep drop in confidence for measurements close to the boundary, such that most measurements give 100% confidence. Therefore, the one incorrect data point gives a confidence of being tracheal of 45.12% and is identified as oesophageal, as displaying both confidences on the same figure means that those below 50% are identified as being the other tissue in Fig. 4.26b. Therefore, the confidence of this data point being oesophageal is only 55.12% and would be rejected given an appropriate confidence threshold. The same process can then be applied to the  $R_2$  values.



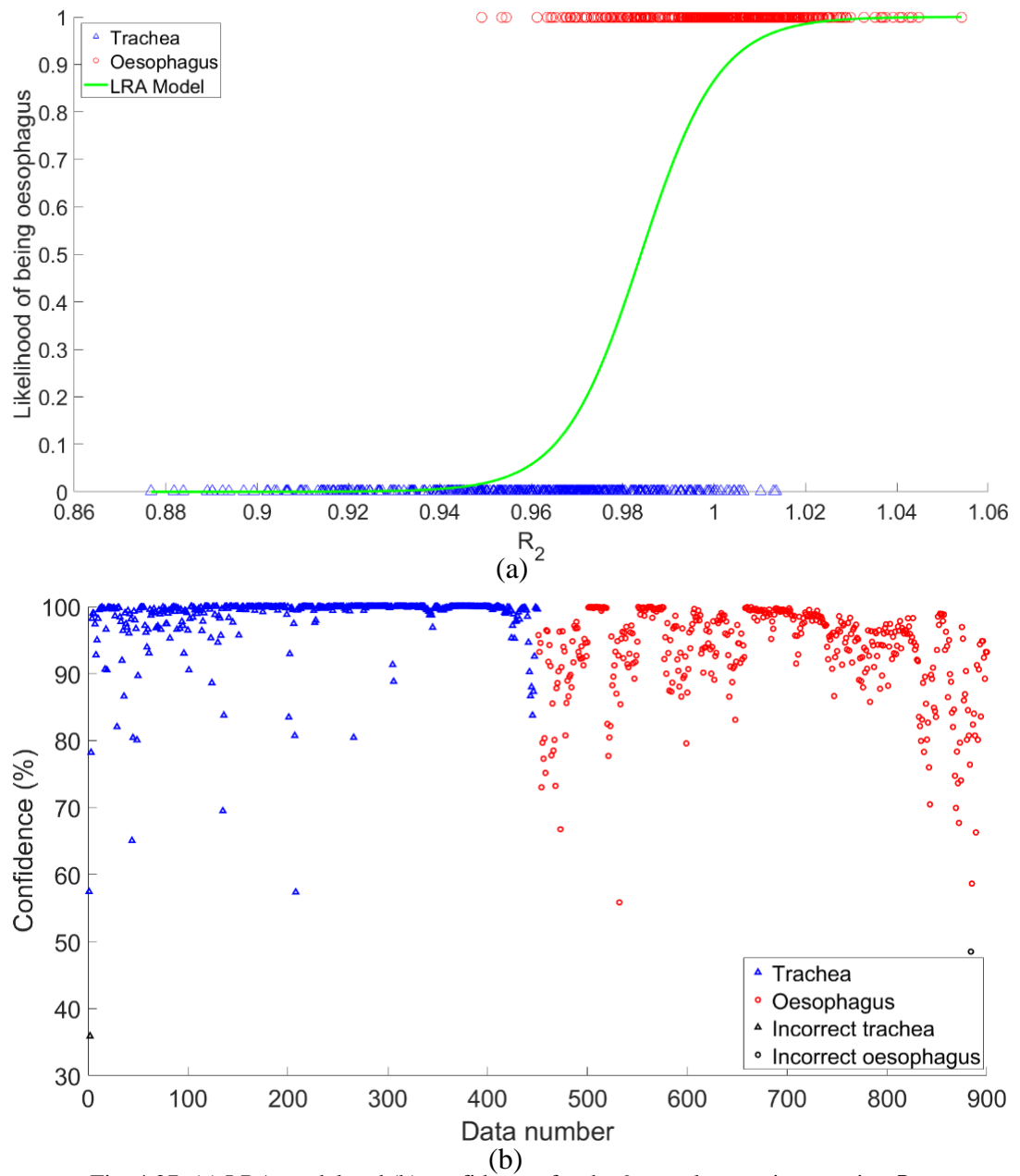


Fig. 4.27: (a) LRA model and (b) confidences for the 9-sample experiment using  $R_2$ .

Using  $R_2$  the LRA model has a sensitivity of 99.8% and a specificity of 99.8%. Most of the other methods have been able to perfectly separate the tissues in the 9-sample experiment, with LRA performing slightly worse. However, its ability to assign a likelihood to each measurement is advantageous.

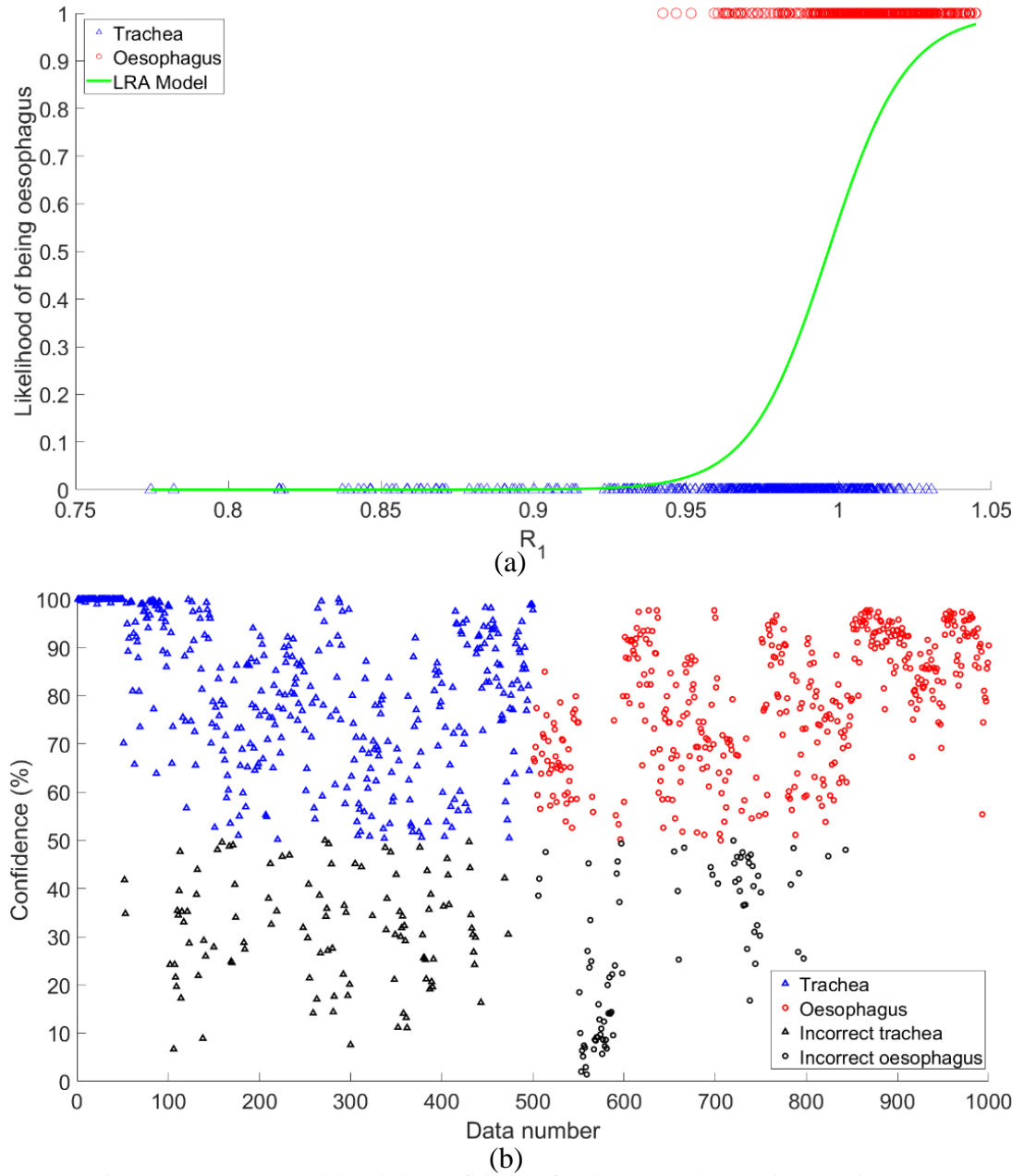


Fig. 4.28: (a) LRA model and (b) confidences for the 9-sample experiment using  $R_1$ .

LRA was then performed on the 10-sensor experiment (Fig. 4.28). Due to the overlapping  $R_1$  values in this data (Fig. 4.28a) and the maximum oesophageal values being close to that of the tracheal and with a small spread, the LRA model falls off sharply as it approaches the end of the oesophageal data, producing no oesophageal likelihoods of  $\sim 100\%$ . However, this causes a low likelihood for data close to the boundary. The LRA model produced a sensitivity of 83.4% and a specificity of 78.2%.

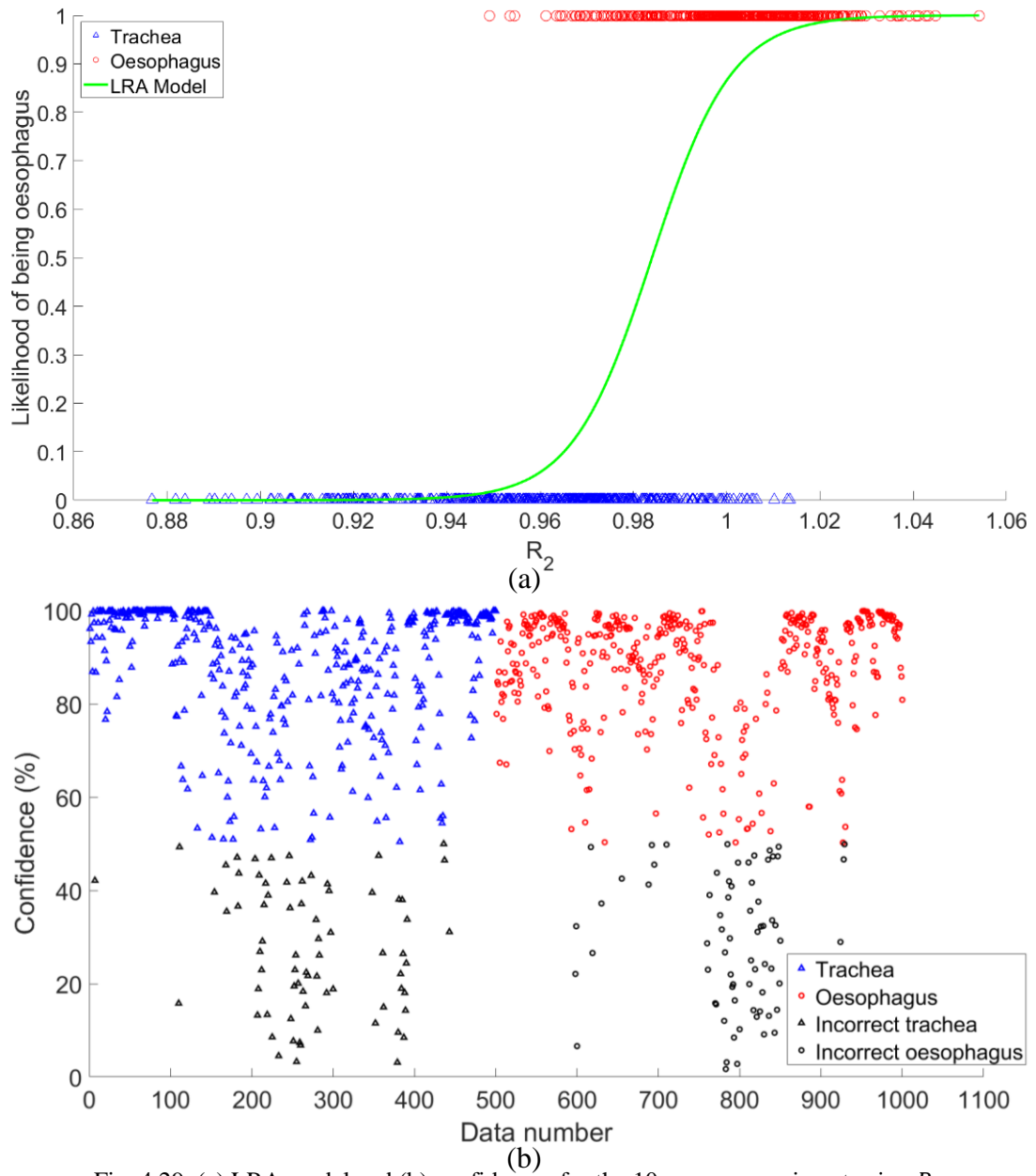


Fig. 4.29: (a) LRA model and (b) confidences for the 10-sensor experiment using  $R_2$ .

The  $R_2$  values processed with the LRA model (Fig. 4.29a) gave a sensitivity of 86.2% and a specificity of 85.6%. Overlapping values and a larger spread in the data cause higher confidence in the incorrect tissue identifications, as can be seen from Fig. 4.29b.

### 4.5.3 Support Vector Machine

A Support vector machine (SVM) is a popular type of supervised machine learning model [165,166]. It functions by forming a hyperplane which has its position and orientation influenced by data points close to the margins of the classes, known as the support vectors. Therefore, only the data points close to the boundary impact the hyperplane. Margins are then formed between the hyperplane and the support vectors. A process known as the ‘kernel trick’ allows for data to be more easily separated by forming the hyperplane in one higher dimension. The hyperplane is then projected onto the lower dimension plane and the margins are maximised.

An SVM was first applied to the 9-sample data. The data is well separated when combining the  $R_1$  and  $R_2$ , and a linear support vector machine could well separate the tissues. However, by implementing the kernel trick (increasing the number of dimensions and then projecting to the reduced dimensionality) and forming a quadratic hyperplane a more robust algorithm can be developed.

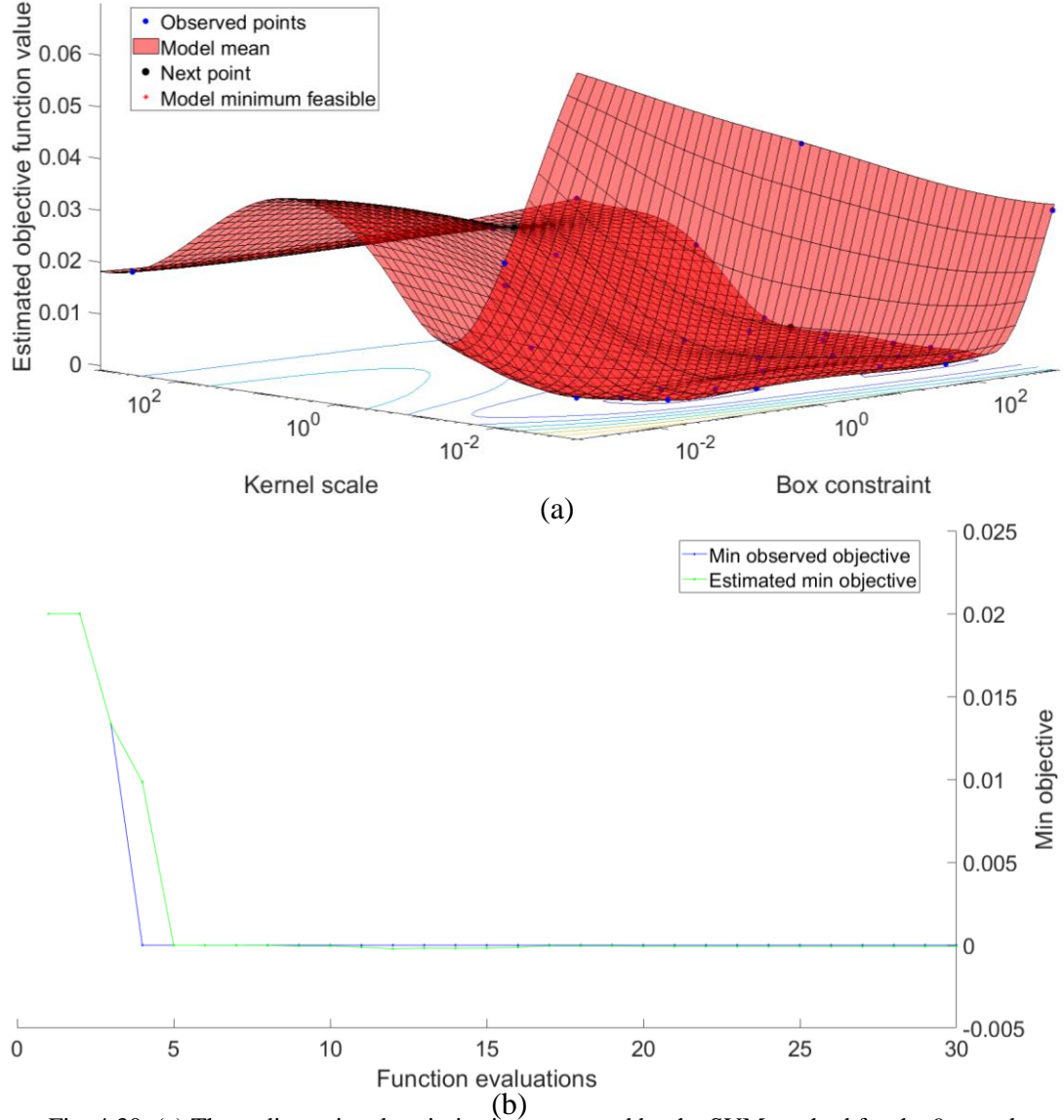


Fig. 4.30: (a) Three-dimensional optimisation generated by the SVM method for the 9-sample experiment. (b) The minimum of the objective function (hyperplane) with the number of function evaluations (iterations).

The boundary is formed over an iterative process and can be seen in Fig. 4.30a, where 30 function evaluations were chosen, although this could be increased for a larger more complicated data set, with the minimum of the objective function being  $\sim 0$  after the first 5 function evaluations (Fig. 4.30b). The kernel scale is a hyperparameter which determines the width of the kernel, where the kernel is used to transform the hyperplane to a lower dimension. The box constraint controls the penalty imposed on the data points violating the margins.

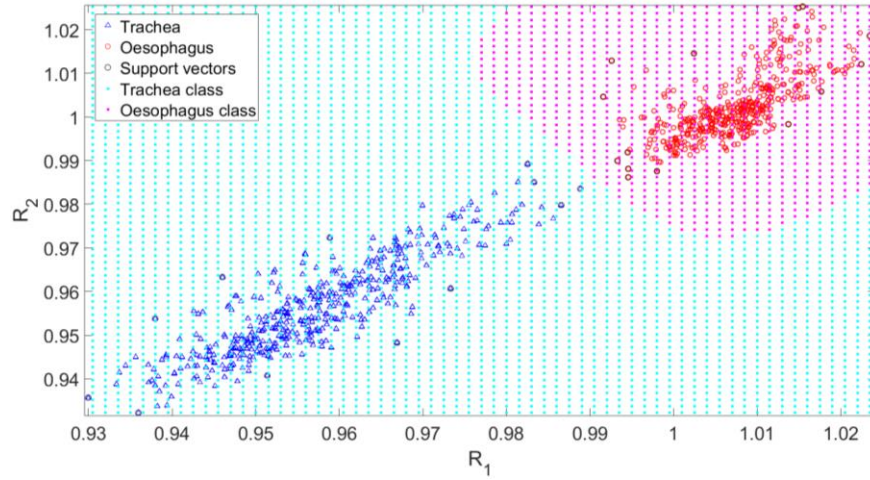


Fig. 4.31: SVM processed data from the 9-sample experiment. The support vectors are shown with a black circle.

The SVM model (Fig. 4.31) provides a perfect separation with 100% sensitivity and specificity. Using a quadratic SVM is unnecessary here as a straight line can also separate the tissues perfectly. However, the data from the 10-sensor experiment cannot be perfectly separated and provides a better test of the SVM model.

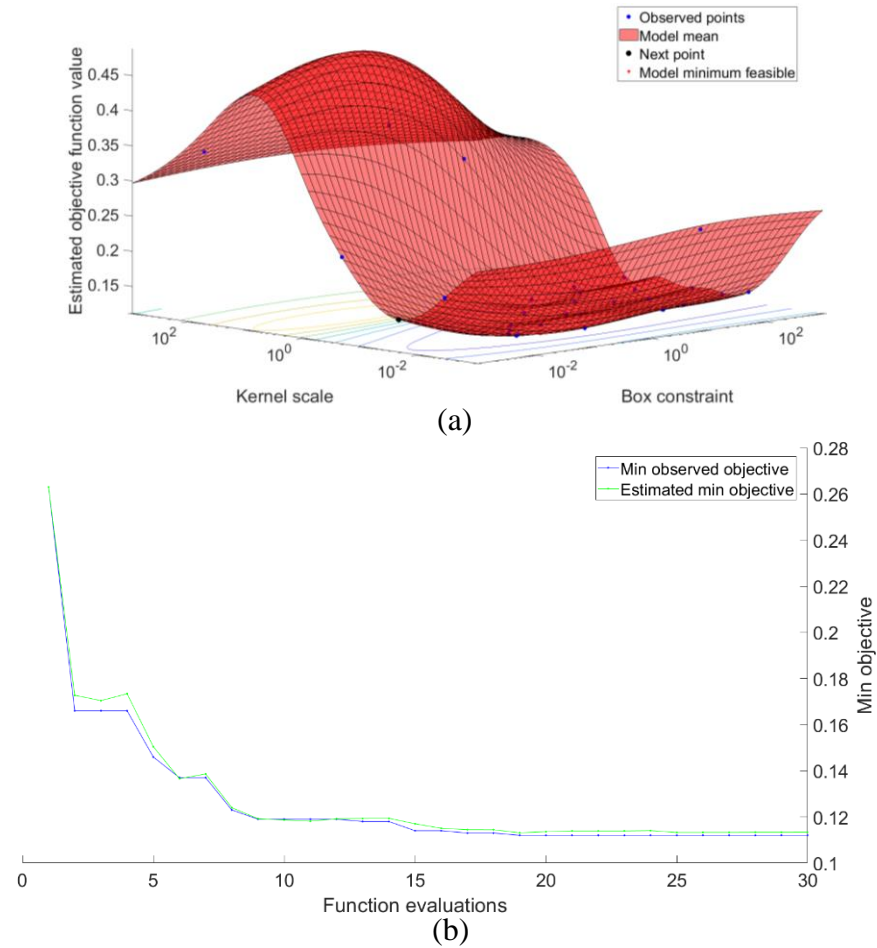


Fig. 4.32: (a) Three-dimensional optimisation generated by the SVM method for the 10-sensor experiment. (b) The minimum of the objective function (hyperplane) with the number of function evaluations (iterations).



The SVM was operated over 30 iterations and produced the structure seen in Fig. 4.32a. The minimum objective function stabilised at 16 iterations with a final minimum objective function value of 0.113 and was unable to perform a perfect separation.

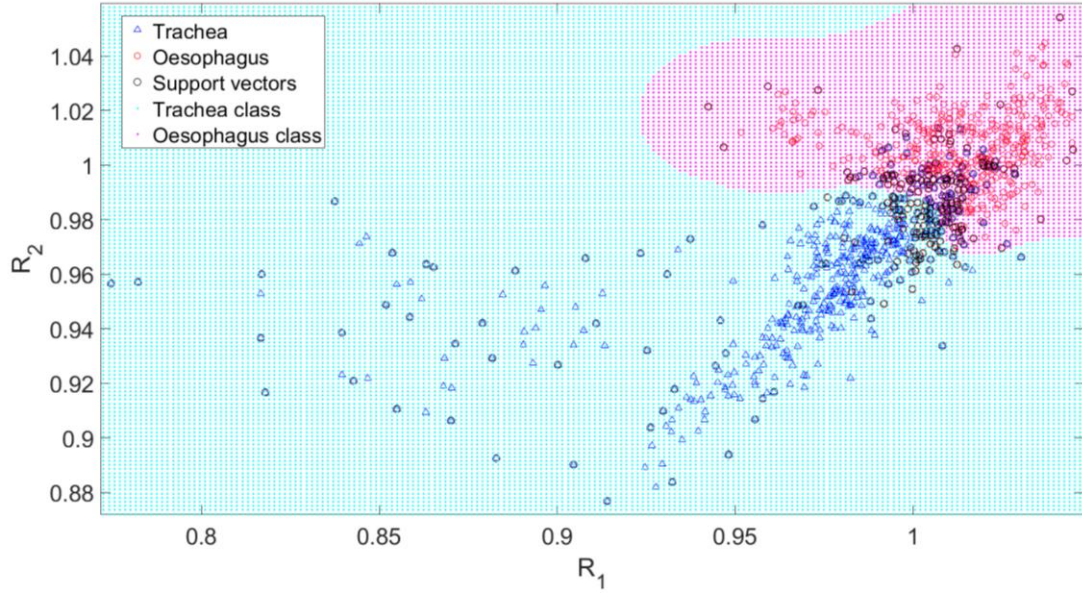


Fig. 4.33: SVM processed data from the 10-sensor experiment. The support vectors are shown with a black circle.

A boundary is formed around the oesophageal data in the SVM-processed 10-sensor experiment data (Fig. 4.33). This is typical of an SVM classification as the class that contains more variance surrounds the class with less variance. This classification algorithm gave a sensitivity of 91.2% and a specificity of 87.2%.

SVMs are a powerful classification method with a correct tissue identification of 100% for the 9-sample experiment and 89.2% for the 10-sensor experiment, although they are computationally demanding, taking several times longer to process than the other methods presented previously in this chapter for the 30 iterations. However, in practical application, the hyperplane is determined only once, and its projection into two dimensions (the boundary on Fig. 4.31 and Fig. 4.33) could be stored as an equation and used to classify an unknown measurement quickly, as could all methods that form a boundary. Furthermore, although not utilised here, the margins formed by the SVM can be used as confidence values given an appropriate threshold. A tight boundary around the oesophageal data forms a precise shape that is highly sensitive to the support vectors (data points closest to the boundaries). Therefore, SVMs are highly susceptible to overfitting, and given more data, the shape of the boundary could change and approach a linear approximation at the boundary.

#### 4.5.4 K-Nearest Neighbour

The K-nearest neighbour (KNN) algorithm [167,168] is another supervised machine learning algorithm. KNN has a simple concept, data is classified by the data around it. The distance between the test data point and all the training data points is calculated and then uses the most frequent label of its K-nearest neighbours to classify the query



data point, where  $K$  is the number of neighbours chosen. The Euclidian distance  $d(p, q)$  between two data points  $p = (x_1, y_1)$ , and  $q = (x_2, y_2)$  in two-dimensional space is given by Pythagoras theorem (Eq. (4.8)).

$$d(p, q) = \sqrt{(x_1 - x_2)^2 + (y_1 - y_2)^2} \quad (4.8)$$

The distances are calculated for all data points and then the query data point is assigned to the class with the largest number of its  $K$ -nearest neighbours. The KNN algorithm was applied to both the 9-sample data and the 10-sensor data.

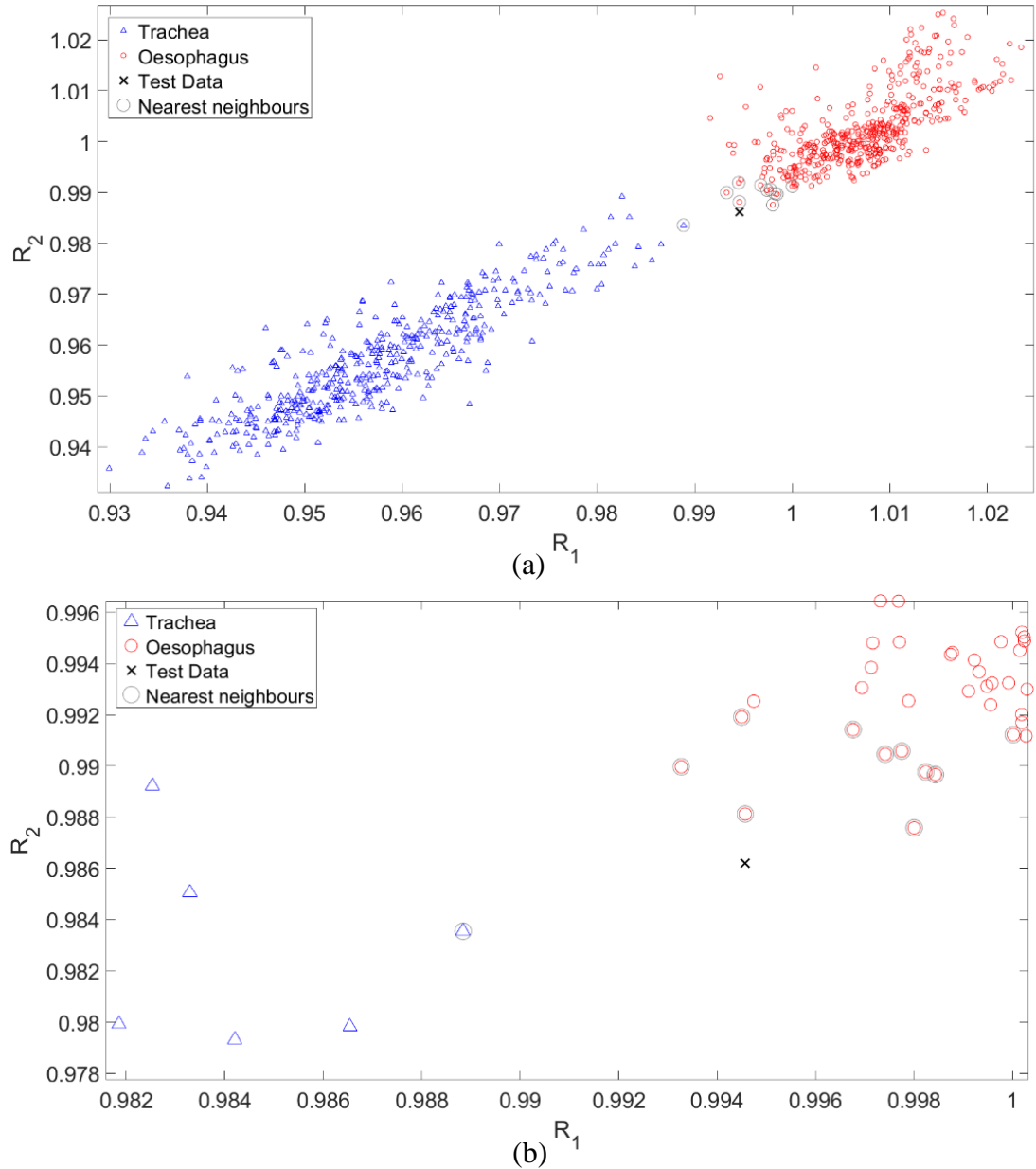


Fig. 4.34: 9-sample data classification confidences with the KNN algorithm. (a) Full range of data, and (b) data showing only the test data and its neighbours.

A random example of one of the data points used as the test data is shown in Fig. 4.34. A  $K$  value of 11 was used so that the algorithm uses the 11 nearest neighbours of the test data point to classify it. Using an odd number of neighbours avoids a test data

point having the same frequency of closest neighbours for both classes. For example, a K value of 10 may lead to 5 tracheal and 5 oesophageal neighbours and an unclear classification. Permutating through the data such that 1 data point is the test and the other 899 data points are the training gives 100% sensitivity and specificity for the 9-sample data. A confidence percentage on the classifications (Fig. 4.35) can be found by counting the number of neighbours used that belong to each class.

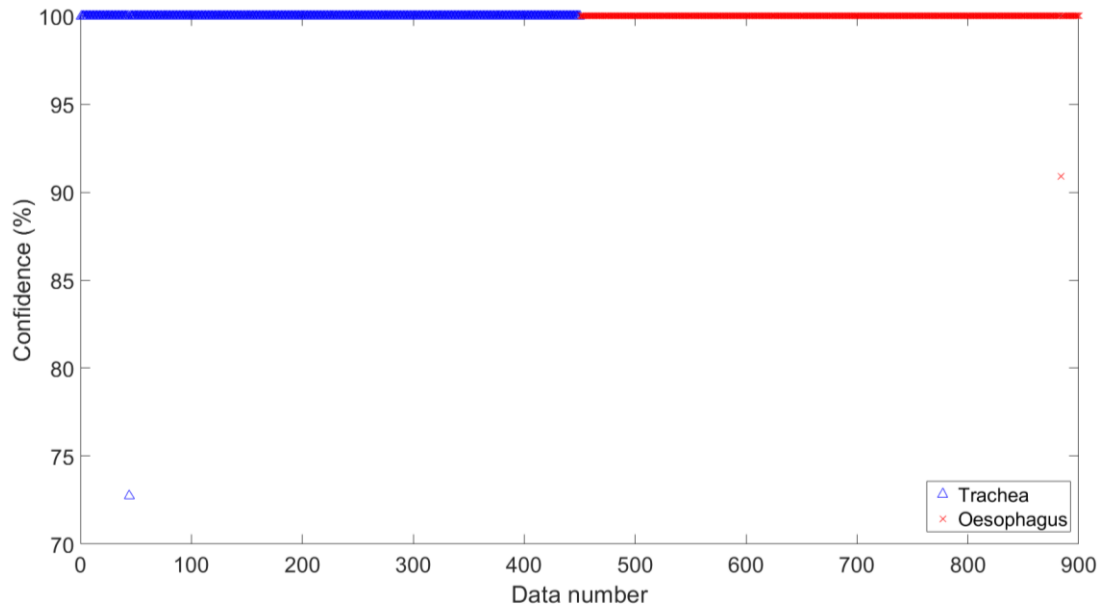


Fig. 4.35: 9-sample data classification confidences with the KNN algorithm.

All but two data points are classified with 100% confidence, meaning that they had all 11 of their neighbours as the correct class. One tracheal and one oesophageal data point didn't have 100% confidence, with 72.7 and 90.9%, respectively. Therefore, these two data points had 8 and 10 of their 11 closest neighbours as the correct tissue type, respectively.

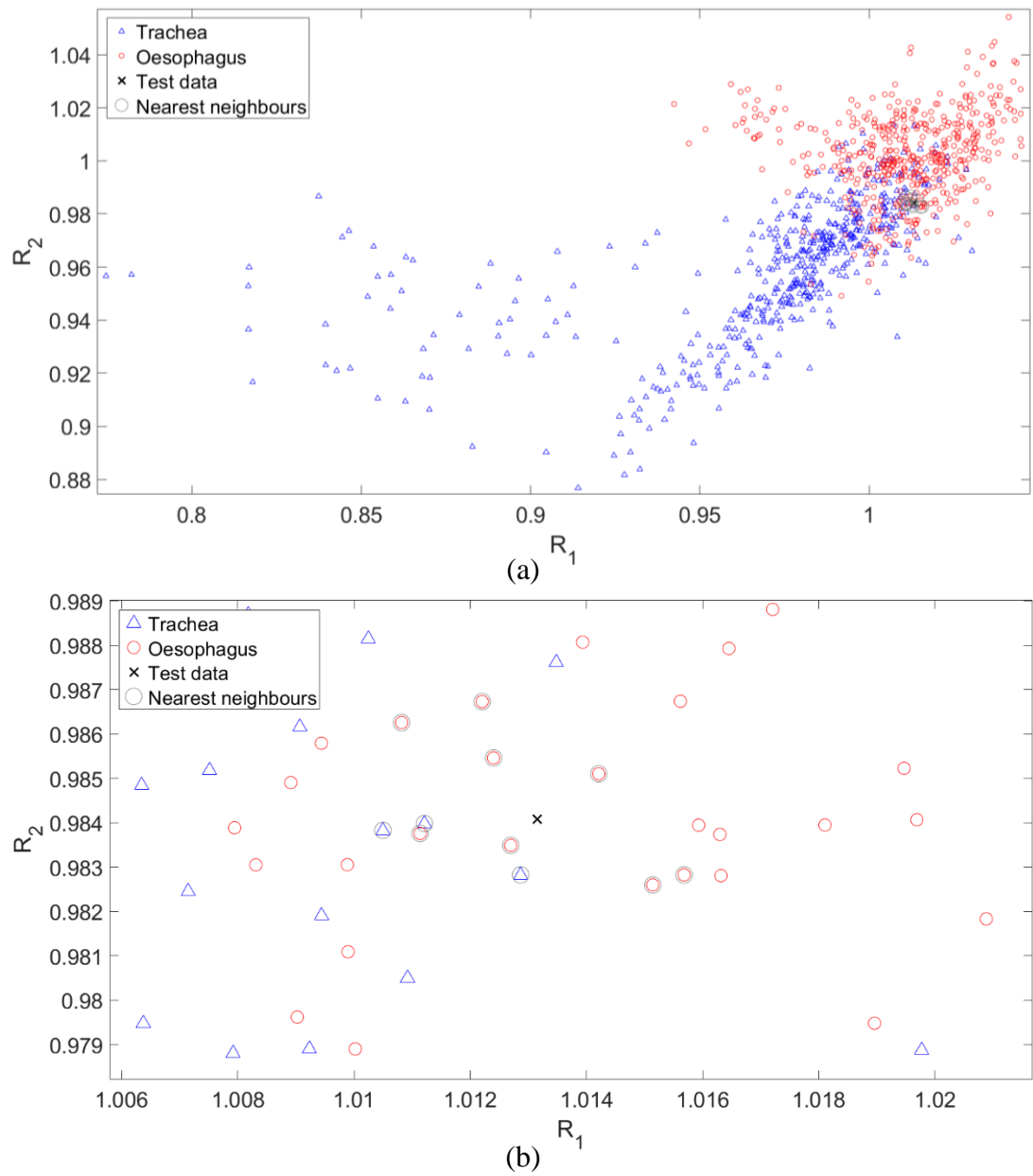


Fig. 4.36: 10-sensor data classification confidences with the KNN algorithm. (a) Full range of data, and (b) data showing only the test data and its neighbours.

The same algorithm was then applied to the 10-sensor data (Fig. 4.36), permutating through with one test and the rest training gives a sensitivity of 90.0% and a specificity of 85.4%.

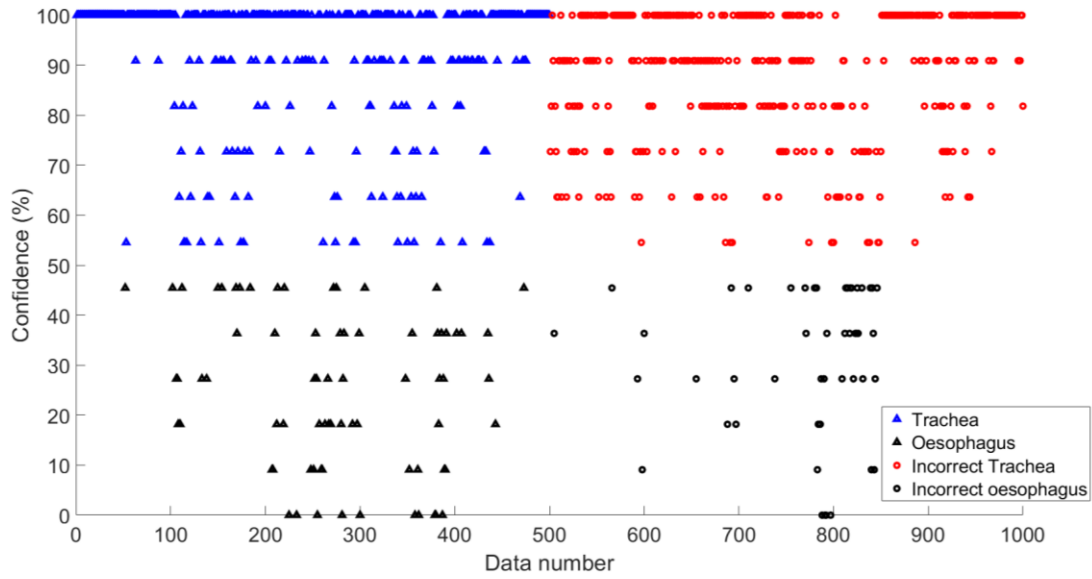


Fig. 4.37: 10-sensor data classification confidences with the KNN algorithm.

The confidence in the classifications (Fig. 4.37) was found from the percentage of the number of the test data's 11 closest neighbours, where a confidence below 50% gives an incorrect tissue identification. For example, a confidence on a tracheal measurement of 45.4% is incorrectly classified as oesophageal with a confidence of 54.6%, having 6 of its 11 closest neighbours as oesophageal.

The KNN algorithm provides another suitable option to classify the data, correctly identifying 100% of the tissues in the 9-sample experiment and 87.7% in the 10-sensor experiment. Furthermore, the number of nearest neighbours (K value) can be varied easily to optimize the algorithm. A small K value decreases the region around the test data point that the algorithm uses to classify it, giving it a low bias but a high variance, and the decision boundary is more irregular. A higher K value incorporates a larger region into the decision and is less affected by outliers, and therefore gives a more regular decision boundary. The number of neighbours was used to generate confidence in a classification. Incorporating the combined distance between a test data point and its nearest neighbours could increase decision-making accuracy. Therefore, if no close neighbours are available the test data could be labelled as an outlier. KNN is computationally demanding as every data point needs to be stored and then compared to the test data. Increasing the training database increases the computational power needed, whereas other methods form a boundary which needs only to be stored as an equation and updated once with more data.

## 4.6 Summary & Discussion

Several computational methods have been explored in this chapter and their performance with the two data sets from the 9-sample and the 10-sensor experiment (Section 4.1) was tested.

Table 4.2: Summary of the computational methods used to differentiate tracheal and oesophageal tissues from 9 *ex-vivo* porcine samples.

		Sensitivity (%)	Specificity (%)	Correct tissue identification (%)
<b>Spectral ratios</b>	$R_1$	100	100	<b>100</b>
	$R_2$	100	99.8	99.9
<b>PCA</b>		100	100	<b>100</b>
<b>Statistical measures</b>	<b>Mean</b>	100	100	<b>100</b>
	<b>Skewness</b>	76.9	74.9	75.9
	<b>Kurtosis</b>	93.9	74.9	84.4
<b>LDA</b>		100	100	<b>100</b>
<b>LRA</b>	$R_1$	100	99.8	99.9
	$R_2$	99.8	99.8	99.8
<b>SVM</b>		100	100	<b>100</b>
<b>KNN</b>		100	100	<b>100</b>

Table 4.3: Summary of the computational methods used to differentiate tracheal and oesophageal tissues using 10 sensors in 1 *ex-vivo* porcine sample.

		Sensitivity (%)	Specificity (%)	Correct tissue identification (%)
<b>Spectral ratios</b>	$R_1$	90.2	66.8	78.5
	$R_2$	87.6	82.2	84.9
<b>PCA</b>		90.4	83.6	87.0
<b>Statistical measures</b>	<b>Mean</b>	82.8	75.0	78.9
	<b>Skewness</b>	75.0	48.0	61.5
	<b>Kurtosis</b>	75.0	63.0	69.0
<b>LDA</b>		<b>92.0</b>	80.2	86.4
<b>LRA</b>	$R_1$	83.4	78.2	80.8
	$R_2$	86.2	85.6	85.9
<b>SVM</b>		91.2	<b>87.2</b>	<b>89.2</b>
<b>KNN</b>		90.0	85.4	87.7

In Table 4.2 and Table 4.3, sensitivity refers to the percentage of correct oesophageal identifications and specificity refers to the number of correct tracheal identifications. The spectral ratios  $R_1$ , PCA, statistical measure: mean, LDA, SVM, and KNN method all gave 100% correct tissue classification for the 9-sample experiment, with all other methods except skewness and kurtosis giving a minimum of 99.8%. A strong classification for this data is expected in all classifiers due to the high separability, with skewness and kurtosis proving to not be good indicators of tissue type. The best-performing classifier in the 10-sensor experiment was the SVM method with a correct tissue identification of 89.2%, followed by KNN, PCA, spectral ratio  $R_2$  and LRA  $R_2$ , all with above 85.9%. Using only the ratio values,  $R_2$  performs better in the 10-sensor experiment where the tissues are less separable, with a similar performance as  $R_1$  in the 9-sample experiment. Reducing the required wavelengths reduces the need for wider spectral measurements. Therefore, if only one ratio is used it should be  $R_2$ . However, by utilizing both ratios a more accurate tissue identification can be achieved by up to 4.3%.

SVM gives the highest correct tissue identification. However, it is highly susceptible to changes in the extremes of the test data and therefore performs poorly in data sets with outliers and more noise. There is also no confidence value implemented with this method, although one could be designed from the distance to the hyperplane. SVMs excel with higher dimension problems such as image recognition where an array of size  $w \times h \times c$  is commonly used for images and text recognition where  $w$  is the width,  $h$  is the height of the image and  $c$  is the RGB channel values, forming a large multidimensional array for many images. Since only two dimensions  $R_1 \times R_2$  are used for oesophageal identification a simpler linear boundary such as that of LDA yields similar results.

KNN performs well, correctly classifying 87.7% of the tissues. However, the distance between every data point and the test needs to be computed for each identification which may lead to a slow response. LRA using the  $R_2$  values gave a correct tissue identification of 85.9%. Combining the  $R_1$  and  $R_2$  values may provide a stronger identification. Using multiple variables in LRA is a method known as multiple logistic regression analysis (MLRA) and involves the formation of a three-dimensional surface from the variables and the likelihood, in our case,  $R_1$ ,  $R_2$ , and the likelihood of being oesophagus. However, MLRA was not analysed as it is generally reserved for regression analysis of large multivariate data sets and was not likely to yield better results than the other better-suited classifiers. LDA forms a linear boundary between the groups that maximises the variance between classes and achieved the fourth-best tissue classification percentage, although it is relatively easy to implement and update as required. This method is expected to improve as more data is acquired and the boundary between the classes becomes more linearly separable.

PCA is useful in initially characterizing the tracheal and oesophageal tissues, allowing the variation between the spectra to be highlighted. PCA also gave the third highest correct tissue identifications, although the full characteristic wavelength range between 530 and 590 nm was used. Furthermore, the method of comparing the first and second principal components still requires the use of an appropriate classifier to generate a decision boundary or to classify the data by other means, where a boundary



was formed through trial and error to maximise the number of correct tissue identifications. Therefore, the use of PCA over the characteristic range used in conjunction with a classifier may yield a higher percentage of correct tissue identifications. However, PCA can still be utilised to distinguish the two tissue types, with the possibility of wavelength ranges not explored by the USAISR helping to identify the tissue. Furthermore, a smart ETT could provide more physiological measurements, as discussed later in Chapter 5. These physiological measurements could be used as more variables to distinguish the trachea and oesophagus, whereas PCA could reduce the dimensionality of this matrix of variables into a smaller number of more interpretable ones.

In summation, using only two wavelengths in the form of the ratio values  $R_2$ , a correct tissue identification of 99.9% can be achieved using the same sensor across multiple *ex-vivo* porcine trachea and oesophagi and a correct tissue identification of 84.9% if multiple sensors are used on a single *ex-vivo* porcine sample. By utilizing three wavelengths in the form of the ratio values  $R_1$  and  $R_2$  this can be increased to 100% across multiple samples and 89.2% across multiple sensors. However, the SVM method and KNN are both highly dependent on the extreme values in the data set, and a simple linear boundary formed by LDA may be more appealing in practice as the amount of training data is increased. Furthermore, the lower percentage of tissue classifications in the 10-sensor experiment demonstrates that there is variability between the sensors that is not entirely accounted for by the light and dark referencing. Therefore, a more consistent sensor with less batch-to-batch variability may improve performance, or a method for calibrating each sensor in a ‘phantom trachea’ may be required. However, the sensor design was changed between the two experiments and could also explain the less separable data in the 10-sensor experiment. In the 10-sensor experiment, a sensor with a separation of 0.875 mm between the detection and illumination fibres was used. This produces a more compact sensor, although the penetration depth of the light is reduced and may contribute to the reduced classification rates. However, the two tissues are distinguishable using the developed classifiers, in both experiments.

## Chapter 5 iTraXS & The Animal Studies

### 5.1 Introduction

This chapter's focus is to describe and analyse data from two animal studies. This first animal study was conducted before this author started their PhD research and hence it was with this author's role to analyse the data obtained. This analysis subsequently led to a publication [178] for the author. The sensors were limited to detecting only perfusion and cuff-trachea contact pressure information. The main findings and knowledge gained are described in Section 5.3.3, as this informed the design of the ETT placement sensor. However, firstly, a brief description of iTraXS is provided so that context can be given to some of the findings and developments of the sensors. In the second study, the integrated sensors could detect ETT placement and contact pressure, along with physiological parameters such as heart rate and oxygen saturation. The protocol was also expanded to include capillary refill time (CRT) measurements and more systematic cuff inflation cycles. However, that section describes only the ETT placement aspect of the second animal study, as that is relevant to this research project.

Both studies were formed from a collaboration between the School of Veterinary Medicine and Science, the Faculty of Engineering at the University of Nottingham, and the Sutton Bonington campus. The first study's ethical approval was under Home Office license PPL 40-3410 and was provided by the University of Nottingham. Funding for this research was provided by the National Institute for Health Research (II-LA-0813-20008) and the Medical Research Council (MR/T025638/1). The second study was funded by the NIHR i4i programme – grant number RA45S9 and contained three porcine subjects with a refined iTraXS device.

### 5.2 iTraXS

iTraXS (intra-tracheal multiplexed sensing) represents an ETT with integrated optical fibre sensors to make measurements in the trachea. Literature relating to the device has been published in recent years by the Nottingham group. A 2018 journal article, by Sinha, R. *et al.* [169], provides a histological assessment by two veterinary pathologists of the removed tracheas from the “first animal study” (Section 5.3.3). All six porcine trachea presented more histopathological damage than previously described with a cuff pressure maintained at 25-45 cmH<sub>2</sub>O.

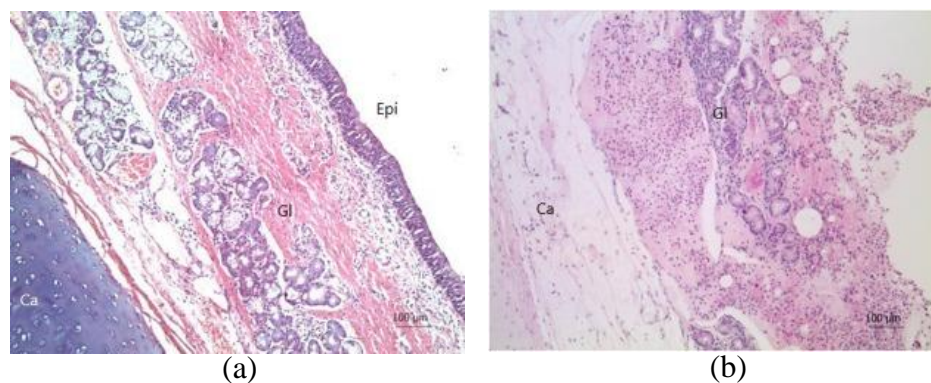


Fig. 5.1: Tracheal section from Sinha *et al.* shows an (a) unintubated, and (b) intubated, porcine subject. Gl = submucosal glands; Ep = epithelium; Ca = cartilage [169].

The intubated tracheal mucosa (Fig. 5.1) presented diffuse ulceration, a greater number of neutrophils, and pale oedema when compared to the unintubated tracheal section. These factors indicate damage to the trachea caused by intubation. Therefore, a sensor that could detect contact pressure and perfusion in the trachea may mitigate these effects. These parameters could indicate to the clinician that the cuff pressure is too high and blood flow is being restricted, or that the cuff pressure is too low and there are folds in the cuff and an improper seal.

In a 2018 journal article, Liu, C. *et al.* [170], developed a relatively small optical fibre pulse oximeter with combined contact force detection (Fig. 5.2). This was developed as it has been documented that SpO<sub>2</sub> measurements can be affected by contact force [171]. The sensor contained 45° cleaved fibres to couple light out of the face of the sensor.

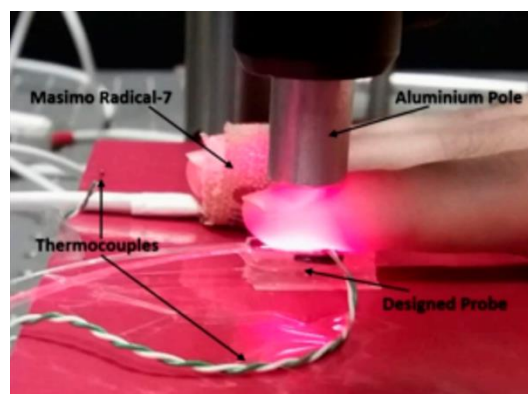


Fig. 5.2: Epoxy sensor from Liu *et al.* [170], containing POFS to detect a PPG and an FBG silica fibre to measure contact force.

The sensor (Fig. 5.2) was reported to have a high correlation with a commercial SpO<sub>2</sub> and pressure reference device. A fibre optic sensor with combined PPG measurements and pressure detection that is integrated into the cuff of an ETT could better inform clinicians of the condition of the ETT cuff in the trachea. However, the sensor is too large ( $20 \times 10 \times 2 \text{ mm}$ ) for integration into the cuff of an ETT and would impact its primary function. The pressure sensitivity of 0.1446pm/kPa (0.01418 pm/cmH<sub>2</sub>O) is also too low for use with the 20-30 cmH<sub>2</sub>O of pressure typically seen in an ETT cuff.

A summary of the main findings and developments of the iTraXS device is described in this section. The iTraXS device contains POFS capable of determining core physiological parameters measured in the trachea. A single POFS sensor can attain HR, blood flow, and oxygen saturation, as well as determining oesophageal intubation, which is the focus of the research described here. A second sensor can make contact pressure measurements between the ETT cuff and the tracheal wall.

## 5.3 First Animal Study

### 5.3.1 Perfusion Sensor

PPG measurements can be made using the same sensor as for ETT placement (Fig. 5.3) as it was designed with two illumination fibres, which allow connection to two LEDs (one for visible and one for IR light). A detailed description of pulse oximetry

is described in Section 1.3.3. For pulse oximetry, typically red at 660 nm and IR light at 940 nm wavelengths are used, as they are on either side of an isosbestic point of OHb and Hb and absorb these wavelengths differently. A single LED requires only one illumination fibre, although it would have to produce light in the red and IR wavelength region for pulse oximetry, as well as the 530 – 590 nm wavelength region for ETT placement detection. A suitable, cost-effective light source solution could not be found for both of these wavelengths. Red and IR light is used specifically as the body scatters and absorbs these wavelengths significantly [172]. However, recently, the use of other wavelengths (such as green and orange light) has indicated success, with the possibility of reducing the impact of movement artefacts [173], which may be used in future iTraXS designs to reduce the size of the sensor and the number of LEDs required.

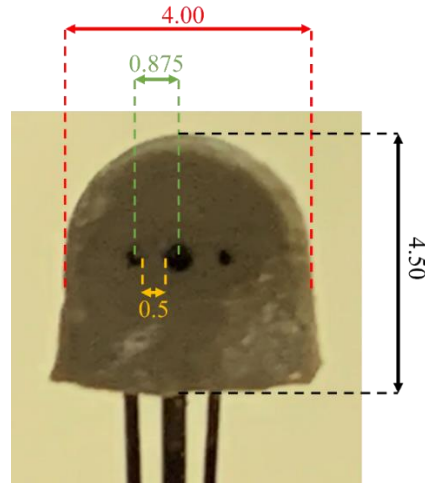


Fig. 5.3: Sensor used for ETT placement detection and PPG measurements. Units are in mm

### 5.3.2 Contact Pressure Sensor

The ETT cuff pressure is important to control during intubation as a cuff pressure that is too high can lead to tracheal stenosis [174,175], and a cuff pressure that is too low can lead to insufficient ventilation and ventilator-associated pneumonia (VAP) [176,177]. Guideline intracuff inflation pressure is between 20 and 30 cmH<sub>2</sub>O, although this is usually up to the clinician's discretion. Therefore, by using contact pressure sensors integrated into the cuff of an ETT, the pressure exerted on the tracheal wall by the cuff can be measured and a seal can be formed without damaging the trachea. A fibre Bragg grating (FBG) is a sensitive fibre optic strain gauge formed by laser-inscribing a fibre with a periodic variation of refractive index. At each grating plane, a small amount of light transmitted down the fibre reflects at each change in refractive index due to the Fresnel effect. The result is a narrow bandwidth of light being reflected. The wavelength ( $\gamma_{Bragg}$ ) is determined by the refractive index of the fibre ( $n$ ) and the period of the grating ( $\Delta$ ), given by Eq. (5.1).

$$\gamma_{Bragg} = 2n\Delta \quad (5.1)$$

The Bragg wavelength changes as a function of the grating period, where a strain imposed on the fibre ( $S$ ) and expansion of the fibre due to temperature ( $T$ ) causes a

change in the wavelength. Therefore, the change in Bragg wavelength ( $\frac{\Delta\gamma_{Bragg}}{\gamma_{Bragg}}$ ) can be defined as Eq. (5.2)

$$\frac{\Delta\gamma_{Bragg}}{\gamma_{Bragg}} = (1 - p_e)S + [(1 - p_e)\alpha + \zeta]\Delta T \quad (5.2)$$

Where  $p_e$  is the photoelastic constant,  $\alpha$  is the thermal expansion coefficient, and  $\zeta$  is the thermo-optic coefficient.

For the fibre to be used as a pressure sensor the transverse force (F) must be transduced into axial strain. This can be achieved by encasing the fibre in an epoxy whose deformation causes the fibre to be pulled from either side of the FBG. Therefore, when a pressure is applied, the grating period increases due to frictional forces between the fibre and the epoxy (Fig. 5.4). A second FBG inscribed closer to the distal end of the fibre is not embedded in epoxy and left to compensate for temperature induced changes.

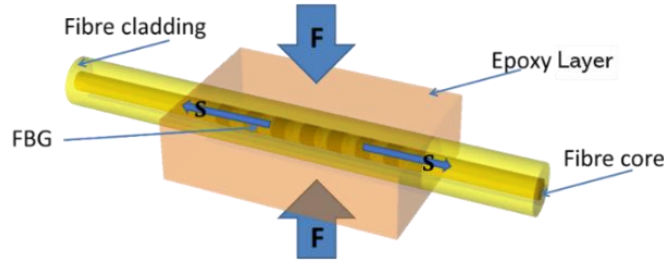


Fig. 5.4: Fibre Bragg grating (FBG) encased in a pressure transducing epoxy layer. A transverse force (F) is transduced into axial strain (S) [178].

### 5.3.3 First Animal Study

An earlier design of iTraXS contained a perfusion sensor, which was formed of two POFs cleaved at 45° and embedded in an epoxy layer (Section 3.2). A single green LED was used for heart rate (HR) and perfusion (the pulsatile component of the photoplethysmogram over the non-pulsatile) measurements. Therefore, oxygen saturation and ETT placement measurements could not be made. The ETT also contained a silica optical fibre with two FBGs to make contact pressure measurements. One FBG was embedded in an epoxy layer and the other fibre was designed to control for temperature. The sensors were embedded between the cuffs of a double-cuff ETT (Section 3.5). This design was used in an animal study of 6 porcine subjects and produced valuable measurements and information on the strengths and weaknesses of this approach. The research resulted in a journal article written by this author and others, Correia, R., Gadsby, B., *et al.* [178]. A summary of the main findings of this journal article is provided here.

A high-volume, low-pressure (HVLP) Mallinckrodt ETT (Covidien, model 107-80) was used (Fig. 5.5b). The ETT was modified with a dual cuff as described in Section 3.5 so that the sensors were positioned between the inner and outer cuffs. The sensors were placed on the inside (Magill) curve of the ETT. The opto-electronic units are described in Fig. 5.5. The FBG contact pressure sensor was connected to a fibre optic

interrogator (smart fibres, model SmartScan), with a scanning frequency of 2.5 kHz per channel which operated over a wavelength range of 1528-1568 nm. The resolution was 16 pm with a repeatability of < 1 pm. The interrogator was connected to a computer via a USB port which stored the pressure data (laptop running windows 7). The illumination fibre of the perfusion sensor was connected to an LED (Fiber-Coupled LED, Thorlabs, model M530F1), emitting a central wavelength of 530 nm (green light). The LED driver (T-Cube LED Driver, Thorlabs, model LEDD1B) delivered a current of 1000 mA to the LED. The detection fibre was connected to a photodetector with an integral trans-impedance amplifier (Thorlabs, model PDA36A-EC) set to a gain of 60 dB. All connections were a SubMiniature version (SMA) 905. A data acquisition card (National Instruments, model USB-6361) was used to acquire the output of the photodetector via connection to the analogue-to-digital converter (ADC) channel. The sampling frequency was 5 kHz with a 5 Hz anti-aliasing filter and had 16-bit resolution.

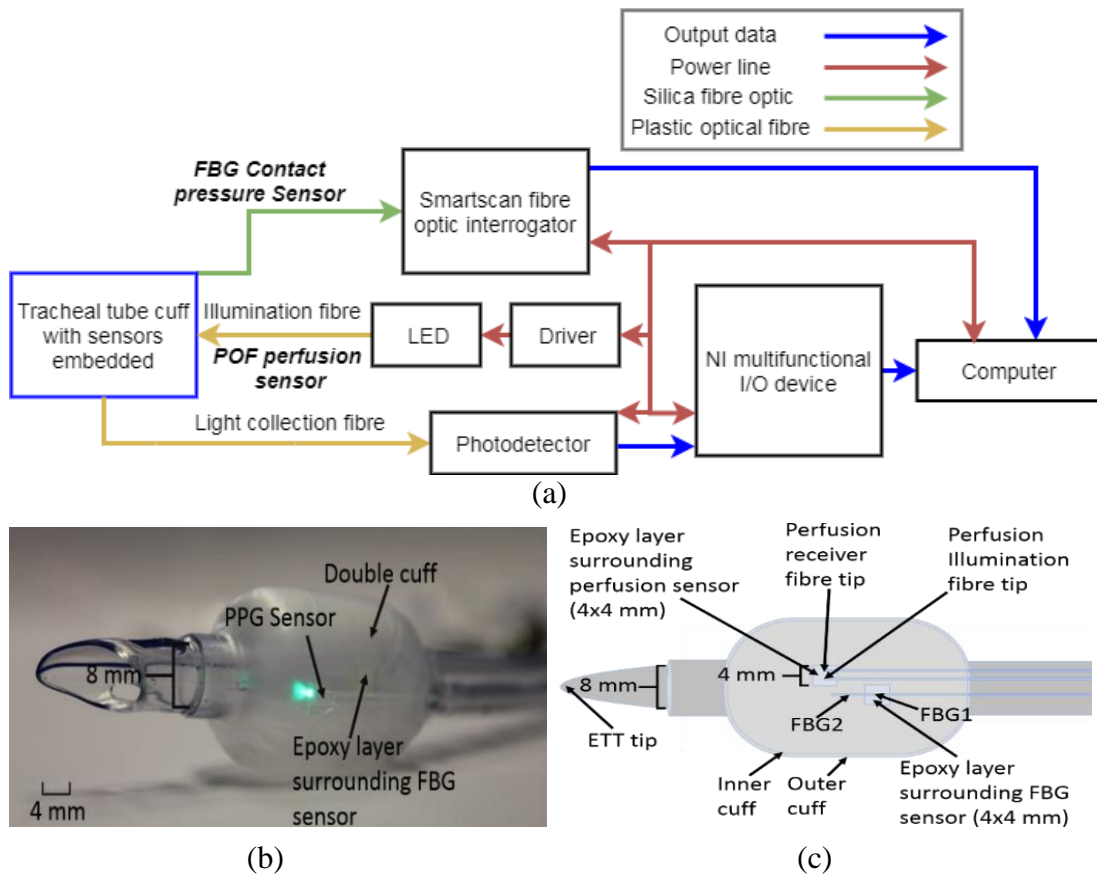


Fig. 5.5: iTraXS design. (a) Opto-electronic design block diagram (FBG – fibre Bragg grating, NI – National Instruments, POF – plastic optical fibre, LED – light emitting diode.) (b) Photograph of the ETT with a sensor integrated into the cuff. (c) Schematic (fibres in blue are between the inner and outer cuff) [178].

The animal study consisted of 6 porcine subjects, that had ages between 10-12 weeks and a mean weight of 60.6 kg (Canberra 12 mixed breed; Landrace/Large White/Duroc). The subjects were sedated and then placed under general anaesthesia. The subjects were intubated with the iTraXS tubes and ventilated with a veterinary anaesthesia ventilator (Matrx 3000, Midmark). Tidal ventilation began in the 10 to 12 ml/kg range and ETCO<sub>2</sub> was maintained at 6 to 8 kPa. The FBGs for subjects 5 and 6



were damaged during intubation and no contact pressure measurements could be obtained as the subjects could not be reintubated with a spare tube as this would contradict the animal licence. The damage to the fibres is discussed in Section 5.3.4.

The protocol consisted of varying the intracuff pressure as measured by a manometer, for different rotational orientations of the sensor in the trachea (Fig. 5.6). The sampling rates were; manometer - 1s; contact pressure - 0.4 ms; and perfusion sensor - 0.2 ms. Initially, the ETT was orientated so that the sensors were facing towards the posterior of the trachea and then the cuff was inflated. Data was acquired in that quadrant of the trachea and then the ETT's cuff was deflated and then the whole ETT was rotated by  $90^\circ$  to the next quadrant. Therefore, the sensors were positioned towards the posterior, left lateral, right later, and anterior, respectively. For each rotation, the cuff was inflated to an intracuff pressure between 20 and 80 cmH<sub>2</sub>O.

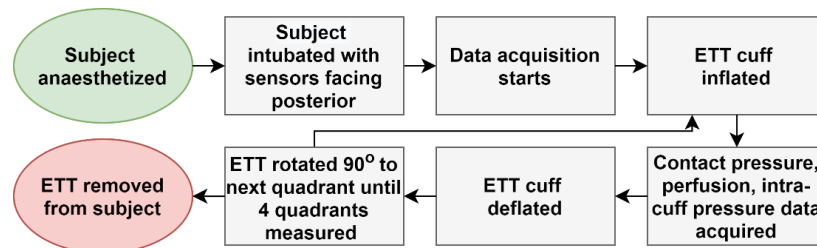


Fig. 5.6: Flow chart of the experimental protocol [178].

An example of one of the inflations, when the sensor was at the posterior of the trachea, is shown in Fig. 5.7. The ventilator response is present in the contact pressure forming low-frequency oscillations of approximately 4s (approximately between points 6 and 7 on Fig. 5.7). At point 3 a slight decrease in manometer pressure is observed due to relaxation of the ETT cuff in the trachea. Point 5 is an apparent ballistocardiograph response which is approximately the same frequency as the HR ( $\sim 1.6$  Hz, 96 BPM), as measured by the perfusion sensor. Point 8 is the peak inspiratory pressure, which is typically at the maximum of the ventilator inhalation. Interestingly, this likely means the ventilator produces a positive pressure just before exhalation.

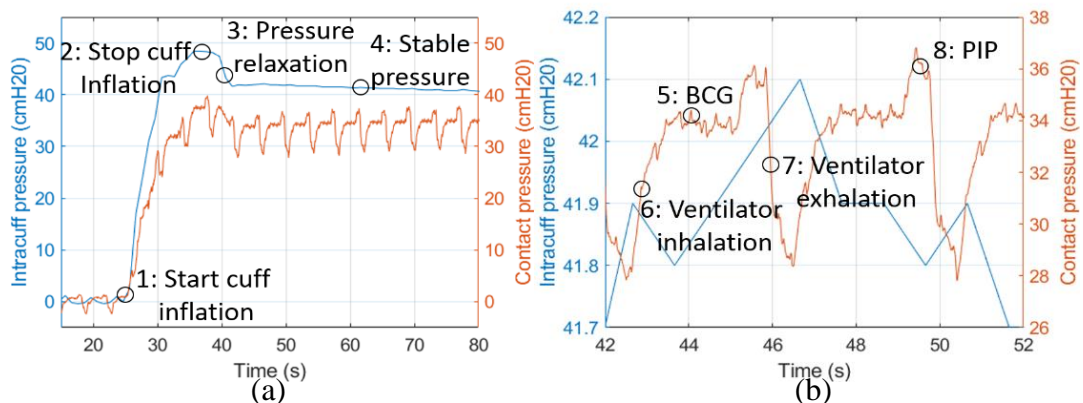


Fig. 5.7: Intracuff pressure (blue) versus cuff-trachea contact pressure (red) for subject 1, sensors are at the posterior of the trachea. (a) The initial inflation and resulting pressures. (b) A 10s section after the cuff was fully inflated. 5: BCG refers to a ballistocardiograph response. 8: PIP refers to the peak inspiratory pressure [178].

The experimental data was used to calculate the sensitivity of the contact pressure sensor. Therefore, the gradient of a linear model between the two pressures (Fig. 5.8) predicts a relationship of  $1 \pm 0.1$ , with an R-squared of 93%. Indicating a high statistical consistency between the measured intracuff pressure and the cuff-trachea contact pressure.

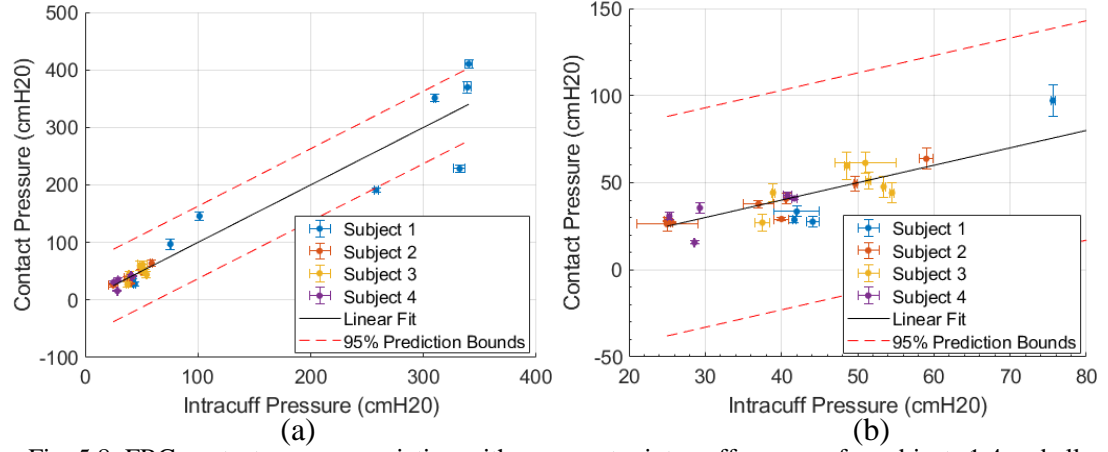


Fig. 5.8: FBG contact pressure variation with manometer intracuff pressure for subjects 1:4 and all tracheal quadrants. (a) Full pressure range. (b) Lower contact pressure region of 20 to 80 cmH2O.

A clear PPG can be seen throughout the perfusion data (Fig. 5.9a). The ventilator response can also be seen in the perfusion data, along with the pulsatile signal originating from blood flow. Removal of the ventilator signal was achieved by filtering the perfusion data with a high-pass filter, resulting in Fig. 5.9b. Fourier analysis performed on the unfiltered perfusion data further highlights the pulsatile signal (1.6 Hz) and the ventilator signal (0.15 to 0.47 Hz).

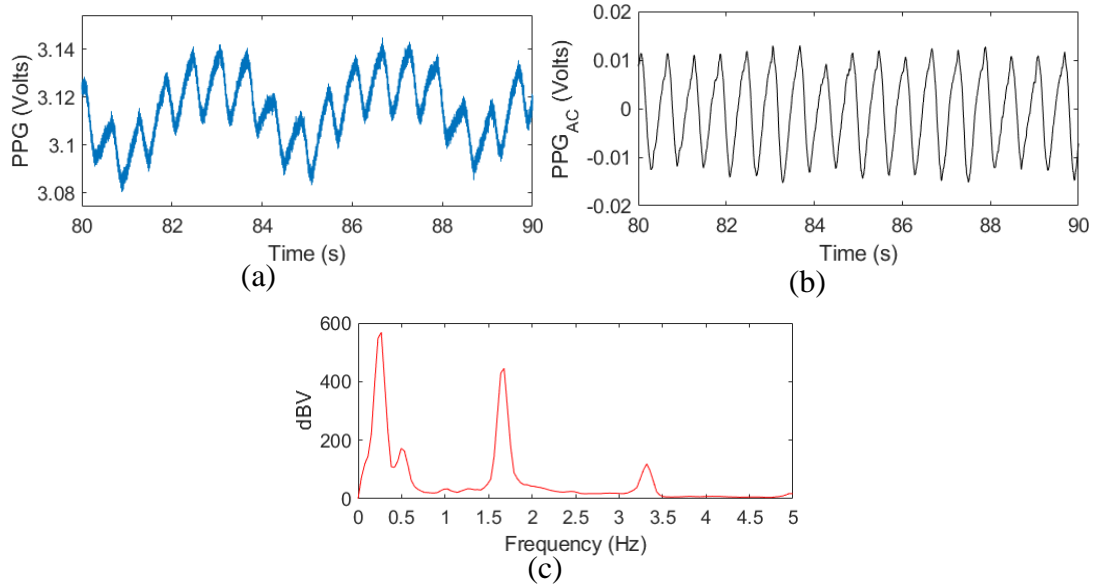


Fig. 5.9: Example of a PPG signal from tracheal mucosa. (a) Unfiltered PPG signal. (b) PPG signal with low-frequency content removed. (c) A Fourier spectrum of the unfiltered PPG signal [178].

### 5.3.4 Discussion

A full description of this animal study is found in [178], with only a summary presented here to highlight the benefits and limitations of the described fibre optic ETT design. Perfusion measurements could be reliably obtained at the trachea using

the iTraXS device (Fig. 5.9) when the sensors are positioned in the cuff. This is further evidence of the benefits of positioning the sensors in the cuff. However, without multiple LEDs or a single broadband LED providing light from the required wavelengths, oxygen saturation and ETT placement measurements were impossible. Therefore, later designs would need to incorporate this. In this study, two of the FBGs were damaged during intubation. Inscribing FBGs onto optical fibres using a UV laser can weaken them. In future, recoating the fibres can help to strengthen them so that breakages can be avoided. The anterior of the trachea provided weakly correlated intracuff pressure and contact pressure results. This is potentially caused by the asymmetrical shape of the trachea so that the sensors were not in good contact with the trachea at the anterior. Therefore, this is not likely to be a good position for the sensors. To obtain measurements from multiple orientations in the trachea the ETT was rotated throughout the experiments. This would not be possible during clinical use of the ETT, and at times it was difficult to determine the orientation of the sensors during the study. Multiple sensors in a single cuff positioned so they are facing the posterior (muscle at back), left and right lateral (cartilage at sides) provides the most reliable measurements. The animal study occasionally produced weak PPG and perfusion measurements, although a rotation to another side always improved these. However, this is unnecessary for ETT placement measurements alone as no significant difference has been found between tissue identification measurements in the trachea on the cartilage and muscle in *ex-vivo* porcine samples measured here. No difference was also found in *in-vivo* measurements in literature [87-89]. However, more sensors benefit ETT placement measurements with more information being provided.

Furthermore, variations in perfusion and contact pressure measurements at different orientations indicated that an ETT with multiple sensors of each kind is beneficial. There was a large amount of direct coupling between the fibre tips as well as some of the ambient light from the room, which increased the DC light level and suppresses the AC component of PPG. A sensor design that reduced these effects would produce a higher SNR. Furthermore, cleaving the fibres at 45° may not be the optimal method for emitting light out of the sensor face, with an alternative method of bending the fibres being preferable.

The opportunity to unravel this data from the first animal study has provided this PhD research with an important foundation for the design and testing of an improved smart ETT presented in the following chapter.

## 5.4 Second Animal Study

The sensor design used for the second animal study was a ‘combined sensor’ which combines the ETT placement sensor fabricated using a metal mould (Fig. 3.32) and a contact pressure sensor. However, the functional part of the sensor for ETT placement (Fig. 5.10) is the same design as described previously (Section 3.5). A non-transparent temperature curable epoxy (two-part epoxy, Permabond, model ET5143) was used to form the epoxy layer and the PMMA fibres were coated in a black pigment as described in Section 3.6.2. The separation between the detection and illumination fibres was 0.875 mm from centre to centre.

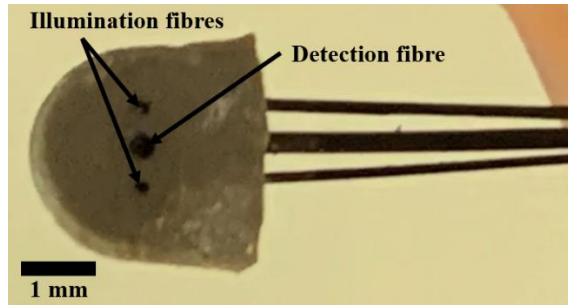
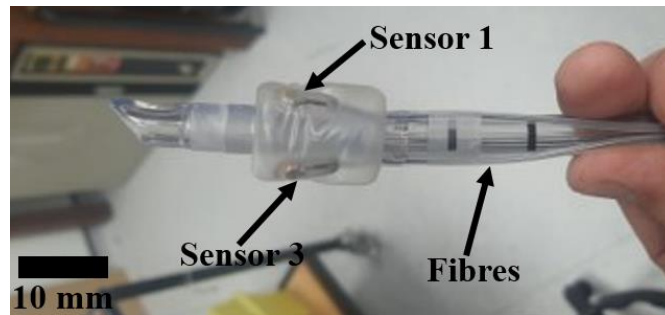
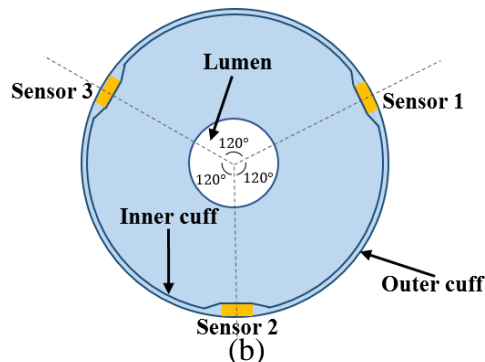


Fig. 5.10: ETT placement sensor used in the animal study.

Three sensors were placed at  $120^\circ$  intervals from each other (Fig. 5.11b) in the cuff (Fig. 5.11a) of each ETT. Three sensors were used to make measurements at three different orientations in the trachea. Measurements from multiple orientations give information about the contact pressure and perfusion of the trachea at different locations without having to rotate the ETT. However, although not essential, it's beneficial to have more measurements for ETT placement detection. The sensors were integrated between the cuffs of a double cuff size 8 Mallinckrodt ETT (Covidien, model 107-80) as described in Section 3.5. Sensor 1 was positioned on the outside curve of the ETT, with sensors 2 and 3 positioned clockwise around the cuff (Fig. 5.11). A detailed description of the orientation of each sensor in the trachea is given at the start of the analysis of each subject. The sensors were adhered to the inner cuff using two drops of transparent UV curable epoxy (Panacol, model Vitalit 1655). The same epoxy was used to attach the outer cuff to the inner cuff at its top and bottom. The fibres ran between the two cuffs and down the outside lumen of the ETT. A small plastic tube was placed around the fibres from each sensor that ran out of the cuff to provide durability to the fibres not in the cuff.



(a)



(b)

Fig. 5.11: (a) Photograph of the sensors integrated between the cuffs of an ETT. The third sensor is not visible and is behind the ETT in the photograph. (b) Schematic showing the cross-section of the cuff with the three sensors.

The opto-electronic components used for ETT placement measurements and oxygen saturation are described here (Fig. 5.12), although other components were used for contact pressure measurements. Each sensor had two 250  $\mu\text{m}$  diameter illumination fibres (commercial grade PolymethylMethacrylate (PMMA), Asahi, model DB-200), and one 500  $\mu\text{m}$  central detection fibre (commercial grade PolymethylMethacrylate (PMMA), Asahi, model DB-500). One illumination fibre was connected to a broadband white LED (Fiber-Coupled LED, Thorlabs, model MBB1F1), and the other to an IR LED (Fiber-Coupled LED, Thorlabs, model M850F3). Both LEDs were powered by drivers (T-Cube LED Driver, Thorlabs, model LEDD1B), set to deliver a current of 500 mA. The connections in the illumination leg were bare fibre terminators (Thorlabs, model BFT1) with 510  $\mu\text{m}$  SMA connectors (Thorlabs, model B10510A) for the 500  $\mu\text{m}$  diameter fibres and 1050  $\mu\text{m}$  SMA connector (Thorlabs, model B11050A) for the 1000  $\mu\text{m}$  fibre. Therefore, there was a total of six LEDs and drivers (2 for each sensor). The drivers were connected to an Arduino (Arduino, model nano A000005), via a Bayonet Neil-Concelman (BNC) cable. The Arduino generated a square wave to trigger the drivers in a time-division multiple access (TDMA) configuration so that a single sensor was illuminating at any one time. This allowed a single spectrometer to detect light from each sensor sequentially. The time division chosen was 30s, so one sensor illuminated and detected for 30s then turned off and the next sensor began, cycling through the three sensors. From a research perspective, this allowed multiple full inflation and deflation ETT cuff cycles to be detected by a single sensor. Increasing this time provides longer measurement windows for each sensor and decreasing this time means that multiple sensors were more likely to detect the same physiological changes in the animal. Therefore, a balance between these two was chosen. In a clinical setting, the time division could be decreased to a fraction of a second so that spectra could be generated from all sensors during intubation.

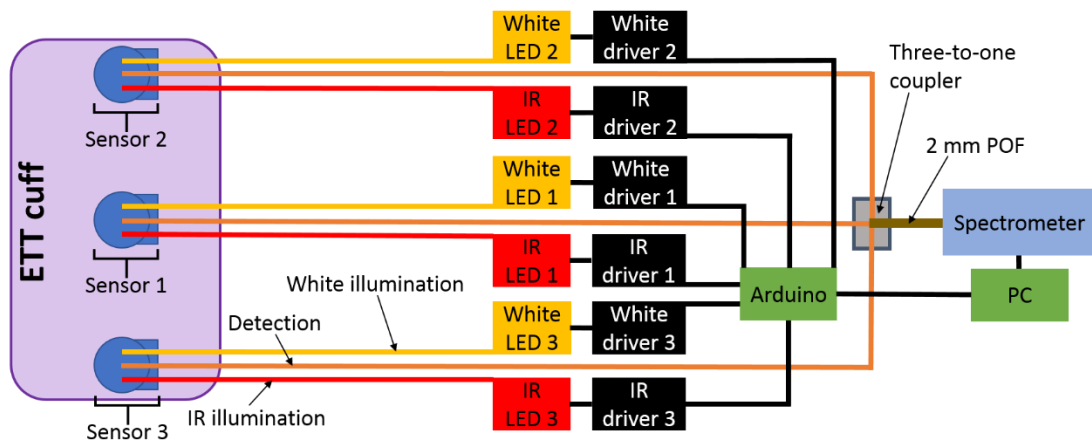


Fig. 5.12: Schematic diagram of the opto-electronic units used for ETT placement detection. The yellow and red lines are the 250  $\mu\text{m}$  diameter illumination fibres for the broadband white and IR LEDs. The orange line is the 500  $\mu\text{m}$  diameter detection fibre.

Each of the three detection fibres were bundled together forming a three-to-one coupler and then connected to a single larger diameter fibre to allow detection from all three sensors on a single spectrometer. The detection fibres were held together in a 'triangle formation' and placed through an SMA connector (Fig. 5.13). The fibres were held in the ferrule with the same UV-curable transparent epoxy used to adhere the

sensors to the cuff. Another SMA connector with a 2 mm diameter fibre was then connected to a spectrometer (Ocean Optics, model OCEAN-HDX-XR).

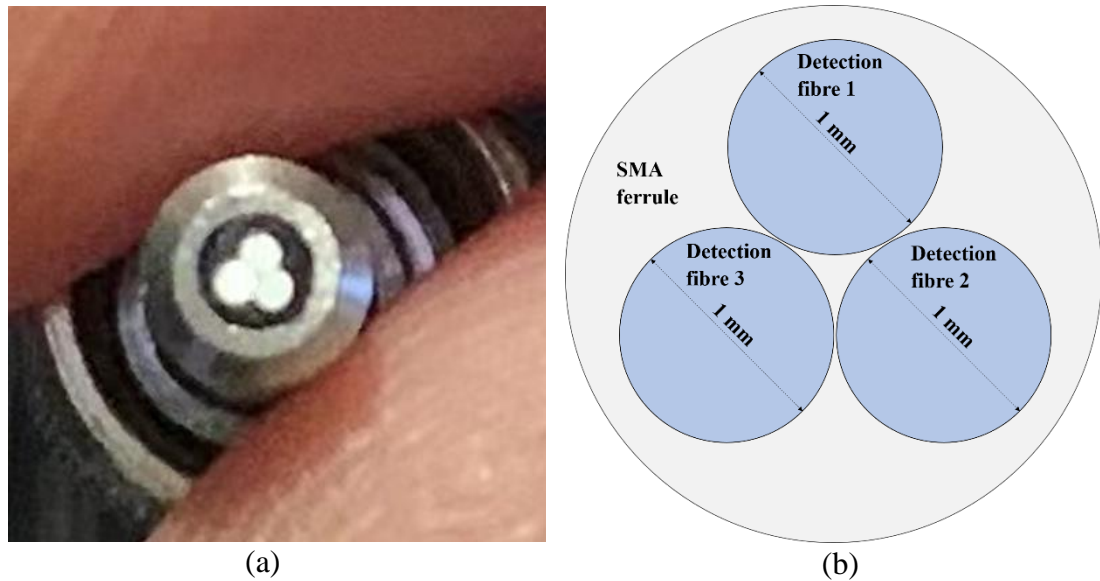


Fig. 5.13: (a) Photograph of the bundle of detection fibres in a triangle formation and adhered to the inside of a ferrule.

Ethical approval was provided under Home Office license PP 3998512 by The University of Nottingham. Three porcine subjects (Canberra 12 mixed breed; Landrace/Large White/Duroc), with ages 5-6 months, and weights of 50-60 kg underwent surgery for alternative non-recovery experiments on acute and chronic kidney disease. The subjects were fasted for 24h before sedation, which was initiated with intramuscular buprenorphine (0.05 mg/kg), ketamine (5mg/kg), and detomidine (0.1 mg/kg). The subjects were then left for 15 minutes and given alfaxalone (1 mg/kg) intravenously to further relax the larynx. Standard intubation procedures were then followed using the ETT with integrated sensors (Fig. 5.14). Two different ETTs were used for the three subjects, labelled ETT1 and ETT2. ETT1 was used for subjects 1 and 3 and ETT2 was used for subject 2. Initially, three different tubes were planned to be used (one for each subject). However, the contact pressure fibres were damaged during initial tests and so the same tube was used for subjects 1 and 3. The subjects were moved to the operating room and placed under general anaesthesia with isoflurane (2%), oxygen, and an air mix. A veterinary anaesthesia ventilator (Matrx, model 3000) started ventilation at a rate of 11 ml/kg, although this was adjusted throughout the surgery to maintain oxygen saturation above 95% and an ETCO<sub>2</sub> of 7 kPa. The ETT cuff pressure was initially brought to 30 cmH<sub>2</sub>O and was varied throughout the experiment to correlate with cuff-trachea contact pressure and to induce physiological changes in the trachea such as inducing capillary refill so that the capillary refill time (CRT) could be measured. Although not viable in the animal license for this study, future protocols could incorporate *in vivo* oesophageal measurements by intubating the oesophagus with an ETT or attaching the sensor to an oesophageal temperature probe.



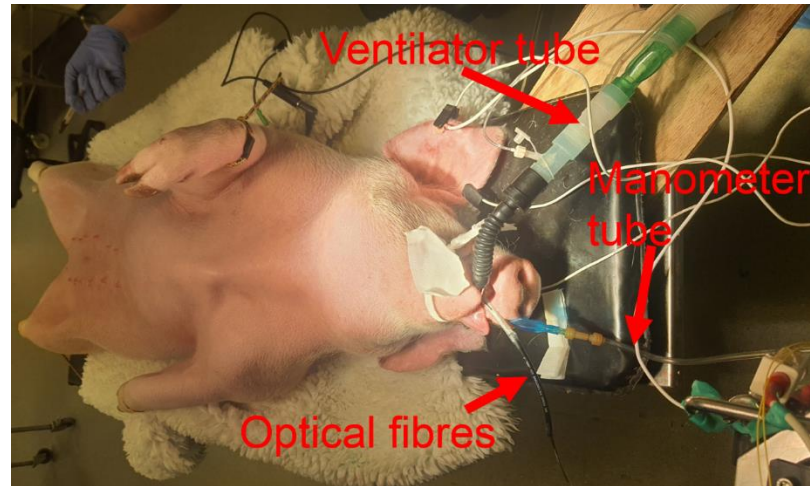


Fig. 5.14: Porcine subject after intubation and connection of tubes and fibres.

The ETT was orientated such that sensor 1 was at the posterior of the trachea (the muscular side closest to the oesophagus), and sensors 2 and 3 were on the left lateral and right lateral cartilaginous sides, respectively. However, there may have been some rotations of the ETT in the trachea due to movements. The pressure valve of the ETT cuff was connected to a syringe pump and manometer so that the intracuff pressure (pressure inside the cuff) could be varied and measured. A series of experiments were then performed (Fig. 5.15) and then the subject was euthanised following the animal license protocol. Following the death of the animal, the ETT was extubated and then placed in the oesophagus where measurements continued.

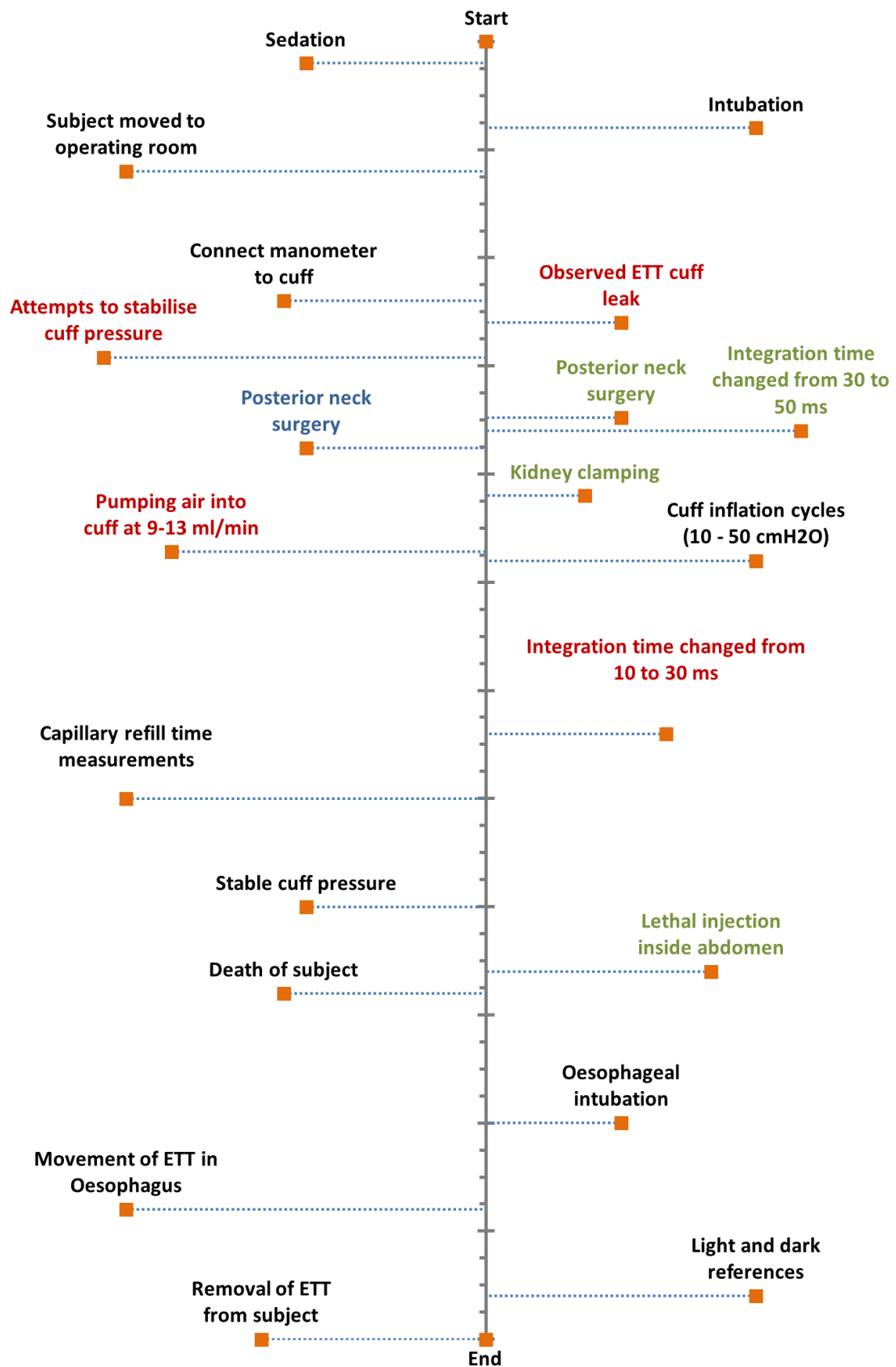


Fig. 5.15: Timeline of the main events of the animal study for all subjects (black) and specific changes to the protocol for subjects 1 (red), 2 (green), and 3 (blue).

During the initial intracuff pressure measurements of subject 1, it was discovered that the cuff had a slow leak and could not maintain pressure. This was caused by the epoxy that sealed the cuffs failing and was the first occurrence of this fault. Future designs should ensure a strong seal under rigorous testing. However, this would be resolved by commercial manufacturing of the double cuff. Attempts were made to stabilise the cuff pressure by manually increasing the pressure back to 30 cmH<sub>2</sub>O when it fell below 25 cmH<sub>2</sub>O. Following this, the syringe pump was set to constantly supply pressure to the cuff at a rate of 9-13 ml/min to stabilise the leak. The integration time of the spectrometer was set between 20-50 ms, depending on the intensity of the detected optical power. Light and dark references were taken at the end of each experiment for each sensor using black felt and a reflectance standard (Spectralon diffuse reflectance targets, Labsphere, model SRT-99-180). The referencing was taken whilst the whole system was fully connected. Cuff inflation cycles refer to increasing the pressure of the cuff in steps of 5 cmH<sub>2</sub>O. CRT measurements consisted of rapidly increasing the pressure and then rapidly decreasing it to induce blanching and then refilling of the capillaries. For ETT placement data, these periods can be considered as having a variable cuff pressure, with a comparison to cuff pressures not investigated here. Once the ETT was in the oesophagus it was rotated and moved in and out in a spiral motion so that multiple orientations in the oesophagus could be measured. A flow chart describes how the data is processed for each subject (Fig. 5.16). Data number refers to the order in which data was acquired. It was sequentially generated for each data point depending on the time it was acquired. This was implemented because of breaks in data acquisition between measurements.

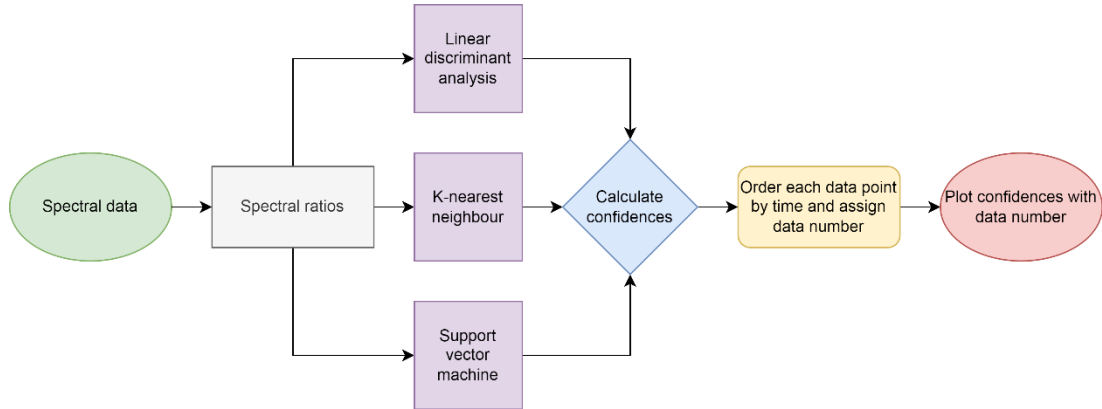


Fig. 5.16: Flow chart summarising the data processing of the spectral data acquired from the animal study.

### 5.4.1 Analysis by Subject

### 5.4.2 Subject 3

The analysis begins with subject 3, as for subject 1 the cuff had a leak during measurements and no oesophageal measurements were made (discussed in Section 5.4.4). The ETT was orientated in the trachea such that sensor 2 was positioned towards the posterior on the muscle side (Fig. 5.17), sensor 1 was on the outer left lateral cartilage and sensor 3 was on the outer right lateral cartilage, confirmed with a post-mortem dissection where an incision was made through the neck of the subject to

reveal the trachea. No imaging of the ETT in the trachea was made during measurements and it could have moved during the experiments. However, the ETT is generally stable in position once inserted due to the cuff expanding and securing its position, along with the pressure the throat and mouth exert on the ETT. Movement of the neck of the patient can dislodge the ETT [179], although the subjects in this animal study were not moved once measurements began.

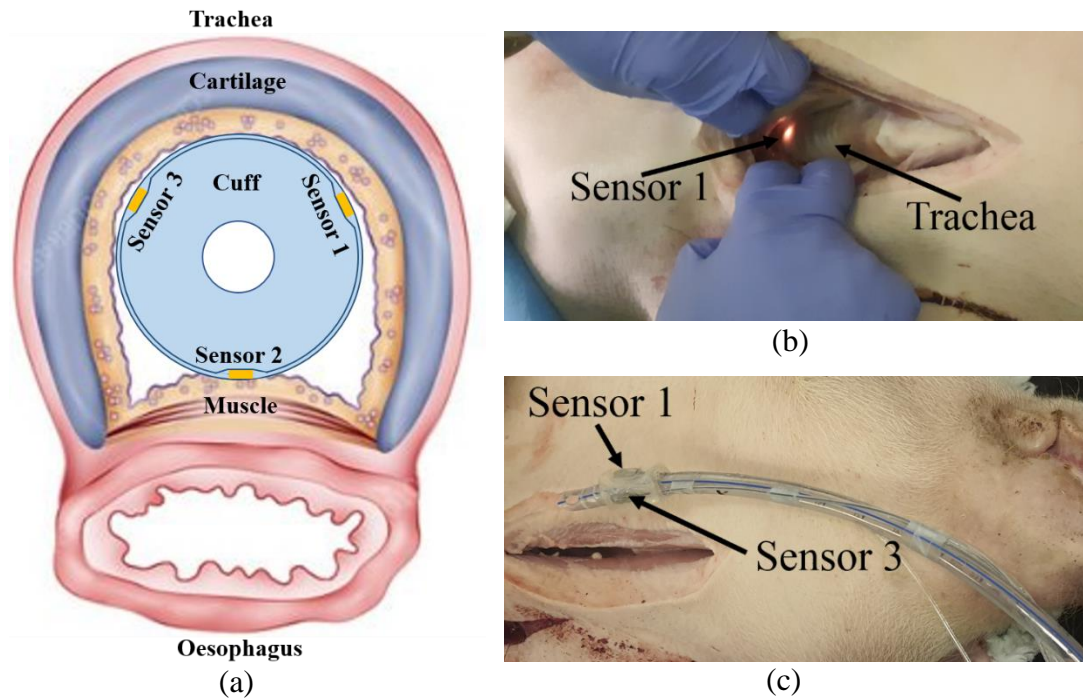


Fig. 5.17: Subject 3 (a) sensor orientation diagram in the trachea. (b) Photograph of the trachea with the ETT inside and with sensor 1 turned on. (c) Photograph of the ETT extubated without rotating and then placed in the approximate position on top of the subject so that the orientation is preserved.

The integration time of the spectrometer was set to 50 ms for subject 3, with the computer taking an additional 2.7 ms to store each spectrum. Therefore, the sample rate was 52.7 ms and resulted in 19 acquired spectra per second. The sensors were TDMA cycled with a 30s time division as described previously in this chapter so that data was only acquired from one sensor at a time for 30s before cycling to the next sensor in the order 1, 2, 3. Data acquisition began with sensor 3. The means of the first full 30s of each sensor are shown in Fig. 5.18. This was formed by averaging the 570 spectra taken in each detection window (90s of acquisition with 1710 spectra across 3 sensors).

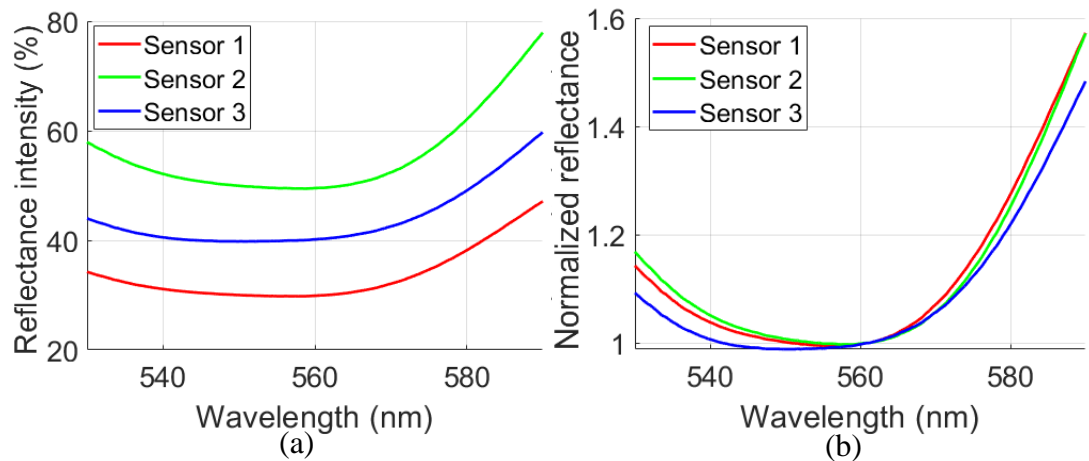


Fig. 5.18: Subject 3 trachea – (a) Spectra normalized with the white reference standard and then (b) further Single wavelength normalization at 561 nm.

The characteristic wavelength feature is observationally absent in all three sensor positions (Fig. 5.18) in this example spectra from the first 30s of acquisition. The absence is believed to arise from the use of a fibre separation distance that is not optimal, such that the penetration depth of the light is decreased and a limited amount of OHb is detected. The spectra were normalized using the white reference standard to produce a reflectance intensity as a percentage (Fig. 5.18a) and then normalized to the central peak of the OHb characteristic at a wavelength of 561 nm (Fig. 5.18b). There is absorption in the 530 – 590 nm wavelength region that can be seen most clearly in Fig. 5.18a. However, the typical peak at 561 nm is not visible. The same process was then applied to the first 30s of the oesophageal data from each sensor as an example.

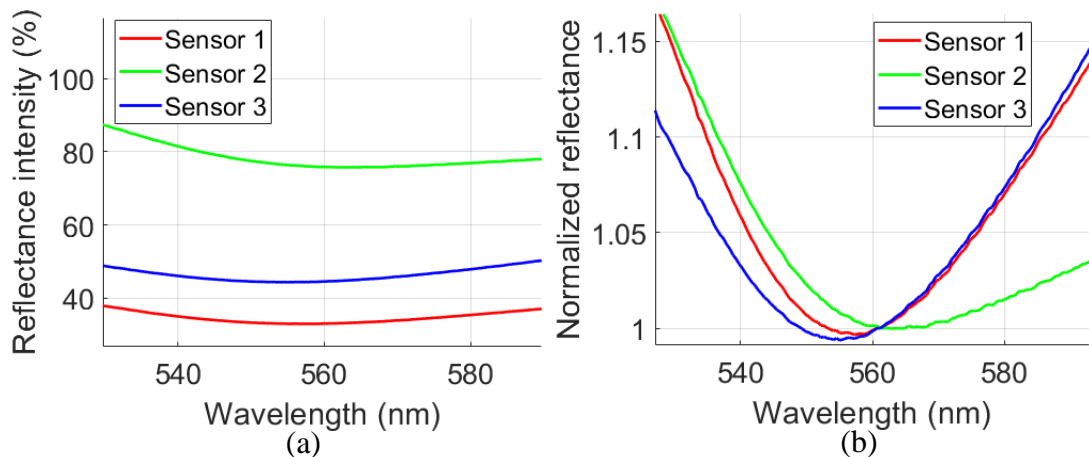


Fig. 5.19: Subject 3 Oesophagus - (a) Spectra normalized with the white reference standard and then (b) further Single wavelength normalization at 561 nm.

The oesophageal spectra (Fig. 5.19) also differ from those measured in *ex-vivo* samples, where typically the OHb characteristic consisting of a trough-peak-trough is present. However, there is low absorbance (high reflectance) in the 530 - 590 nm wavelength region as can be seen in Fig. 5.19 when compared to the tracheal spectra. Since oesophageal data was measured only after the death of the subject, a comparison to the post-mortem tracheal data is first made for 30s of the data from sensor 1 (Fig. 5.20).

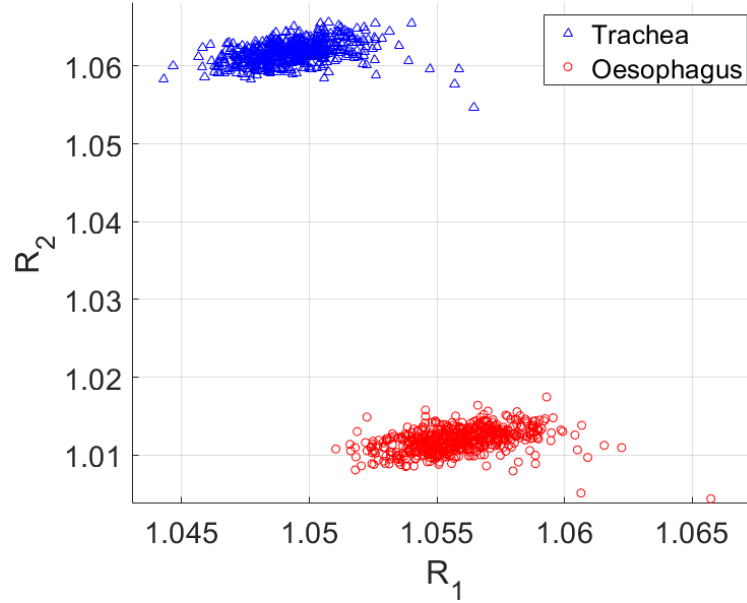


Fig. 5.20: 30s of spectral data taken shortly post-mortem (*in-situ*) for subject 3, sensor 2 ( $n = 1126$ ).

The increase in the number of spectra is caused by decreasing the integration time from 50 ms to 25 ms. The ratios  $R_1$  and  $R_2$  are used in Fig. 5.20 to compare the tissues, described in Section 4.3.1. A separation between the two tissues forms, with  $R_2$  providing a stronger separation as can be seen by the overlapping  $R_1$  values. However, the tracheal ratio values are different to those measured in *ex-vivo* samples, where typically they would be below 1, as discussed in Section 4.3.1. A tracheal ratio above 1 is caused by the absence of the trough-peak-trough spectral feature in the 530 – 590 nm wavelength region. The lack of a central peak at a wavelength of 561 nm can be seen in Fig. 5.18. Therefore, relative to the central peak, the normalized reflectance at 543 and 578 nm is higher, causing ratio values greater than 1 for the trachea. However, the tissues can still be separated from each other because of the increased absorption of the tracheal tissue in the spectral range of interest. The steep increase in reflectance from the 561 nm wavelength in the tracheal data causes higher ratio values than what is seen in the oesophagus for  $R_2$ , which is typical throughout the data. A discussion on this difference is found at the end of this chapter.

Stable oesophageal measurements were made for a total of 6 minutes (2 minutes total per sensor), where stable refers to the ETT not being moved and the cuff pressure not being changed. Therefore, the last 6 minutes of stable post-mortem tracheal data are compared to the oesophageal data and then separated by sensor, as this provides a comparison between the tissue where the physiological state of the subject is most similar (Fig. 5.21).



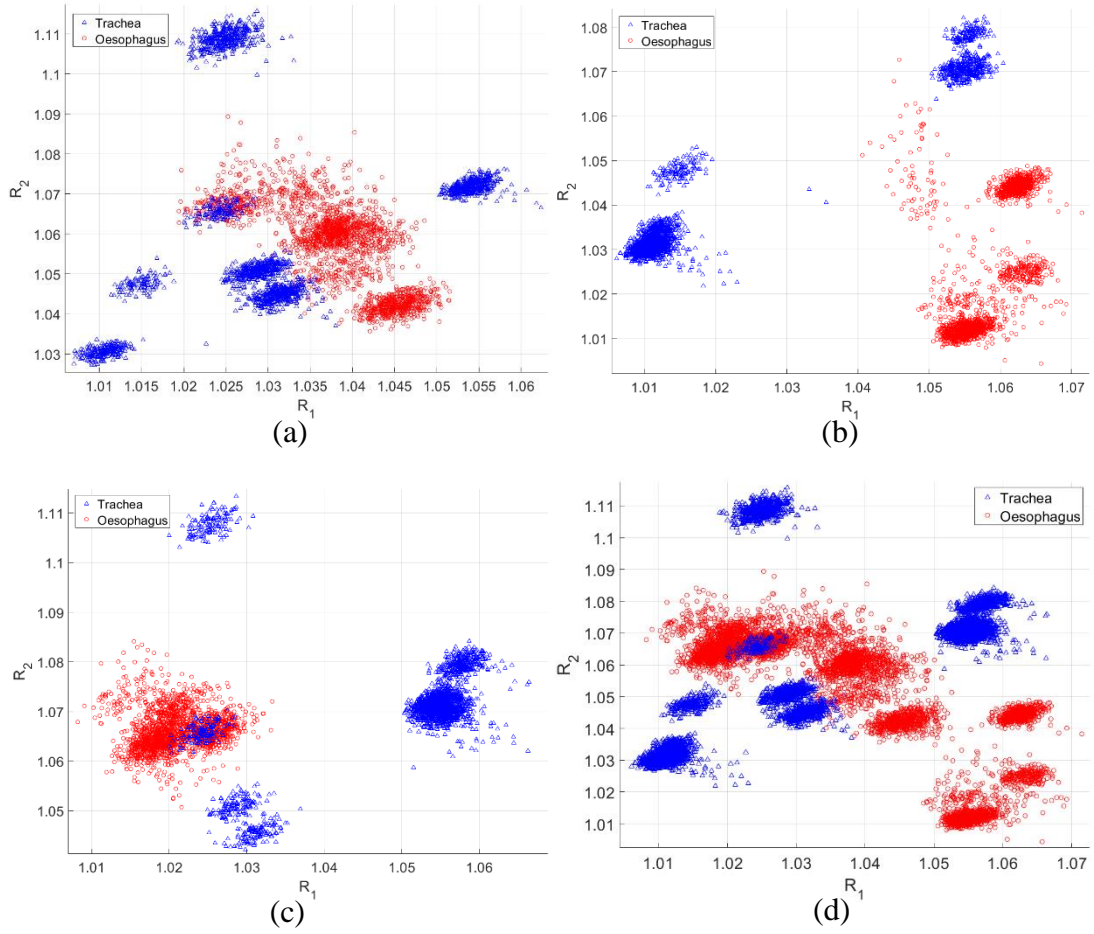


Fig. 5.21: Post-mortem (*in-situ*) comparison between tracheal and oesophageal  $R_1$  and  $R_2$  values for subject 3 (a) sensor 1 ( $n = 2280$ ), (b) sensor 2 ( $n = 2280$ ), (c) sensor (3) ( $n = 2280$ ), and (d) combined for all sensors ( $n = 6840$ ).

From Fig. 5.21, the ratios  $R_1$  and  $R_2$  do not perform as good indicators of tissue type when comparing recent post-mortem tracheal results. The data form clusters from variations in the pressure of the ETT cuff. The combined mean and standard deviation for the post-mortem  $R_1$  value (Fig. 5.21d) for the trachea was  $1.03 \pm 0.02$ , whereas the oesophagus was  $1.04 \pm 0.02$ . The  $R_2$  values mean and standard deviation for the trachea and oesophagus were  $1.06 \pm 0.02$  and  $1.05 \pm 0.02$ . Therefore, the ratio values are similar between the trachea and oesophagus for the *in-situ* post-mortem results. The other computational methods described in Chapter 4 may distinguish the tissues. However, due to the inconsistency with *ex-vivo* results and the not significantly different ratio values, the classifications would be unrepresentative for the *in-situ* tracheal results.

The post-mortem oesophageal data was then compared to the tracheal data during the first few minutes of intubation. Although this is a comparison between *in-vivo* tracheal and *in-situ* oesophageal measurements, it may be considered a more representative comparison as the tracheal classification relies upon the presence of the spectral feature originating from OHb. Therefore, the rapid physiological changes that occur during death may inhibit the presence of the OHb spectral feature in the trachea. Therefore, the feature may be more detectable in a living subject's trachea compared to recently deceased ones. However, this may also be viewed as simply distinguishing

between alive and dead tissues. The feature may be more detectable in *ex-vivo* samples due to the presence of highly oxygenated blood inside and outside the samples. An ETT placement decision would ideally be determined during the first few seconds of intubation to minimise the risk to the patient. Further discussion of this idea is explored at the end of this chapter.

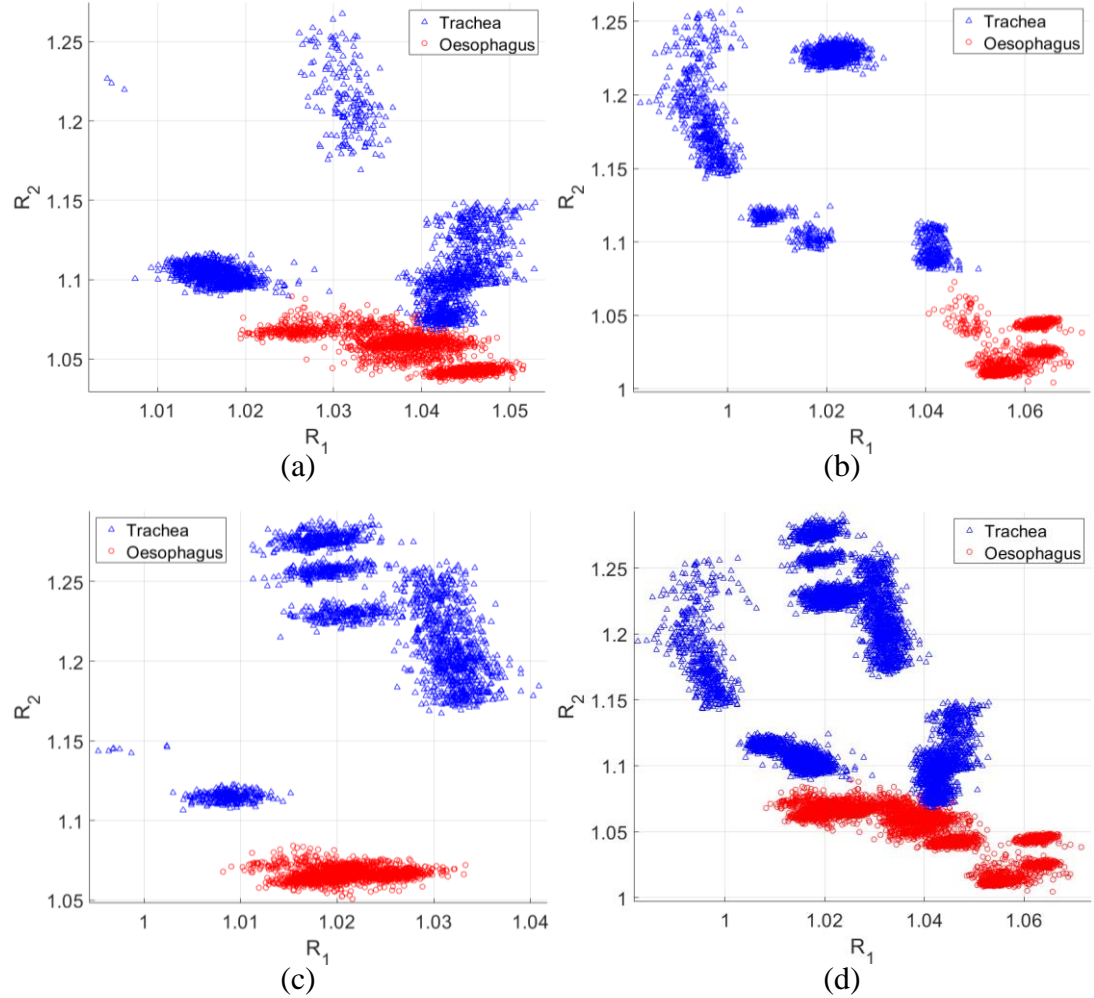


Fig. 5.22: Comparison between *in-vivo* tracheal and recently deceased *in-situ* oesophageal  $R_1$  and  $R_2$  values for subject 3 (a) sensor 1 ( $n = 2280$ ), (b) sensor 2 ( $n = 2280$ ), (c) sensor (3) ( $n = 2280$ ), and (d) combined for all sensors ( $n = 6840$ ).

Comparing the first 6 minutes (2 minutes per sensor) of *in-vivo* tracheal data with 6 minutes of *in-situ* oesophageal data demonstrates a clear separation in  $R_2$  for each sensor (Fig. 5.22a-c), and when the sensors are combined (Fig. 5.22d). However,  $R_1$  is not a good indicator of tissue type for sensors 1 and 3, although a difference can be seen for sensor 2 (Fig. 5.22b). The mean and standard deviation of the  $R_2$  values for the trachea and oesophagus were  $1.17 \pm 0.07$ , and  $1.05 \pm 0.02$ . The  $R_1$  values gave a mean and standard deviation of  $1.02 \pm 0.01$ , and  $1.04 \pm 0.02$ . A t-test was performed on the tracheal and oesophageal  $R_2$  values gives  $z = 135.0$ ,  $p < 0.001$ , concluding a statistical difference.

The full data set consisting of all *in-vivo* tracheal measurements ( $n = 98445$ , 86.39 minutes) and all post-mortem *in-situ* oesophageal measurements ( $n = 9500$ , 8.34

minutes) for subject 3 were then compared, which include periods of unstable cuff pressure and ETT movements, as described in.

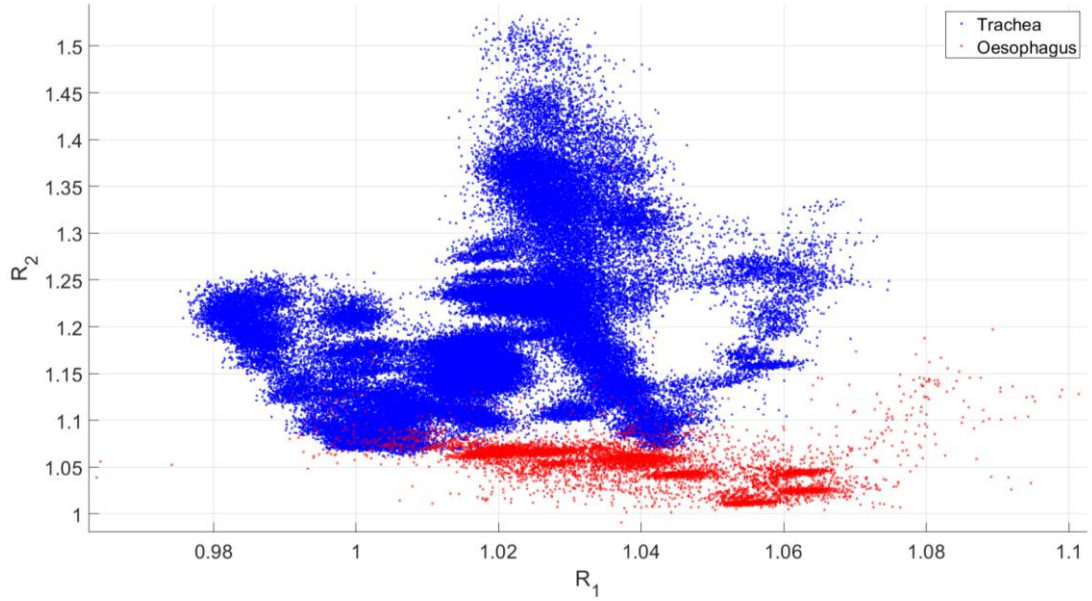


Fig. 5.23: *in-vivo* tracheal and *in-situ* oesophageal measurements over the full acquisition for subject 3 (n = 107946, 94.73 minutes)

A separation in the  $R_2$  values can be seen in Fig. 5.23. The  $R_1$  values classify the tissues less, where there is less separation. The mean and standard deviation for the  $R_2$  values for the trachea and oesophagus across all measurements were  $1.20 \pm 0.08$ , and  $1.05 \pm 0.02$ , with a t-test finding a significant difference  $z = 126.54$ ,  $p < 0.001$ . The mean and standard deviation of the  $R_1$  values for the trachea and oesophagus were  $1.02 \pm 0.02$ , and  $1.04 \pm 0.02$ , respectively. However, by combining each ratio value a stronger classification can be performed.

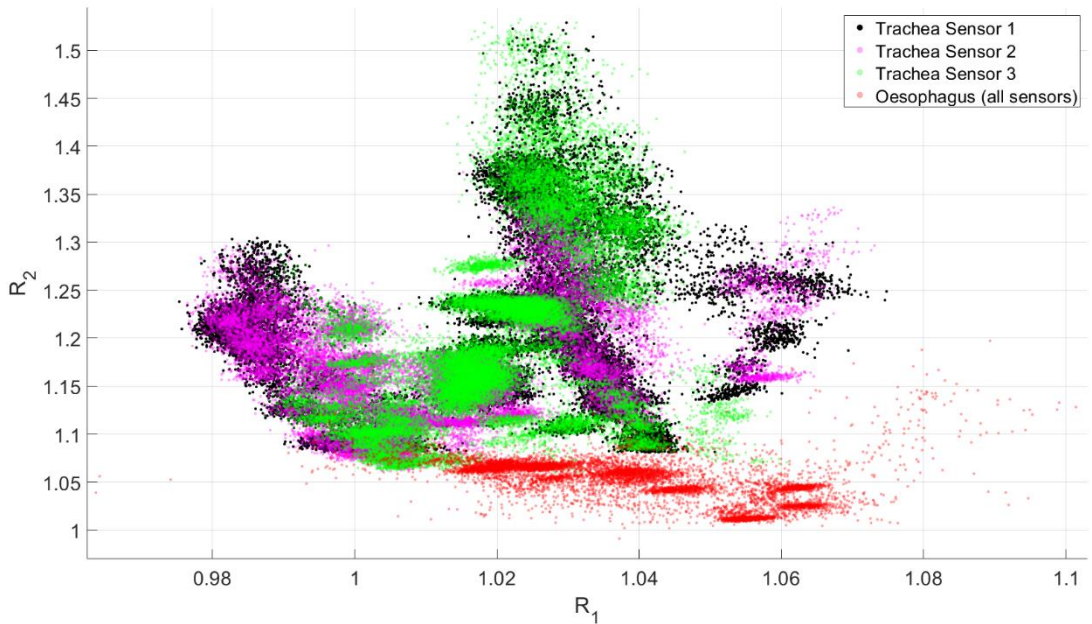


Fig. 5.24: Subject 3 *in-vivo* tracheal measurements separated by sensor and *in-situ* oesophageal measurements (n = 107946, 94.73 minutes).

Separating the tracheal ratios by sensor (Fig. 5.24), reveals that all 3 sensors provide similar ratio values. The mean and standard deviation of the tracheal  $R_2$  values for sensors 1, 2, and 3 are  $1.22 \pm 0.08$ ,  $1.17 \pm 0.06$  and  $1.21 \pm 0.09$ . The  $R_1$  means and standard deviations for sensors 1, 2, and 3 are  $1.02 \pm 0.02$ ,  $1.01 \pm 0.02$ , and  $1.02 \pm 0.02$ , respectively. There is no significant difference between the means of the ratio values  $R_1$  and  $R_2$  for the different sensors. Furthermore, no significant difference was found in the oesophageal mean ratio values between sensors 1, 2, and 3. This agrees with the findings of *ex-vivo* measurements (Chapter 4), and they will therefore be processed collectively.

The tissues were then classified by the three best-performing classifiers described in Chapter 4. The LDA, KNN, and SVM algorithms developed in this chapter offered the best classification and are the chosen methods.

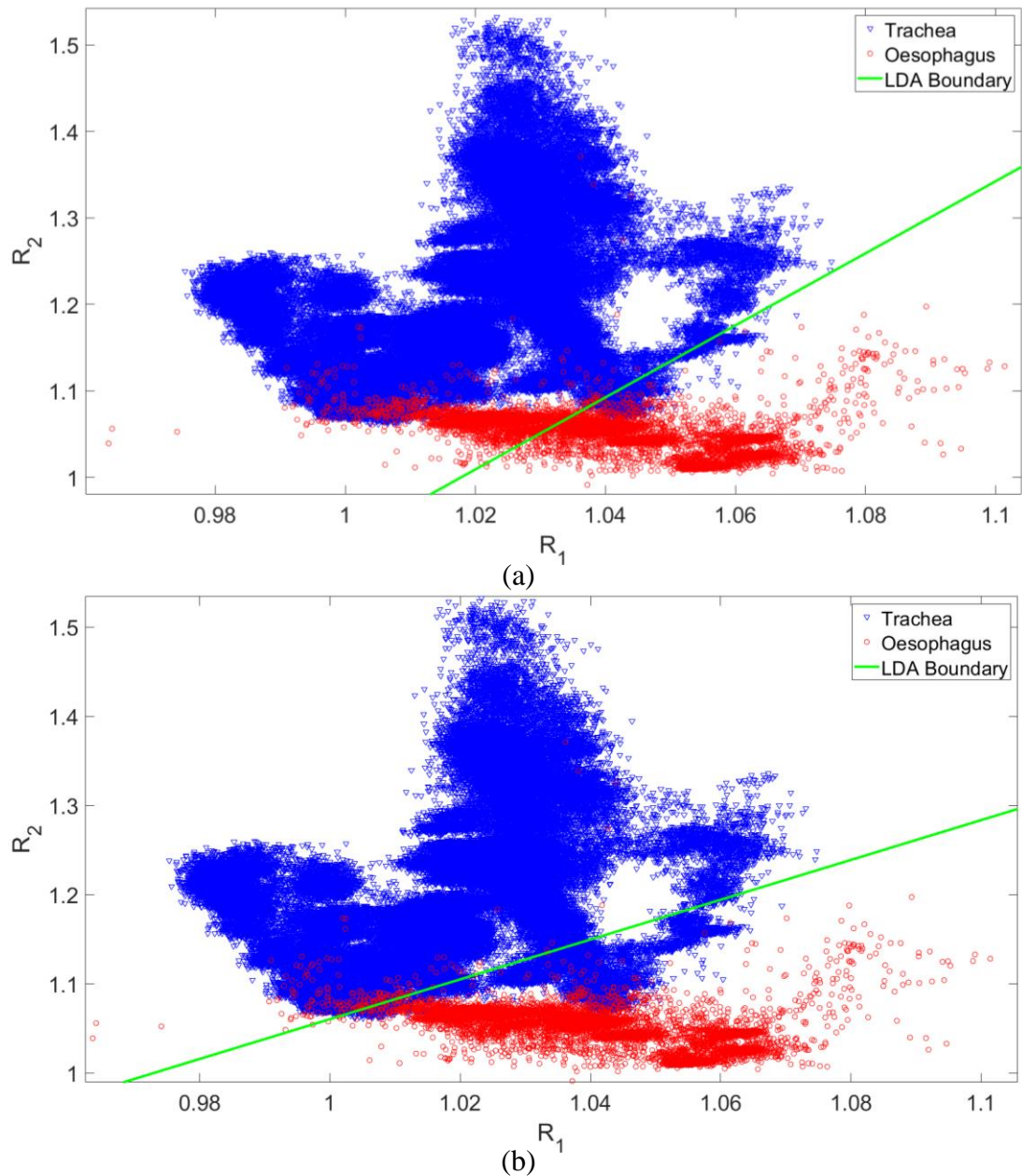


Fig. 5.25: Subject 3 trachea and oesophagus ratio values separated with an, (a) unweighted LDA boundary and, (b) weighted LDA boundary



Applying the LDA method (Section 4.5.1) to the tissues forms a boundary between them (Fig. 5.25a). However, the decision boundary is not close to the optimal position, where a straight horizontal line at approximately  $R_2 = 1.1$  separates the tissues with a higher correct tissue identification. This poorly placed boundary is caused by the sample sizes of the two groups differing greatly, where there are 10.36 times as many tracheal data ( $n = 98445$ ) than oesophageal ( $n = 9501$ ). One option is to compare the tracheal data in batches of equivalent size to the oesophageal, which would produce 10 comparisons. However, a simpler method is to weight the tissues by sample size (i.e. the tracheal data carries 10.36 times as much weight), providing a more representative identification. The group size weighted LDA boundary (Fig. 5.25b) produced a sensitivity of 98.0% and a specificity of 81.8%, giving a total correct tissue identification of 89.9%

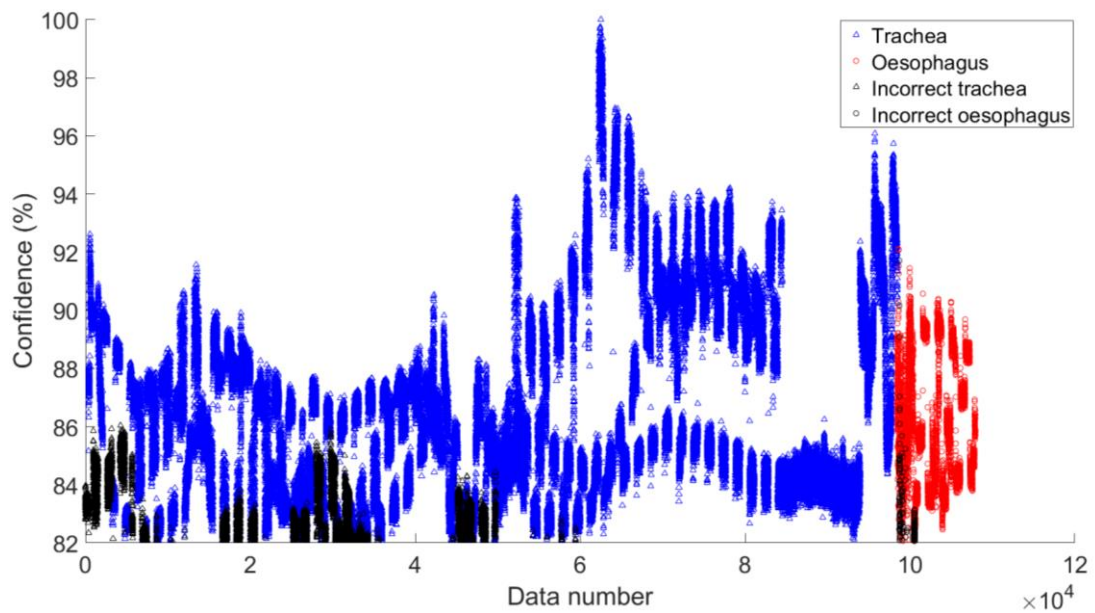


Fig. 5.26: Confidences on LDA classifications for subject 3.

The confidences were found by calculating the distance of each point from the LDA boundary (Fig. 5.26). The data point furthest from the line was assigned a 100% confidence and then the other measurements were scaled by this. Data number refers to the order in which data was acquired, described in the introduction of this chapter. Interestingly, the data numbers form groups with others close to them, where 2 or 3 can be found within a data number range of a few hundred, which gives Fig. 5.26 a striped appearance. This is caused by the varying cuff pressure changing the ratio values such that there are discrete jumps which change the distance from the line and hence the confidences. The data from subject 3 was then processed with the KNN method (Section 4.5.4).

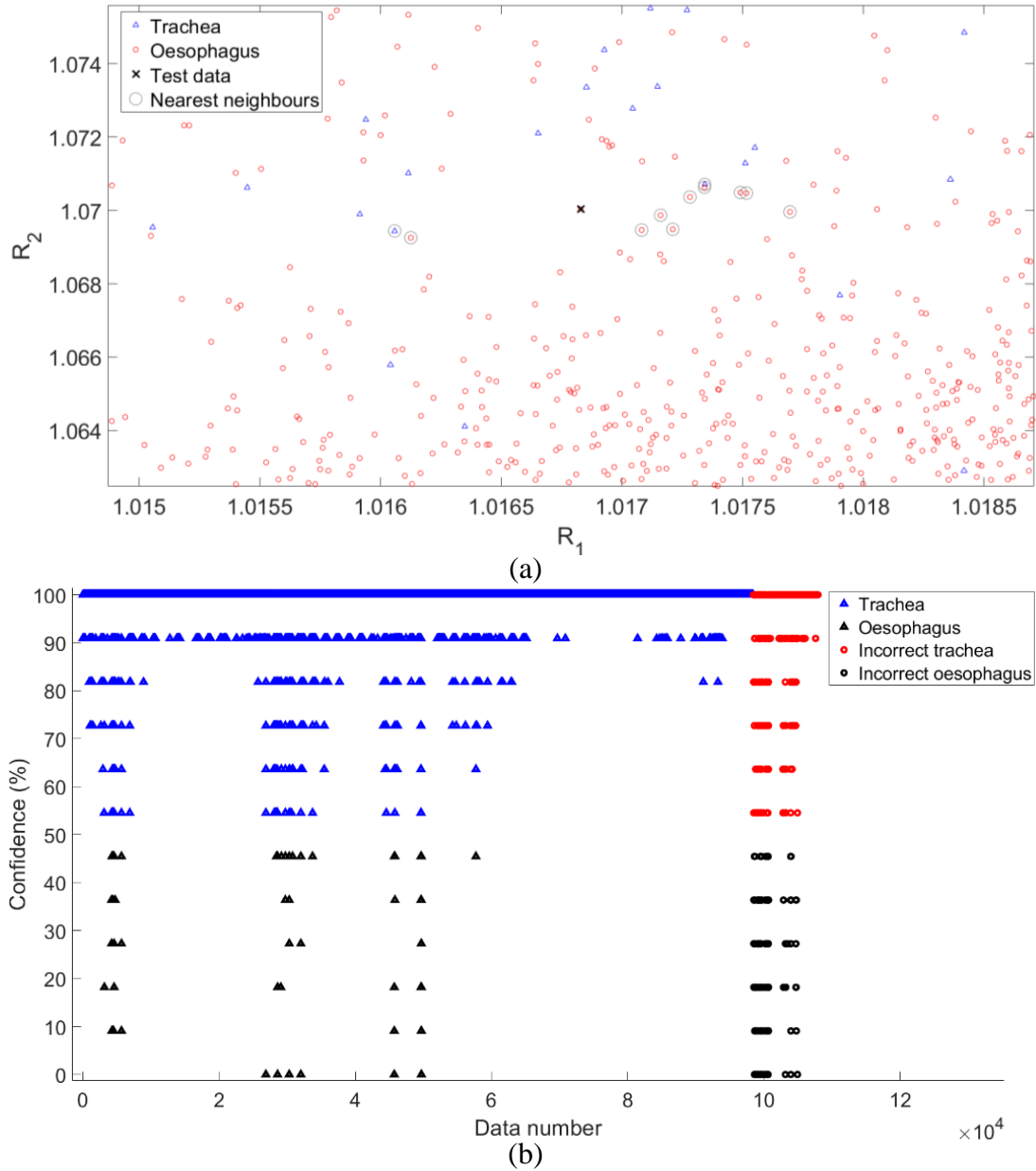


Fig. 5.27 Subject 3 trachea and oesophagus ratio values classified with the KNN method. (a) Example test data, (b) KNN confidences.

The data was permuted by using 1 data point as the test and all other measurements as the training data. During the KNN method, the distance between the test data and each training data is calculated, resulting in  $n(n - 1)$  calculations. A sample size of  $n = 10946$  requires over 10 billion calculations ( $1.17 \times 10^{10}$ ), requiring several hours to process and the response time would be too long for a clinical setting. However, the number of calculations could be reduced significantly by lowering the number of training data by averaging some of the spectra, or by using KNN only close to the boundary between the data sets where the data is less separable. In the example (Fig. 5.27a) the test data point would be correctly classified as oesophageal with an 81.8% confidence (9/11 of its closest neighbours oesophageal). Fig. 5.27b shows the confidence for each data point. The sensitivity for the KNN method was 95.5%, and the specificity was 99.9%, giving a correct tissue identification of 97.7%. The data from subject 3 was then classified using the SVM method (Section 4.5.3).



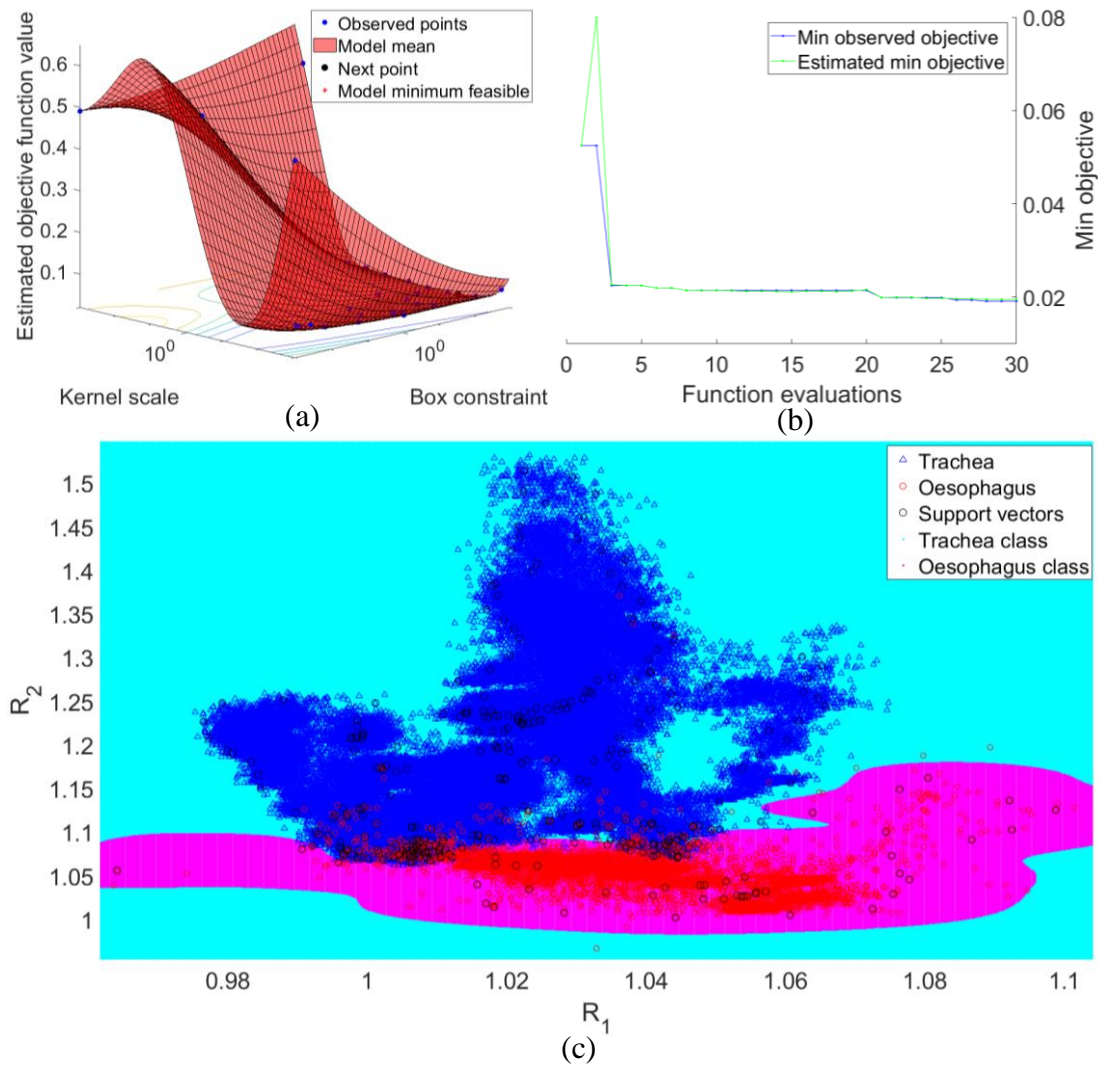


Fig. 5.28: Subject 3 trachea and oesophagus ratio values classified with the SVM method. (a) The objective function. (b) the minimum of the objective function (Min objective) change with the number of function evaluations. (c) the SVM boundary with the trachea and oesophagus classes shaded in light blue and pink, respectively.

The objective function (Fig. 5.28a) shows the shape of the boundary in a higher dimensional space. The minimum of the objective function is an estimate of the strength of the classification and reaches a value of 0.019 over 30 iterations (Fig. 5.28b), where 0 is a perfect separation. Fig. 5.28c shows the boundary formed by the SVM method which provides a sensitivity of 97.1% and specificity of 99.1%, giving a correct tissue identification of 98.1%. A confidence was then assigned to each data point by finding the closest distance to the boundary and then assigning the furthest distance a 100% confidence (Fig. 5.29). The Matlab optimisation of the SVM hyperparameter produced a specific and irregular boundary. This is a form of overfitting and fewer iterations may have produced a more generally representative boundary.

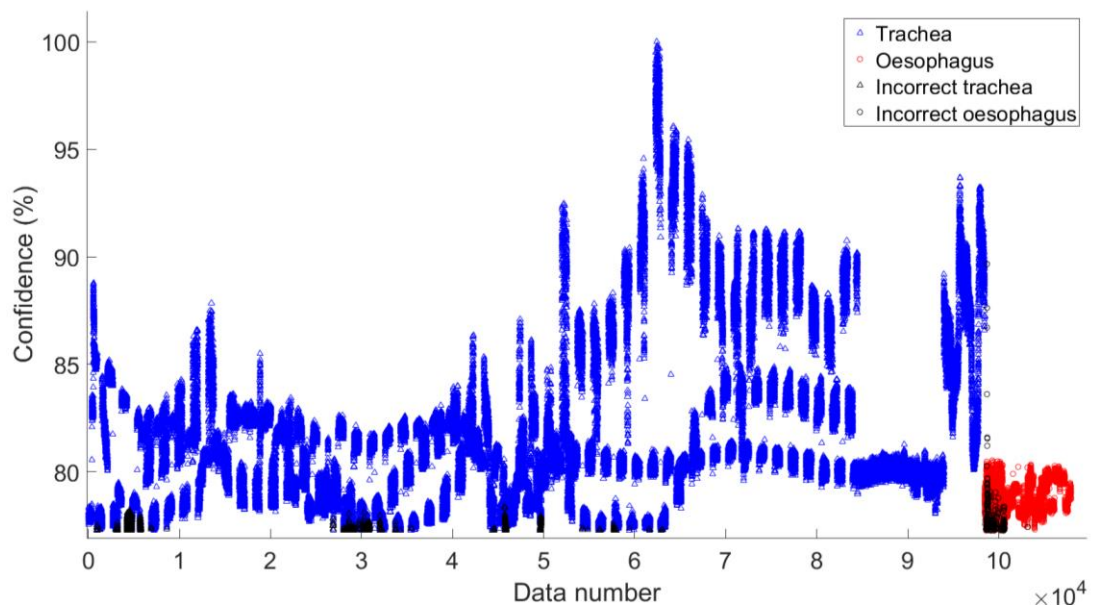


Fig. 5.29: SVM confidence on the subject 3 tissue classifications.

### 5.4.3 Subject 2

A different ETT was used for subject 2, whereas the same ETT was used for subjects 3 and 1, although they were manufactured the same way and contained the same sensor design. The sensors were orientated in approximately the same position as for subject 3, with sensor 2 positioned towards the posterior on the muscle side (Fig. 5.30), sensor 1 on the outer left lateral cartilage and sensor 3 on the outer right lateral cartilage. This was confirmed post-mortem by an incision through the neck once again.

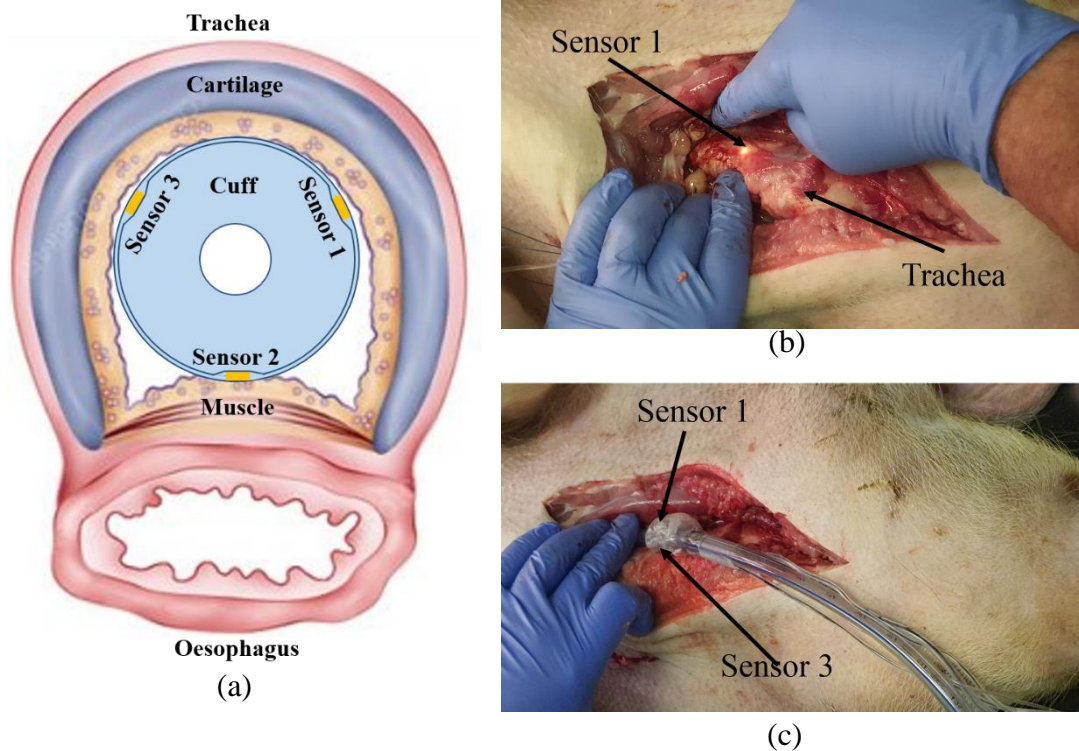


Fig. 5.30: Subject 2 (a) sensor orientation diagram in the trachea. (b) Photograph of the trachea with the ETT inside with sensor 1 turned on. (c) Photograph of the ETT extubated without rotating and then placed in the approximate position on top of the subject so that the orientation is preserved.

The integration time of the spectrometer was initially set to 30 ms for subject 2, although it was changed to 50 ms after 22 minutes of data acquisition to increase the intensity of the spectra. The protocol was the same as for subject 3 and the data was processed in the same way, described in the introduction and the previous section, with only a summary and discussion of the results here.

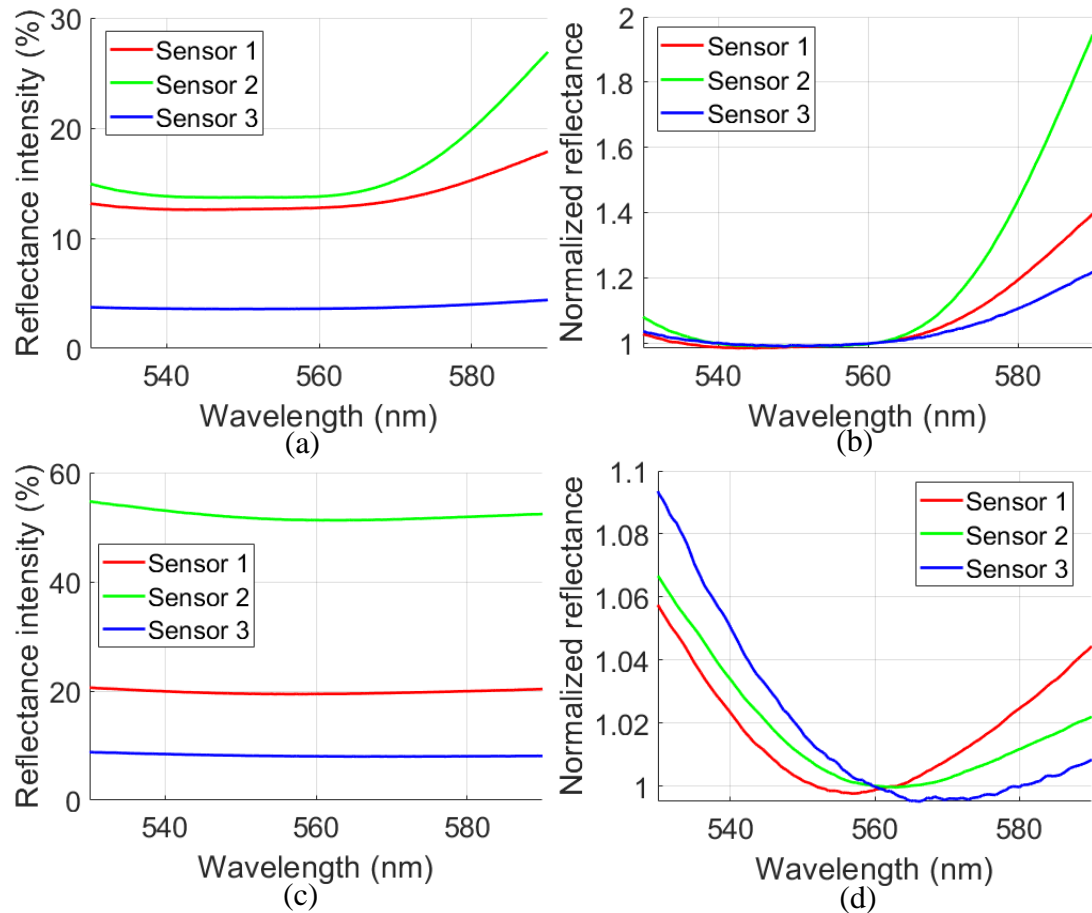


Fig. 5.31: Subject 2 – Porcine trachea (a), (b) and oesophagus (c), (d). Spectra normalized with the white reference standard (a), (c). Then a further Single wavelength normalization at 561 nm (b), (d).

The intensity spectra for subject 2 produce a similar spectrum as for subject 3. There is little presence of a central peak at a wavelength of 561 nm in either tissue, although there is more absorption in the 530 – 590 nm wavelength region in the trachea (Fig. 5.31a-b) than in the oesophagus (Fig. 5.31c-d). The average tracheal intensity spectra were formed by the mean of 970 spectra for each sensor (30s of data acquisition), whereas the average oesophageal intensity spectra contain the mean of 571 spectra, due to increasing the integration time from 30ms to 50ms. The intensity spectra were normalized in the same way as for subject 3.

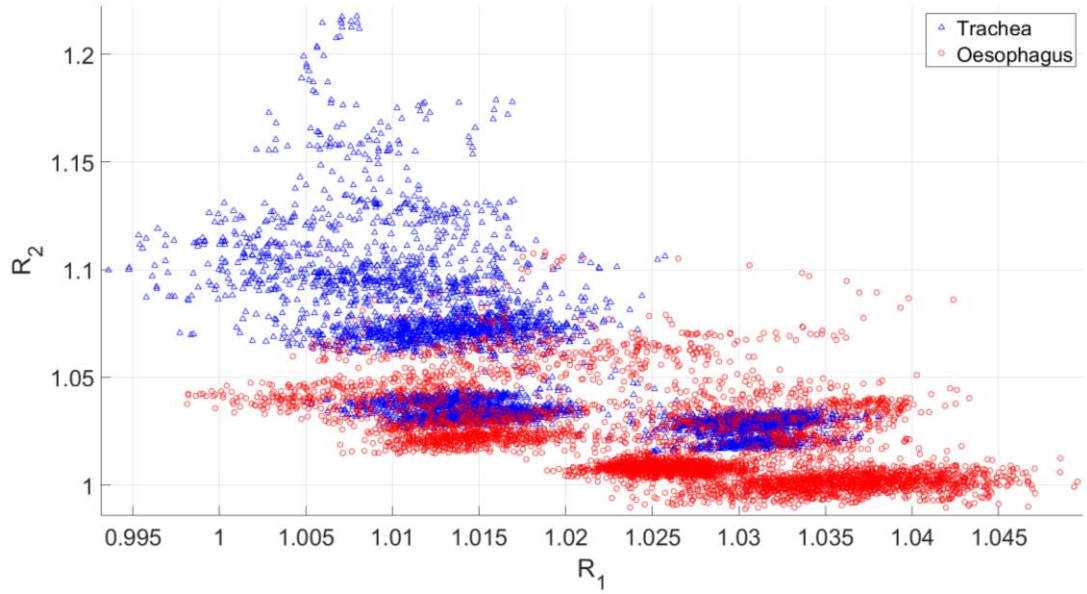


Fig. 5.32: Comparison of the ratio values of the trachea and oesophagus subject 2 shortly after death (*in-situ*), containing 9 minutes of tracheal and oesophageal data (4.5 minutes each tissue,  $n = 10284$  combined).

Interestingly, subject 2  $R_2$  values are more separable post-mortem than they were for subject 3. However, there is still a significant overlap in the values, with a mean and standard deviation for the trachea and oesophagus being  $1.05 \pm 0.03$  and  $1.03 \pm 0.01$ . The post-mortem tracheal and oesophageal  $R_1$  were  $1.02 \pm 0.01$ , and  $1.03 \pm 0.01$ . Therefore, the post-mortem tracheal results will be neglected when comparing the ratio values.

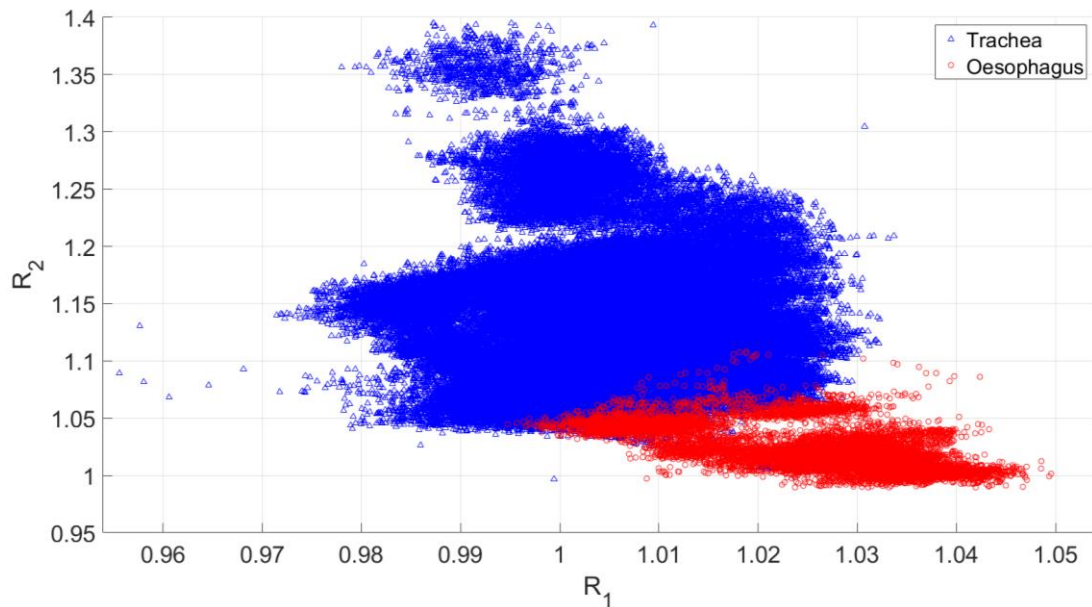


Fig. 5.33: *in-vivo* tracheal and *in-situ* oesophageal measurements over the full acquisition for subject 2 ( $n = 206574$ , 174.24 minutes).

All *in-vivo* tracheal measurements are grouped and compared to all *in-situ* oesophageal measurements in Fig. 5.33. The tracheal data comprises of 193446 spectra, measured over 162.95 minutes, and 13128 oesophageal spectra, over 11.29



minutes. A strong separation between  $R_2$  values can be seen, with a mean and standard deviation for the trachea and oesophagus of  $1.12 \pm 0.05$ , and  $1.02 \pm 0.02$ , respectively. The  $R_1$  values are less well separated with a mean and standard deviation for the trachea and oesophagus of  $1.01 \pm 0.01$ , and  $1.03 \pm 0.01$ , respectively.

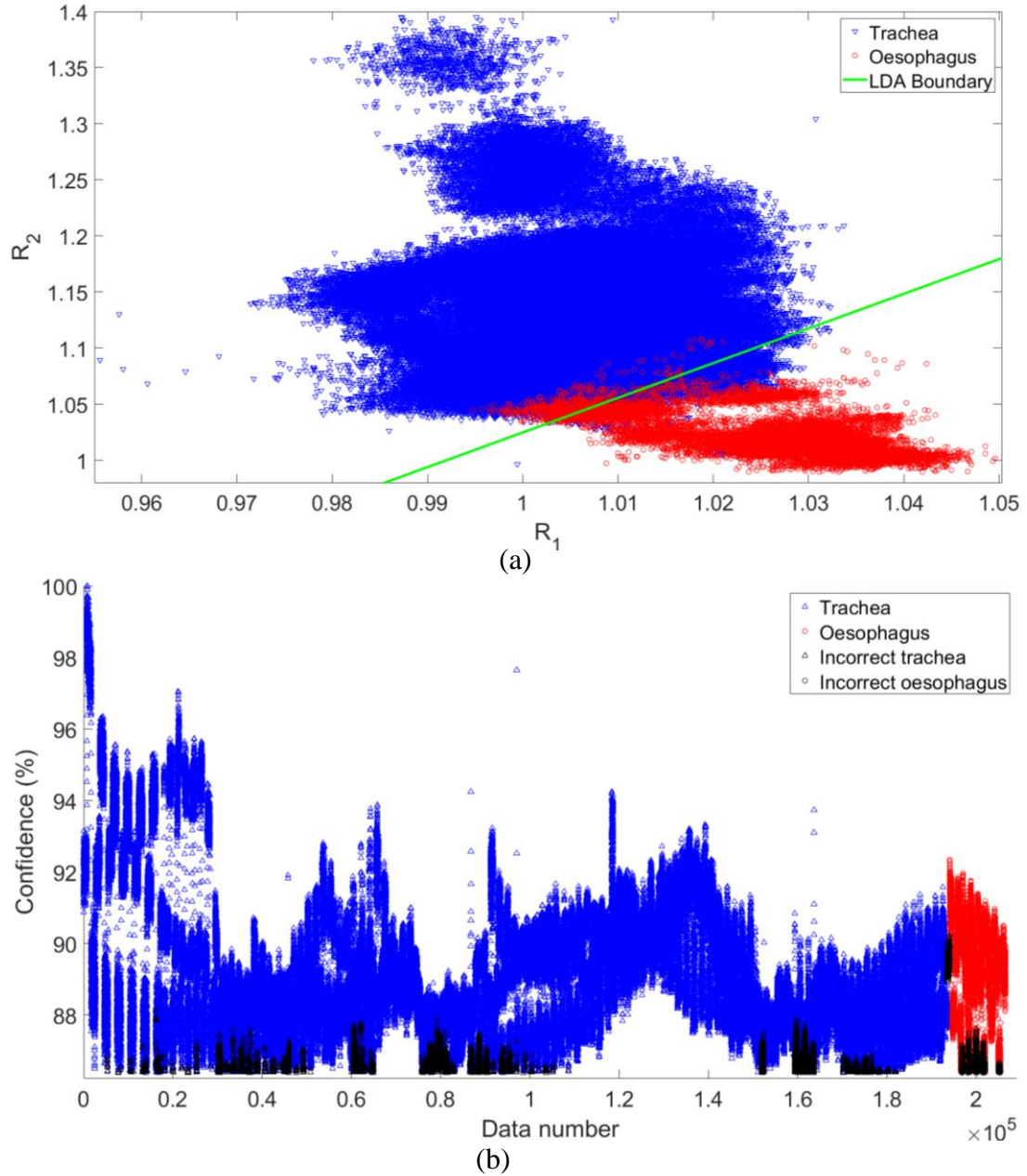


Fig. 5.34: (a) Subject 2 trachea and oesophagus ratio values separated with weighted LDA boundary and, (b) confidence on the identifications.

The LDA method (Fig. 5.34) produces a sensitivity of 95.0% and a specificity of 96.8%, giving a correct tissue identification of 95.9%. The LDA boundary was weighted because of the different group sizes. Therefore, oesophageal values had 14.73 times greater weight, which increases the number of correct tissue identifications.

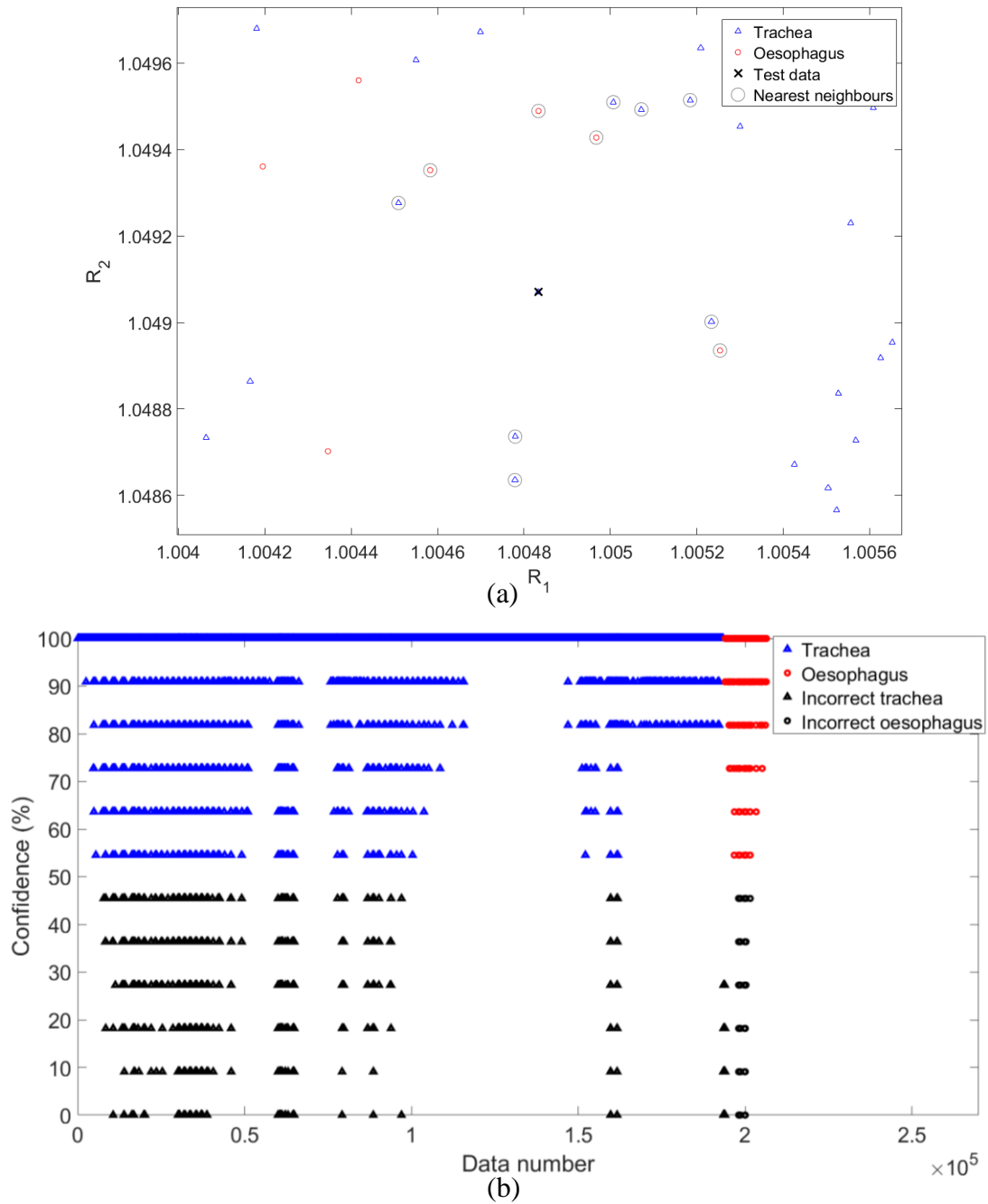


Fig. 5.35: Subject 2 trachea and oesophagus ratio values classified with the KNN method. (a) Example test data, (b) KNN confidences.

The tissues were then classified using the KNN method, with an example shown in Fig. 5.35a. In the example, the test data point was correctly classified as tracheal with a 63.6% confidence. The KNN method for subject 2 achieved a sensitivity of 98.1% and a specificity of 98.6%, giving an average correct tissue identification of 98.3%.



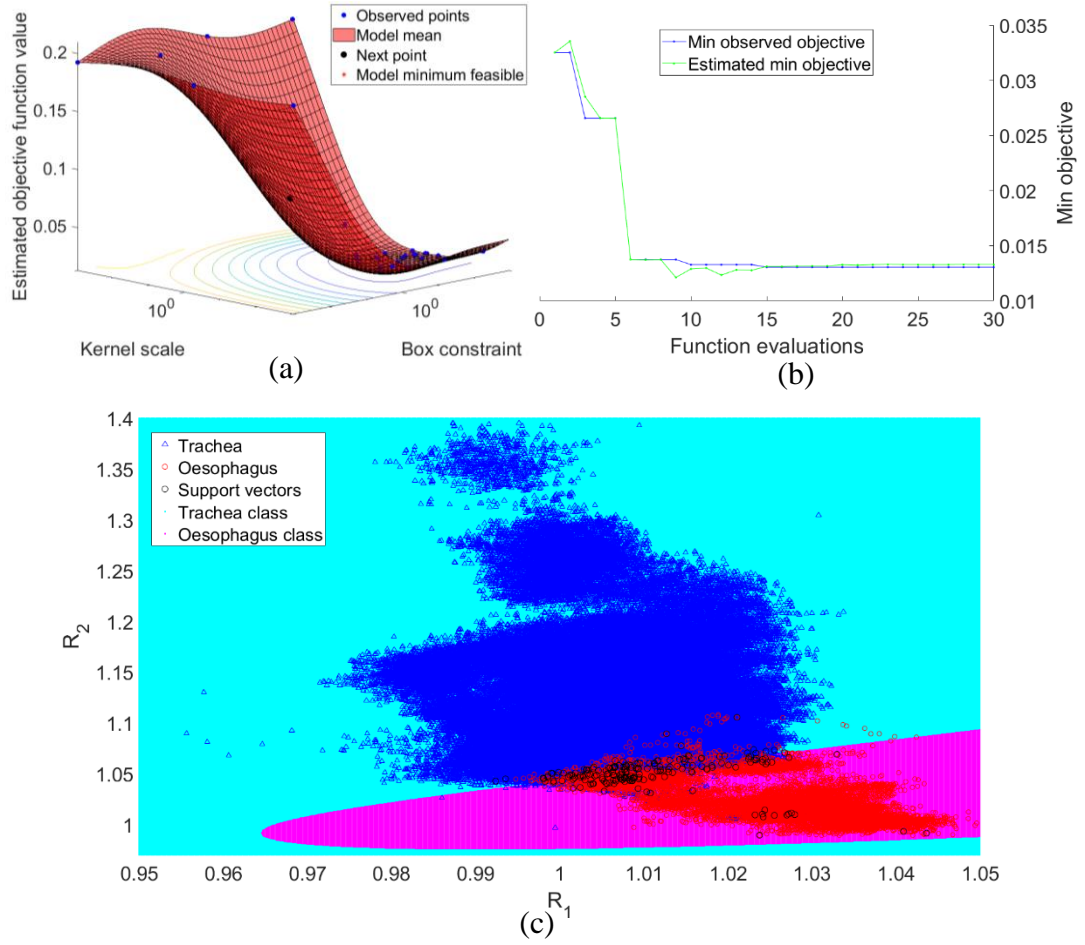


Fig. 5.36: Subject 2 trachea and oesophagus ratio values classified with the SVM method. (a) The objective function (hyperplane). (b) The minimum of the objective function (Min objective) change with the number of function evaluations. (c) The SVM boundary with the trachea and oesophagus classes shaded in light blue and pink, respectively.

The objective function is formed over an iterative process (Fig. 5.36a). The minimum of the objective function was tracked over 30 iterations (Fig. 5.36b). The boundary formed by the SVM method (Fig. 5.36c) gives a sensitivity of 96.7% and a specificity of 99.2%, giving a correct tissue identification average of 97.9%. Confidences were generated by finding the distances to the boundary (Fig. 5.37).

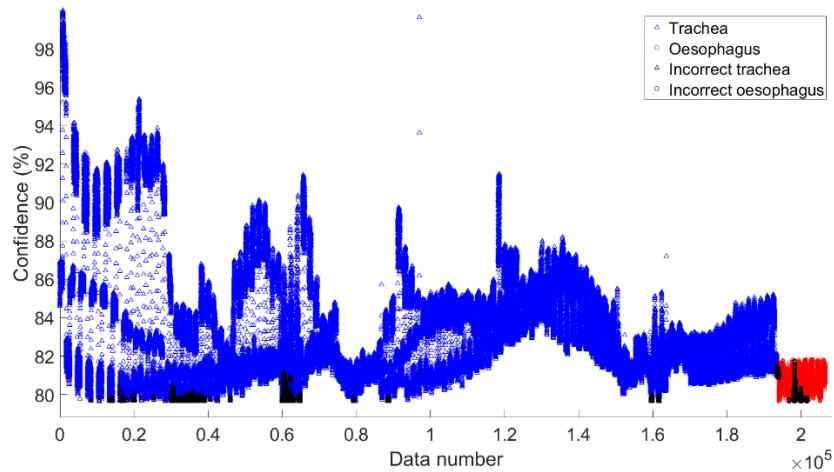


Fig. 5.37: SVM confidence on the subject 2 tissue classifications.

## 5.4.4 Subject 1

For Subject 1, the integration time was set to 10 ms for the first 78.5 minutes and then changed to 30 ms for the remainder of data acquisition to increase the signal-to-noise ratio. The same ETT was reused for subject 3. A leak in the cuff of the ETT was observed in the first few minutes of data acquisition and compensated for by manually increasing the pressure of the cuff back to 30 cmH<sub>2</sub>O every few minutes once the pressure dropped to below 20 cmH<sub>2</sub>O. Later, the syringe pump was set to increase the pressure steadily at a rate between 9-13 ml/min to compensate for the leak, which maintained a stable pressure of approximately 30 cmH<sub>2</sub>O. Confirmation of the ETT orientation in the trachea was not confirmed post-mortem for subject 1. Therefore, its position is unconfirmed, although it is assumed it was approximately the same as for subjects 2 and 3 (Fig. 5.17 and Fig. 5.30). Furthermore, during oesophageal intubation of the ETT, the veterinary physician could not confirm placement into the oesophagus as intended after several attempts. There was no post-mortem incision through the neck to reveal the trachea for subject 1, whereas for subjects 2 and 3 this was performed due to the unclear placement for the first subject. Therefore, it was not confirmed that ETT was in the oesophagus.

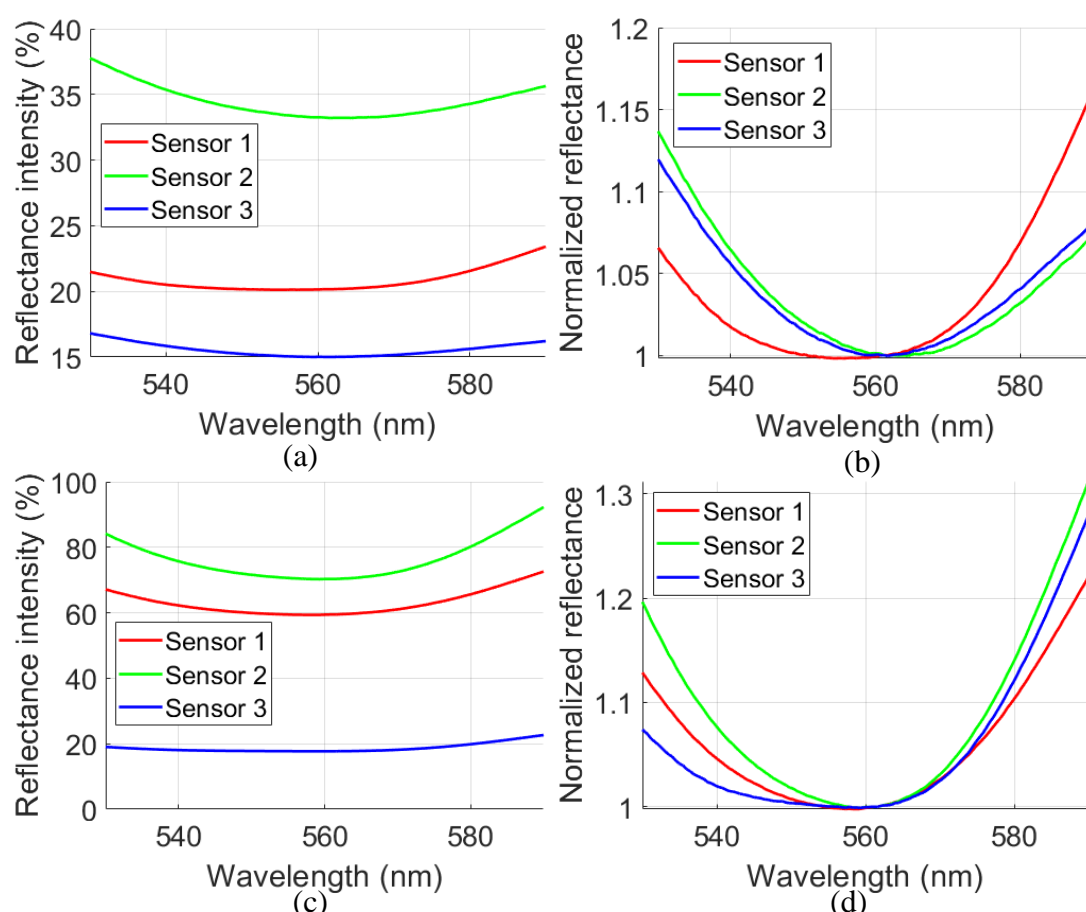


Fig. 5.38: Subject 1 – Porcine trachea (a), (b) and oesophagus (c), (d). Spectra normalized with the white reference standard (a), (c). Then a further Single wavelength normalization at 561 nm (b), (d).

Interestingly, no clear absorbance in the characteristic wavelength range of 530 - 590 nm is seen in the tracheal spectra for the first 30s average after intubation (Fig. 5.38a). Observationally, there is absorbance in the wavelength range for the suspected

oesophagus Fig. 5.38c-d. However, due to the cuff leak described previously for subject 1, likely, the sensors were initially not in good contact with the trachea. This is reinforced when comparing the peak intensities to subject 3, where the same ETT was used for both subjects 3 and 1. The average peak intensity for subject 3, sensor 2, during the first 30s of data acquisition, was  $50,500 \pm 500$ , whereas for subject 1 this was  $17,000 \pm 4000$ . The initial intensity for subject 1 is significantly lower than for subject 3. Furthermore, the standard deviation is significantly more for subject 1 which would be seen for a sensor in poor contact.

Comparing the ratio values for the trachea and suspected oesophagus (Fig. 5.39) shows no difference. The mean and standard deviation of the  $R_1$  values for the trachea and ‘oesophagus’ were both  $1.03 \pm 0.02$ . The  $R_2$  values for the trachea and oesophagus were both  $1.10 \pm 0.04$ . Therefore, it is likely that the oesophageal intubation failed and the ETT was placed into the trachea once again. For this reason, the computational methods will not be applied to the data from this subject 1. The ‘oesophageal’ data from subject 1 will also be removed from any combined computational analysis in the next section, where only confirmed tracheal data will be used.

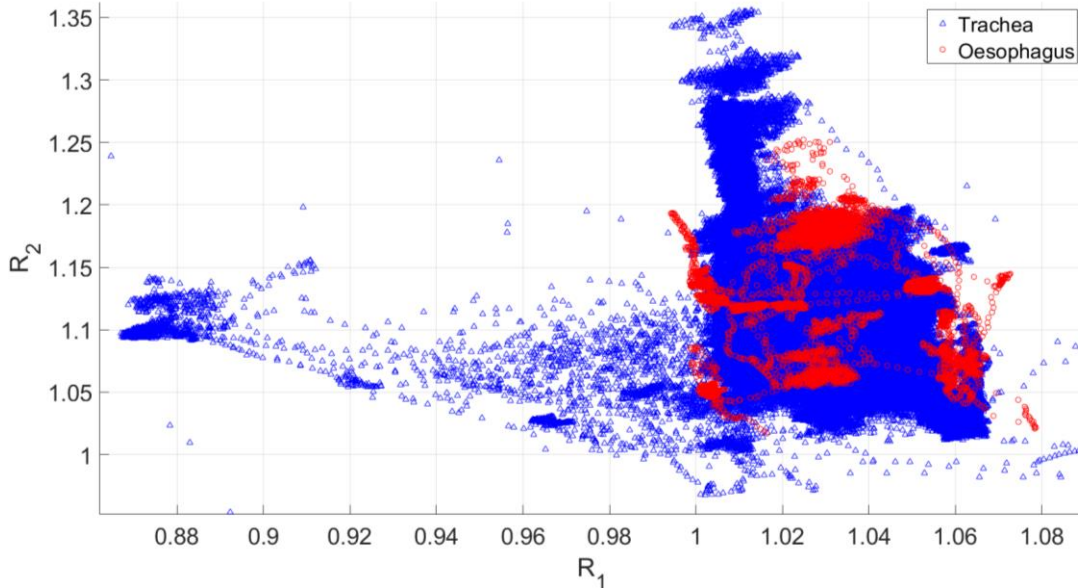


Fig. 5.39: *in-vivo* tracheal and *in-situ* ‘oesophageal’ measurements over the full acquisition for subject 1 (n = 671107, 183.17 minutes).

## 5.5 Combined Analysis

### 5.5.1 LDA, KNN & SVM

The data from the individual subjects were then combined (Fig. 5.40) so that the performance of the sensors and computational methods could be analysed across 3 subjects (9 sensors total). The ‘oesophageal’ measurements for subject 1 were excluded. The mean and standard deviation of the  $R_1$  values across the three subjects for the trachea and oesophagus were  $1.02 \pm 0.02$  and  $1.03 \pm 0.02$ , respectively. The  $R_2$  values were  $1.1 \pm 0.06$ , and  $1.04 \pm 0.03$ .

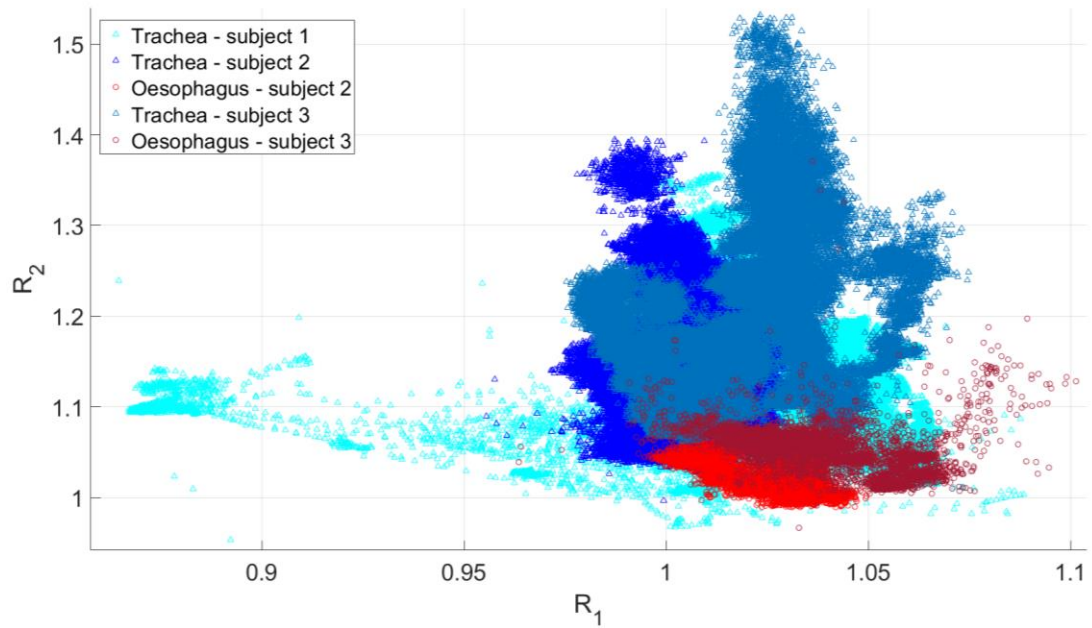
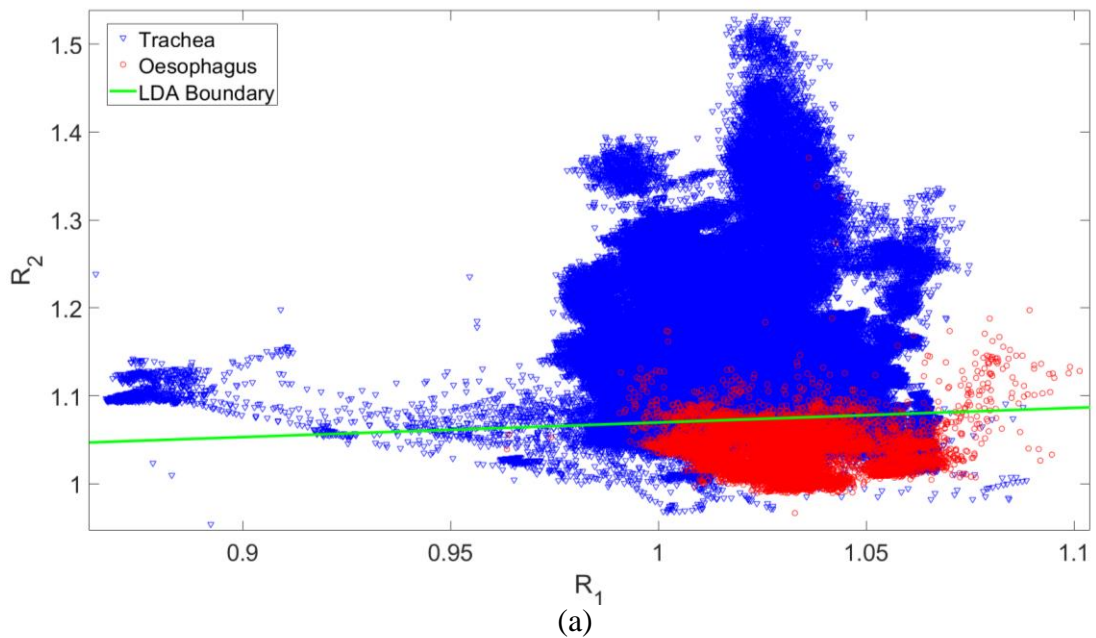


Fig. 5.40: Combined trachea and oesophagus ratio values across the three subjects ( $n = 979706$ , 347.47 minutes across).

Performing LDA on the combined data (Fig. 5.41). The sensitivity using the LDA method was 96.6% and the specificity was 81.8%. The classification is less sensitive and specific when the data from the subjects are combined. This could originate from a variable calibration using the white reference standard or may be naturally occurring variations from the different subjects.



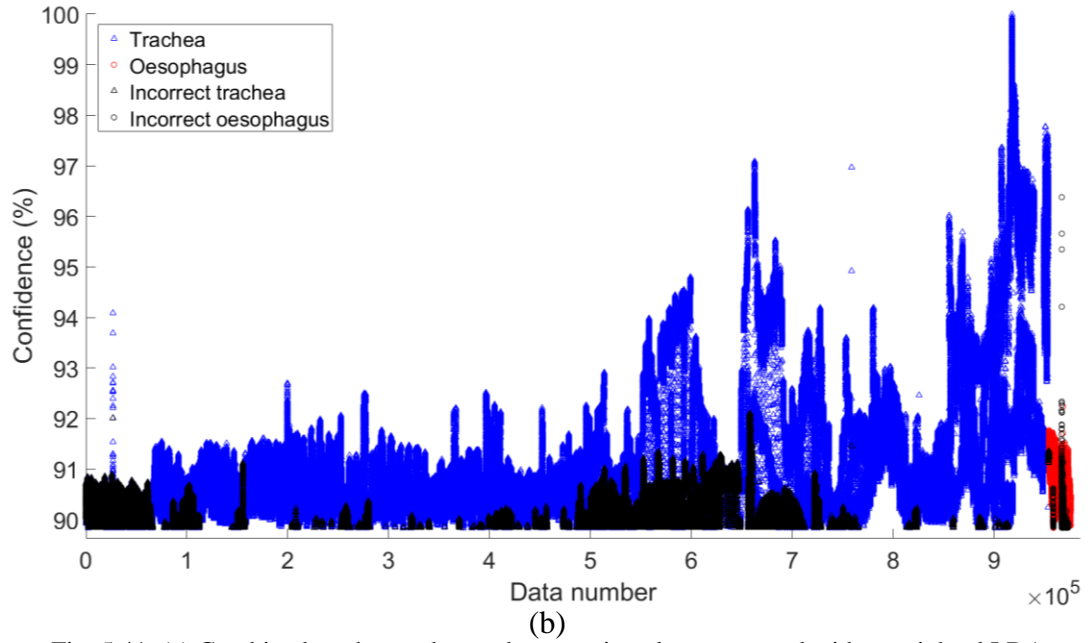


Fig. 5.41: (a) Combined trachea and oesophagus ratio values separated with a weighted LDA boundary. (b) Confidences.

Performing KNN analysis with the combined data from the three subjects yields a sensitivity of 68.1% and a specificity of 93.5%. The sensitivity of this method with the combined data is considerably lower than what we have seen previously when applying this method to individual subjects. This difference is due to the less separable values when combining the data and the substantially different group sizes, where the trachea group has 43 times as many measurements. Unlike the other methods, KNN analysis uses every data point in every calculation and therefore with significantly different group sizes the oesophageal data is more likely to have its closest neighbours as tracheal due to there being more data in that group. If the tissues are highly separable this has a smaller impact on the KNN classification. However, with a stronger overlap between the groups, the oesophageal data is more saturated with tracheal neighbours from the extremes of that group.

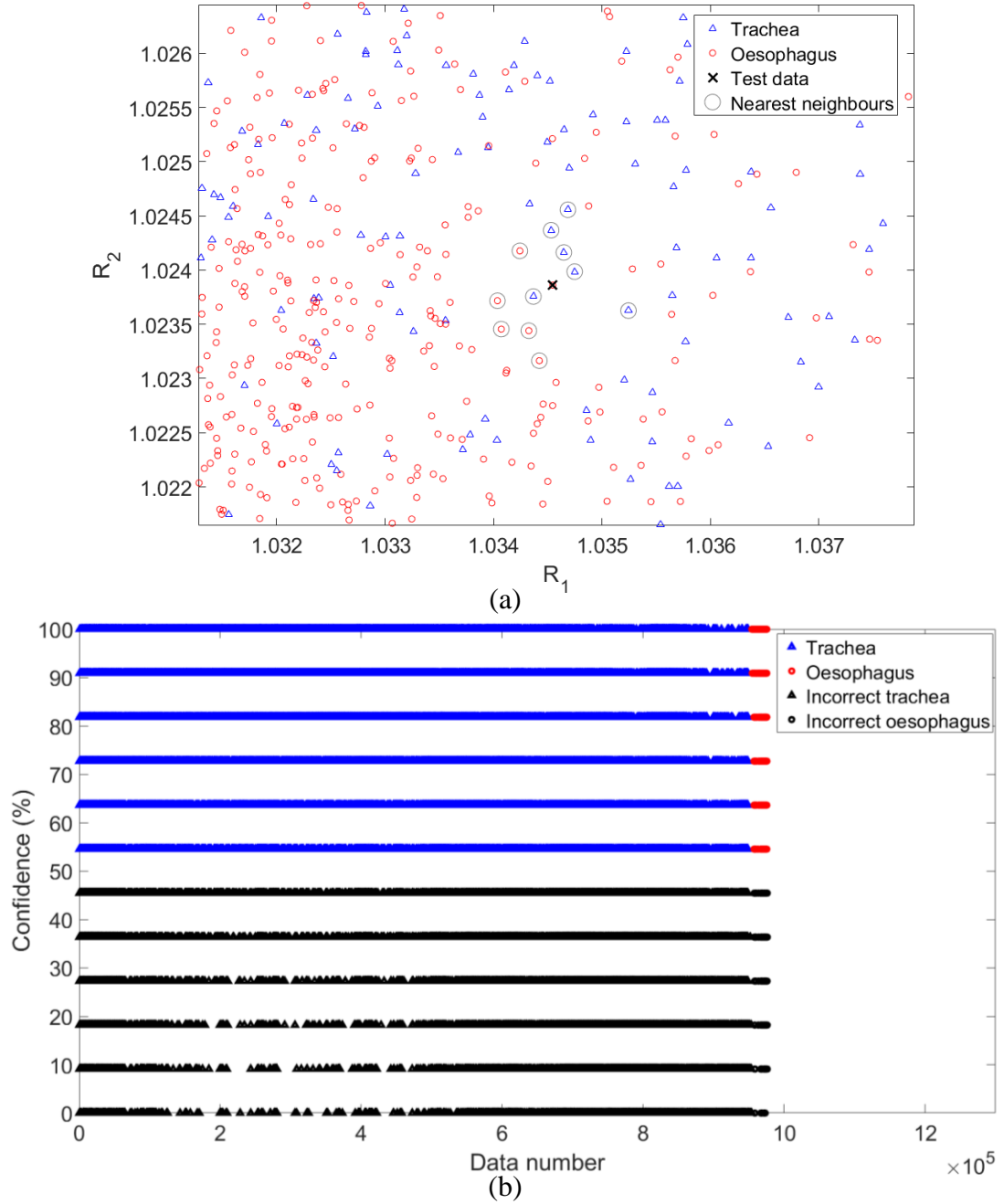


Fig. 5.42: Combined trachea and oesophagus ratio values classified with the KNN method. (a) Example test data, (b) KNN confidences.

The objective function is formed over an iterative process (Fig. 5.43a). The minimum of the objective function reached a value of 0.06 over 30 iterations (Fig. 5.43b). The boundary formed by the SVM method (Fig. 5.43c) gave a sensitivity of 93.5% and a specificity of 89.6%. The confidence in the SVM classifications can be seen in Fig. 5.43d



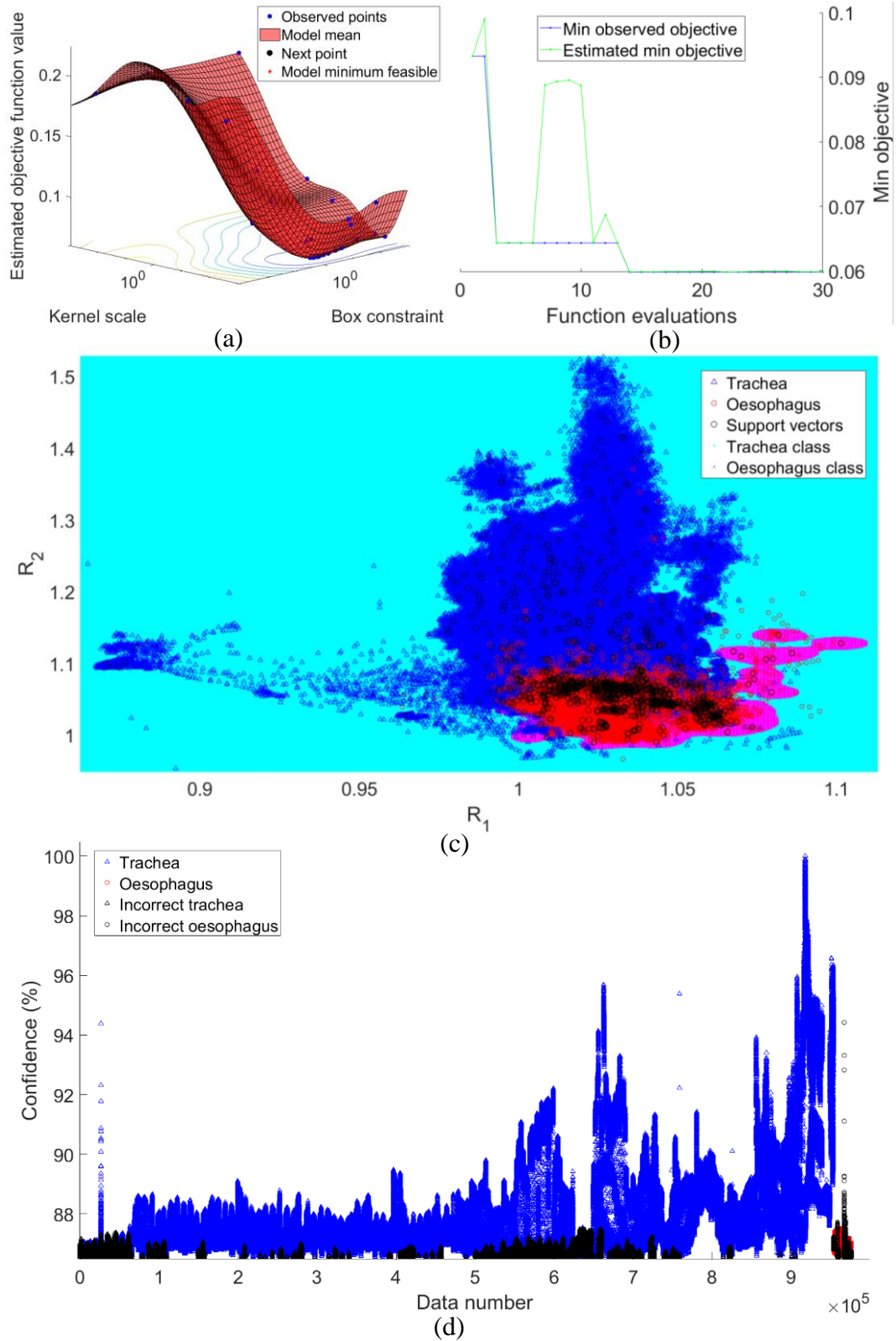


Fig. 5.43: Combined trachea and oesophagus ratio values classified with the SVM method. (a) The objective function (hyperplane). (b) The minimum of the objective function (Min objective) change with the number of function evaluations. (c) The SVM boundary with the trachea and oesophagus classes shaded in light blue and pink, respectively. (d) SVM confidence on the combined tissue classifications.

## 5.5.2 Full Spectrum PCA & SVM

In the previous section, the data from subjects 1, 2, and 3 were combined. The ratio values  $R_1$  and  $R_2$  were then used to classify the spectra as being tracheal or oesophageal using LDA, KNN, and SVM. This current section utilises the entire acquired spectral range by implementing PCA between 450 and 850 nm. Therefore, a maximum of 886 discrete wavelengths are used.

The 979,706 spectra, consisting of 347.47 minutes across 3 subjects were randomly separated into training and testing groups. Each group contained half of the trachea and half of the oesophageal data, such that two groups of size 489,853 were formed. The training data was processed with PCA (Section 4.3.2) so that the features that presented the most variance across the full spectrum were selected. The best-performing components were then used to train an SVM classifier. The SVM model was then verified with the test data whilst utilising an increasing number of components, starting with the most effective.

Table 5.1 Performance of an SVM classifier with an increasing number of the most effective components found from PCA for the combined data from a porcine animal study.

Number of Components used	Sensitivity (%)	Specificity (%)	Correct tissue identification (%)
1	26.1	66.3	46.2
2	40.9	85.7	63.3
3	99.1	90.6	94.9
4	98.1	90.2	94.2
5	99.2	97.2	98.2
10	99.3	97.2	98.3
886	99.3	97.2	98.3

By utilising only 3 PCs a correct tissue identification of 94.9% was achieved. This outperforms the next best classification method (SVM without PCA) where the ratio values  $R_1$  and  $R_2$  (consisting of 3 wavelength total) were used. This implies that the best wavelengths were not used when forming these ratios. Furthermore, by utilising 5 components a correct tissue identification of 98.2% was achieved. The use of 10 components produces a marginal improvement to 98.3%. Increasing the number of components beyond 10 does not produce an increase in either sensitivity or specificity. To determine the most effective wavelength bands to distinguish the tissues, a visual plot of the 5 most effective principal components was generated (Fig. 5.44).

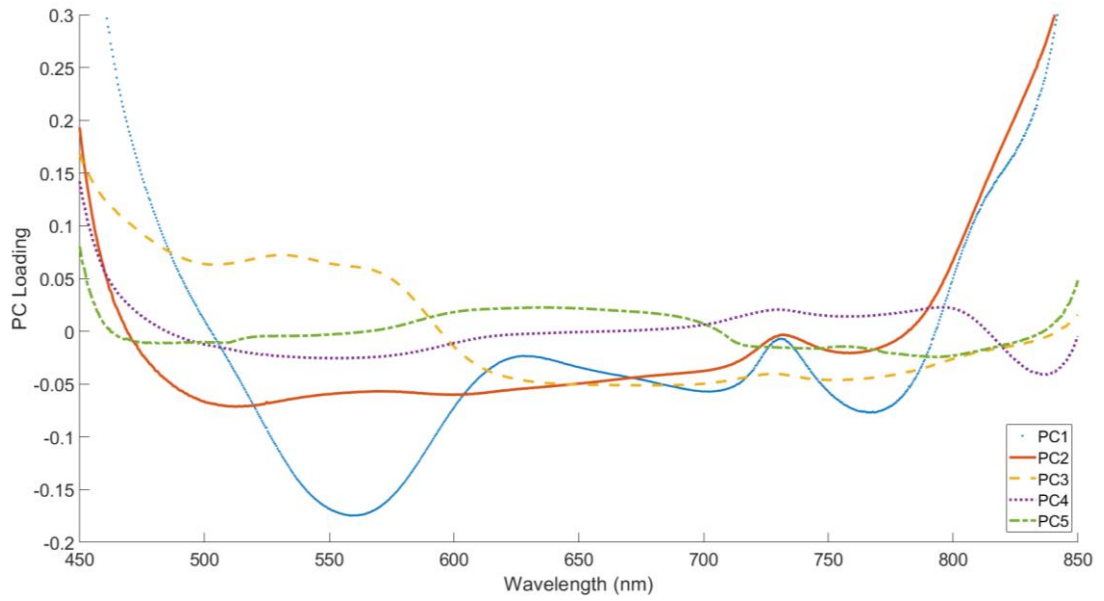


Fig. 5.44: Visual representations of the 5 most effective principal components used to distinguish tracheal and oesophageal tissues.

A large variance can be seen in the PC loadings in the 530 – 590 nm wavelength regions, which corresponds to the haemoglobin band, as is the focus of this research project. However, further patterns emerge as can be seen from Fig. 5.44. Particularly in the wavelength regions of 650, 725, and 825 nm. A large divergence in these PCs in these regions represents a large variance in the acquired spectra at these wavelengths. Therefore, these wavelengths may be of interest in future research to better distinguish the tissues, as is suggested by the increased tissue identification when the first 5 PCs are used when compared to the ratios  $R_1$  and  $R_2$ . However, broadening the utilised wavelengths limits what can be used as a light source and detector, where the production of a minimum viable product (MVP) that implements cheaper LEDs and photodiodes may not be possible (Section 6.2.5) with this method.

## 5.6 Summary & Discussion

The three classifiers explored in this chapter (LDA, KNN, and SVM) are compared in Table 5.2 for subjects 3 and 2, with no classification performed for subject 1 as it is likely that oesophageal measurements were not made. The combined measurements for subjects 3 and 2 along with the tracheal measurements for subject 1 are also presented (combined).

Table 5.2 Comparison of the classifiers used to distinguish the tissues of 3 porcine subjects.

		Sensitivity (%)	Specificity (%)	Correct tissue identification (%)
LDA	Subject 3	98.0	81.8	89.9
	Subject 2	95.0	96.8	95.9
	Combined	96.6	81.8	89.2
KNN	Subject 3	95.5	99.9	97.7
	Subject 2	98.1	98.6	98.3
	Combined	68.1	93.5	80.8
SVM	Subject 3	97.1	99.1	98.1
	Subject 2	96.7	99.2	97.9
	Combined	93.5	89.6	91.6

By utilising the full acquired spectrum to generate the most effective PCs and then using the SVM method to classify the spectra, a correct tissue identification of 98.3% can be achieved by using the first 10 PCs. The best-performing classifier when only  $R_1$  and  $R_2$  are used, was the SVM method which achieved the highest correct tissue identification for the combined subject data of 91.6%, where this refers to the average of the correct tracheal and oesophageal identifications. However, sensitivity (percentage of correct oesophageal identifications) is the most important parameter clinically as they are the most dangerous when incorrectly identified. The LDA method produced a comparable identification of 89.2% (1.4% lower). The KNN method produced a strong identification for the individual subjects, with the highest average correct identifications for subject 2 (0.4% higher than the SVM method). However, the combined KNN analysis performed a weak identification of 80.8%, caused by the severely different group sizes. Therefore, if the group sizes were made comparable by comparing the trachea measurements in batches to the oesophagus this approach would likely be more successful. By averaging the tracheal spectra together, (effectively reducing the integration time) the number of measurements could also be reduced, which may improve the performance of this method.

The study found no difference between the ratio values measured at different orientations in the trachea, with the three sensors in each ETT producing on average the same values. However, there is a greater variance in the trachea when compared to the oesophagus, caused by a varying cuff inflation pressure. The study consisted of 3 subjects and a larger study is required to verify these findings. Practically speaking, it is easier to obtain tracheal spectra as this can be achieved during standard intubation procedures whilst an airway is secured. Achieving measurements in the oesophagus requires a post-mortem measurement, double intubation of both the trachea and oesophagus, or tracheal intubation to be stopped briefly whilst the oesophagus is intubated. All these methods are challenging, especially in a clinical trial.

The tissue identification is performed using the absorption feature of OHb in the 530 – 590 nm wavelength range. Post-mortem a series of physiological changes occur, with the most relevant being rapid oxygen desaturation. This change in the physiological condition of the patient likely inhibits the performance of the ETT placement sensor due to there being no perfusion and little detectable oxygenated blood. Therefore, the sensor may not perform strong tissue identifications for patients in cardiac arrest. However, the USAISR has demonstrated that the spectral feature is detectable during relatively short periods of asphyxiation [87], and further research is required to understand the success of this technology in patients undergoing rapid physiological changes. The post-mortem trachea measurements have been excluded throughout this analysis. Therefore, only a comparison between *in-vivo* (living) tracheal and *in-situ* (recent post-mortem) oesophageal measurements is made. This difference could therefore contribute to a change in the spectra of the tissues and a comparison to an *in-vivo* oesophagus is preferable in future studies.

Interestingly, measurements made in the trachea of *ex-vivo* porcine samples (Chapter 4) present the OHb spectral feature more strongly than *in-vivo* measurements. This can be seen by the *ex-vivo* trachea ratio values being below 1 (indicating more absorption at 543 and 578 than 561 nm), whereas the *in-vivo* measurements were generally above 1. The cause of this originates from multiple factors. The first is that there may be some residual blood on the outside of the *ex-vivo* samples which become highly oxygenated when exposed to air. This blood is more detectable when the sensor is in the trachea due to it being thinner and more transparent than the oesophagus. Furthermore, as the *ex-vivo* samples begin to decompose through autolysis and putrefaction, oxygenated blood is released from the blood vessels making it more detectable. The samples may also be differentially vascularised and the variation between the fibre separations also affects the detectable penetration depth of the light. These effects may explain why the characteristic is more detectable in tracheal *ex-vivo* samples when compared to oesophageal samples. The thicker less transparent oesophageal mucosa attenuates the light and limits the interaction with OHb on the outside of the samples, whereas the thinner less transparent tracheal mucosa does not. An example of this can be found in a study from the literature on the re-oxygenation of livor mortis in a cold environment (see Fig. 5.45, [180]). The bodies were kept in refrigeration between 4 - 6 °C and the absorption feature of OHb gradually became more dominant over time, indicating re-oxygenation of the tissues. A similar effect could artificially increase the detectability of OHb in *ex-vivo* samples.

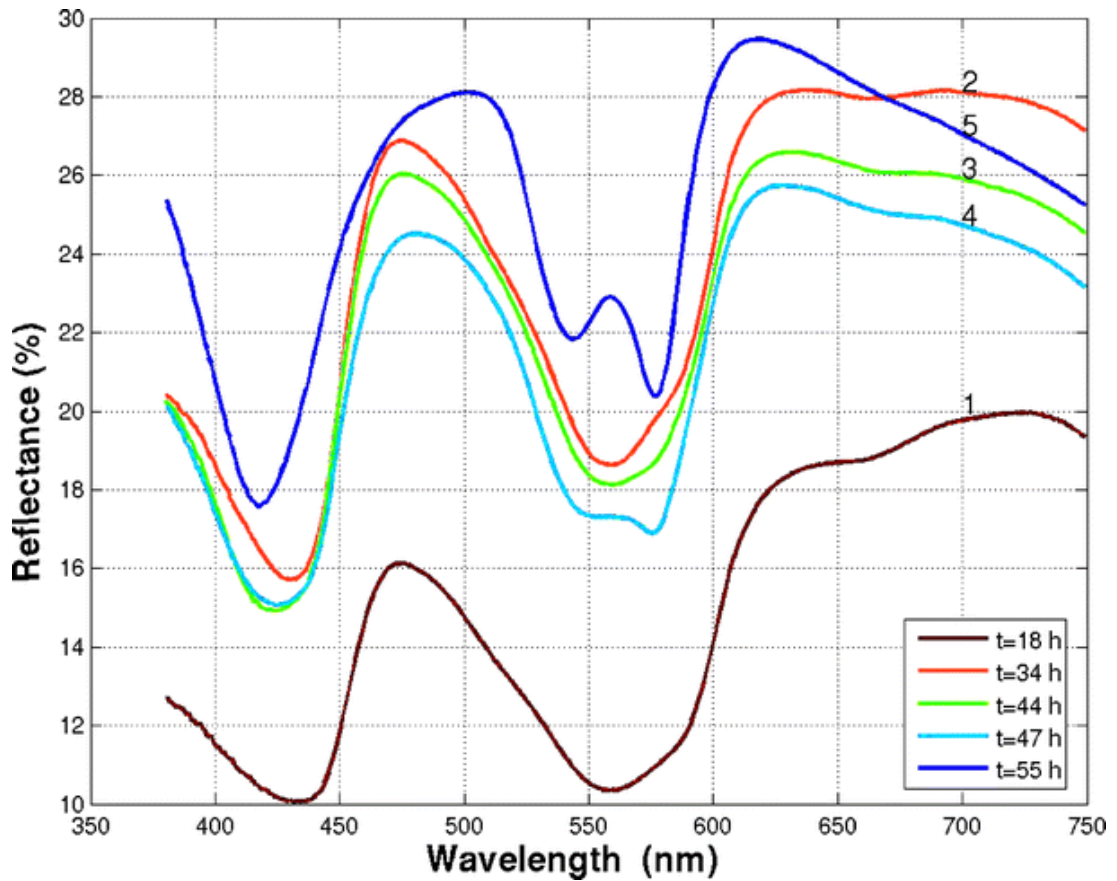


Fig. 5.45: Spectral reflectance of a human livor between 18 and 55 hrs [180].

This level of detectability during *ex-vivo* measurements motivated a more compact sensor design with a smaller fibre separation distance of 0.875 mm, where the optimal was found to be between 1.27 and 2.54 mm (Section 3.3). Therefore, a sensor with a larger fibre separation distance may yield a stronger classification between the two tissues allowing the light to interact with more OHb. Furthermore, an LED with a higher optical output or a sensor design which can receive higher optical power may yield a stronger classification due to a higher signal-to-noise ratio. However, a maximum correct tissue identification of 91.6% was achieved using the SVM method. Therefore, the developed sensor can accurately distinguish the tissues in an animal study, given a range of cuff inflation pressures, movements of the ETT, and during neck operations as described by the timeline (Fig. 5.15).



# Chapter 6 Conclusions & Further Developments

## 6.1 Introduction

This chapter describes further developments to the ETT placement sensor outside the main scope of this research. Suggested improvements to the experimental, and sensor design are provided. A potential method for amplifying the weak presence of the OHb absorption feature in the trachea and then classifying it with an artificial neural network is then described. Guidance on reducing the cost of the opto-electronic units in the form of a minimum viable product (MVP) is then explored. A description of how this technology can be used in different areas other than ETT placement is then given, with its viability assessed. Finally, a conclusion summarises the main findings of this research.

## 6.2 Further Developments

### 6.2.1 Experimental Design

The developed ETT placement sensor has been verified in *ex-vivo* samples and an *in-vivo* animal study. However, there is a potential to improve the design and protocol for both these methods. The *ex-vivo* samples may have contained highly oxygenated blood on their exteriors, which may cause the increased presence of the OHb absorption feature when compared to *in-vivo* models. Cleaning the outside of the samples more thoroughly may make the *ex-vivo* models more representative of the condition of the *in-vivo* tissues. However, there is evidence in the literature that organs and tissues can re-oxygenate post-mortem [180], from the decay of cells and organs in the presence of ambient oxygen in the air. Acquiring samples from a source where they have been excised more recently may mitigate this. The use of *ex-vivo* samples has been beneficial to this research in the development of computational methods. However, it may prove that *ex-vivo* samples are too spectrally different to *in-vivo* measurements, with regard to the absorption features of OHb, to be used as high-quality models in future research.

A large quantity of data was generated from the animal study of 3 porcine subjects over several hours. However, a study consisting of a larger number of subjects is required to validate findings. Furthermore, confirmation of spectral signatures could be performed during bronchoscopy. There is also an absence of *in-vivo* oesophageal data. Intubating the oesophagus of living subjects requires ventilation to be stopped, or both the trachea and oesophagus to be intubated simultaneously. Both these approaches are challenging in an animal or clinical study. Therefore, oesophageal measurements could be performed endoscopically as intubation of the oesophagus can cause damage to the mucosa. Another possible solution is to attach the ETT placement sensor to a smaller medical device, such as a guide bougie, which is sometimes used to assist intubations. Another device the sensor can be incorporated into is an oesophageal thermometer, which is used to measure the core temperature of a patient. Both these devices are smaller than an ETT and may reduce the risk of harm to the subjects in any further studies.

During future animal studies, endoscopic imaging of the trachea would help to verify the position of each sensor relative to the cartilage. Furthermore, movements of the ETT and sensor could be observed, such as those caused by ventilation. Post-mortem excision of the trachea and oesophagus would allow *ex-vivo* measurements in a more controlled environment. Therefore, a comparison could be made between the same trachea and oesophagus during *in-vivo* and *ex-vivo* measurements. This may help to explain some of the spectral differences between the two models.

## 6.2.2 Sensor Design

A compact fibre optic ETT placement sensor has been developed in this research. However, there are many ways to improve this design further. The chosen method for emitting light out of the face of the sensor is to bend the fibres into a ‘J-shape’, which is preferable to cleaving the fibres at 45°. However, there are alternative methods of improving the intensity of optical power interacting with the tissues. Coating or sputtering the tip of the cleaved fibre with a reflective material such as silver (Ag) [181,182,183], or attaching a prism to the fibre [184], may emit a higher light intensity perpendicular to the fibre axis – see Fig. 6.1.

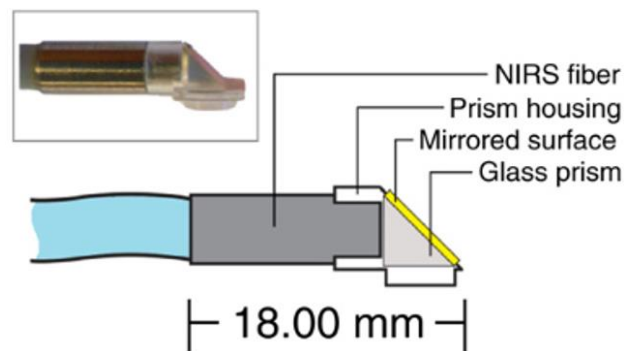


Fig. 6.1: Diagram of near-infrared spectroscopy (NIRS) optical fibre with a prism attached [184].

The optimal fibre separation distance is dependent on the choice of opto-electronic components. However, a distance between 1.27 and 2.56 mm was found to be optimal with those described here. Preliminary measurements demonstrated a reduction in fibre separation distance to 0.875 mm and produced distinguishable tissue spectra. This allowed a more compact sensor to be fabricated. Therefore, an experiment using 10 sensors with a fibre separation distance of 0.875 mm was designed. The experiment had a maximum correct tissue identification of 89.2% using the SVM method, which is comparable to the success of ETCO<sub>2</sub>. An experiment performed on 9 samples with one sensor (fibre separation distance of 1.5 mm) demonstrated a correct tissue identification of 100% using computational methods. Two different sensor designs were used between these experiments, where the difference in the success of the classifications was attributed to batch-to-batch variations in the 10-sensor experiment. However, the change in the sensor design by reducing the fibre separation distance may have impacted the performance of the sensor. The sensor design containing fibres separated by 0.875 mm was used in an animal study of 3 porcine subjects, where a correct tissue identification of 91.6% was achieved. However, the spectral feature of OHb in the 530 – 590 nm wavelength region had less absorption in the two troughs relative to the central peak, producing ratio values that differ from *ex-vivo*

measurements. Therefore, the feature is less clear for *in-vivo* measurements with this sensor. Future designs that incorporate a light source with a higher optical output, a sensor design that causes more light to interact with the tissue, and a larger fibre separation may improve the classification.

### 6.2.3 Differential Method

The OHb absorption feature in the animal study (Section 4.3) can be extracted through a differential method. As an example, this method (Fig. 6.2) was applied to a single spectral example taken in the trachea of subject 2 in the animal study (Section 5.4.3). The intensity spectrum (Fig. 6.2a) was differentiated (Fig. 6.2b) which amplified the spectral absorption feature of OHb in the 530 – 590 nm wavelength region. However, there is a shift in the wavelength position of the feature due to the differential method. This is caused by the wavelengths that lead up to and out of the peaks becoming the regions of the steepest gradient. The spectral feature becomes clear, although the absorption features are shifted by approximately 13 nm to the left. However, the noise is also amplified and therefore a 20-wavelength moving mean filter is applied after differentiation (Fig. 6.2c). The signal is then normalized with the white reference and then at the new central peak of 547 nm. This method highlights the presence of the OHb feature in the trachea with the sensor, although there is less absorption when compared to the *ex-vivo* samples, as described in Section 5.6. Nevertheless, this method demonstrates promise.

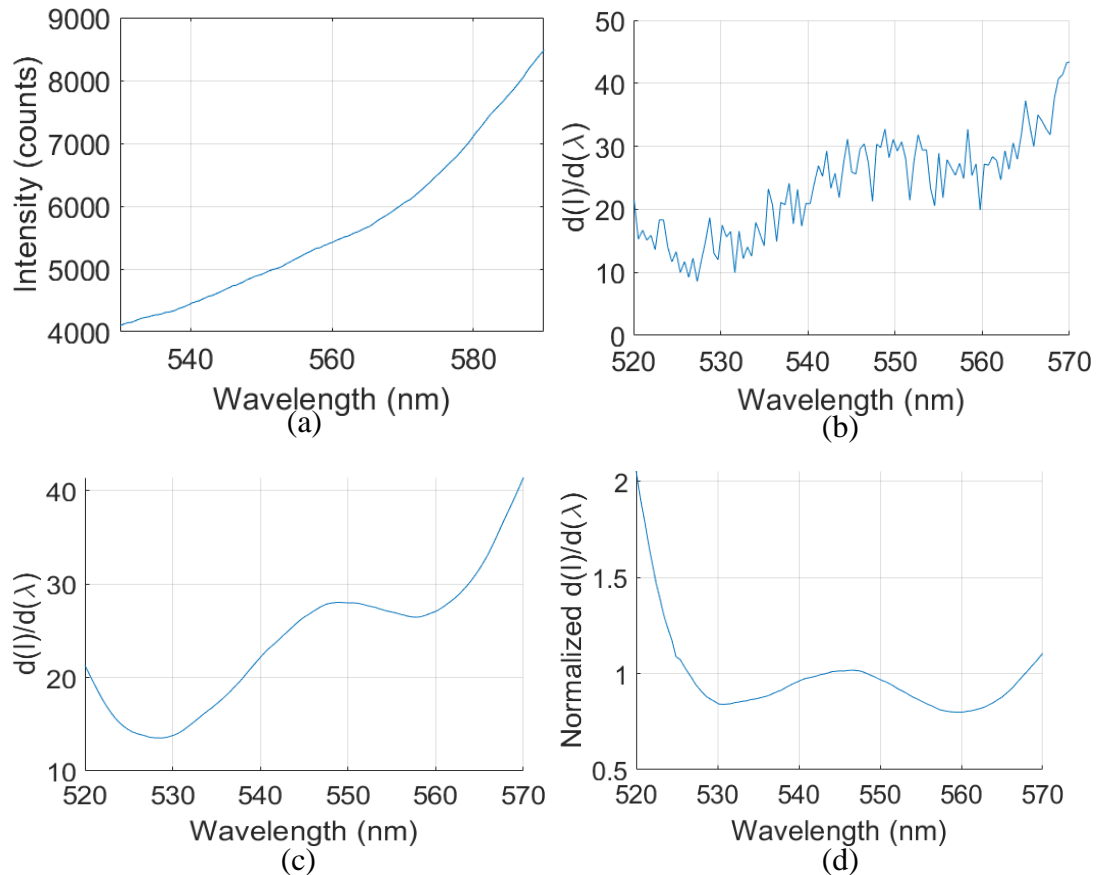


Fig. 6.2: Example differential method used to amplify the spectral feature of OHb. (a) Raw Intensity spectrum. (b) Differential intensity spectrum. (c) Differential intensity spectrum with a 20-wavelength moving mean average applied after differentiation. (d) Differential spectrum normalized by a white reference standard and a single wavelength normalization at 547 nm.

## 6.2.4 Machine Learning

Machine learning algorithms are a popular type of artificial intelligence that allows a computer to ‘learn’ without explicit programming [185,186]. They can be used as powerful classifiers [187]. In this research, machine learning models such as SVMs have been used with reduced spectral data (spectral ratios) and reduced capabilities. However, Machine learning algorithms can be used to classify full spectral data sets. Fredriksson *et al.* applied a machine-learning approach to detect oxygen saturation using diffuse reflectance spectroscopy [188]. Tsui *et al.* explore this approach by using a machine learning algorithm trained on Monte Carlo simulations to model the diffuse reflectance spectra of human skin [189].

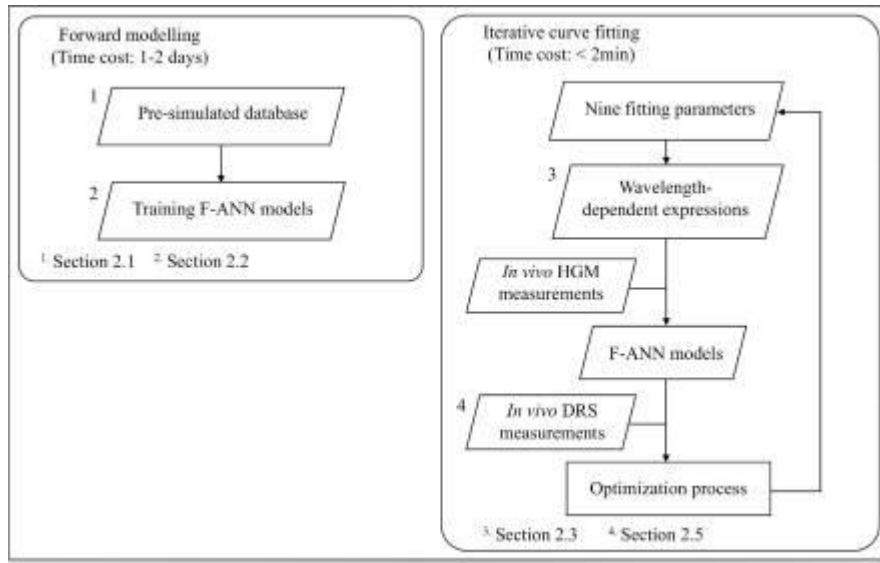


Fig. 6.3: Flowchart of machine learning spectral modelling and a curve fitting iterative process [189].

A similar approach can be used for the spectral data acquired in the trachea and oesophagus with the developed ETT placement sensor. Therefore, a suggested development of this research is to further implement a machine learning model over the full spectral range measured to improve classifications and model the tissues.

## 6.2.5 Minimum Viable Product (MVP)

The iTraXS ETT has fibre optic sensors integrated into the cuff which are capable of PPG measurements, tube placement detection, and pressure measurements. However, by reducing this technology to only tube placement capabilities, the complexity and cost of components can be significantly reduced. There is also scope for the components used for tube placement identification to be reduced further to an MVP, one whose cost is further reduced. This section describes such a product, with preliminary measurements to assess its viability.

The highest-cost opto-electronic component used for fibre optic tube placement detection is the spectrometer. For example, the spectrometer used in the second animal study (Ocean Optics, model OCEAN-HDX-XR), retails in 2022 for ~£6k [190]. However, cheaper alternative spectrometers may offer sufficient resolution. The spectrometer and the other opto-electronic units are multiple-use, with only one being

required for use with one patient at a time, similar to the use of a ventilator. Therefore, unlike the ETT, opto-electronic units only need to be purchased once. However, by reducing the cost of the spectrometer, the price of the product can be reduced significantly. There are cheaper alternative spectrometers that could be used in place, such as Ossila's UV-Vis optical spectrometer (Ossila, model G2001b2), which retails for ~2k. However, from this research, we have seen that there is a relatively narrow wavelength region of interest for ETT placement. Specifically, the wavelengths 543, 561, and 578 nm are required to form the ratio values  $R_1$  and  $R_2$  (Eq. (3.8) and (3.9)). Therefore, the light at these three wavelengths could be detected by relatively cheap photodiodes.

There are two main approaches to achieving detection by a photodiode. Light from three narrow bandwidth LEDs centred at each of the three wavelengths can be cycled through in a TDMA fashion. A single photodiode then detects the reflected tissue light of each of the LEDs (Fig. 6.4). The second approach is to use a single broadband LED which produces light across all three wavelengths which are then optically filtered and detected by three photodiodes.

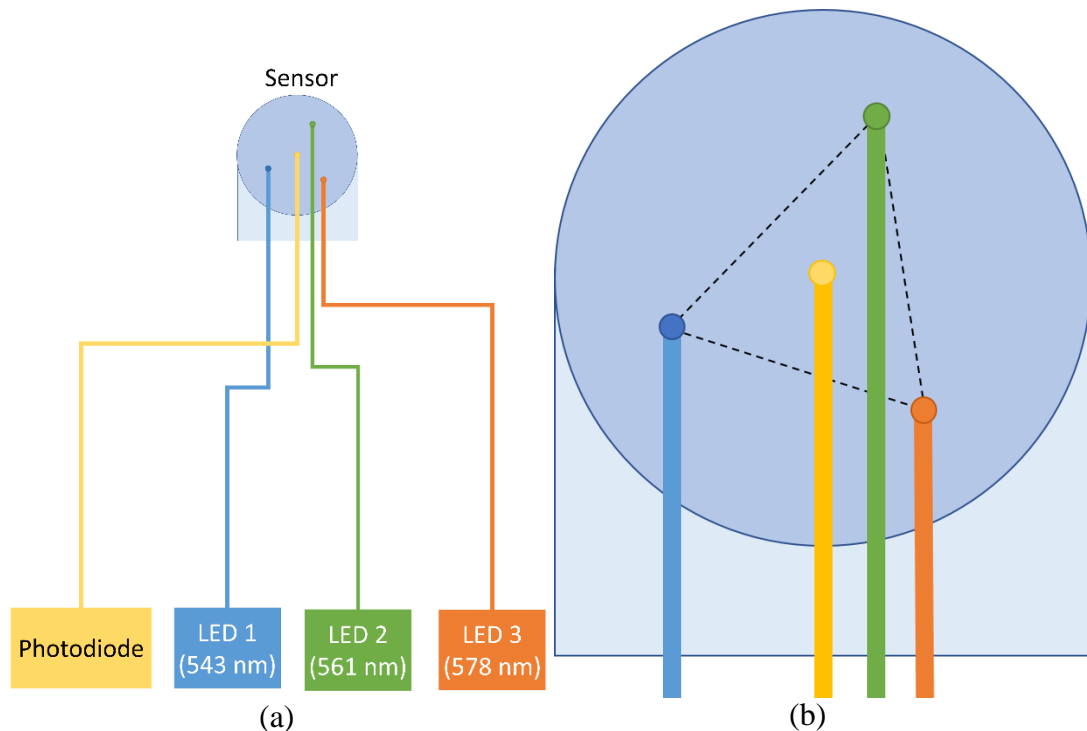


Fig. 6.4: (a) Concept design for an ETT placement sensor which uses a photodiode and 3 narrow bandwidth LEDs. (b) Enlarged sensor configuration with an isosceles triangle (black dashed line) used to highlight the position of the sensors.

The first concept sensor design (Fig. 6.4) contains three illumination fibres, one for each LED, and one detection fibre which connects to a photodiode. The limiting factor is whether LEDs with a narrow enough bandwidth could be acquired, with further research required to verify this. The LEDs would be cycled through so that light is emitted from one LED at a time, assuming appropriate warm-up time and optical power fluctuations etc. can be achieved. Alternatively, three relatively low-power laser diodes could be used in place of the LEDs if narrow enough bandwidth is not achieved. The detection fibre (yellow in Fig. 6.4) is at the centre of the circular sensor head. The

illumination fibres are at each corner of an isosceles triangle centred in the sensor head. The illumination fibres are all the same distance from the detection fibre. Furthermore, by introducing a rotation to the triangle from the central plane of the sensor, the fibres are not on top of each other and the sensor thickness is kept to a minimum. Alternatively, a configuration of a single broadband LED and three photodiodes is another inexpensive alternative to a spectrometer.

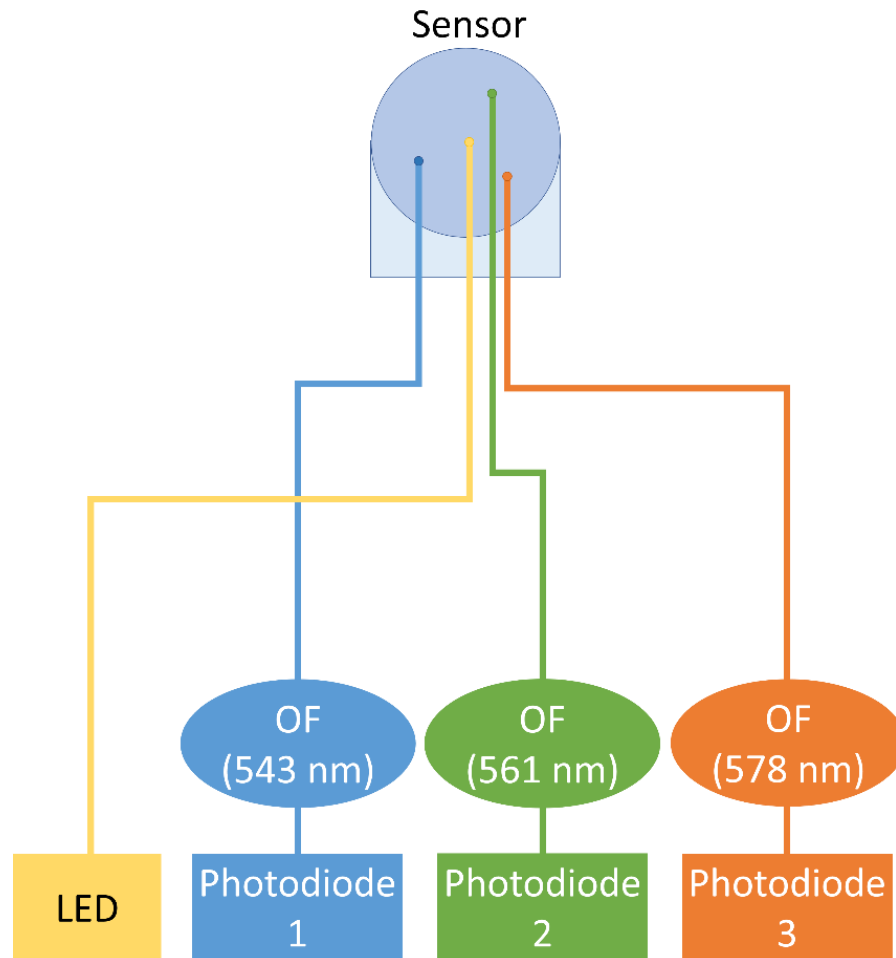


Fig. 6.5: Concept design for an ETT placement sensor which used a single broadband LED and three lens and photodiode pairs. OF refers to a narrow bandpass optical filter, centred on each of the spectral characteristic wavelengths (543, 561, and 578 nm).

The three photodiode concept sensor design (Fig. 6.5) has a similar design to the three LED sensor (Fig. 6.4b). However, the three fibres on the corners of the triangle would be detection fibres, with a single centralised illumination fibre. Each of the detection fibre's light would be filtered by a narrow bandpass optical filter before coupling with a photodiode. In this way, only light with the desired wavelength is detected by the photodiodes. The limiting factor in this design is if a high enough optical power, at a narrow enough bandwidth, is retained after passing through the optical filters. This concept was investigated using the experimental design shown in Fig. 6.6. The broadband LED (Fiber-Coupled LED, Thorlabs, model MBB1F1), was connected to a 500  $\mu\text{m}$  diameter POF (commercial grade PolymethylMethacrylate (PMMA)). The POF was connected to a linear variable optical filter (Ocean Insight, model LVF-HL) set manually to a pass wavelength of 561 nm. Another POF was coupled to the back



of the variable optical filter and a spectrometer (Ocean Optics, model USB2000+UV-VIS-ES). The spectrometer was connected to a computer (tower PC running Windows 7) and processed by OceanView software (Ocean Insight, version 1.6.7). The spectrometer integration time was set to 30 ms. Spectra were acquired for 60s and then averaged by the ocean view software, generating a single averaged spectrum.

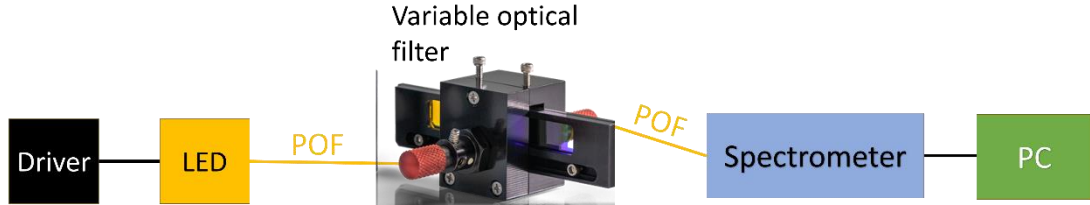


Fig. 6.6: Experimental design of light from a broadband LED being passed through a variable optical filter and detected by a spectrometer.

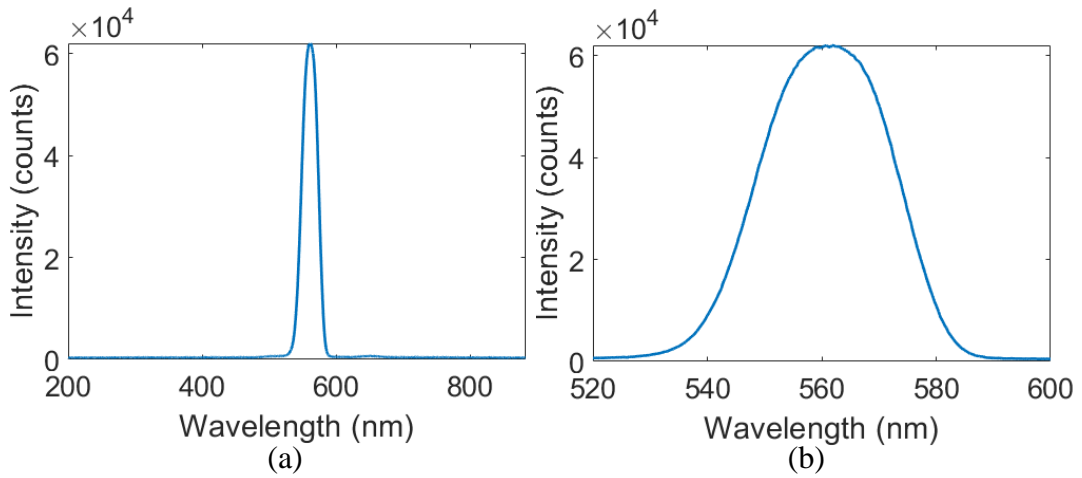


Fig. 6.7: Spectra from a broadband LED coupled to a variable optical filter set to 561 nm. (a) Full spectral wavelength range. (b) 520 – 600 nm wavelength range.

By coupling the LED directly to the variable optical filter with a plastic optical fibre a high intensity is measured by the spectrometer at an integration time of 30 ms. The peak intensity was  $6.14 \times 10^4$  counts. By neglecting the wavelength variations of the detected light and utilizing only the area under the spectra, a comparison to the optical power measured by a photodiode is made. The area of the spectrum in Fig. 6.7 was  $1.73 \times 10^6$ . Therefore, the viability of using photodiodes and optical filters can be modelled by the use of a spectrometer. The full width half maximum (FWHM) of the resulting spectra is 13.5 nm, with a transmission band (wavelength range where the intensity reduces to 99 % of maximum) of 26.8 nm. The intensity detected at wavelengths of 543 and 578 nm were 25.9 and 27.9% of the maximum. The first POF (on the left in Fig. 6.6) was then removed and replaced with one of the illumination fibres in the ETT placement sensor (three-fibre circular sensor with a rectangular base, Fig. 3.44). The detection fibre was then connected to the input of the variable optical filter. The ETT placement sensor was then placed inside an *ex-vivo* porcine trachea.

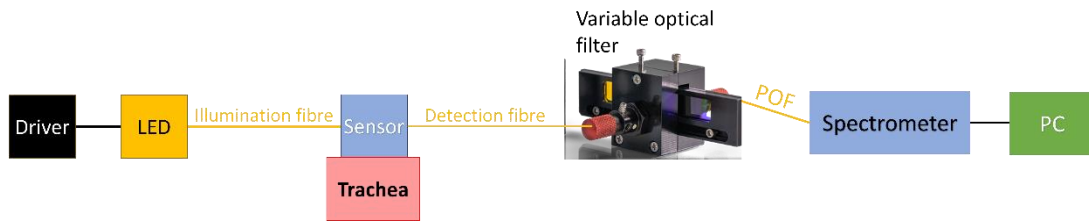


Fig. 6.8: Experimental design of light from a broadband LED being connected to the ETT placement sensor and then placed in contact with an *ex-vivo* porcine sample and connected to a variable optical filter and detected by a spectrometer.

The experimental design described in Fig. 6.8 closely resembles the concept for use with a photodiode as opposed to a spectrometer. However, a spectrometer was used here due to its simplicity and availability at the time. A different spectrometer with a higher sensitivity (Ocean Optics, model OCEAN-HDX-XR) was used because of the decreased light intensity. The integration time was kept at 30 ms. 3 spectra were averaged by the OceanView software, which was chosen to give a response time of less than 100 ms, although this is conservative, and a higher integration may have been appropriate.

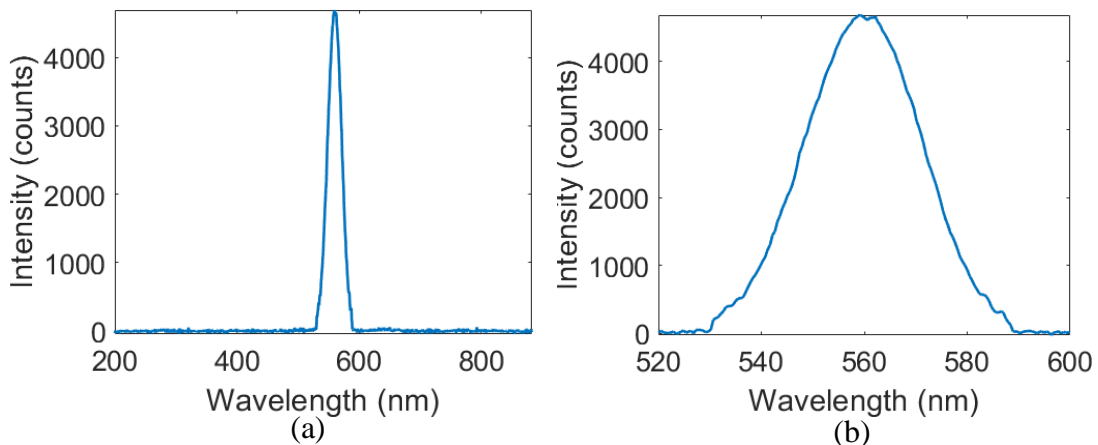


Fig. 6.9: Spectra from a broadband LED coupled to the ETT placement sensor placed on an *ex-vivo* porcine sample and then through a variable optical filter set to 561 nm. (a) Full spectral wavelength range. (b) 520 – 600 nm wavelength range. Note the reduced count compared to Fig. 6.7, indicative of the reduction in light power

The intensity of the peak detected optical power has been reduced to 4693 counts. The spectra area has been reduced to  $1.34 \times 10^5$ . The signal is closer to the limit of detection due to the low optical power, even with the use of a spectrometer with higher sensitivity. The optical filter used was variable so that the appropriate bandpass could be chosen. A standard optical filter with a specific bandpass is a cheaper alternative, although due to the very specific requirements a custom design may need to be manufactured. Furthermore, a spectrometer was used to detect the light, whilst the purpose of this experiment was to see the possibility of the use of a cheaper alternative such as using a photodiode.

## 6.3 Applications in Other Areas

The technology developed here has many potential applications throughout healthcare other than ETTs. A clear alternative is identifying the correct placement of a naso-/oro- gastric tube [191] in the oesophagus (and then the stomach), as opposed to the

trachea (Fig. 6.10a, [192]). It may also be easier to obtain preliminary data from human subjects in this application when compared to UOI. A naso-/oro- gastric tube is a thin hollow plastic cylinder (Fig. 6.10b, [193]), which is inserted through the nose in the case of a nasogastric (NG) tube, or through the mouth for an orogastric (OG) tube. A gastric tube is used as a temporary feeding tube for patients and can also be used to deliver medicines. The gastric tube may also be used to suction fluids from the stomach. For example, during a gastric lavage (stomach pumping) to remove ingested toxins. The developed ETT placement sensor could be applied to this area of healthcare with relatively few modifications, as the problem is reversed. The desired outcome is therefore to correctly identify whether the gastric tube has been placed down the oesophagus. Furthermore, the ideal placement is where the tip of the tube has just entered the stomach through the gastro-oesophageal junction. Typically, gastric tubes have a diameter of 3 - 6 mm, with nasogastric tubes generally being smaller to fit through the nasal cavity [194,195]. However, smaller diameter tubes may be used for neonates or larger diameter tubes for a more rapid gastric lavage. Due to the developed sensor having a compact size, it could potentially be integrated onto a naso-/oro- gastric tube with no impact on its performance.

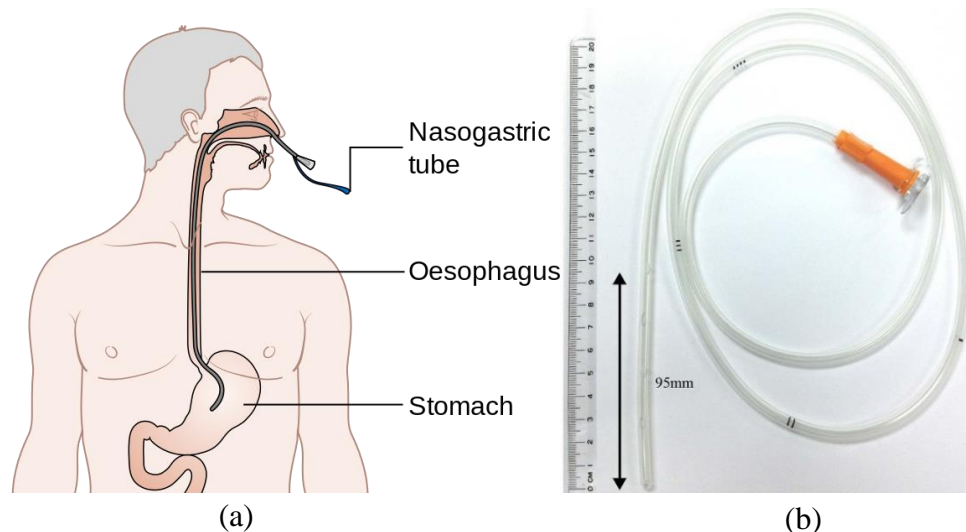


Fig. 6.10: Nasogastric tube placement in the body [192]. Nasogastric tube [193]. An alternative example of where the technology in this research could be applied in Healthcare.

Some of the same techniques used for ETT placement detection in healthcare are used for gastric tubes (with reversed predictors), such as capnographical methods and imaging techniques. However, there is less implementation of these techniques for a few reasons. The procedure is much less time sensitive and several slow attempts can be made with little risk to the patient. The gastric tube is also thinner and more malleable than an ETT and can be more easily curved into the oesophagus. Unrecognised gastric tube placement has severe complications, mainly due to the delivery of food substances to the lungs. These substances retain in the lungs and limit respiration. Furthermore, the decay of food substances can lead to pneumonia and other diseases. A 2021 publication by Motta *et al.*, titled ‘Nasogastric/nasenteric tube-related adverse events: an integrative review’ [196], reviewed 69 primary studies, finding death reported in 16 articles. Most of the adverse effects were from respiratory

harm related to gastric tubes. A 2016 report [197], found a 2% tracheopulmonary complication rate with an associated 0.3% mortality rate.

A naso-/oro- gastric tube placement sensor could have similar rates of correct tissue identifications as the ETT placement sensor. Furthermore, a spectral difference between the oesophagus and stomach could be used to verify that the gastric tube has passed the gastro-oesophageal junction, although there is no such evidence of this currently. However, it is theorised that there would be a drop in the detected light intensity as the sensor moves through the junction. As the sensor passes from the oesophageal wall into the top of the stomach there will be free space, or liquid formed from stomach secretions and ingested substances. This may cause a reduction in the detected light intensity which could be used to identify passage through the junction. This was investigated in a very simple stomach model, consisting of a plastic container filled with 500 ml of water, 2 tablespoons of salt and 160g of noodles, to model stomach contents. The opto-electronic units are described in Section 4.2, with the three-fibre circular sensor used. The spectrometer was set to an integration time of 400 ms. The sensor was dipped into the stomach model and moved around whilst spectra were recorded (Fig. 6.11a). The sensor was then moved from the top to the bottom of an *ex-vivo* porcine oesophagus whilst spectra were recorded (Fig. 6.11b).

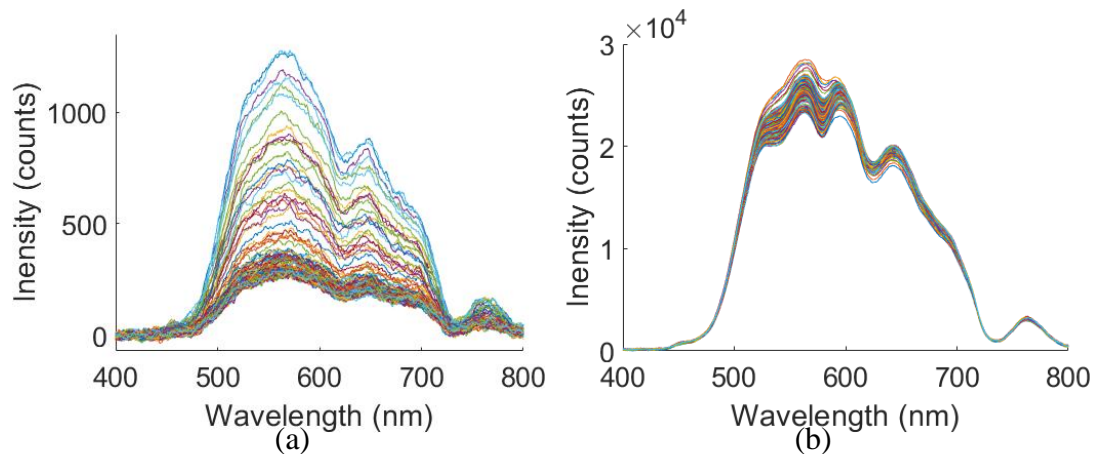


Fig. 6.11: (a) Spectra from the ETT placement sensor placed in a stomach model. (b) Moved down an *ex-vivo* porcine oesophagus.

A significant light intensity decrease was found when the sensor was in the stomach model compared to the oesophagus. The mean and standard deviation of the peak light intensity (intensity at a wavelength of 563 nm) for the stomach model and oesophagus were found to be  $300 \pm 200$  and  $25700 \pm 900$  counts, respectively. The maximum intensity in the stomach was measured at 1300 counts, likely caused by the sensor occasionally passing a piece of food floating in the water. The drop in the detected light intensity can be used to identify that the gastric tube has passed the gastro-oesophageal junction into the stomach, indicating correct placement. However, this is a much-simplified model, where stomach contents would in general be thicker and less transparent due to secretions and partially digested food substances. Furthermore, if the sensor contacts the stomach wall then the light intensity would sharply increase. However, if the sensor moves into free space i.e. there is an air gap at the entrance to the stomach, then the position could be well identified.

This feature may be able to distinguish more than the trachea and oesophagus, with more subtle differences in the shape of the feature being used to distinguish more similar tissue types. Furthermore, there are spectral features not explored with this research that may distinguish other tissues and physiological parameters. For example, diffuse reflectance spectroscopy can be used as a tool for real-time assessment of abnormal and cancerous growth on tissues [198,199,200]. Particularly relevant is the use of this technique to diagnose dysplasia in Barrett’s oesophagus [201,202]. There is also evidence that diffuse reflectance spectroscopy can give neurosurgical guidance and can discriminate blood vessels from bleeding [203,204]. However, commercial fibre optic probes are used for these measurements, with the device developed here being significantly smaller, less invasive, and mountable to other healthcare devices. Therefore, the described device has the potential to be integrated into surgical equipment and a variety of medical devices to give clinicians real-time perfusion, tissue identification, and abnormality information. However, before these capabilities enter the clinical and detailed analysis of the pros and cons, these alternative applications need to be explored similarly to the work described in this thesis.

## 6.4 Conclusion

Reflectance spectroscopy is a well-established technique for quantifying the properties and characteristics of a variety of materials. Innovations of technology and developments in the field have driven applications in healthcare through reflectance spectroscopy performed on tissues. The spectroscopic properties of tissues can be obtained non-invasively by the harmless illumination of light. An interesting application of this technology is its integration with invasive medical devices. A device such as an ETT offers a window into the core physiological condition of a patient, unobtainable from measurements made on the periphery of the body. The development of such a technology has been described, producing a  $4.5 \times 4 \times 1 \text{ mm}$  fibre optic sensor. There are no electronics or metals contained in the invasive components and the shape is well-suited for integration into an ETT. The use of a non-transparent epoxy and coating of the fibres in a black pigment reduces the impact of direct coupling between the fibres, and ambient light. The ability of this sensor to distinguish tracheal and oesophageal tissues has been established in *ex-vivo* and *in-vivo* porcine models.

Measurements on *ex-vivo* porcine samples produced highly classifiable trachea and oesophagus measurements. 100% correct tissue identification was achieved when using a single sensor on 9 *ex-vivo* samples. 89.2% identification was achieved when using 10 sensors on a single *ex-vivo* sample, although the sensor was modified between the two experiments. There is clear evidence that the tracheal spectral feature originates from OHb. Dissection of *ex-vivo* porcine samples has indicated the spectral feature to be present in the tracheal mucosa but not the oesophageal mucosa, likely due to the thicker, and less transparent composition of the oesophageal mucosa.

The iTraXS device has further capabilities of cuff-trachea contact pressure and PPG measurements. The sensor was designed with two illumination fibres so that it can function as a PPG pulsatile sensor. However, although these capabilities exist, they

are not explored in this research which focuses on the development of an ETT placement sensor that does not require a pulsatile signal.

A second animal study consisted of *in-vivo* tracheal measurements and recently post-mortem (*in-situ*) oesophageal measurements. The SVM method performed the strongest with a tissue classification of 91.6% when the data from the 3 subjects were combined. The typical identification rate of ETCO<sub>2</sub> is > 90% [79,80], with the developed ETT placement sensor being comparable. However, under circumstances such as patient cardiac arrest, detection using ETCO<sub>2</sub> can reduce to 64% [82,83,84], where the developed sensor may be more robust. The OHb absorption feature in the 530 – 590 nm wavelength range is much less clear throughout tracheal measurements made *in-vivo* when compared to those made on *ex-vivo* measurements in this research. Furthermore, the characteristic is also less clear when comparing *in-vivo* measurements in this research to those made in literature by the USAISR with a commercial reflection probe. A possible solution to this is increasing the fibre separation distance to approximately 1.5 mm, which was found to be in the optimal range. However, alternative methods of transmitting and detecting more light that has interacted with OHb would also likely produce a stronger classification. By interrogating the full acquired spectral range between 450 and 850 nm using PCA, a correct tissue identification of 98.3% was achieved in the animal study. Therefore, the implementation of more spectral bands will likely yield better results in future studies.

Further developments in this research have been described and there are potential improvements to the experimental and sensor design. A simple method for amplifying the absorption feature of OHb is explored for the current sensor and opto-electronic units, although its efficacy and consistency need to be verified. A concept for producing an MVP has been explored, with the biggest reduction in cost produced by exchanging the spectrometer for photodiodes. However, this relies upon there being enough optical power at a sufficiently narrow bandwidth to be detected after filtering, which needs to be investigated. Finally, the application of this technology to other areas has been explored, with a compact tissue reflectance sensor having a broad application. The clearest alternative is in the integration of the sensor with gastric tubes. However, there are other applications in invasive medical devices where the physiological parameters and spectral properties of tissues are relevant.

Overall, the future is bright for the application of fibre optics in healthcare. Developments in this technology, such as those described here, offer tremendous social and economic benefits.



# References

- [1] Vaz, F. (2017). Airway management. In *ENT: An Introduction and Practical Guide*, CRC Press, 151-153.
- [2] Cook, T. M., & MacDougall-Davis, S. R. (2012). Complications and failure of airway management. *British journal of anaesthesia*, 109(suppl\_1), i68-i85.
- [3] Carlson, J. N., & Wang, H. E. (2010). Noninvasive airway management. *Tintinalli's Emergency Medicine: A Comprehensive Study Guide*. 7th ed. New York, NY: McGraw-Hill Education.
- [4] Gupta, S., & Donn, S. M. (2016). Continuous positive airway pressure: physiology and comparison of devices. In *Seminars in Fetal and Neonatal Medicine*, 21(3), 204-211.
- [5] Global Airway Management Devices Market Size Report, Airway Management Devices Market Size, Share & Trends Analysis Report By Product (Supraglottic, Infraglottic, Resuscitators, Laryngoscopes), By Application (Anesthesia, Emergency Medicine), By End Use, And Segment Forecasts, 2018 – 2025, Report ID: GVR-1-68038-776-6, <https://www.grandviewresearch.com/industry-analysis/airway-management-devices-market>
- [6] Airway Management Devices Market by type (Endotracheal tubes, Tracheostomy tube, LMA, Oropharyngeal, Nasopharyngeal, Laryngoscopes, Bougies, Application (Anesthesia Emergency medicine, End user (Hospitals) – Global Forecast to 2026, (2021), Report Code: MD 6439, <https://www.marketsandmarkets.com/Market-Reports/airway-management-device-market-116806061.html>
- [7] Chronic obstructive pulmonary disease (COPD). (2022). World Health Organization. [https://www.who.int/news-room/fact-sheets/detail/chronic-obstructive-pulmonary-disease-\(copd\)](https://www.who.int/news-room/fact-sheets/detail/chronic-obstructive-pulmonary-disease-(copd))
- [8] The top 10 causes of death. (2020). World Health Organization. <https://www.who.int/news-room/fact-sheets/detail/the-top-10-causes-of-death>
- [9] Blausen.com staff (2014). "Medical gallery of Blausen Medical 2014". *WikiJournal of Medicine* 1 (2). DOI:10.15347/wjm/2014.010. ISSN 2002-4436
- [10] Furlow, P. W., & Mathisen, D. J. (2018). Surgical anatomy of the trachea. *Annals of cardiothoracic surgery*, 7(2), 255.
- [11] Karmali, S., & Rose, P. (2020). Tracheal tube size in adults undergoing elective surgery—a narrative review. *Anaesthesia*, 75(11), 1529-1539.
- [12] Adamiec, E., Dzięciołowska-Baran, E., Czerwiński, F., Miklaszewska, D., & Teul, I. (2002). Prenatal development of the human trachea. *Folia Morphologica*, 61(2), 123-125.
- [13] Trachea (Windpipe) Definition, Anatomy, Function, Diagram. (2022, September 16). The Respiratory System. <https://www.therespiratorysystem.com/trachea/>
- [14] Oezcelik, A., & DeMeester, S. R. (2011). General anatomy of the esophagus. *Thoracic surgery clinics*, 21(2), 289-297.
- [15] Ferhatoglu, M. F., & Kivilcim, T. (2017). Anatomy of esophagus. In *Esophageal Abnormalities*. IntechOpen.
- [16] Graham, T. M., MD. (2018). Esophagus Histology. *Iheartpathology*. <https://www.iheartpathology.net/post/gi-esophagus-histology>
- [17] Paxton, S. (2003). Respiratory: The Histology Guide. <https://www.histology.leeds.ac.uk/respiratory/conducting.php>
- [18] Salassa, J. R., Pearson, B. W., & Payne, W. S. (1977). Gross and microscopical blood supply of the trachea. *The Annals of thoracic surgery*, 24(2), 100-107.
- [19] Downey, R. P., & Samra, N. S. (2021). Anatomy, Thorax, Tracheobronchial Tree. In *StatPearls [Internet]*. StatPearls Publishing.
- [20] File:Kehlkopf Schema.png. (2022). Wikimedia Commons, the free media repository. [https://commons.wikimedia.org/w/index.php?title=File:Kehlkopf\\_Schema.png&oldid=620838220](https://commons.wikimedia.org/w/index.php?title=File:Kehlkopf_Schema.png&oldid=620838220).
- [21] Noordzij, J. P., & Ossoff, R. H. (2006). Anatomy and physiology of the larynx. *Otolaryngologic Clinics of North America*, 39(1), 1-10.
- [22] Underbrink, M. P. (2019). Vocal Cord Paresis (Paralysis): Symptoms, Causes, and Treatment Options. *Houston & Allergy*. <https://www.houstonent.com/blog/vocal-cord-paresis-paralysis-symptoms-causes-and-treatment-options>
- [23] Joshi, R., Hypes, C. D., Greenberg, J., Snyder, L., Malo, J., Bloom, J. W., ... & Mosier, J. M. (2017). Difficult airway characteristics associated with first-attempt failure at intubation using video laryngoscopy in the intensive care unit. *Annals of the American Thoracic Society*, 14(3), 368-375.
- [24] Walls, R. M., & Murphy, M. F. (Eds.). (2008). *Manual of emergency airway management*. Lippincott Williams & Wilkins.

- 
- [25] Juran, S., Ljungman, D., Gründl, M., & Marks, I. (2018). Global Surgery & Anaesthesia Statistics-The Importance of Data Collection.
- [26] Endotracheal Tube Market Size, Trends And Forecast To 2027. (2020). Coherent Market Insights, Code: CMI2564, <https://www.coherentmarketinsights.com/market-insight/endotracheal-tube-market-2564>
- [27] Endotracheal Tube Market Size, Share & Trends Analysis Report By Product Type (Regular Endotracheal Tube, Reinforced Endotracheal Tube), By Route Type, By Application, By End-use, By Region, And Segment Forecasts, 2021 - 2028, Report ID: GVR-4-68038-727-8, <https://www.grandviewresearch.com/industry-analysis/endotracheal-tubes-market>
- [28] Arulkumaran, N., McLaren, C. S., Arulkumaran, K., Philips, B. J., & Cecconi, M. (2018). An analysis of emergency tracheal intubations in critically ill patients by critical care trainees. *Journal of the Intensive Care Society*, 19(3), 180-187.
- [29] Endotracheal Tube Cuffed. (2022). Indiamart. <https://www.indiamart.com/proddetail/endotracheal-tube-cuffed-25573467388.html>
- [30] D. J. Stone, (2005). *Airway Management*. 6th ed. Miller's Anesthesia, Philadelphia: Elsevier Churchill Livingstone.
- [31] Mariyaselvam, M. Z., Marsh, L. L., Bamford, S., Smith, A., Wise, M. P., & Williams, D. W. (2017). Endotracheal tubes and fluid aspiration: an in vitro evaluation of new cuff technologies. *BMC anesthesiology*, 17(1), 1-9.
- [32] Birmingham, P. K., Cheney, F. W., & Ward, R. J. (1986). Esophageal intubation: a review of detection techniques. *Anesthesia & Analgesia*, 65(8), 886-891.
- [33] Cobas, M. A., De la Pena, M. A., Manning, R., Candiotti, K., & Varon, A. J. (2009). Prehospital intubations and mortality: a level 1 trauma center perspective. *Anesthesia & Analgesia*, 109(2), 489-493.
- [34] Peter Saint. (2017). Courts and Tribunals Judiciary. Ref: 2017-0404. <https://www.judiciary.uk/prevention-of-future-death-reports/peter-saint/>
- [35] Sharon Grierson. (2018). Courts and Tribunals Judiciary. Ref: 2018-0034. <https://www.judiciary.uk/prevention-of-future-death-reports/sharon-grierson/>
- [36] Judiciary. (2018). UK. In the Milton Keynes Coroner's Court. Inquest into the death of Glenda May Logsdail, Regulation 28: report to prevent future deaths, 2021. [https://www.judiciary.uk/wp-content/uploads/2021/09/Glenda-Logsdail-Prevention-of-future-deaths-report-2021-0295\\_Published.pdf](https://www.judiciary.uk/wp-content/uploads/2021/09/Glenda-Logsdail-Prevention-of-future-deaths-report-2021-0295_Published.pdf)
- [37] Cheney, F. W. (1999). The American Society of Anesthesiologists Closed Claims Project: what have we learned, how has it affected practice, and how will it affect practice in the future?. *The Journal of the American Society of Anesthesiologists*, 91(2), 552-556.
- [38] Honardar, M. R., Posner, K. L., & Domino, K. B. (2017). Delayed detection of esophageal intubation in anesthesia malpractice claims: brief report of a case series. *Anesthesia and analgesia*, 125(6). 1948
- [39] Domino, K. B., Posner, K. L., Caplan, R. A., & Cheney, F. W. (1999). Airway injury during anesthesia: a closed claims analysis. *The Journal of the American Society of Anesthesiologists*, 91(6), 1703-1703.
- [40] Foglia, E. E., Ades, A., Sawyer, T., Glass, K. M., Singh, N., Jung, P., ... & NEAR4NEOS Investigators. (2019). Neonatal intubation practice and outcomes: an international registry study. *Pediatrics*, 143(1).
- [41] Schmölzer, G. M., & Roehr, C. C. (2014). Techniques to ascertain correct endotracheal tube placement in neonates. *Cochrane Database of Systematic Reviews*, (9).
- [42] Cook, T. M., Bland, L., Mihai, R., & Scott, S. (2009). Litigation related to anaesthesia: an analysis of claims against the NHS in England 1995–2007. *Anaesthesia*, 64(7), 706-718.
- [43] Russotto, V., Myatra, S. N., Laffey, J. G., Tassistro, E., Antolini, L., Bauer, P., ... & Giacomucci, A. (2021). Intubation practices and adverse peri-intubation events in critically ill patients from 29 countries. *Jama*, 325(12), 1164-1172.
- [44] Chrimes, N., Higgs, A., Hagberg, C. A., Baker, P. A., Cooper, R. M., Greif, R., ... & Cook, T. M. (2022). Preventing unrecognised oesophageal intubation: a consensus guideline from the Project for Universal Management of Airways and international airway societies. *Anaesthesia*, 77(12), 1395-1415.
- [45] Cobas, M. A., De la Pena, M. A., Manning, R., Candiotti, K., & Varon, A. J. (2009). Prehospital intubations and mortality: a level 1 trauma center perspective. *Anesthesia & Analgesia*, 109(2), 489-493.

- 
- [46] Williamson, J. A., Webb, R. K., Szekely, S., Gillies, E. R. N., & Dreosti, A. V. (1993). Difficult intubation: an analysis of 2000 incident reports. *Anaesthesia and intensive care*, 21(5), 602-607.
- [47] Combes, X., Jabre, P., Jbeili, C., Leroux, B., Bastuji-Garin, S., Margenet, A., ... & Dhonneur, G. (2006). Prehospital standardization of medical airway management: incidence and risk factors of difficult airway. *Academic Emergency Medicine*, 13(8), 828-834.
- [48] Pavia, D. L., Lampman, G. M., Kriz, G. S., & Vyvyan, J. A. (2014). *Introduction to spectroscopy*. Cengage learning.
- [49] Milton, E. J., Schaepman, M. E., Anderson, K., Kneubühler, M., & Fox, N. (2009). Progress in field spectroscopy. *Remote Sensing of Environment*, 113, S92-S109.
- [50] Hollas, J. M. (2004). *Modern spectroscopy*. John Wiley & Sons.
- [51] Gauglitz, G., & Moore, D. S. (Eds.). (2014). *Handbook of spectroscopy* (Vol. 1). Weinheim: Wiley-Vch.
- [52] Siesler, H. W., Kawata, S., Heise, H. M., & Ozaki, Y. (Eds.). (2008). *Near-infrared spectroscopy: principles, instruments, applications*. John Wiley & Sons.
- [53] Mills, G. D. (2012). *Ultraviolet/visible spectroscopy*. ASTM International.
- [54] Bovey, F. A., Mirau, P. A., & Gutowsky, H. S. (1988). *Nuclear magnetic resonance spectroscopy*. Elsevier.
- [55] Long, D. A. (1977). *Raman spectroscopy*. New York, 1.
- [56] Agarwal, B. K. (2013). *X-ray spectroscopy: an introduction* (Vol. 15). Springer.
- [57] Chastain, J., & King Jr, R. C. (1992). *Handbook of X-ray photoelectron spectroscopy*. Perkin-Elmer Corporation, 40, 221.
- [58] Schwaighofer, A., Brandstetter, M., & Lendl, B. (2017). Quantum cascade lasers (QCLs) in biomedical spectroscopy. *Chemical Society Reviews*, 46(19), 5903-5924.
- [59] Goldberg, M. E. (1987). *Spectrophotometry & spectrofluorimetry: A practical approach*: edited by DA Harris and CL Bashford. IRL Press, Oxford, 192.
- [60] Wallace, M. B., Wax, A., Roberts, D. N., & Graf, R. N. (2009). Reflectance spectroscopy. *Gastrointestinal endoscopy clinics of North America*, 19(2), 233-242.
- [61] Baker, W. B., Parthasarathy, A. B., Busch, D. R., Mesquita, R. C., Greenberg, J. H., & Yodh, A. G. (2014). Modified Beer-Lambert law for blood flow. *Biomedical optics express*, 5(11), 4053-4075.
- [62] Kocsis, L., Herman, P., & Eke, A. (2006). The modified Beer-Lambert law revisited. *Physics in Medicine & Biology*, 51(5), N91.
- [63] Webster, J. G. (Eds.). (1997). *Design of pulse oximeters*. CRC Press.
- [64] File:Oxy and Deoxy Hemoglobin Near-Infrared absorption spectra.png. (2021). Wikimedia Commons, the free media repository. [https://commons.wikimedia.org/w/index.php?title=File:Oxy\\_and\\_Deoxy\\_Hemoglobin\\_Near-Infrared\\_absorption\\_spectra.png&oldid=594623503](https://commons.wikimedia.org/w/index.php?title=File:Oxy_and_Deoxy_Hemoglobin_Near-Infrared_absorption_spectra.png&oldid=594623503).
- [65] Mannheimer, P. D., Cascini, J. R., Fein, M. E., & Nierlich, S. L. (1997). Wavelength selection for low-saturation pulse oximetry. *IEEE transactions on biomedical engineering*, 44(3), 148-158.
- [66] Sinex, J. E. (1999). Pulse oximetry: principles and limitations. *The American journal of emergency medicine*, 17(1), 59-66.
- [67] Allen, J. (2007). Photoplethysmography and its application in clinical physiological measurement. *Physiological measurement*, 28(3), R1.
- [68] Tamura, T. (2019). Current progress of photoplethysmography and SPO2 for health monitoring. *Biomedical engineering letters*, 9(1), 21-36.
- [69] Berkow, L. C., Morey, T. E., & Urdaneta, F. (2018). The technology of video laryngoscopy. *Anesthesia & Analgesia*, 126(5), 1527-1534.
- [70] VS-10 series - video laryngoscope by Medcaptain Medical Technology: Medicaexpo. The B2B marketplace for medical equipment. (n.d.). Retrieved September 27, 2022, from <https://www.medicalexpo.com/prod/medcaptain-medical-technology/product-118704-930977.html>
- [71] Cook, T. M., & Kelly, F. E. (2017). A national survey of videolaryngoscopy in the United Kingdom. *BJA: British Journal of Anaesthesia*, 118(4), 593-600.
- [72] Norris, A., & Heidegger, T. (2016). Limitations of videolaryngoscopy. *BJA: British Journal of Anaesthesia*, 117(2), 148-150.
- [73] Sethi, A. K., Salhotra, R., Chandra, M., Mohta, M., Bhatt, S., & Kayina, C. A. (2019). Confirmation of placement of endotracheal tube—A comparative observational pilot study of three ultrasound methods. *Journal of Anaesthesiology, Clinical Pharmacology*, 35(3), 353.

- 
- [74] Das, S. K., Choupoo, N. S., Haldar, R., & Lahkar, A. (2015). Transtracheal ultrasound for verification of endotracheal tube placement: a systematic review and meta-analysis. *Canadian Journal of Anesthesia/Journal canadien d'anesthésie*, 62(4), 413-423.
- [75] Thomas, V. K., Paul, C., Rajeev, P. C., & Palatty, B. U. (2017). Reliability of ultrasonography in confirming endotracheal tube placement in an emergency setting. *Indian journal of critical care medicine: peer-reviewed, official publication of Indian Society of Critical Care Medicine*, 21(5), 257.
- [76] Nellcor Adult/Pediatric Colorimetric CO<sub>2</sub> Detector. Medtronic. (n.d.). Retrieved September 28, 2022, from <https://www.medtronic.com/covidien/en-us/products/intubation/nellcor-adult-pediatric-colorimetric-co2-detector.html>
- [77] Walsh, B. K., Crotwell, D. N., & Restrepo, R. D. (2011). Capnography/Capnometry during mechanical ventilation: 2011. *Respiratory care*, 56(4), 503-509.
- [78] Quantitative waveform capnography. ACLS Medical Training. (2020, September 16). Retrieved September 28, 2022, from <https://www.aclsmedicaltraining.com/quantitative-waveform-capnography/>
- [79] Li, J. (2001). Capnography alone is imperfect for endotracheal tube placement confirmation during emergency intubation. *The Journal of emergency medicine*, 20(3), 223-229.
- [80] Long, B., Koyfman, A., & Vivirito, M. A. (2017). Capnography in the emergency department: a review of uses, waveforms, and limitations. *The Journal of emergency medicine*, 53(6), 829-842.
- [81] Pandit, J. J. (2022). 'No trace, wrong place' does not mean 'positive trace, right place'. Identifying and managing misplaced or displaced tracheal tubes in cardiopulmonary resuscitation. *Anaesthesia*, 77(1), 16-21.
- [82] Sandroni, C., De Santis, P., & D'Arrigo, S. (2018). Capnography during cardiac arrest. *Resuscitation*, 132, 73-77.
- [83] Tanigawa, K., Takeda, T., Goto, E., & Tanaka, K. (2001). The efficacy of esophageal detector devices in verifying tracheal tube placement: a randomized cross-over study of out-of-hospital cardiac arrest patients. *Anesthesia & Analgesia*, 92(2), 375-378.
- [84] Sheak, K. R., Wiebe, D. J., Leary, M., Babaeizadeh, S., Yuen, T. C., Zive, D., ... & Abella, B. S. (2015). Quantitative relationship between end-tidal carbon dioxide and CPR quality during both in-hospital and out-of-hospital cardiac arrest. *Resuscitation*, 89, 149-154.
- [85] Nawn, C. D., Souhan, B., Carter III, R., Kneapler, C., Fell, N., & Ye, J. Y. (2016). Distinguishing tracheal and esophageal tissues with hyperspectral imaging and fiber-optic sensing. *Journal of biomedical optics*, 21(11), 117004.
- [86] Nawn, C. D., Blackburn, M. B., De Lorenzo, R. A., & Ryan, K. L. (2019). Using spectral reflectance to distinguish between tracheal and oesophageal tissue: applications for airway management. *Anaesthesia*, 74(3), 340-347.
- [87] Blackburn, M. B., Nawn, C. D., & Ryan, K. L. (2019). Testing of novel spectral device sensor in swine model of airway obstruction. *Physiological Reports*, 7(19), e14246.
- [88] Berard, D., Sen, C., Nawn, C. D., Blackburn, A. N., Ryan, K. L., & Blackburn, M. B. (2020). Spectral Reflectance Can Differentiate Tracheal and Esophageal Tissue in the Presence of Bodily Fluids and Soot. *Sensors*, 20(21), 6138.
- [89] Bedolla, C. N., Rauschendorfer, C., Havard, D. B., Guenther, B. A., Rizzo, J. A., Blackburn, A. N., ... & Blackburn, M. B. (2022). Spectral Reflectance as a Unique Tissue Identifier in Healthy Humans and Inhalation Injury Subjects. *Sensors*, 22(9), 3377.
- [90] Krüger, L., Gonzalez, L. M., Pridgen, T. A., McCall, S. J., von Furstenberg, R. J., Harnden, I., ... & Garman, K. S. (2017). Ductular and proliferative response of esophageal submucosal glands in a porcine model of esophageal injury and repair. *American Journal of Physiology-Gastrointestinal and Liver Physiology*, 313(3), G180-G191.
- [91] Judge, E. P., Hughes, J. L., Egan, J. J., Maguire, M., Molloy, E. L., & O'Dea, S. (2014). Anatomy and bronchoscopy of the porcine lung. A model for translational respiratory medicine. *American journal of respiratory cell and molecular biology*, 51(3), 334-343.
- [92] Zmuidzinas, J. (2003). Thermal noise and correlations in photon detection. *Applied Optics*, 42(25), 4989-5008.
- [93] Alkemade, C. T. J., Snelleman, W., Boutilier, G. D., Pollard, B. D., Winefordner, J. D., Chester, T. L., & Omenetto, N. (1978). A review and tutorial discussion of noise and signal-to-noise ratios in analytical spectrometry—I. Fundamental principles of signal-to-noise ratios. *Spectrochimica Acta Part B: Atomic Spectroscopy*, 33(8), 383-399.
- [94] File:Oxy and Deoxy Hemoglobin Near-Infrared absorption spectra.png. (2021, September 30). Wikimedia Commons, the free media repository. Retrieved 09:22, November 30, 2022 from

---

[https://commons.wikimedia.org/w/index.php?title=File:Oxy\\_and\\_Deoxy\\_Hemoglobin\\_Near-Infrared\\_absorption\\_spectra.png&oldid=594623503](https://commons.wikimedia.org/w/index.php?title=File:Oxy_and_Deoxy_Hemoglobin_Near-Infrared_absorption_spectra.png&oldid=594623503).

- [95] Prahl, S. (n.d.). Tabulated Molar Extinction Coefficient for Hemoglobin in Water. Omlc. <https://omlc.org/spectra/hemoglobin/summary.html>
- [96] Townsend, D., D'Aiuto, F., & Deanfield, J. (2014). Super actinic 420 nm light-emitting diodes for estimating relative microvascular hemoglobin oxygen saturation. *J. Med. Biol. Eng.*, 34(2), 172-177.
- [97] Liu, P., Zhu, Z., Zeng, C. C., & Nie, G. (2012). Specific absorption spectra of hemoglobin at different PO<sub>2</sub> levels: potential noninvasive method to detect PO<sub>2</sub> in tissues. *Journal of biomedical optics*, 17(12), 125002.
- [98] May, A., Günter, E., Roth, F., Gossner, L., Stolte, M., Vieth, M., & Ell, C. (2004). Accuracy of staging in early oesophageal cancer using high resolution endoscopy and high resolution endosonography: a comparative, prospective, and blinded trial. *Gut*, 53(5), 634-640.
- [99] Takubo, K., Aida, J., Sawabe, M., Kurosumi, M., Arima, M., Fujishiro, M., & Arai, T. (2007). Early squamous cell carcinoma of the oesophagus: the Japanese viewpoint. *Histopathology*, 51(6), 733-742.
- [100] Solheim, J. H., Borondics, F., Zimmermann, B., Sandt, C., Muthreich, F., & Kohler, A. (2021). An automated approach for fringe frequency estimation and removal in infrared spectroscopy and hyperspectral imaging of biological samples. *Journal of Biophotonics*, 14(12), e202100148.
- [101] Tafintseva, V., Lintvedt, T. A., Solheim, J. H., Zimmermann, B., Rehman, H. U., Virtanen, V., ... & Kohler, A. (2022). Preprocessing strategies for sparse infrared spectroscopy: a case study on cartilage diagnostics. *Molecules*, 27(3), 873.
- [102] Solheim, J. H., Gunko, E., Petersen, D., Großröschkamp, F., Gerwert, K., & Kohler, A. (2019). An open-source code for Mie extinction extended multiplicative signal correction for infrared microscopy spectra of cells and tissues. *Journal of biophotonics*, 12(8), e201800415.
- [103] Stratonnikov, A. A., & Loschenov, V. B. (2001). Evaluation of blood oxygen saturation in-vivo from diffuse reflectance spectra. *Journal of biomedical optics*, 6(4), 457-467.
- [104] Bachir, W., & Hamadah, O. (2021). Second derivative diffuse reflectance spectroscopy for estimating tissue hypoxia. *OSA Continuum*, 4(2), 650-664.
- [105] Fanjul-Vélez, F., Pampín-Suárez, S., & Arce-Diego, J. L. (2020). Application of classification algorithms to diffuse reflectance spectroscopy measurements for ex-vivo characterization of biological tissues. *Entropy*, 22(7), 736.
- [106] Stelzle, F., Tangermann-Gerk, K., Adler, W., Zam, A., Schmidt, M., Douplik, A., & Nkenke, E. (2010). Diffuse reflectance spectroscopy for optical soft tissue differentiation as remote feedback control for tissue-specific laser surgery. *Lasers in Surgery and Medicine: The Official Journal of the American Society for Laser Medicine and Surgery*, 42(4), 319-325.
- [107] Baltussen, E. J., Snæbjörnsson, P., De Koning, S. G. B., Sterenborg, H. J., Aalbers, A. G., Kok, N., ... & Ruers, T. J. (2017). Diffuse reflectance spectroscopy as a tool for real-time tissue assessment during colorectal cancer surgery. *Journal of biomedical optics*, 22(10), 106014.
- [108] Seo, I., Liu, Y., Bargo, P. R., & Kollias, N. (2012). Assessing human skin with diffuse reflectance spectroscopy and colorimetry. In *Photonic Therapeutics and Diagnostics VIII*, SPIE, 8207, 148-152.
- [109] Feiner, J. R., Severinghaus, J. W., & Bickler, P. E. (2007). Dark skin decreases the accuracy of pulse oximeters at low oxygen saturation: the effects of oximeter probe type and gender. *Anesthesia & Analgesia*, 105(6), S18-S23.
- [110] Zonios, G., Bykowski, J., & Kollias, N. (2001). Skin melanin, hemoglobin, and light scattering properties can be quantitatively assessed in-vivo using diffuse reflectance spectroscopy. *Journal of Investigative Dermatology*, 117(6), 1452-1457.
- [111] Kim, O., McMurdy, J., Lines, C., Duffy, S., Crawford, G., & Alber, M. (2012). Reflectance spectrometry of normal and bruised human skins: experiments and modeling. *Physiological measurement*, 33(2), 159.
- [112] Lim, L., Nichols, B. S., Rajaram, N., & Tunnell, J. W. (2011). Probe pressure effects on human skin diffuse reflectance and fluorescence spectroscopy measurements. *Journal of biomedical optics*, 16(1), 011012.
- [113] Popov, A. P., Bykov, A. V., & Meglinski, I. V. (2017). Influence of probe pressure on diffuse reflectance spectra of human skin measured in-vivo. *Journal of Biomedical Optics*, 22(11), 110504.
- [114] Nseir, S., Duguet, A., Copin, M. C., De Jonckheere, J., Zhang, M., Similowski, T., & Marquette, C. H. (2007). Continuous control of endotracheal cuff pressure and tracheal wall damage: a randomized controlled animal study. *Critical Care*, 11(5), 1-8.

- 
- [115] Guyton, D. C., Barlow, M. R., & Besselièvre, T. R. (1997). Influence of airway pressure on minimum occlusive endotracheal tube cuff pressure. *Critical care medicine*, 25(1), 91-94.
- [116] Lee, H., Ko, H., & Lee, J. (2016). Reflectance pulse oximetry: Practical issues and limitations. *Ict Express*, 2(4), 195-198.
- [117] May, J. M., Phillips, J. P., Fitchat, T., Ramaswamy, S., Snidvongs, S., & Kyriacou, P. A. (2019). A novel photoplethysmography sensor for vital signs monitoring from the human trachea. *Biosensors*, 9(4), 119.
- [118] Kyriacou, P. A. (2005). Pulse oximetry in the oesophagus. *Physiological measurement*, 27(1), R1.
- [119] McCabe, S. O., & Scott, J. B. (2016). New MRI-safe implant electrode design. In 2016 IEEE MTT-S International Microwave Symposium (IMS), 1-3/
- [120] Davenport, J. J., Hickey, M., Phillips, J. P., & Kyriacou, P. A. (2016). Method for producing angled optical fiber tips in the laboratory. *Optical Engineering*, 55(2), 026120-026120.
- [121] Zhao, Y. G., Lu, W. K., Ma, Y., Kim, S. S., Ho, S. T., & Marks, T. J. (2000). Polymer waveguides useful over a very wide wavelength range from the ultraviolet to infrared. *Applied Physics Letters*, 77(19), 2961-2963.
- [122] Beadie, G., Brindza, M., Flynn, R. A., Rosenberg, A., & Shirk, J. S. (2015). Refractive index measurements of poly (methyl methacrylate)(PMMA) from 0.4–1.6  $\mu\text{m}$ . *Applied Optics*, 54(31), F139-F143.
- [123] Hickey, M., & Kyriacou, P. A. (2007). Optimal spacing between transmitting and receiving optical fibres in reflectance pulse oximetry. In *Journal of Physics: Conference Series* (Vol. 85, No. 1, p. 012030). IOP Publishing.
- [124] Niwayama, M., & Unno, N. (2021). Tissue oximeter with selectable measurement depth using spatially resolved near-infrared spectroscopy. *Sensors*, 21(16), 5573.
- [125] Ash, C., Dubec, M., Donne, K., & Bashford, T. (2017). Effect of wavelength and beam width on penetration in light-tissue interaction using computational methods. *Lasers in medical science*, 32(8), 1909-1918.
- [126] Marti, D., Aasbjerg, R. N., Andersen, P. E., & Hansen, A. K. (2018). MC: an open-source, user-friendly, MATLAB-integrated three-dimensional Monte Carlo light transport solver with heat diffusion and tissue damage. *Journal of biomedical optics*, 23(12), 121622-121622.
- [127] Jacques, S. L. (2013). Optical properties of biological tissues: a review. *Physics in Medicine & Biology*, 58(11), R37.
- [128] Ebert, D. W., Roberts, C. J., Farrar, S. K., Johnston, W. M., Litsky, A. S., & Bertone, A. L. (1998). Articular cartilage optical properties in the spectral range 300–850 nm. *Journal of Biomedical Optics*, 3(3), 326-333.
- [129] Hohmann, M., Lengenfelder, B., Kanawade, R., Klämpfl, F., Douplik, A., & Albrecht, H. (2018). Measurement of optical properties of pig esophagus by using a modified spectrometer set-up. *Journal of biophotonics*, 11(1), e201600187.
- [130] Sung, K. B., & Chen, H. H. (2012). Enhancing the sensitivity to scattering coefficient of the epithelium in a two-layered tissue model by oblique optical fibers: Monte Carlo study. *Journal of biomedical optics*, 17(10), 107003-107003.
- [131] Wei, H. J., Xing, D., Lu, J. J., Gu, H. M., Wu, G. Y., & Jin, Y. (2005). Determination of optical properties of normal and adenomatous human colon tissues in vitro using integrating sphere techniques. *World Journal of Gastroenterology: WJG*, 11(16), 2413.
- [132] Kafian-Attari, I., Nippolainen, E., Bergmann, F., Mirhashemi, A., Paakkari, P., Foschum, F., ... & Afara, I. O. (2023). Impact of experimental setup parameters on the measurement of articular cartilage optical properties in the visible and short near-infrared spectral bands. *Biomedical Optics Express*, 14(7), 3397-3412.
- [133] Nunes, S. F., Murcia, P. R., Tiley, L. S., Brown, I. H., Tucker, A. W., Maskell, D. J., & Wood, J. L. N. (2010). An ex vivo swine tracheal organ culture for the study of influenza infection. *Influenza and other respiratory viruses*, 4(1), 7-15.
- [134] Widdicombe, J. H. (2002). Regulation of the depth and composition of airway surface liquid. *Journal of anatomy*, 201(4), 313-318.
- [135] Abood, D. A., Dawood, M. S., Mohammed, L. E., & Karim, A. J. (2023). Histological and histochemical characteristics of the esophagus in local breed donkey (*Equus asinus*). *Journal of Advanced Veterinary and Animal Research*, 10(1), 14.



- 
- [136] Dogan, I., Puckett, J. L., Padda, B. S., & Mittal, R. K. (2007). Prevalence of increased esophageal muscle thickness in patients with esophageal symptoms. *Official journal of the American College of Gastroenterology* | *ACG*, 102(1), 137-145.
- [137] Klantsataya, E., Jia, P., Ebendorff-Heidepriem, H., Monro, T. M., & François, A. (2016). Plasmonic fiber optic refractometric sensors: From conventional architectures to recent design trends. *Sensors*, 17(1), 12.
- [138] Boechat, A. A., Su, D., Hall, D. R., & Jones, J. D. (1991). Bend loss in large core multimode optical fiber beam delivery systems. *Applied Optics*, 30(3), 321-327.
- [139] Schermer, R. T., & Cole, J. H. (2007). Improved bend loss formula verified for optical fiber by simulation and experiment. *IEEE Journal of Quantum Electronics*, 43(10), 899-909.
- [140] Boechat, A. A., Su, D., Hall, D. R., & Jones, J. D. (1991). Bend loss in large core multimode optical fiber beam delivery systems. *Applied Optics*, 30(3), 321-327.
- [141] Jaeger, J. M., & Durbin Jr, C. G. (2001). Specialized endotracheal tubes. *Clinical Pulmonary Medicine*, 8(3), 166-176.
- [142] He, C., Korposh, S., Correia, R., Liu, L., Hayes-Gill, B. R., & Morgan, S. P. (2021). Optical fibre sensor for simultaneous temperature and relative humidity measurement: Towards absolute humidity evaluation. *Sensors and Actuators B: Chemical*, 344, 130154.
- [143] Koike, Y., & Asai, M. (2009). The future of plastic optical fiber. *NPG Asia Materials*, 1(1), 22-28.
- [144] Sakr, H., Chen, Y., Jasion, G. T., Bradley, T. D., Hayes, J. R., Mulvad, H. C. H., ... & Poletti, F. (2020). Hollow core optical fibres with comparable attenuation to silica fibres between 600 and 1100 nm. *Nature communications*, 11(1), 1-10.
- [145] Payne, D., & Gambling, W. A. (1974). New silica-based low-loss optical fibre. *Electronics Letters*, 10(15), 289-290.
- [147] Salpekar, P. D. (1971). Double-cuff endotracheal tube. *British Medical Journal*, 3(5773), 525.
- [148] Private Communication with Dr Andrew Norris, [andrewnorris@kfshrc.edu.sa](mailto:andrewnorris@kfshrc.edu.sa)
- [149] Chappelle, E. W., Kim, M. S., & McMurtrey III, J. E. (1992). Ratio analysis of reflectance spectra (RARS): an algorithm for the remote estimation of the concentrations of chlorophyll a, chlorophyll b, and carotenoids in soybean leaves. *Remote sensing of environment*, 39(3), 239-247.
- [150] Mallia, R. J., Thomas, S. S., Mathews, A., Kumar, R., Sebastian, P., Madhavan, J., & Subhash, N. (2008). Oxygenated hemoglobin diffuse reflectance ratio for in-vivo detection of oral pre-cancer. *Journal of biomedical optics*, 13(4), 041306.
- [151] Berger, V. W., & Zhou, Y. (2014). Kolmogorov–smirnov test: Overview. *Wiley statsref: Statistics reference online*.
- [152] Hubert, M., & Van der Veeken, S. (2008). Outlier detection for skewed data. *Journal of Chemometrics: A Journal of the Chemometrics Society*, 22(3-4), 235-246.
- [153] Boneau, C. A. (1960). The effects of violations of assumptions underlying the t test. *Psychological bulletin*, 57(1), 49.
- [154] Nachar, N. (2008). The Mann-Whitney U: A test for assessing whether two independent samples come from the same distribution. *Tutorials in quantitative Methods for Psychology*, 4(1), 13-20.
- [155] Nosheen, S., Alam, S., Irfan, M., Qureshi, M. U. A., & Ahmad, S. (2013). Optical Emission Spectrometer, Principle and Latest Industrial Applications. *International Journal of Material Science*, 3(4), 139-144.
- [156] Van Der Maaten, L., Postma, E., & Van den Herik, J. (2009). Dimensionality reduction: a comparative. *J Mach Learn Res*, 10(66-71), 13.
- [157] Abdi, H., & Williams, L. J. (2010). Principal component analysis. *Wiley interdisciplinary reviews: computational statistics*, 2(4), 433-459.
- [158] Tzeng, D. Y., & Berns, R. S. (2005). A review of principal component analysis and its applications to color technology. *Color Research & Application: Endorsed by Inter-Society Color Council, The Colour Group (Great Britain), Canadian Society for Color, Color Science Association of Japan, Dutch Society for the Study of Color, The Swedish Colour Centre Foundation, Colour Society of Australia, Centre Français de la Couleur*, 30(2), 84-98.
- [159] Beattie, J. R., & Esmonde-White, F. W. (2021). Exploration of principal component analysis: deriving principal component analysis visually using spectra. *Applied Spectroscopy*, 75(4), 361-375.
- [160] Beattie, J. R., & Esmonde-White, F. W. (2021). Exploration of principal component analysis: deriving principal component analysis visually using spectra. *Applied Spectroscopy*, 75(4), 361-375.
- [161] Izenman, A. J. (2013). Linear discriminant analysis. In *Modern multivariate statistical techniques*, Springer, New York, NY, 237-280.

- 
- [162] Balakrishnama, S., & Ganapathiraju, A. (1998). Linear discriminant analysis-a brief tutorial. Institute for Signal and information Processing, 18(1998), 1-8.
- [163] Menard, S. (2002). Applied logistic regression analysis (No. 106). Sage.
- [164] Sperandei, S. (2014). Understanding logistic regression analysis. *Biochimica medica*, 24(1), 12-18.
- [165] Noble, W. S. (2006). What is a support vector machine?. *Nature biotechnology*, 24(12), 1565-1567.
- [166] Suthaharan, S. (2016). Support vector machine. In *Machine learning models and algorithms for big data classification*, Springer, Boston, MA, 207-235.
- [167] Peterson, L. E. (2009). K-nearest neighbor. *Scholarpedia*, 4(2), 1883.
- [168] Bezdek, J. C., Chuah, S. K., & Leep, D. (1986). Generalized k-nearest neighbor rules. *Fuzzy Sets and Systems*, 18(3), 237-256.
- [169] Sinha, R., Correia, R., Gardner, D., Grau-Roma, L., de Brot, S., Hardman, J., ... & Norris, A. (2018). Mucosal injury following short-term tracheal intubation: A novel animal model and composite tracheal injury score. *Laryngoscope investigative otolaryngology*, 3(4), 257-262.
- [170] Liu, C., Correia, R., Ballaji, H. K., Korposh, S., Hayes-Gill, B. R., & Morgan, S. P. (2018). Optical fibre-based pulse oximetry sensor with contact force detection. *Sensors*, 18(11), 3632.
- [171] Teng, X. F., & Zhang, Y. T. (2004). The effect of contacting force on photoplethysmographic signals. *Physiological measurement*, 25(5), 1323.
- [172] Wukitsch, M. W., Petterson, M. T., Tobler, D. R., & Pologe, J. A. (1988). Pulse oximetry: analysis of theory, technology, and practice. *Journal of clinical monitoring*, 4(4), 290-301.
- [173] Alharbi, S., Hu, S., Mulvaney, D., Barrett, L., Yan, L., Blanos, P., ... & Adema, S. (2018). Oxygen saturation measurements from green and orange illuminations of multi-wavelength optoelectronic patch sensors. *Sensors*, 19(1), 118.
- [174] El-Boghdady, K., Bailey, C. R., & Wiles, M. D. (2016). Postoperative sore throat: a systematic review. *Anaesthesia*, 71(6), 706-717.
- [175] Farzanegan, R., Farzanegan, B., Zangi, M., Eraghi, M. G., Noorbakhsh, S., Tabarestani, N. D., & Shadmehr, M. B. (2016). Incidence rate of post-intubation tracheal stenosis in patients admitted to five intensive care units in Iran. *Iranian Red Crescent Medical Journal*, 18(9).
- [176] Lorente, L., Lecuona, M., Jiménez, A., Lorenzo, L., Roca, I., Cabrera, J., ... & Mora, M. L. (2014). Continuous endotracheal tube cuff pressure control system protects against ventilator-associated pneumonia. *Critical Care*, 18(2), 1-8.
- [177] Richards, M. J., Edwards, J. R., Culver, D. H., & Gaynes, R. P. (1999). Nosocomial infections in medical intensive care units in the United States. *Critical care medicine*, 27(5), 887-892.
- [178] Correia, R., Gadsby, B., Korposh, S., Norris, A. M., Hayes-Gill, B. R., Sinha, R., ... & Morgan, S. P. (2022). Intra-tracheal multiplexed sensing of contact pressure and perfusion. *Biomedical Optics Express*, 13(1), 48-64.
- [179] Yap, S. J., Morris, R. W., & Pybus, D. A. (1994). Alterations in endotracheal tube position during general anaesthesia. *Anaesthesia and intensive care*, 22(5), 586-588.
- [180] Bohnert, M., Schulz, K., Belenkaia, L., & Liehr, A. W. (2008). Re-oxygenation of haemoglobin in livores after post-mortem exposure to a cold environment. *International Journal of Legal Medicine*, 122(2), 91-96.
- [181] Boehm, J., François, A., Ebendorff-Heidepriem, H., & Monro, T. M. (2011). Chemical deposition of silver for the fabrication of surface plasmon microstructured optical fibre sensors. *Plasmonics*, 6(1), 133-136.
- [182] Novotný, M., Bulíř, J., Pokorný, P., Lančok, J., Fekete, L., Musil, J., & Čekada, M. (2013). RF magnetron sputtering of silver thin film in Ne, Ar and Kr discharges—plasma characterisation and surface morphology. *Surface and Coatings Technology*, 228, S466-S469.
- [183] Paiva, J. S., Jorge, P. A., Rosa, C. C., & Cunha, J. P. (2018). Optical fiber tips for biological applications: from light confinement, biosensing to bioparticles manipulation. *Biochimica et Biophysica Acta (BBA)-General Subjects*, 1862(5), 1209-1246.
- [184] Yücel, M. A., Selb, J., Boas, D. A., Cash, S. S., & Cooper, R. J. (2014). Reducing motion artifacts for long-term clinical NIRS monitoring using collodion-fixed prism-based optical fibers. *Neuroimage*, 85, 192-201.
- [185] Mitchell, T. M. (2007). *Machine learning* (Vol. 1). New York: McGraw-hill.
- [186] Belabbas, M. A., & Wolfe, P. J. (2009). Spectral methods in machine learning and new strategies for very large datasets. *Proceedings of the National Academy of Sciences*, 106(2), 369-374.

- 
- [187] Hamm, C. A., Wang, C. J., Savic, L. J., Ferrante, M., Schobert, I., Schlachter, T., ... & Letzen, B. (2019). Deep learning for liver tumor diagnosis part I: development of a convolutional neural network classifier for multi-phasic MRI. *European radiology*, 29(7), 3338-3347.
- [188] Fredriksson, I., Larsson, M., & Strömberg, T. (2020). Machine learning for direct oxygen saturation and hemoglobin concentration assessment using diffuse reflectance spectroscopy. *Journal of Biomedical Optics*, 25(11), 112905-112905.
- [189] Tsui, S. Y., Wang, C. Y., Huang, T. H., & Sung, K. B. (2018). Modelling spatially-resolved diffuse reflectance spectra of a multi-layered skin model by artificial neural networks trained with Monte Carlo simulations. *Biomedical optics express*, 9(4), 1531-1544.
- [190] Ocean HDX-XR Spectrometer. (n.d.). Ocean Insight. <https://www.oceaninsight.com/products/spectrometers/high-sensitivity/ocean-hdx-xr/?qty=1>
- [191] Metheny, N. A., & Titler, M. G. (2001). Assessing placement of feeding tubes. *AJN The American Journal of Nursing*, 101(5), 36-45.
- [192] Education, O. M. (2016). Nasogastric (NG) Tube Placement. Oxford Medical Education. <https://oxfordmedicaleducation.com/clinical-skills/procedures/nasogastric-ng-tube/>
- [193] Chen, Y. C., Wang, L. Y., Chang, Y. J., Yang, C. P., Wu, T. J., Lin, F. R., ... & Wei, T. S. (2014). Potential risk of malposition of nasogastric tube using nose-ear-xiphoid measurement. *PloS one*, 9(2), e88046.
- [194] Metheny, N. A., & Titler, M. G. (2001). Assessing placement of feeding tubes. *AJN The American Journal of Nursing*, 101(5), 36-45.
- [195] Leder, S. B., Lazarus, C. L., Suiter, D. M., & Acton, L. M. (2011). Effect of orogastric tubes on aspiration status and recommendations for oral feeding. *Otolaryngology--Head and Neck Surgery*, 144(3), 372-375.
- [196] Motta, A. P. G., Rigobello, M. C. G., Silveira, R. C. D. C. P., & Gimenes, F. R. E. (2021). Nasogastric/nasoenteric tube-related adverse events: an integrative review. *Revista Latino-Americana de Enfermagem*, 29.
- [197] Mohiuddin, S. A., Al Kaabi, S., Butt, T., Yakoob, R., & Khanna, M. (2016). Down the wrong road—a case report of inadvertent nasogastric tube insertion leading to lung laceration and important pearls to avoid complications. *Qatar medical journal*, 2016(2), 12.
- [198] Baltussen, E. J., Snæbjörnsson, P., De Koning, S. G. B., Sterenborg, H. J., Aalbers, A. G., Kok, N., ... & Ruers, T. J. (2017). Diffuse reflectance spectroscopy as a tool for real-time tissue assessment during colorectal cancer surgery. *Journal of biomedical optics*, 22(10), 106014.
- [199] Nogueira, M. S., Maryam, S., Amissah, M., Lu, H., Lynch, N., Killeen, S., ... & Andersson-Engels, S. (2021). Evaluation of wavelength ranges and tissue depth probed by diffuse reflectance spectroscopy for colorectal cancer detection. *Scientific Reports*, 11(1), 1-17.
- [200] Palmer, G. M., Zhu, C., Breslin, T. M., Xu, F., Gilchrist, K. W., & Ramanujam, N. (2003). Comparison of multiexcitation fluorescence and diffuse reflectance spectroscopy for the diagnosis of breast cancer (March 2003). *IEEE Transactions on Biomedical engineering*, 50(11), 1233-1242.
- [201] Georgakoudi, I., & Van Dam, J. (2003). Characterization of dysplastic tissue morphology and biochemistry in Barrett's esophagus using diffuse reflectance and light scattering spectroscopy. *Gastrointestinal Endoscopy Clinics*, 13(2), 297-308.
- [202] Georgakoudi, I., & Feld, M. S. (2004). The combined use of fluorescence, reflectance, and light-scattering spectroscopy for evaluating dysplasia in Barrett's esophagus. *Gastrointestinal Endoscopy Clinics*, 14(3), 519-537.
- [203] Laurence, A., Bouthillier, A., Robert, M., Nguyen, D. K., & Leblond, F. (2020). Multispectral diffuse reflectance can discriminate blood vessels and bleeding during neurosurgery based on low-frequency hemodynamics. *Journal of Biomedical Optics*, 25(11), 116003.
- [204] Eslami, P., DePaoli, D., Goetz, L., Parent, M., & Côté, D. (2021). Neurosurgical guidance with diffuse reflectance spectroscopy. In *2021 Photonics North (PN)*, 1-1.

## List of Figures

Fig. 1.1: (a) The anatomy of the trachea [9]. (b) Cross-section of the trachea and oesophagus [13] .....	10
Fig. 1.2: Labelled histological cross-section of the (a) oesophagus [16], and (b) trachea [17]. .....	11
Fig. 1.3: Blood vessel network of the trachea and oesophagus [10]. .....	12
Fig. 1.4: (a) Anatomy of the larynx [20]. (b) Cross-section of the larynx showing the open and closed vocal cords [22]. .....	13
Fig. 1.5: A labelled diagram of an endotracheal tube (ETT), showing the key standard features [29]. .....	14
Fig. 1.6: Results of the question ‘What reduction in complications would be most important to you? Please rank them from 0 to 10, with 10 being most important for you’, for oesophageal intubation. ....	16
Fig. 1.7: Diagram of how incident visible light interacts with a generic tissue [60].	18
Fig. 1.8: Absorption characteristic of oxyhaemoglobin (red) and deoxyhaemoglobin (blue) [64]. .....	19
Fig. 1.9: photoplethysmogram diagram [68]. .....	20
Fig. 1.10: An example of a video laryngoscope (Medcaptain, model VS-10 series) [70] .....	21
Fig. 1.11: (a) Colorimetric device for the detection of CO <sub>2</sub> (Nellcor, model EASYCAPII), used to assess correct ETT placement [76]. (b) Typical ETCO <sub>2</sub> waveform for a healthy patient [78]. .....	22
Fig. 1.12: Reflectance spectra for (a) two <i>ex-vivo</i> porcine oesophagi and (b) trachea, with photographs of the tissues, highlighting the positions sampled [85]. .....	23
Fig. 1.13 Spectra from human cadavers, with the faint grey lines representing the averaged spectra for each cadaver, and the dark black line representing the average spectra of all human cadavers, with (a) being trachea and (b) being the oesophagus [86]. .....	24
Fig. 1.14: Spectra captured (Bedola <i>et al.</i> ) in the trachea of healthy human subjects, subjects admitted to BICU with inhalation injury, and BICU patients with non-inhalation injury [89]. .....	25
Fig. 1.15: An example of one of the commercial fibre optic probes used by the USAISR during research by Gulf Fiberoptics (R200-7-UV-VIS). .....	27
Fig. 2.1: Schematic of the opto-electronic components set-up used to make tissue reflectance measurements. ....	29
Fig. 2.2: Porcine sample used for <i>ex-vivo</i> measurements. ....	29
Fig. 2.3: Spectra from a porcine trachea (a), and oesophagus (b). – note the different response at the 530 – 590 nm wavelength region .....	30
Fig. 2.4: (a) Absorption spectrum of oxyhaemoglobin (HbO <sub>2</sub> red) and deoxyhaemoglobin (Hb blue). (b) The log of the reciprocal of reflectance spectrum (negative log) of a porcine tracheal sample (pink). (c) All three spectra with the negative log of the tracheal spectrum translated so that the first peak of the tracheal characteristic is equal to the first peak of the HbO <sub>2</sub> characteristic. ....	32
Fig. 2.5: Dissected trachea and oesophagus <i>ex-vivo</i> samples. ....	33

Fig. 2.6: (a) Porcine trachea showing the inside lumen (anterior and posterior), exterior, mucosa only, and cartilage only. (b) Porcine oesophagus, showing the inside lumen (interior mucosa), the exterior (exterior muscle), and the interior with the mucosa having been cut through (interior w/o mucosa). .....	34
Fig. 2.7: Spectra produced from the dissected porcine sample (Fig. 2.6), for the trachea (a) and the oesophagus (b). FP fringes = Fabry–Pérot fringes.....	35
Fig. 3.1: Concept design for a fibre optic sensor containing fibres cleaved at 90° for the (a) emission fibre and (b) resultant patch design to maximise light intensity.....	39
Fig. 3.2: Optical fibre cleaved at 45° showing how light is reflected and refracted..	40
Fig. 3.3: Experimental set-up used to measure the distribution of light around a fibre tip. (a) Photograph of the equipment. (b) Close-up showing how the photodetector rotates around the fibre tip (detector at 90° to fibre axis). .....	41
Fig. 3.4: The optical power distribution of light around the tip of a 90° (red) and 45° (blue) cleaved optical fibres, with the interpolated 45° plot (black) with peaks (green circles), .....	42
Fig. 3.5: The optical power distribution of light around the tip of, (a) a 90° and (b) a 45° cleaved optical fibres, with the distribution < 0° found by mirroring the measured distribution. ....	42
Fig. 3.6: Modelled effective transmittance and reflectance at the boundary of a 45° cleaved fibre. ....	43
Fig. 3.7: Cleaved optical fibres placed into a hollowed-out ribbon cable.....	45
Fig. 3.8: Measured reflectance spectra for 45° cleaved fibres in the 530 - 590 nm wavelength region with varying illumination and detection fibre distance (d). The individual repeats are shown as faint lines with the average of each 10 repeats shown as thicker lines.....	45
Fig. 3.9: Normalized reflectance spectra for 45° cleaved fibres in the 530 - 590 nm wavelength region with varying illumination and detection fibre separation - d. ....	46
Fig. 3.10: 3D model of the (a) trachea and (b) oesophagus. ....	47
Fig. 3.11: Fluence rate of all simulated photons propagated from the tip of an optical fibre into an oesophagus.....	48
Fig. 3.12: (a) Trachea (b) Oesophagus. Fluence rate of only the photons collected by the detection fibre at a separation distance from the emission fibre of 0.875 mm. ...	49
Fig. 3.13: Mean penetration depth of the simulated photons that were collected by a detection fibre in a trachea (blue) and oesophagus (red) model. The error bars in the penetration depth are from the standard deviation on 5 repeat simulations. There error bars on the fibre separations are from the number of pixels used in the 3D voxel models. ....	50
Fig. 3.14: A 45° cleaved fibre in a patch showing how light is emitted perpendicular to the fibre axis and the patch face (sensor dimension 6 × 4 × 1 mm). (a) Front view. (b) Back view. ....	51
Fig. 3.15: 3D model of a mould used to form a two-fibre patch (sensor dimension 6 × 4 × 1 mm). ....	52
Fig. 3.16: Photographs of the (a) 3D printed mould, (b) epoxy casting using the mould, (c) resulting sensor with optical fibres embedded in the epoxy (sensor dimension 6 × 4 × 1 mm). ....	53

Fig. 3.17: Epoxy sensor highlighting the directionality of the emitted light, (a) parallel and (b) perpendicular (sensor dimension $6 \times 4 \times 1$ mm).....	53
Fig. 3.18: Bend loss coefficient of a PMMA multimode optical fibre with a NA of 0.5 at varying bend radius. ....	55
Fig. 3.19: Design of an experiment to investigate how varying fibre bend radius ( $r$ ) optical power loss at the bend. (a) Schematic. (b) Photograph of fibre at a bend radius $r = 10$ mm. ....	56
Fig. 3.20: POF bent into a J-shape. The fibres would be cut at the bend for use in a sensor. The loss of optical power is seen as yellow light at the bend. ....	57
Fig. 3.21: Average intensity spectra for the first POF with varying bend radius from a straight fibre to a radius of 1 mm. ....	57
Fig. 3.22: Area under the curve of the mean spectra for three fibres at each bend radius. The fitted curves are of an exponential form. ....	58
Fig. 3.23: mean area under the curve of the spectra for three fibres at each bend radius from the mean of the repeats in Fig. 3.22. The fitted curve is of an exponential form. ....	59
Fig. 3.24: (a) J-shape bent emission fibre in an epoxy layer. (b) 3D rendering of the J-shape fibres in an epoxy layer. ....	60
Fig. 3.25: (a) Photograph of J-shape fibre sensor being cast, (b) sensor curing with a UV torch, (c) and (d) showing the directionality of the light emitted is mostly perpendicular to the sensor face. ....	61
Fig. 3.26: Concept designs for different three-fibre sensors. (a) Three-fibre rectangle sensor; (b) Three-fibre circular sensor. (c) Three-fibre circular sensor with a rectangular base. (d) Square patch that reduces overall patch dimension by reducing the length of the rectangular patch from 6 to 4 mm. ....	62
Fig. 3.27: Possible sensor locations for the ETT placement sensor. ....	64
Fig. 3.28: Two-fibre sensor integrated into the (a) inside lumen (b) outside lumen, and (c) behind cuff of an ETT. ....	65
Fig. 3.29: Porcine sample with the ETT placement sensor integrated into the cuff of the ETT and then placed into the trachea. ....	66
Fig. 3.30: Normalized reflectance spectra for an <i>ex-vivo</i> porcine trachea (blue) and oesophagus (red) when the ETT placement sensor is integrated (a,e) inside the ETT lumen, (b,f) outside the ETT lumen, (c,g) behind a deflated cuff, and (d,h) behind an inflated cuff. The thinner lines on each figure are the individual measurements and the thicker line is the average of the repeats. ....	67
Fig. 3.31: Boxplots of the ratios $R1$ (Eq. (3.8)) and $R2$ (Eq. (3.9))) for the ETT placement sensor in an <i>ex-vivo</i> porcine trachea (Trach) and oesophagus (Oeso), when the sensor is positioned (a) inside the lumen, (b) outside the lumen, (c) behind a deflated cuff, and (d), behind an inflated cuff. The statistical significance of a t-test is denoted by an asterisk, with n.s denoting the results not being statistically significant, * symbolises $p < 0.05$ , and *** represents $p < 0.001$ . ....	68
Fig. 3.32: 3D rendering of step-by-step sensor formation made by Bluefrog Design with a photograph of the finished sensor. ....	70
Fig. 3.33: Base mould for positioning the fibres in a circular cavity. ....	71
Fig. 3.34: Base sensor mould with (a) epoxy-filled cavity and (b) fibres bent and then clamped into position. ....	71



Fig. 3.35: (a) Top sensor mould and (b) combined moulds. ....	72
Fig. 3.36: Three sensors manufactured with metal moulds using a fibre separation of (a) 1.375 mm, (b) 1.125 mm, and (c) 0.875 mm. ....	72
Fig. 3.37: Intensity of light detected by the detection fibre from the two illumination fibres at separations of 1.375 mm (black), 1.125 mm (blue), and 0.875 mm (red). ..	73
Fig. 3.38: Photographs of a sensor made with (a) a transparent UV curable epoxy (Panacol, model Vitralit 1655), (b) a non-transparent temperature curable epoxy (two-part epoxy, Permabond, model ET5143). (c) shows the non-transparent epoxy being mixed for use. ....	74
Fig. 3.39: Comparison of a sensor manufactured with (a), (b) transparent epoxy, and (c), (d) non-transparent epoxy. ....	74
Fig. 3.40: Example of ‘glowing’ optical fibre as light from an LED is coupled to it, demonstrating a high loss of optical power through the cladding of plastic optical fibres. ....	76
Fig. 3.41: (a) ‘production line’ for consistently coating large lengths of optical fibre, and (b) close-up of coating pipette used to coat fibres. ....	76
Fig. 3.42: Black pigment-coated optical fibres fabricated using the “production line” process of Fig. 3.41. ....	77
Fig. 3.43: Spectra comparing coated (red lines) and uncoated (black lines) sensors when a finger is on (squares) and off (no squares inside inset plot) the sensor. ....	78
Fig. 3.44: Final sensor design with dimensions in mm. ....	80
Fig. 4.1: Flow chart of the computational methods used in this chapter to analyse data from experimentation. ....	82
Fig. 4.2: (a) Photograph of the two-fibre rectangular sensor with J-shape fibres. (b) 3D rendering of the sensor. ....	83
Fig. 4.3: Photograph of the tube placement Sensor integrated between a double-cuff ETT ....	84
Fig. 4.4: Experimental set-up used for ETT placement measurements with a sensor-integrated ETT. ....	84
Fig. 4.5: (a) 10 ETT placement sensors fabricated using the metal mould. (b) ETT placement sensor integrated ETT inside the oesophagus of an <i>ex-vivo</i> porcine oesophagus. ....	85
Fig. 4.6: (a) Normalized reflectance spectrum with the dark and white references in the 400-900 nm wavelength region. ....	86
Fig. 4.7: (a) Normalized reflectance spectrum in the 530 – 590 nm region. (b) Normalized reflectance spectrum with another single wavelength normalization performed at 561 nm. ....	87
Fig. 4.8: Normalised spectra from 9 <b>different</b> porcine tracheal and oesophageal <i>ex-vivo</i> samples. (a) and (b) are from sample 1, (c) and (d) are from sample 2 etc., up to (q) and (r) being from sample 9. The blue spectra, which are the left-side figures (a), (c), (e), ... , (q) are tracheal. The red spectra, which are the right-side figures (b), (d), (f), ... , (r) are oesophageal. The individual spectra are shown with faint colours, with the thicker line showing the average for all 50 measurements. ....	89
Fig. 4.9: Boxplot comparing the 9 trachea and oesophagi by ratios (a) <i>R</i> 1 and (b) <i>R</i> 2. Each boxplot contains 450 spectra per tissue, leading to 450 <i>R</i> 1 and 450 <i>R</i> 2 data points	

(900 total). The statistical significance of a t-test is denoted by an asterisk, with *** representing $p < 0.001$ .....	90
Fig. 4.10: Spectra from 10 ETT placement sensors measured in a <b>single</b> tracheal and oesophageal <i>ex-vivo</i> sample. (a) and (b) are from sensor 1, (c) and (d) are from sensor 2 etc., up to (s) and (t) being from sensor 10. The blue spectra, which are the left-side figures (a), (c), (e), ... , (s) are tracheal. The red spectra, which are the right-side figures (b), (d), (f), ... , (t) are oesophageal. The individual spectra are shown with faint colours, with the thicker line showing the average for all 50 measurements. ....	92
Fig. 4.11: Boxplot comparing the 10 sensors in a single trachea and oesophagus by ratios (a) $R1$ and (b) $R2$ . Each boxplot contains 500 spectra per tissue, leading to 500 $R1$ and 500 $R2$ data points (1000 total). The statistical significance of a t-test is denoted by an asterisk, with *** representing $p < 0.001$ .....	93
Fig. 4.12: ROC curve for the 10-sensors using $R1$ and $R2$ , the true positive rate refers to a correct identification of oesophageal tissue, whereas the false positive rate is for the incorrect identification of oesophageal tissue. ....	94
Fig. 4.13: Average <i>ex vivo</i> porcine tracheal and oesophageal spectra highlighting the similarity between the first principal component (PC1) and second principal component (PC2). ....	95
Fig. 4.14: Sample 1 oesophageal spectra from the 9-sample experiment.....	96
Fig. 4.15: 9-sample experiment comparing the first two principal components (PC1 and PC2) found from performing PCA over the characteristic range (530 – 590 nm) (N = 900 spectra).....	96
Fig. 4.16: 10-sensor experiment comparing the first two principal components (PC1 and PC2) found from performing PCA over the characteristic range (530 – 590 nm) (N = 1000).....	97
Fig. 4.17: 10-sensor experiment processed with PCA and a boundary drawn between the two.....	97
Fig. 4.18: (a) Mean, (b) skewness, and (c) kurtosis for the 9 porcine sample experiment, where the statistical measures are calculated over the characteristic range (530 – 590 nm) for each spectrum and then separated into trachea and oesophagus. The statistical significance of a t-test is denoted by an asterisk, with *** representing $p < 0.001$ . ....	98
Fig. 4.19: (a) Mean, (b) skewness, and (c) kurtosis for the 10-sensor experiment, where the statistical measures are calculated over the characteristic range (530 – 590 nm) for each spectrum and then separated into trachea and oesophagus.....	99
Fig. 4.20: Comparison of the ratios $R1$ and $R2$ for the (a) 9 <i>ex-vivo</i> samples with the same sensor and (b) 10 different sensors with the same single sample experiments. ....	101
Fig. 4.21: Comparison of the means of ratios $R1$ and $R2$ for the (a) 9-sample and (b) 10-sensor experiments. The error bars refer to the standard deviation. ....	102
Fig. 4.22: LDA boundary formation for the 9-sample experiment. ....	103
Fig. 4.23: Confidence estimate on the LDA tissue identification method for the 9-sample experiment. ....	104
Fig. 4.24: LDA boundary formation for the 10-sensor experiment. ....	105
Fig. 4.25: Confidence estimate on the LDA tissue identification method for the 10-sensor experiment. The black data points refer to incorrect tissue identifications. .	105

Fig. 4.26: (a) LRA model and (b) confidences for the 9-sample experiment using R1.	107
Fig. 4.27: (a) LRA model and (b) confidences for the 9-sample experiment using R2.	108
Fig. 4.28: (a) LRA model and (b) confidences for the 9-sample experiment using R1.	109
Fig. 4.29: (a) LRA model and (b) confidences for the 10-sensor experiment using R2.	110
Fig. 4.30: (a) Three-dimensional optimisation generated by the SVM method for the 9-sample experiment. (b) The minimum of the objective function (hyperplane) with the number of function evaluations (iterations).	111
Fig. 4.31: SVM processed data from the 9-sample experiment. The support vectors are shown with a black circle.	112
Fig. 4.32: (a) Three-dimensional optimisation generated by the SVM method for the 10-sensor experiment. (b) The minimum of the objective function (hyperplane) with the number of function evaluations (iterations).	112
Fig. 4.33: SVM processed data from the 10-sensor experiment. The support vectors are shown with a black circle.	113
Fig. 4.34: 9-sample data classification confidences with the KNN algorithm. (a) Full range of data, and (b) data showing only the test data and its neighbours.	114
Fig. 4.35: 9-sample data classification confidences with the KNN algorithm.	115
Fig. 4.36: 10-sensor data classification confidences with the KNN algorithm. (a) Full range of data, and (b) data showing only the test data and its neighbours.	116
Fig. 4.37: 10-sensor data classification confidences with the KNN algorithm.	117
Fig. 5.1: Tracheal section from Sinha <i>et al.</i> shows an (a) unintubated, and (b) intubated, porcine subject. Gl = submucosal glands; Ep = epithelium; Ca = cartilage [169]...	121
Fig. 5.2: Epoxy sensor from Liu <i>et al.</i> [170], containing POFs to detect a PPG and an FBG silica fibre to measure contact force.	122
Fig. 5.3: Sensor used for ETT placement detection and PPG measurements. Units are in mm	123
Fig. 5.4: Fibre Bragg grating (FBG) encased in a pressure transducing epoxy layer. A transverse force (F) is transduced into axial strain (S) [178].	124
Fig. 5.5: iTraXS design. (a) Opto-electronic design block diagram (FBG – fibre Bragg grating, NI – National Instruments, POF – plastic optical fibre, LED – light emitting diode.) (b) Photograph of the ETT with a sensor integrated into the cuff. (c) Schematic (fibres in blue are between the inner and outer cuff) [178].	125
Fig. 5.6: Flow chart of the experimental protocol [178].	126
Fig. 5.7: Intracuff pressure (blue) versus cuff-trachea contact pressure (red) for subject 1, sensors are at the posterior of the trachea. (a) The initial inflation and resulting pressures. (b) A 10s section after the cuff was fully inflated. 5: BCG refers to a ballistocardiograph response. 8: PIP refers to the peak inspiratory pressure [178].	126
Fig. 5.8: FBG contact pressure variation with manometer intracuff pressure for subjects 1:4 and all tracheal quadrants. (a) Full pressure range. (b) Lower contact pressure region of 20 to 80 cmH <sub>2</sub> O.	127

Fig. 5.9: Example of a PPG signal from tracheal mucosa. (a) Unfiltered PPG signal. (b) PPG signal with low-frequency content removed. (c) A Fourier spectrum of the unfiltered PPG signal [178].	127
Fig. 5.10: ETT placement sensor used in the animal study.	129
Fig. 5.11: (a) Photograph of the sensors integrated between the cuffs of an ETT. The third sensor is not visible and is behind the ETT in the photograph. (b) Schematic showing the cross-section of the cuff with the three sensors.	129
Fig. 5.12: Schematic diagram of the opto-electronic units used for ETT placement detection. The yellow and red lines are the 250 $\mu\text{m}$ diameter illumination fibres for the broadband white and IR LEDs. The orange line is the 500 $\mu\text{m}$ diameter detection fibre.	130
Fig. 5.13: (a) Photograph of the bundle of detection fibres in a triangle formation and adhered to the inside of a ferrule.	131
Fig. 5.14: Porcine subject after intubation and connection of tubes and fibres.	132
Fig. 5.15: Timeline of the main events of the animal study for all subjects (black) and specific changes to the protocol for subjects 1 (red), 2 (green), and 3 (blue).	133
Fig. 5.16: Flow chart summarising the data processing of the spectral data acquired from the animal study.	134
Fig. 5.17: Subject 3 (a) sensor orientation diagram in the trachea. (b) Photograph of the trachea with the ETT inside and with sensor 1 turned on. (c) Photograph of the ETT extubated without rotating and then placed in the approximate position on top of the subject so that the orientation is preserved.	135
Fig. 5.18: Subject 3 trachea – (a) Spectra normalized with the white reference standard and then (b) further Single wavelength normalization at 561 nm.	136
Fig. 5.19: Subject 3 Oesophagus - (a) Spectra normalized with the white reference standard and then (b) further Single wavelength normalization at 561 nm.	136
Fig. 5.20: 30s of spectral data taken shortly post-mortem ( <i>in-situ</i> ) for subject 3, sensor 2 (n = 1126).	137
Fig. 5.21: Post-mortem ( <i>in-situ</i> ) comparison between tracheal and oesophageal R1 and R2 values for subject 3 (a) sensor 1 (n = 2280), (b) sensor 2 (n = 2280), (c) sensor (3) (n = 2280), and (d) combined for all sensors (n = 6840).	138
Fig. 5.22: Comparison between <i>in-vivo</i> tracheal and recently deceased <i>in-situ</i> oesophageal R1 and R2 values for subject 3 (a) sensor 1 (n = 2280), (b) sensor 2 (n = 2280), (c) sensor (3) (n = 2280), and (d) combined for all sensors (n = 6840).	139
Fig. 5.23: <i>in-vivo</i> tracheal and <i>in-situ</i> oesophageal measurements over the full acquisition for subject 3 (n = 107946, 94.73 minutes).	140
Fig. 5.24: Subject 3 <i>in-vivo</i> tracheal measurements separated by sensor and <i>in-situ</i> oesophageal measurements (n = 107946, 94.73 minutes).	140
Fig. 5.25: Subject 3 trachea and oesophagus ratio values separated with an, (a) unweighted LDA boundary and, (b) weighted LDA boundary	141
Fig. 5.26: Confidences on LDA classifications for subject 3.	142
Fig. 5.27 Subject 3 trachea and oesophagus ratio values classified with the KNN method. (a) Example test data, (b) KNN confidences.	143
Fig. 5.28: Subject 3 trachea and oesophagus ratio values classified with the SVM method. (a) The objective function. (b) the minimum of the objective function (Min objective) change with the number of function evaluations. (c) the SVM boundary	

with the trachea and oesophagus classes shaded in light blue and pink, respectively.	144
Fig. 5.29: SVM confidence on the subject 3 tissue classifications.	145
Fig. 5.30: Subject 2 (a) sensor orientation diagram in the trachea. (b) Photograph of the trachea with the ETT inside with sensor 1 turned on. (c) Photograph of the ETT extubated without rotating and then placed in the approximate position on top of the subject so that the orientation is preserved.	145
Fig. 5.31: Subject 2 – Porcine trachea (a), (b) and oesophagus (c), (d). Spectra normalized with the white reference standard (a), (c). Then a further Single wavelength normalization at 561 nm (b), (d).	146
Fig. 5.32: Comparison of the ratio values of the trachea and oesophagus subject 2 shortly after death ( <i>in-situ</i> ), containing 9 minutes of tracheal and oesophageal data (4.5 minutes each tissue, n = 10284 combined).	147
Fig. 5.33: <i>in-vivo</i> tracheal and <i>in-situ</i> oesophageal measurements over the full acquisition for subject 2 (n = 206574, 174.24 minutes).	147
Fig. 5.34: (a) Subject 2 trachea and oesophagus ratio values separated with weighted LDA boundary and, (b) confidence on the identifications.	148
Fig. 5.35: Subject 2 trachea and oesophagus ratio values classified with the KNN method. (a) Example test data, (b) KNN confidences.	149
Fig. 5.36: Subject 2 trachea and oesophagus ratio values classified with the SVM method. (a) The objective function (hyperplane). (b) The minimum of the objective function (Min objective) change with the number of function evaluations. (c) The SVM boundary with the trachea and oesophagus classes shaded in light blue and pink, respectively.	150
Fig. 5.37: SVM confidence on the subject 2 tissue classifications.	150
Fig. 5.38: Subject 1 – Porcine trachea (a), (b) and oesophagus (c), (d). Spectra normalized with the white reference standard (a), (c). Then a further Single wavelength normalization at 561 nm (b), (d).	151
Fig. 5.39: <i>in-vivo</i> tracheal and <i>in-situ</i> ‘oesophageal’ measurements over the full acquisition for subject 1 (n = 671107, 183.17 minutes).	152
Fig. 5.40: Combined trachea and oesophagus ratio values across the three subjects (n = 979706, 347.47 minutes across).	153
Fig. 5.41: (a) Combined trachea and oesophagus ratio values separated with a weighted LDA boundary. (b) Confidences.	154
Fig. 5.42: Combined trachea and oesophagus ratio values classified with the KNN method. (a) Example test data, (b) KNN confidences.	155
Fig. 5.43: Combined trachea and oesophagus ratio values classified with the SVM method. (a) The objective function (hyperplane). (b) The minimum of the objective function (Min objective) change with the number of function evaluations. (c) The SVM boundary with the trachea and oesophagus classes shaded in light blue and pink, respectively. (d) SVM confidence on the combined tissue classifications.	156
Fig. 5.44: Visual representations of the 5 most effective principal components used to distinguish tracheal and oesophageal tissues.	158
Fig. 5.45: Spectral reflectance of a human liver between 18 and 55 hrs [180].	161
Fig. 6.1: Diagram of near-infrared spectroscopy (NIRS) optical fibre with a prism attached [184].	163

Fig. 6.2: Example differential method used to amplify the spectral feature of OHb. (a) Raw Intensity spectrum. (b) Differential intensity spectrum. (c) Differential intensity spectrum with a 20-wavelength moving mean average applied after differentiation. (d) Differential spectrum normalized by a white reference standard and a single wavelength normalization at 547 nm. ....	164
Fig. 6.3: Flowchart of machine learning spectral modelling and a curve fitting iterative process [189]. ....	165
Fig. 6.4: (a) Concept design for an ETT placement sensor which uses a photodiode and 3 narrow bandwidth LEDs. (b) Enlarged sensor configuration with an isosceles triangle (black dashed line) used to highlight the position of the sensors. ....	166
Fig. 6.5: Concept design for an ETT placement sensor which used a single broadband LED and three lens and photodiode pairs. OF refers to a narrow bandpass optical filter, centred on each of the spectral characteristic wavelengths (543, 561, and 578 nm). ....	167
Fig. 6.6: Experimental design of light from a broadband LED being passed through a variable optical filter and detected by a spectrometer. ....	168
Fig. 6.7: Spectra from a broadband LED coupled to a variable optical filter set to 561 nm. (a) Full spectral wavelength range. (b) 520 – 600 nm wavelength range. ....	168
Fig. 6.8: Experimental design of light from a broadband LED being connected to the ETT placement sensor and then placed in contact with an <i>ex-vivo</i> porcine sample and connected to a variable optical filter and detected by a spectrometer. ....	169
Fig. 6.9: Spectra from a broadband LED coupled to the ETT placement sensor placed on an <i>ex-vivo</i> porcine sample and then through a variable optical filter set to 561 nm. (a) Full spectral wavelength range. (b) 520 – 600 nm wavelength range. Note the reduced count compared to Fig. 6.7, indicative of the reduction in light power ....	169
Fig. 6.10: Nasogastric tube placement in the body [192]. Nasogastric tube [193]. An alternative example of where the technology in this research could be applied in Healthcare. ....	170
Fig. 6.11: (a) Spectra from the ETT placement sensor placed in a stomach model. (b) Moved down an <i>ex-vivo</i> porcine oesophagus. ....	171

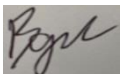



## List of Tables

Table 3.1: Normalized reflectance variation at the characteristic wavelength of OHb with varying illumination and detection fibre separation, with errors on the normalized reflectance originating from the standard deviation on repeats. ....	46
Table 3.2: Optical properties and thicknesses of the tissue layers of the trachea and oesophagus. ....	47
Table 3.3: Summary of the ETT placement sensor specifications with the chosen design shown in green and the tested and unchosen design in red. ....	79
Table 4.1: Comparison of the performance of using the mean, skewness, and kurtosis of each spectrum over the characteristic range (530 – 590 nm) to distinguish the tissues. ....	99
Table 4.2: Summary of the computational methods used to differentiate tracheal and oesophageal tissues from 9 <i>ex-vivo</i> porcine samples. ....	118
Table 4.3: Summary of the computational methods used to differentiate tracheal and oesophageal tissues using 10 sensors in 1 <i>ex-vivo</i> porcine sample. ....	118
Table 5.1 Performance of an SVM classifier with an increasing number of the most effective components found from PCA for the combined data from a porcine animal study. ....	157
Table 5.2 Comparison of the classifiers used to distinguish the tissues of 3 porcine subjects. ....	159

# Appendix A

## Ethics for this research was reviewed and approved by The University of Nottingham Faculty of Engineering Research Ethics Committee

Assessment Number: <i>(Leave blank)</i>	Location / Building and Room Number: 2 <sup>nd</sup> floor. Tower Building. Room 1006
Title of Process: Using fibre optic sensors placed on the body and in the mouth for contact pressure measurements, and to generate a reflectance spectrum, which can be used to determine tissue composition, PPG signal and SpO2.	
Assessor Name: <i>Brett Gadsby</i>  Status: PhD researcher  Signature:   Date: 16/10/2020	Academic/Line Manager/Other Supervisor Name: Assoc. Prof. Serhiy Korposh  Status: Associate Professor in Electronics  Signature:   Date: 16.12.2020
Laboratory Supervisor Name: Ricardo Goncalves Correia  Signature:  Date:	Area Safety Officer Name:  Signature:  Date:
<b>Emergency Shut-Off Procedure:</b> <i>(Include annotated digital photographs on a separate page)</i>  SEE ATTACHED FOR PROCEDURE  <b>IN CASE OF EMERGENCY CONTACT DETAILS:</b>  Name: Ricardo Correia                      Contact Telephone Number(s):Ext. Mobile:07913026694	
<b>Physical conditions of rig/activity:</b>  Temperature: working temperature 10- 40 °C  Pressure: No pressure control- atmospheric pressure  Machinery: See below for equipment details  Electrics: Power input 220~230VAC 50Hz/60Hz	<b>Chemicals involved:</b> <i>(List any chemicals used in the process)</i>  No chemicals involved.
<b>Environmental considerations:</b>  None	<b>Special precautions for chemicals and experimental work:</b>  None required.
<b>Equipment details:</b> <i>(identify tools and equipment to be used)</i>  <b>Diffuse reflectance kit:</b> <ol style="list-style-type: none"> <li>1. Plastic optical fibres</li> <li>2. Spectrometer</li> <li>3. White light source</li> <li>4. Sterile sensor sleeves</li> </ol>	<b>Details of any biological effects:</b>
<b>Other notes:</b>	

### **Brief description of the study design**

Title of the study: Using fibre optic sensors placed on the body and in the mouth for contact pressure measurements, and to generate a reflectance spectrum, which can be used to determine tissue composition, PPG signal and SpO<sub>2</sub>.

In collaboration with the anaesthesia department of Queens Medical Centre (QMC), the University of Nottingham's Optics and Photonics group is developing a fibre optic sensor to be used in endotracheal tubes (ET) during patient intubation. The sensor has been designed to provide a determination of tracheal tissues to verify tube placement, as well as accurate and continuous PPG, SpO<sub>2</sub> and contact pressure measurements via spectral reflectance measurements of the tracheal wall.

Intubation is a necessary and common medical procedure to secure a patient's airway to deliver oxygen to their lungs when their ability to do so is compromised. Successful intubation requires that the endotracheal tube be placed inside the trachea at an appropriate depth and cuff pressure. However, a patient may be intubated incorrectly, where the tube is placed down their oesophagus via accidental oesophageal intubation, this means a patient would not be receiving the necessary supply of oxygen and pulmonary aspiration of the stomach contents into the lungs is possible. There is also the possibility of the cuff being over or under-inflated, allowing for the blood perfusion to be cut off from the mucosa of the trachea leading to postintubation laryngotracheal injury or an insufficient seal of the cuff.

Our fibre optic sensor eventually aims to distinguish tracheal and esophageal tissue in real-time to notify clinicians of accidental esophageal intubation. The fibres will eventually be integrated into the cuff of an ET, where they will be pressed against the trachea. From the reflectance spectra, a PhotoPlethysmoGram (PPG) signal can also be ascertained which can ultimately be used for internal SpO<sub>2</sub> measurements; highly coveted vital sign monitoring for clinicians. A Fibre Bragg grating etched into the fibres will also allow for accurate contact pressure measurements of the cuff-to-trachea.

Before the human studies begin, initially some work will be done on ex-vivo animal tissue where a completely different set of fibre optic sensors will be placed on the samples. Multiple pieces of animals (sheep and pigs) trachea and oesophagus samples will be obtained. The samples are treated and stored as normal meat before they are received by us. Therefore, this provides as much health risk as standard raw meat. Standard safety procedures will be followed, Gloves will be worn when handling all samples, and all measurements will be made on a tray that will be thoroughly disinfected after use. Anything that touches the meat will be disposed of or disinfected and only used with the meat samples.

After initial work with animal samples and establishing sensor performance parameters, we would like to test this on people as this will provide us with real-time vital signs unavailable using animal samples. We are looking to recruit up to 20

healthy volunteers to have the sensors applied to various parts of the body, including the inside of their mouths. The fibre will be cleaned with an Isopropyl alcohol (IPA) solution and then placed inside a sterile plastic sensor sleeve. The sensor will be given to the volunteer who will then lightly press (pressure below 5kPa measured using a manometer) against the volunteer's thumb, ear, bicep and calf. The sensor will then be removed from the sleeve, cleaned with IPA solution, and placed in a new sterile sensor sleeve, and then the volunteers will themselves place the sensor-containing sleeve on the inside of their cheek, rough of mouth and tongue.

A fresh sterile sleeve will be used between volunteers so that cross-contamination is not possible, and the same sleeve will not be used on external parts of the body and in the mouth. The fibre is made from a plastic that is biocompatible and safe to be placed inside the mouth. The fibres are embedded in an epoxy patch that is biocompatible and placed in a sterile plastic sleeve that is sterile and biocompatible.

The volunteer will be required to place the fibre-containing sleeve on the described various parts of their body, including their mouth and hold it there with their finger for up to 2 minutes at a time. The pressure exerted by the volunteer is deemed to be lower than the smallest British standard for compression bandages of 14-17mmHg and will last no longer than 2 minutes, this will be the same for external body parts.

To comply with COVID regulations for human studies, the researcher will wear a mask and gloves at all times and will minimise contact with the volunteer by leaving the room whilst the volunteer places the fibres around their body. Time spent in the same room will not exceed 15 minutes. The volunteer will wear gloves at all times. The volunteer will wear a mask at all times, except when the sensor is placed in their mouth by themselves, whilst the researcher has left the room. After data has been taken, the volunteer will place the face mask back on, before disposing of the sleeve around the fibre themselves in a secure bio-hazard bin.

The volunteers will be taken from within the project team and research group, but staff from the faculty of engineering may be approached if more participants are required. Each volunteer will be asked to complete a maximum of 15 repetitions, though for most participants this number will be significantly less.

The device that is to be attached to the volunteer is two fibre optic cables one which will provide light from a halogen light source, and one which will bring the reflected light to a spectrometer. The electronics for the sensor are housed separately and so there is no electrical contact with the volunteer.

The personal details of the volunteer are not needed for the study so none shall be recorded. It is the readings of the sensor whilst it is on the subject that is of interest and does not require any personal information. Participants will be given a confidential identification number so that their data can be removed if they wish to withdraw. However, in the recorded data this number will be the only identifier, so it will be impossible to identify individual volunteers from the stored data. All the information will be logged and stored electronically on a password-protected laptop and a password-protected data storage system. After 7 years all the data will be securely destroyed.

The data recorded may be published anonymously in papers or studies. It will also be shared with commercial organisations interested in developing the technology into a product. It will not be possible to identify any individuals from the data shared or published.

Volunteers will not be paid.

### **Participant Information Sheet**

Using fibre optic sensors placed on the body and in the mouth for contact pressure measurements, and to generate a reflectance spectrum, which can be used to determine tissue composition, PPG signal and SpO<sub>2</sub>.

In collaboration with the anaesthesia department of Queens Medical Centre (QMC), the University of Nottingham's Optics and Photonics group is developing a fibre optic sensor to be used in endotracheal tubes (ET) during patient intubation. The sensor has been designed to provide determination of tracheal tissues to verify tube placement, and tracheal contact pressure, as well as accurate and continuous PPG and SpO<sub>2</sub> measurements via spectral reflectance measurements of the tracheal wall.

Intubation is a necessary and common medical procedure to secure a patient's airway to deliver oxygen to their lungs when their ability to do so is compromised. Successful intubation requires that the endotracheal tube be placed inside the trachea at an appropriate depth and cuff pressure. However, a patient may be intubated incorrectly, where the tube is placed down their oesophagus via accidental oesophageal intubation, this means a patient would not be receiving the necessary supply of oxygen and pulmonary aspiration of the stomach contents into the lungs is possible. There is also the possibility of the cuff being over or under-inflated, allowing for the blood perfusion to be cut off from the mucosa of the trachea leading to postintubation laryngotracheal injury or an insufficient seal of the cuff.

Why do this study? - Our fibre optic sensor will help clinicians and medical members properly perform intubations. It will allow for important vital sign monitoring to be achieved on any patient that has been intubated with these sensors attached to the tube. Our fibre optic sensors have already been tested on animal tissues, and we now need to progress the research by researching human volunteers.

What will participation involve? – A plastic sleeve containing two optical fibres will be handed to you. Whilst wearing gloves and a face mask, you will place the sensors on your thumb then the ear, then the bicep then the calf. You will then be given a new fibre-containing sterile sleeve to place inside your mouth (cheek, roof of mouth and tongue) to lightly press for a maximum of two minutes. You will be asked to repeat this no more than 15 times. You will have to press the sleeve in your mouth with only enough force to keep it in place.

How will my data be used? – No personal data will be taken or recorded. The only data recorded will be spectral reflectance recorded by the fibres and a spectrometer. The data recorded may be published anonymously in papers or studies. It will also be shared with commercial organisations interested in developing the technology into a

product. It will not be possible to identify any individuals from the data shared or published.

What else do I need to know? - The device that is to be attached to you is a sterile plastic sleeve containing fibre optic cable. The electronics for the sensor are housed separately and so there is no risk of electrical contact. The sleeves that will be used are sterile and biocompatible.

Participation is completely voluntary, and you have the right to withdraw at any time during the experiment. You will be given a unique identification number and if you wish to withdraw from the study after your data has been collected please use this number in correspondence so that your data can be identified and removed. Please note that once the study has been published it will not be possible to remove your data. However, if you get in touch to ask to withdraw, your data will be deleted and not used for future work. After 7 years your data will be securely destroyed.

If you wish to make a complaint on ethical grounds, you can send emails to this address:

EZ-Eng-Ethics@exmail.nottingham.ac.uk

The personal details and collected data will be kept confidentially in a password-protected PC. Only the research team on this project have access to it. It is not possible to identify individuals based on

these data and the data will be kept for seven years after finishing this study.

For further details please contact:

Researcher: Brett Gadsby (ppybjg@nottingham.ac.uk)

Project Supervisor: Assoc Prof. Serhiy Korposh ([ezzsk2@exmail.nottingham.ac.uk](mailto:ezzsk2@exmail.nottingham.ac.uk))



# Appendix B

## iTraXS Clinician Questionnaire

Dear Clinician,

The University of Nottingham and Nottingham University Hospital have developed a prototype disposable endotracheal tube equipped with optical fibre sensors (Figure 1), capable of real-time measurement of contact pressure, blood perfusion at the cuff-tissue interface, SpO<sub>2</sub>, heart and respiration rates, and core temperature. However, the number of measurands can be extended. The immediate aims are to address two problems: (i) pressure-induced injury, particularly laryngotracheal stenosis via measurement of the contact pressure and blood perfusion at the point of cuff-tissue contact; and (ii) ventilator-associated pneumonia by reverting from poorly fitting high volume low pressure cuffs to lower volume elastic high-pressure cuffs with control of contact pressure. The prototype was successfully tested on animals and human volunteers.

Your opinion is crucial for future development and refinement

Would you be able to spare 5-10 minutes of your time to answer a few questions? If you would like to have a chat with our representative to discuss this or other applications, please feel free to contact Sandor Erdody via email: [sandor.erdody@nottingham.ac.uk](mailto:sandor.erdody@nottingham.ac.uk)

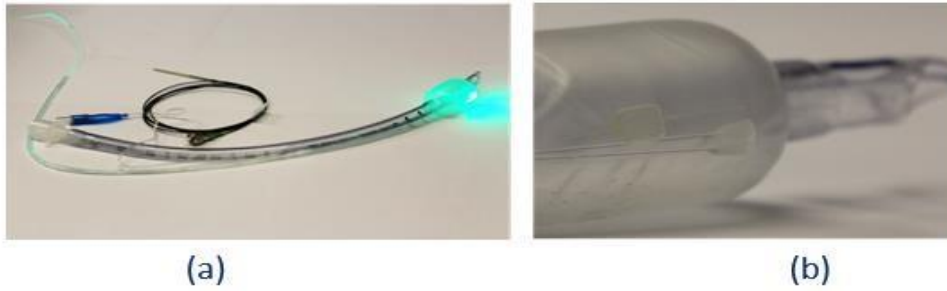
Thank you in advance,

OPG group,

Faculty of Engineering

University of Nottingham

Endotracheal tube equipped with optical fibre sensors (a) lights shining down the optical fibre attached to the ETT; (b) location of the optical fibre inside the cuff

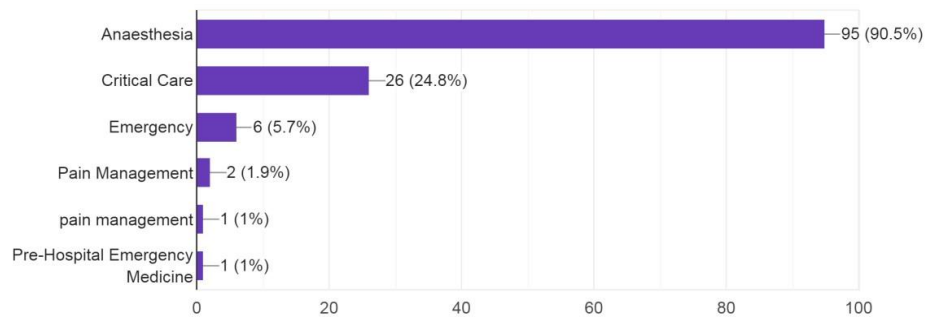


105 responses so far

Please tell us a little bit about yourself, by answering the next few questions

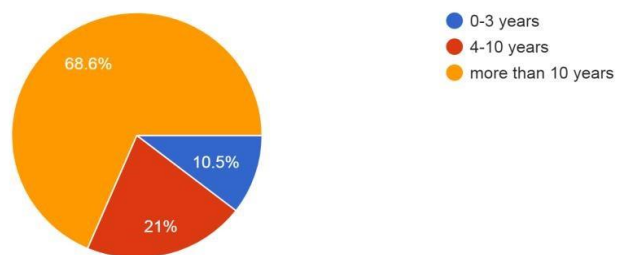
1. In what clinical area are you working (you may select more than one)?

105 responses



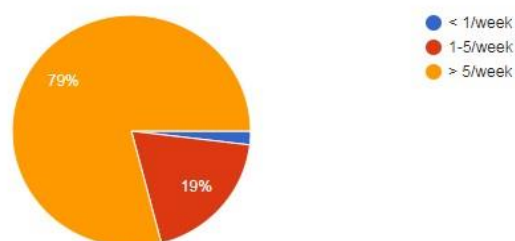
2. How many years of practice do you have?

105 responses



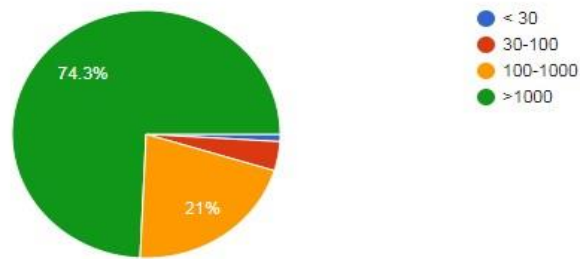
3. How often do you conduct ETT intubation in your current practice

105 responses



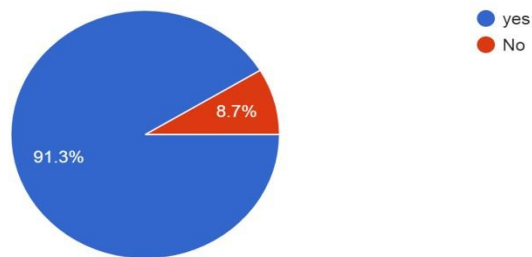
4. How many tracheal intubations do you estimate you have performed in your practice

105 responses



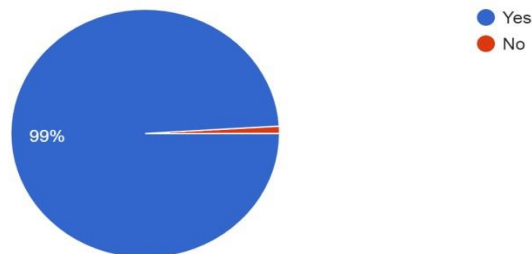
5. Are you familiar with PILTS (Post Intubation Laryngotracheal Stenosis) caused by endotracheal intubation?

104 responses



6. Are you familiar with VAP (Ventilator-Associated Pneumonia) caused by endotracheal intubation?

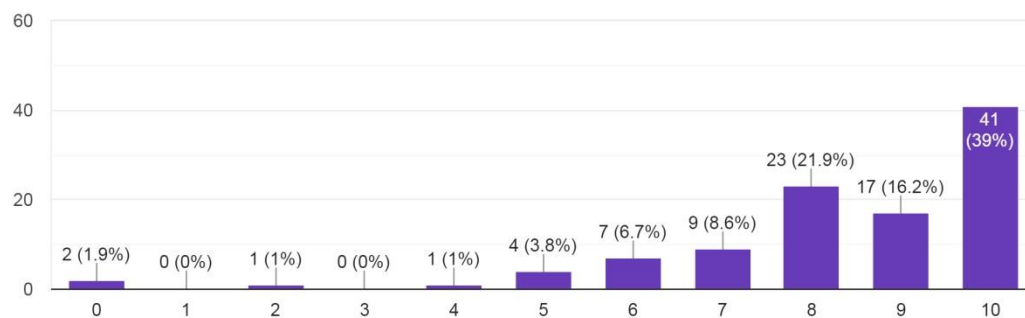
105 responses



7. What parameters are you interested in inside the trachea during endotracheal intubation?

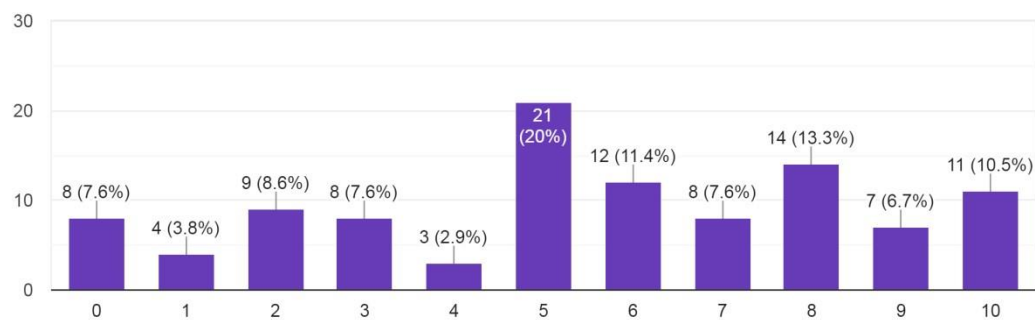
### 7.1 Cuff to trachea contact pressure

105 responses



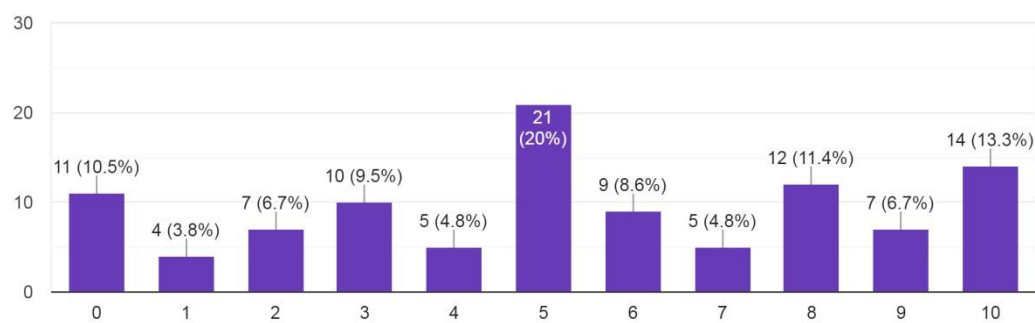
### 7.2 Heart rate

105 responses



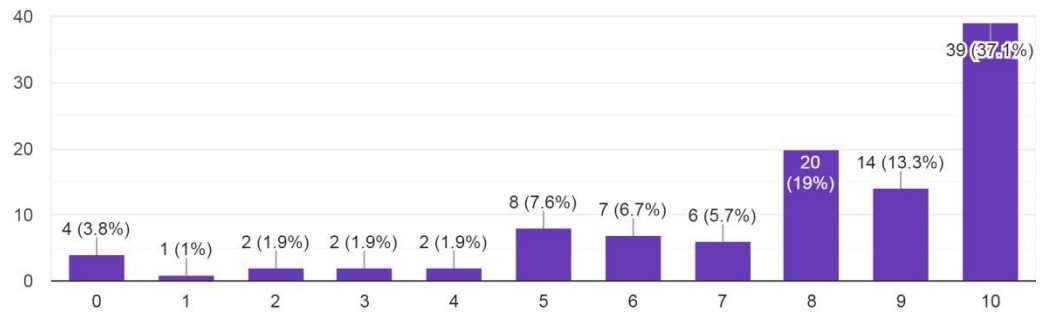
### 7.3 Respiration rate

105 responses



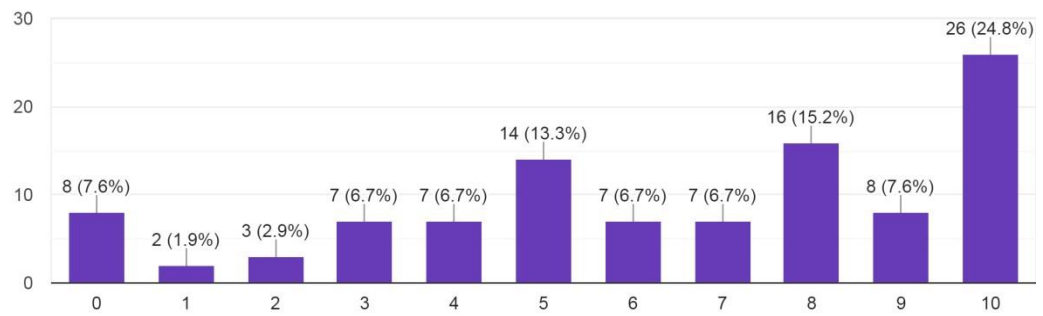
#### 7.4 SpO2

105 responses



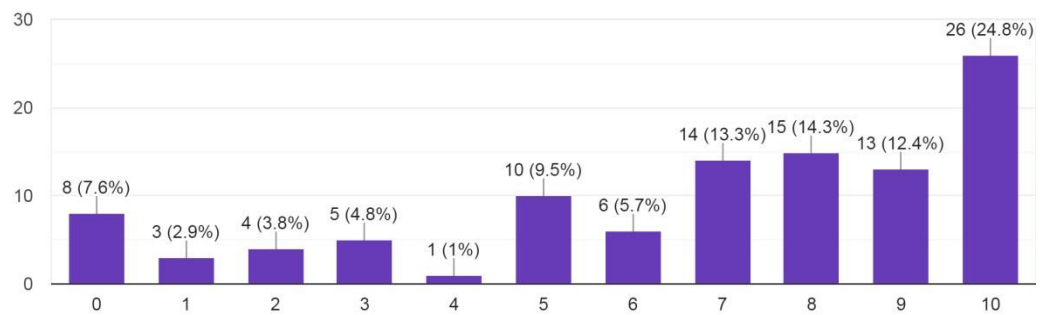
#### 7.5 Blood pressure

105 responses



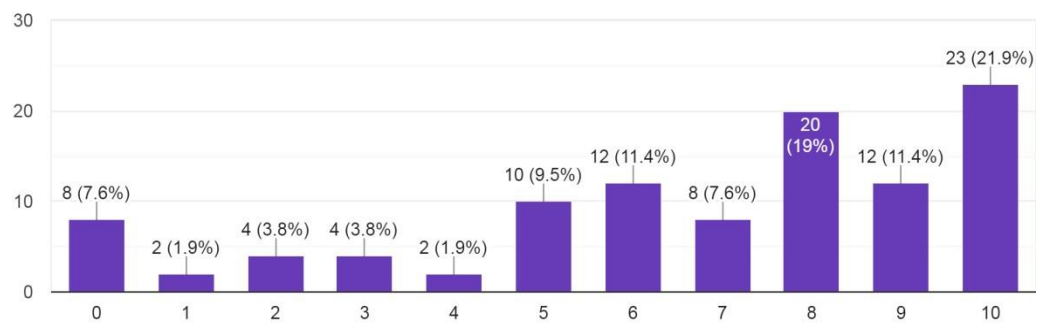
#### 7.6 Capillary refill

105 responses



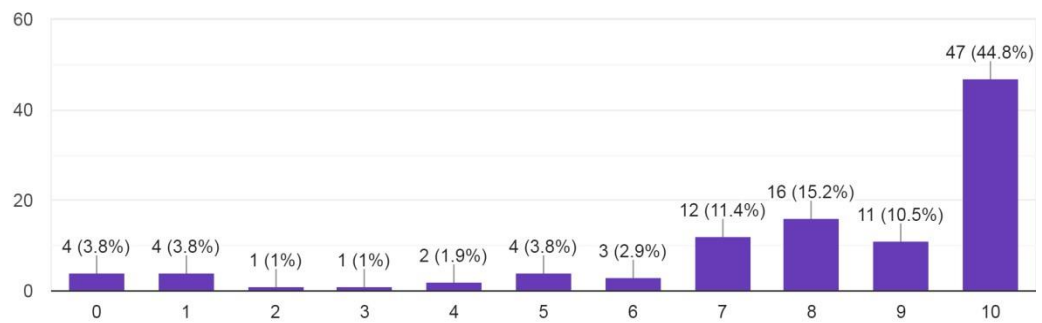
### 7.7 pH

105 responses



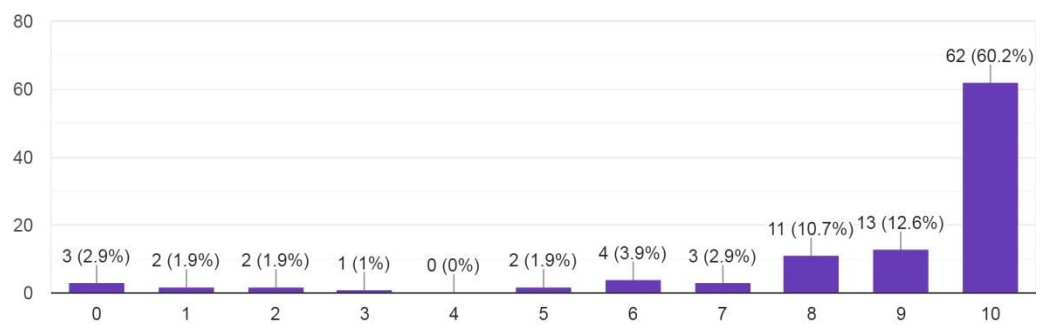
### 7.8 CO<sub>2</sub>

105 responses



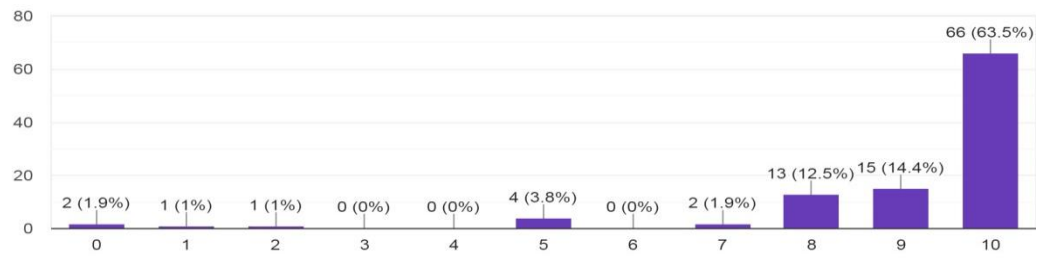
### 7.9 Tracheal identification

103 responses



### 7.10 Tube displacement

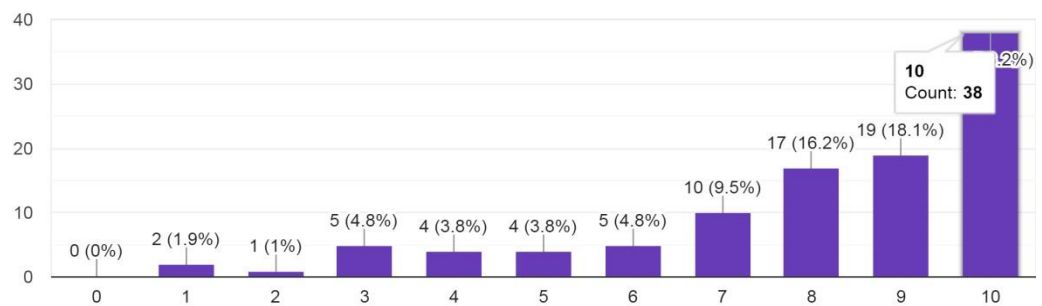
104 responses



8. What reduction in complications would be most important to you? Please rank them from 0 to 10, with 10 being most important for you

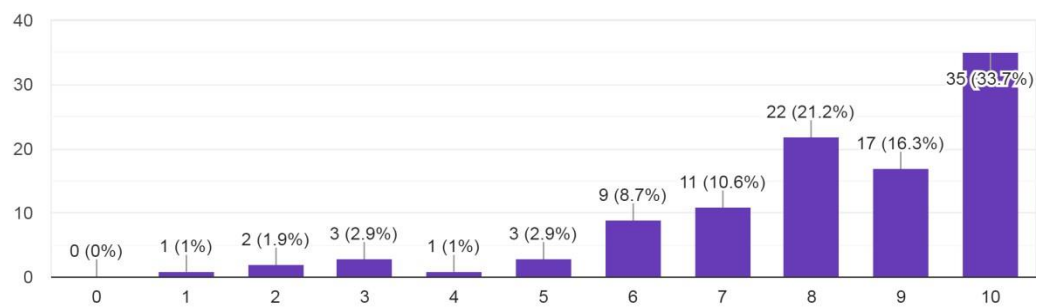
### 8.1 VAP (Ventilator-associated pneumonia)

105 responses



### 8.2 PILTS (Post Intubation Laryngotracheal Stenosis)

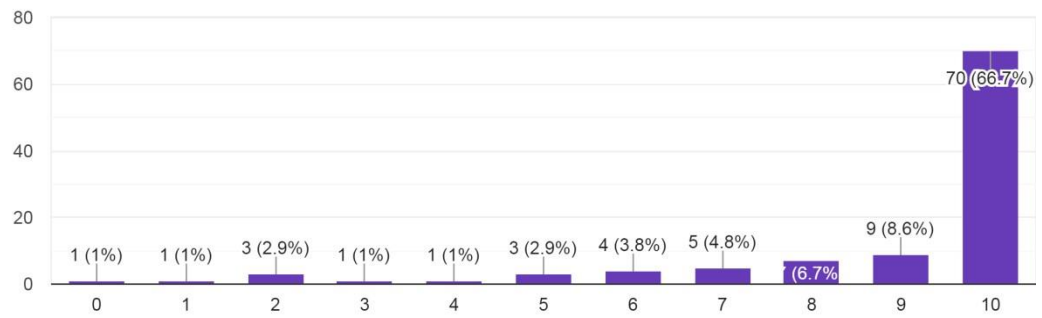
104 responses





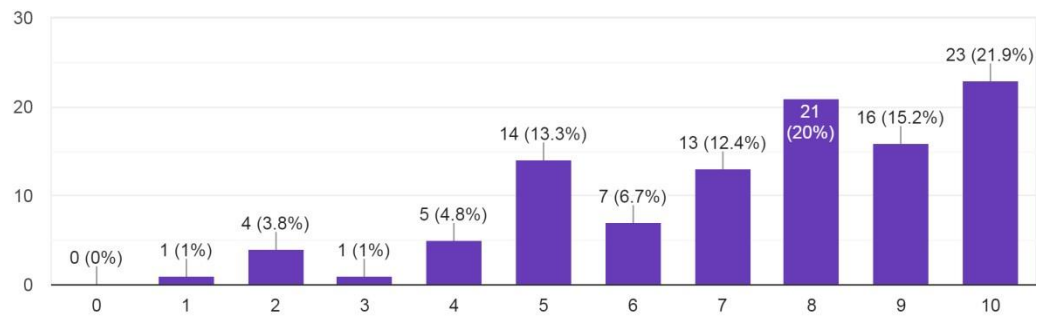
### 8.3 Oesophageal intubation

105 responses



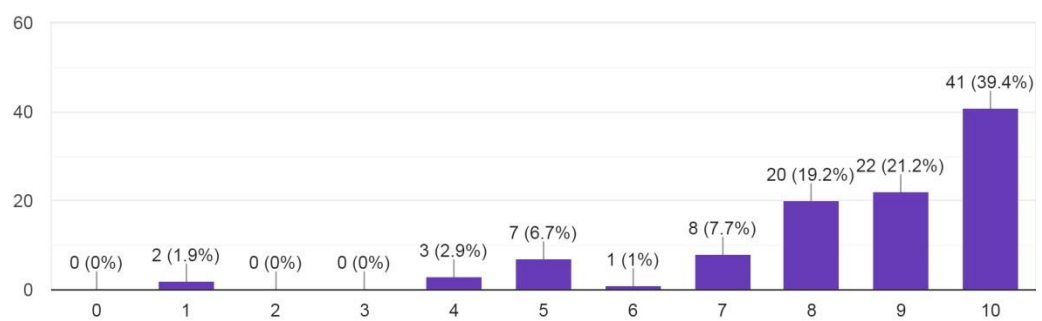
### 8.4 Sore throat

105 responses



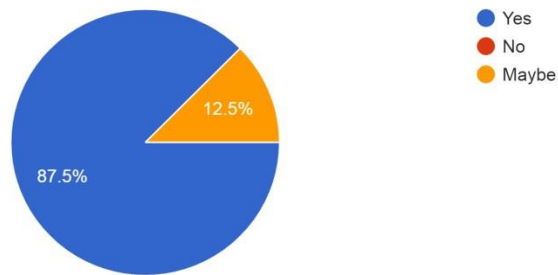
### 8.5 Ischaemia

104 responses



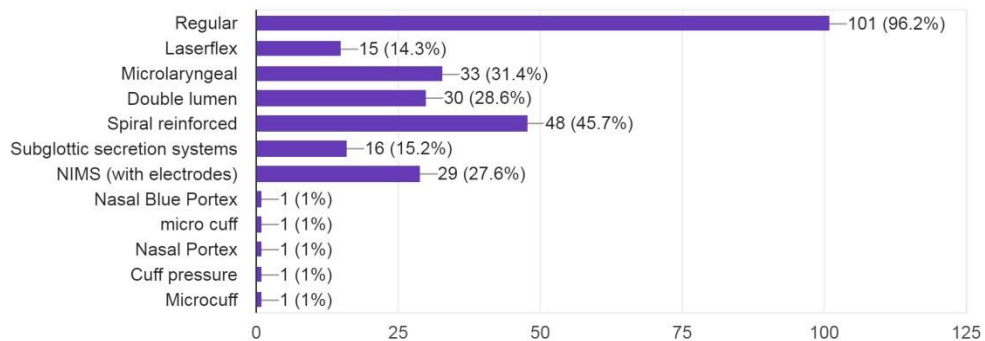
9. If smart ET tubes reduced complications from intubation, would you want to use them?

104 responses



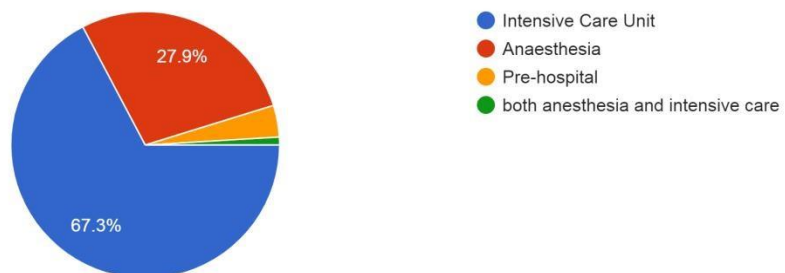
10. What type of ET do you usually use in your practice, regular or specialized endotracheal tubes?

105 responses



11. In which area of practice, you would see the iTraXS smart tube, as most relevant?

104 responses



## Appendix C

### Alternative normalization methods

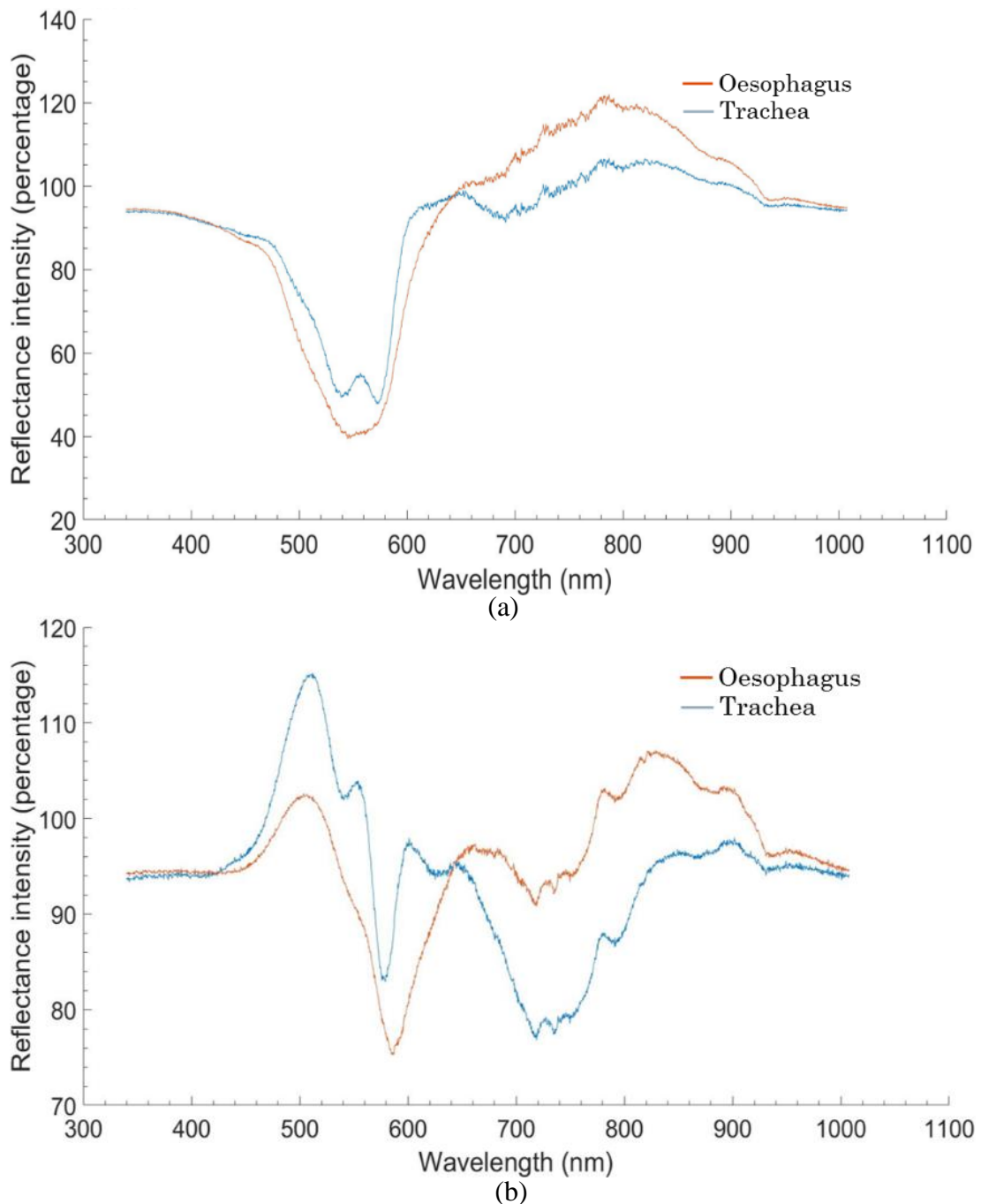


Fig. C1: Spectra from a porcine trachea (blue) and oesophagus (red) with referencing from a mirror (a) and phantom skin (b).

The probe was placed against a standard commercial mirror to verify the performance of an inexpensive alternative to a white diffuse reflectance standard (Fig. C1a) and then phantom skin (Fig. C1b) for the same reason. The reference spectra were normalized and subtracted from the tissue spectra. The mirror referencing produces spectra comparable to the direct illumination of the spectrometer, with the added

benefit of the light coupling with the detection fibre of the probe, therefore the reflection intensities are closer to those of the tissues. The phantom skin referencing produces poor results since the tracheal characteristic is absent from the resulting spectra.

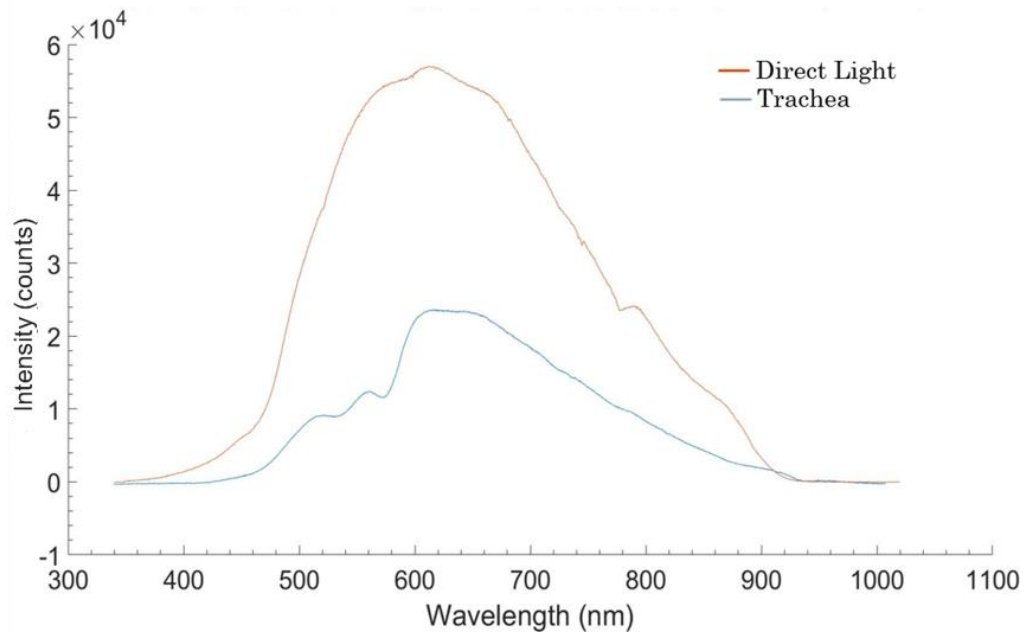


Fig. C2: Spectra from a porcine trachea (blue), and light coupled directly from the reflection probe to the spectrometer (red). Each plot is an average of 10 individual spectrum captures.

By directly illuminating light into the spectrometer from the reflection probe, the spectral shape of the emitted light from a halogen light source was obtained, with the average from 10 repeated measurements shown in Fig. C2. The optical power and peak intensity of the detected light will not be equivalent to what the tissue experiences, or what the spectrometer detects if a white reference standard was used. When acquiring spectra from tissues, the probe is placed directly onto the surface of the tissue ( $n = 10$ ), therefore light is only detectable if it is reflected or scattered back into the detection fibres. However, if it is only the spectral shape of the light we are interested in, and we assume it varies proportionally with wavelength, the absolute intensity is not relevant.

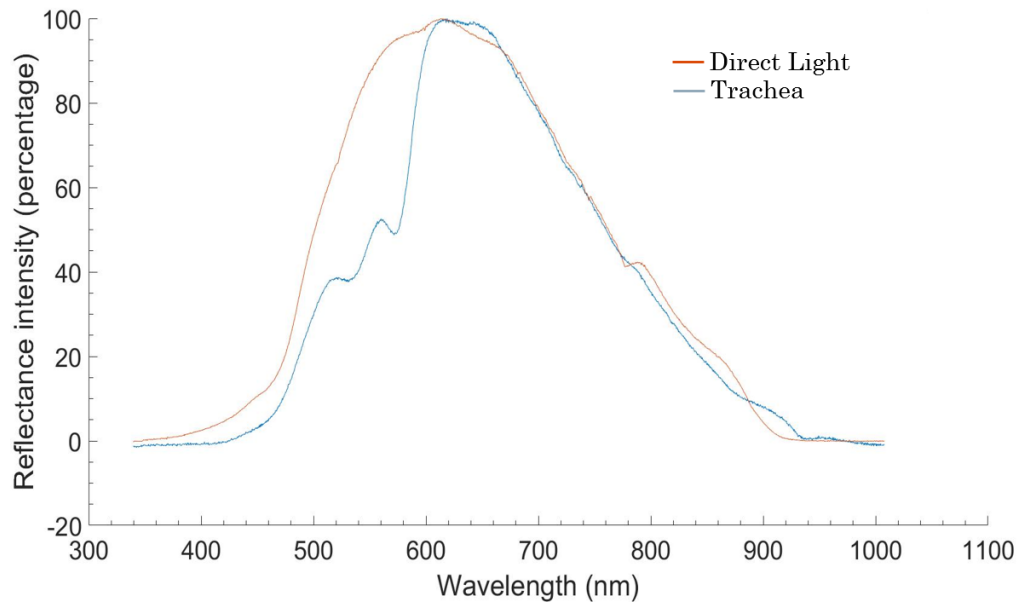


Fig. C3: Normalized spectra from a porcine trachea (blue), and light coupled directly from the reflection probe to the spectrometer (red).

Next, we can normalize the spectra such that the peak intensities are aligned at 100% for each Fig. C3. By performing this single wavelength normalization, the maximum amount of light that is detected is assigned a value of ~100%, although the wavelength used (616 nm) is arbitrary as all values are scaled by a single intensity, this method is reasonable as this is the maximum intensity that can be detected.

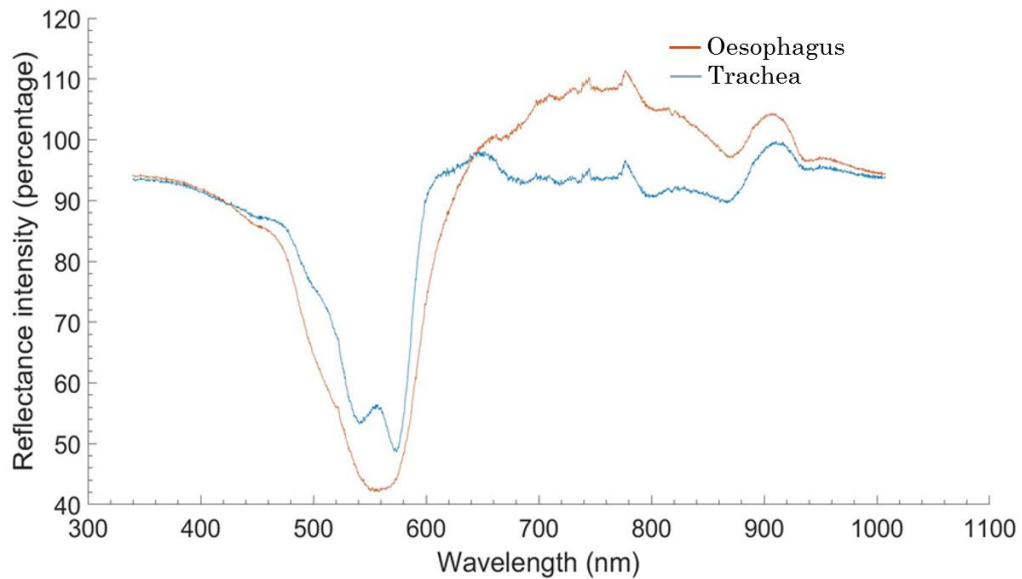


Fig. C4: Direct light source normalized spectra from a porcine trachea (blue) and oesophagus (red).

The difference between the single wavelength normalized direct light and the normalized trachea and oesophagus spectra is illustrated in Fig. C4 which highlights only the difference between the light source and the tissues. In this case, the characteristic consisting of a trough-peak-trough is present in the trachea, with only an absorption trough in the oesophagus. A reflectance intensity greater than 100% can be measured if higher light intensity is detected at that wavelength in the tissue when compared to direct light. These qualitative comparisons of different referencing

methods are to guide future research in this project. The use of a white reference standard is still considered the gold standard and is used in most studies, although the tracheal characteristic is detectable and observationally different from the oesophagus when direct light and mirror referencing is used. Direct light referencing doesn't account for changes in the shape of the spectra from light travelling through the detection leg of the equipment, and the mirror will not be a perfect reflector of visible light which may change the shape of the spectra, it may also be susceptible to aberrations. However, both methods account partially for the use of different light sources.

# Appendix D

ETT placement research paper (pre-submission to IEEE Trans. Biomed. Eng. )

## Smart endotracheal tube for identifying oesophageal intubation

Brett Gadsby, Stephen P Morgan, Ricardo Correia, Chenyang He, Barrie R. Hayes-Gill, Andrew M. Norris, Jonathan G. Hardman, Sergiy Korposh

**Abstract— Objective:** Unrecognised intubation of the oesophagus results in severe consequences for the patient. The design and implementation of a smart endotracheal tube (ETT) with integrated optical fibre sensors for distinguishing between oesophageal and tracheal tissues is described. Computational methods are used to distinguish and classify 9 *ex vivo* porcine tissue samples using the spectral properties at 50 different positions in the trachea and 50 in the oesophagus in the 530 – 600 nm wavelength range. Two classifiers (K-nearest neighbour (K-NN) and linear discriminant analysis (LDA)) were investigated. 100% of the tissues sampled were correctly distinguished, with LDA being the preferred choice when considering both performance and applicability. The relative confidence on these classifications are also explored. In clinical practice, we envisage that intubation would be performed in single step with no additional interventions, with the smart ETT indicating correct tube placement.

**Index Terms—** biosensor, endotracheal tube, optical fibre sensors, spectral reflectance, unrecognised oesophageal intubation

### I. INTRODUCTION

TRACHEAL intubation is used to secure a patient's airway and to deliver mechanical ventilation, oxygen, anaesthesia, and medicines. Unrecognised oesophageal intubation (UOI) refers to the incorrect and unnoticed placement of the endotracheal tube (ETT) in the oesophagus. Medical complications occur within minutes of UOI and can result in cardiac arrest, severe brain damage or death due to hypoxia by asphyxiation [1, 2]. The current gold standard for confirming correct placement of the tube in the trachea is based on visual confirmation of the tube passing the vocal cords and the presence of a continuous carbon dioxide waveform from exhaled gas. However, direct visualization is not always possible and can be mistaken, and CO<sub>2</sub> waveform is subject to equipment issues and faulty interpretation resulting in failure to identify tube placement in up to 10% of cases [3]. These issues are particularly relevant in emergency situations. [4]. Medical conditions such as obesity, a swollen airway, limited neck mobility, and haemorrhaging can also provide a difficult

airway. [5].

Difficult airways present in 4.6% to 23% of intensive care unit (ICU) patients [6, 7], with this increasing to 50% in the prehospital condition [8]. A review of the American Society of Anaesthesiologists (ASA) closed claims database before 1990 found that 3-8% of closed claims per year were linked to oesophageal intubation, with this falling to 1-2% between 1990-2013 [9, 10]. An analysis of UK anaesthesia related closed claims between 1995-2007 estimated 6% of claims are for UOI [11]. In 2016, in the UK, two routine surgical patients died from UOI [12, 13], causing it to be added to the National Health Service (NHS) Never Events list, i.e. an event with severe consequences that is entirely avoidable. There are deaths in the UK from UOI as recent as 2020, [14], deaths that the NHS describes as avoidable.

A device that can be integrated into a standard ETT and provide easily interpretable evidence of a UOI would reduce the incidence of patient harm. Nawn et al. [15, 16] through use of hyperspectral imaging and a bifurcated fibre optic probe in porcine and human cadaver models, documented the presence of a unique spectral characteristic in the trachea in the 530 – 600 nm wavelength range, which could be used to identify UOI. However, routine insertion of a fibre optic scope in every tracheal intubation is not a practical solution. It would be of great benefit to integrate sensing technology into the ETT so that incorrect placement can be identified immediately and automatically during intubation in a single step. In this paper an innovative smart ETT is presented, in which fibre optic sensing is integrated within the ETT, providing the potential for UOI to be identified during intubation. This builds on previous research by our team, in which a smart ETT containing fibre optic sensors has been developed to monitor cuff interface pressure and tracheal perfusion *in vivo* [17], significantly extending the capability of intra tracheal multiplexed sensing (iTraXS). Furthermore, a computational method has been developed to accurately distinguish tracheal and oesophageal tissues. The new system is tested on 9 *ex vivo* porcine trachea and oesophagus samples. manuscript.

This work was supported by the Medical Research Council, U.K. under Grant MR/T025638/1. Brett Gadsby is supported by an Engineering and Physical Sciences Research Council PhD studentship. SPM is supported by a Royal Society Industry Fellowship.

Brett Gadsby, Stephen P Morgan, Ricardo Correia, Chenyang He, Barrie R. Hayes-Gill, and Sergiy Korposh are with the Optics and Photonics Research Group, Faculty of Engineering, University of Nottingham, UK.

Andrew M. Norris is with the Department of Anaesthesiology, King Faisal Specialist Hospital and Research Centre, Riyadh, Saudi Arabia.

Jonathan G. Hardman is with the Department of Anaesthesia and Critical Care, Nottingham University Hospitals NHS Trust, Nottingham, UK and also with the Department of Anaesthesia, Division of Clinical Neurosciences, University of Nottingham, UK. (correspondence e-mail: ezzsk2@exmail.nottingham.ac.uk).



## I. METHODS

The investigation involved fabrication of a two-optical fibre tube placement sensor and integration into the cuff of an ETT. Fig. 1 shows a schematic of the overall system in which white light from an LED is delivered into the smart ETT and the spectrum of the reflected light is analysed. The smart ETT was then placed inside 9 tracheal and oesophageal samples and spectra were acquired. The two classifiers, k-nearest neighbour (K-NN) [i], and linear discriminant analysis (LDA) [ii], were then used to investigate whether tracheal and oesophageal tissues can be distinguished.

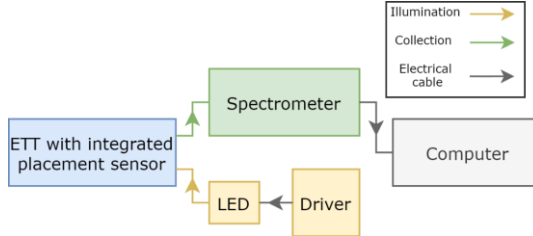


Fig. 1. Opto-electronic instrumentation, with the fibres and units that provide illumination and collection of light shown in yellow and green, respectively.

### A. Sensor Fabrication

Two plastic optical fibres (Poly methacrylate (PMMA), Asahi DB-500, US) were bent to 90° under moderate heating to produce two J-shaped fibres. The fibres were bent into a J-shape so that the tips are flush and normal to the surface of the ETT cuff to maximise illumination and collection. The fibres were then placed into a 3D printed mould (dimensions 6x4x1 mm) with a separation between the fibres of 3 mm which is typical for effective pulse oximetry measurements [iii], where a similar operating principal is used here. The fibres bend was centralised and then two drops of UV curable, transparent, biocompatible optical adhesive (Panacol, Vitralit, 1655, US) were pipetted into the mould. This epoxy was then cured by a UV torch (UV395, Tattu, U1S, UK), emitting a power of 5 W with a central wavelength of 395 nm for approximately 40 minutes. Although the curing time may affect the mechanical properties of the epoxy, it is not critical since it is the optical properties that impact the spectra. Afterwards, the top of the sensor was then filed and polished so that it was flush to the mould surface, resulting in sensor dimensions of 6x4x1 mm (Fig. 2a-b). A size 8 Mallinckrodt cuffed ETT (107-80, Covidien, UK) with a high volume, low pressure (HVLP) cuff made from polyvinylchloride (PVC) was used in a ‘double cuff’ arrangement (inner and outer cuff) described previously [17]. The sensor was placed between the two cuffs and secured to inside of the outer cuff with a drop of the optical adhesive (Fig. 2c).

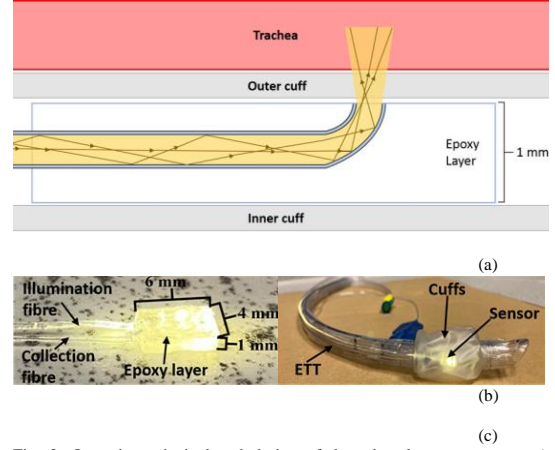


Fig. 2. Operating principle and design of the tube placement sensor. a) Schematic illustration showing the illumination fibre in an epoxy layer, and

### B. Opto-Electronic Unit

The illumination fibre of the sensor was coupled to a broadband LED with wavelength range 470 – 850 nm (Fiber-Coupled LED, Thorlabs, MBB1F1, US). The LED driver was set to deliver a drive current of 500 mA with a current ripple of 8mA (T-Cube LED Driver, Thorlabs, LEDD1B, US). The detection fibre was coupled to a UV-visible spectrometer (USB2000+UV-VIS-ES, Ocean Optics, US), set to a 200 ms integration time, a BoxCar width of 1 (no wavelength averaging) and with no scan averaging. The spectrometer was connected to a Windows PC via USB for data acquisition and to supply power. All connectors were universal bare fibre terminators (Thorlabs, BFT1, US), with 0.5 mm SubMiniature A (SMA) multimode connector (B10125A – SMA905, Thorlabs, US).

### C. Spectra Acquisition

9 porcine (Tamworth breed, Female) tracheae and oesophagi were obtained from a local abattoir and each sample consisted of the connected trachea and oesophagus, from the larynx to the vessels surrounding the heart (Fig. 3). The ETT was placed in a transparent medical sensor sleeve (Pegasus Surgi Safe Tubing Sleeve, small (18"×" 1.75"), Dental Sky, SKU: 50-137, UK) so that the fluids from the sample did not have to be cleaned from the ETT with each intubation. The ETT with integrated placement sensor was first covered with a non-transparent black felt cover and a dark reference spectrum taken. A white reference spectrum was then taken by placing the sensor inside the ETT cuff and medical sensor sleeve against a white reference standard (Spectralon diffuse reflectance target, Labsphere, AA-00827-000, US). The light and dark references were then used to initially normalise the signal to give reflectance percentages, and to remove any background signals. For each sample, the smart ETT was first passed through larynx and vocals chords and into the trachea. The first spectrum was taken when the ETT cuff had just passed the vocal cords. Each sequential spectrum was then taken after further inserting the

ETT and rotating the ETT. The distance of each further insertion was approximately 4 mm, ensuring the sensor was positioned alternatively on the hyaline cartilage rings and between them so that an even distribution of tissues was acquired. Each ETT rotation was approximately 20°, ensuring data acquisition from the posterior, left and right lateral, and anterior of the trachea. When the tip of the ETT reached the bottom of the trachea (Carina) it was retracted and rotated out of the trachea in a similar manner to insertion until 50 spectra were obtained. The sensor sleeve was then replaced and the ETT was placed into the oesophagus, where the same method of insertion and rotation was used until 50 spectra were again acquired. The ETT was then removed, the sensor sleeve replaced, and the next samples used until all 9 tracheae and oesophagi had been fully measured and a total of 900 spectra acquired.

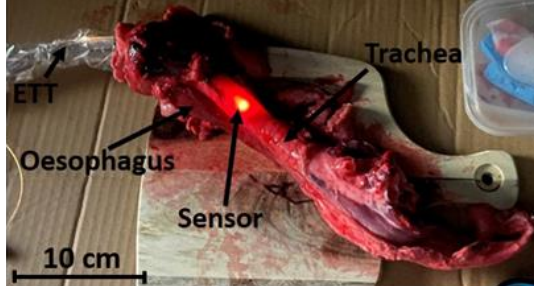


Fig. 3. The porcine trachea and oesophagus sample with smart ETT placed through the larynx and into the trachea.

## I. RESULTS

### A. Spectral Processing

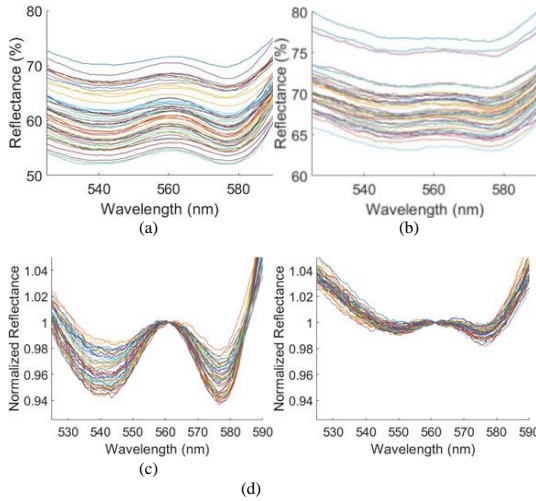


Fig. 4. 50 spectra of the trachea (a, c), and the oesophagus (b, d), with the unprocessed spectra (a, b) and the spectra normalized at 561 nm (c, d) for

The 50 spectra for both the trachea and oesophagus of sample 1 are shown in Fig. 4a-d. The tracheal characteristic consisting of a trough-peak-trough at ~543, 561, and 578 nm, respectively, can be seen in the trachea spectra (Fig. 4a). Although this characteristic is present in the oesophagus sample, it is less pronounced. Throughout the results, the

spectra were normalized at the central peak (561 nm), resulting in the variance mostly being expressed in the two reflectance troughs (543, and 578 nm), providing two variables with which to distinguish the two tissues.

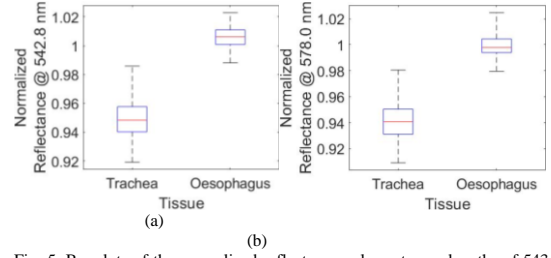


Fig. 5. Boxplots of the normalized reflectance values at wavelengths of 543

When the reflectance values are analysed separately, the two tissues can be well distinguished. For the reflectance at 543 nm, with a boundary of 0.9884, all the tissues can be correctly identified as tracheal or oesophageal. For the reflectance at 578 nm, with a boundary of 0.9795, 100% of the oesophagus data can be correctly classified, and 99.6% of the trachea data can be correctly classified.

### B. K-Nearest Neighbour

By combining the reflectance values at both characteristic wavelengths (543, and 578 nm), and plotting them against each other, a classification of the tissues can be performed.

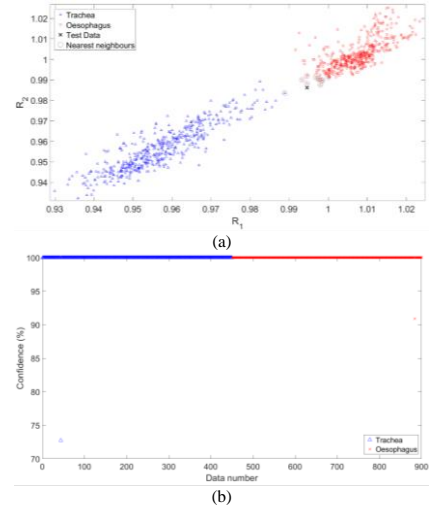


Fig. 6. a) Example of the Minkowski K-NN classifier on a single data point, with the 10 nearest neighbours highlighted with a circle around the data point. b) Percentage confidence of the K-NN classifier for all trachea (blue) and oesophagus (red) data.

For the test data point labelled 'X' in Fig. 6a, there are 8 tracheal neighbours and 2 oesophageal neighbours, so that test

data would be classified as trachea, with 80% confidence. From Fig. 6b, the K-NN classifier correctly identifies 100% of the data, with 7 data points not having its 10 nearest neighbours as the correct tissue, and therefore not being classified with 100% confidence. Data in Fig. 6b is plotted as discrete points but appear as a straight line due to the high proportion of points being identified with 100% confidence.

#### A. Linear Discriminant Analysis

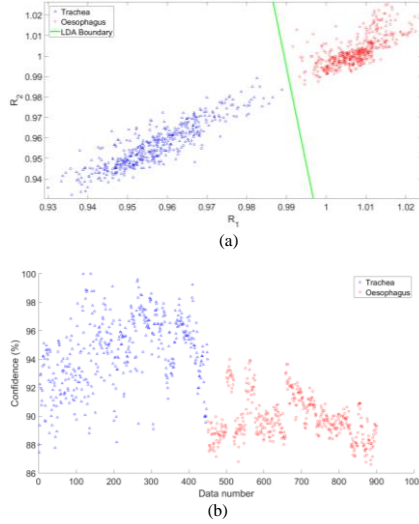


Fig. 7. a) Scatter plot of the trachea (blue triangle) and the oesophagus (red circles) normalized reflectance data, with an LDA boundary (green line). b) Percentage confidence of the LDA classifier for all trachea (blue) and oesophagus (red) data.

By performing linear discriminant analysis (LDA) on the data as described in the method section, a boundary between the two tissue types can be found (Fig. 7a), and 100% of the tissues can be correctly classified. If a data point is below the line it is classified as tracheal, if the data point is above the line it is classified as oesophageal. Fig. 7b shows the confidence on each data point, where it has been scaled such that the data point furthest from the line gives a 100% confidence.

## II. DISCUSSION

Using appropriate classifiers, 100% of the tissue data samples can be correctly classified by both the K-NN method and the LDA method. For LDA, the weighting function amplified values close to the boundary, but realistic confidences require more *in vivo* research to determine the optimum weighting. Fig. 7b was produced by calculating the distance from each data point to the LDA boundary, and then scaling the distance exponentially such that data closer to the line have a higher percentage confidence, with the furthest data point from the line giving 100% confidence, and the data closest to the boundary giving a 63% confidence. For the K-NN method, the number of nearest neighbours can be varied, with 10 having been found to work well. However, by increasing the number of nearest neighbours, more of the tissues to

which the test data does not belong would be found, especially near the boundary, lowering the percentage confidence for these results, but producing a more representative percentage confidence.

Both LDA and K-NN perform well but LDA can be more easily and rapidly applied. During clinical use of the smart ETT, only a single straight-line equation would be stored and compared to an unknown tissue measurement, as opposed to the K-NN method where every training data point needs to be compared to the unknown. Although the K-NN confidences presented (Fig. 6b) are higher than the LDA's (Fig. 7b), these were chosen only as examples, and the scaling of them would be modified once more data is acquired. Other classifiers such as logistic regression analysis (LRA) [i], and support vector machines (SVMs) [ii], were also investigated (data not shown here) and proved successful in distinguishing the two tissue types. However, they are both more computationally expensive to implement than K-NN and LDA and yielded similar success rates. These may be explored further in future research where the data is less easily classified, such as with *in vivo* measurements in the presence of blood and aspiratory fluids from the trachea and oesophagus.

The presence of the tracheal characteristic has been documented previously by Nawn et al. [12]. This research provides a more practical and convenient application of this characteristic, in the form of smart ETT that can identify incorrect intubation in a single step without additional clinical intervention. The smart ETT incorporates a small optical reflectance sensor into a standard ETT, along with the prospective classifiers to distinguish the tissues. Further advantages include utilising an LED which produces a high proportion of light in the relevant wavelength region of 530 – 600 nm; a J-shaped sensor design to launch and collect light more efficiently to/from the tissue; and integration of the sensor into the cuff. The latter brings the sensor into intimate contact with the tissues, thus reducing motion artefacts and achieving high quality signals [14], supporting better classification. Principal component analysis (PCA) has been demonstrated by Nawn et al. [13] to help distinguish the two tissue types. However, due to the normalization of the spectra at the central peak (561 nm), the variance is mostly expressed in the two troughs of the characteristic (578 and 543 nm) and dimensionality reduction is unnecessary. The similarity between the two spectra types and the first two principal components is less desirable to distinguish the tissues when compared to the classifiers explored in this paper, due to complexity and success. PCA may be of use in future research when other variables are measured alongside the spectral characteristic, such as blood perfusion, oxygen saturation and interface pressure between the cuff and the tissue [17]. These variables may be used to help distinguish the two tissues, where PCA can reduce the dimensions of the matrix into a smaller number of uncorrelated variables which maximise variance, increase interpretability, whilst still retaining most of the information.

The origin of the tracheal reflectance characteristic has been suggested to originate from the presence of oxyhaemoglobin

(Nawn et al. [13]) due to its similarity to the well documented absorption characteristic. Although not presented, through dissection of tracheal samples, the clear presence of the characteristic can be seen in the tracheal mucosa, and its absence in the tracheal cartilage. The characteristic can also be seen in the muscular layer surrounding the oesophagus, but not in the mucosa. Therefore, it is likely that the characteristic does originate from oxyhaemoglobin, and due to the thinner more transparent composition of the tracheal mucosa along with the white reflective cartilage, incident light can more readily interact with the oxygenated blood, whereas the thicker, less transparent mucosa of the oesophagus scatters and absorbs the light. Therefore, tears in the oesophageal lining could allow the light to penetrate the mucosa and the muscular layer and result in false negative results. However, it is likely possible to distinguish the trachea in the presence of blood and soot, although with a lower success rate [1]. Multiple sensors and a voting system could also be used to reduce false negatives.

Future work will focus on the repeatability of multiple sensors, to determine if a calibration of each individual sensor is necessary to accurately distinguish the two tissues, or if a single boundary can be found that satisfies new sensors. *In vivo* experimentation will also reveal if the sensor can perform under more clinically applicable conditions.

#### I. CONCLUSION

Unrecognised oesophageal intubation (UOI) can result in cardiac arrest, severe brain damage or death due to hypoxia

by asphyxiation. A new smart ETT has been demonstrated with integrated optical fibre sensing to indicate UOI in a single step without additional clinical intervention. By utilizing the spectral properties of the trachea, acquired with a two-fibre sensor integrated into the cuff of a standard ETT, *ex vivo* tracheal and oesophageal porcine tissues can be well distinguished with 100% success for 9 pairs of samples and 50 measurements per sample. The K-NN and LDA classifiers have been highlighted due to their ease of implementation and rapid processing, although other classifiers perform well due to the high separability of the data.

- [1] P. K. Birmingham *et al.*, "Esophageal intubation: a review of detection techniques.", *Anesthesia & Analgesia*, vol. 65, no. 8, pp. 886-891, 1986.
- [1] M. Cobas *et al.*, "Prehospital intubations and mortality: a level 1 trauma center perspective.", *Anesthesia & Analgesia*, vol. 109, no. 2, pp. 489-493, 2009.
- [1] J. Li, "Capnography alone is imperfect for endotracheal tube placement confirmation during emergency intubation.", *The Journal of emergency medicine*, vol. 20, no. 3, pp. 223-229, 2001.
- [1] M. A. Cobas *et al.*, "Prehospital intubations and mortality: a level 1 trauma center perspective.", *Anesthesia & Analgesia*, vol. 109, no. 2, pp. 489-493, 2009.
- [1] A. J. Williamson *et al.*, "Difficult intubation: an analysis of 2000 incident reports.", *Anaesthesia and intensive care*, vol. 21, no. 5, pp. 602-707, 1993.
- [1] F. J. Heuer *et al.*, "Incidence of difficult intubation in intensive care patients: analysis of contributing factors." *Anaesthesia and intensive care*, vol. 40, no. 1, pp. 120-127, 2012
- [1] S. A. Workeneh *et al.*, "Magnitude and predisposing factors of difficult airway during induction of general anaesthesia.", *Anesthesiology research and practice*, vol. 2017, no. 5836397, pp. 1-6, 2017
- [1] X. Combes *et al.*, "Prehospital standardization of medical airway management: incidence and risk factors of difficult airway.", *Academic Emergency Medicine*, vol. 13, no. 8, pp. 828-834, 2006
- [1] J. Metzner *et al.*, "Closed claims' analysis. Best Practice & Research Clinical Anaesthesiology.", vol. 25, no. 2, pp. 263-276, 2011
- [1] M. Honardar *et al.*, "Delayed detection of esophageal intubation in anesthesia malpractice claims: brief report of a case series.", *Anesthesia and analgesia*, vol. 125, no. 6, pp. 1948, 2017
- [1] T. Cook *et al.*, "Litigation related to anaesthesia: an analysis of claims against the NHS in England 1995-2007.", *Anaesthesia*, vol. 64, no. 7, pp. 706-718, 2009
- [1] Courts and Tribunals Judiciary. Prevention of future deaths. Peter Saint. Available from <https://www.judiciary.uk/publications/peter-saint/> [Accessed 22 March 2021].
- [1] Courts and Tribunals Judiciary. Prevention of future deaths. Sharon Grierson. Available from <https://www.judiciary.uk/publications/sharon-grierson/> [Accessed 22 March 2021]
- [1] Judiciary. UK. In the Milton Keynes Coroner's Court. Inquest into the death of Glenda May Logsdail, Regulation 28: report to prevent future deaths, 2021. [https://www.judiciary.uk/wp-content/uploads/2021/09/Glenda-Logsdail-Prevention-of-future-deaths-report-2021-0295\\_Published.pdf](https://www.judiciary.uk/wp-content/uploads/2021/09/Glenda-Logsdail-Prevention-of-future-deaths-report-2021-0295_Published.pdf), accessed 22/03/2021.
- [1] C. D. Nawn *et al.*, "Distinguishing tracheal and esophageal tissues with hyperspectral imaging and fiber-optic sensing.", *Journal of biomedical optics*, vol. 21, no. 11, pp. 117004, 2016
- [1] C. D. Nawn *et al.*, "Using spectral reflectance to distinguish between tracheal and oesophageal tissue: applications for airway management.", *Anaesthesia*, vol. 74, no. 3, pp. 340-347, 2019
- [1] R. Correia *et al.*, "Intra-tracheal multiplexed sensing of contact pressure and perfusion", *Biomedical Optics Express*, vol. 13, no. 1, pp. 48-64, 2022
- [1] P. Cunningham *et al.*, k-Nearest neighbour classifiers: (with Python examples).", arXiv preprint arXiv, pp. 2004.04523, 2020
- [1] A. Tharwat, A *et al.*, "Linear vs. quadratic discriminant analysis classifier: a tutorial.", *International Journal of Applied Pattern Recognition*, vol. 3, no. 2, pp. 145-180, 2016
- [1] C. Liu *et al.*, "Optical fibre-based pulse oximetry sensor with contact force detection. *Sensors*.", vol. 18, no. 11, pp. 3632, 2018
- [1] S. Menard, "Applied logistic regression analysis", Sage, vol. 106, 2002
- [1] W. S. Noble, "What is a support vector machine?" *Nature biotechnology*, vol. 24, no. 12, pp. 1565-1567, 2006
- [1] D. Berard *et al.*, "Spectral Reflectance Can Differentiate Tracheal and Esophageal Tissue in the Presence of Bodily Fluids and Soot.", *Sensors*, vol. 20, no. 21, pp. 6138, 2020



# Appendix E

## iTraXS Poster (Midlands Health and Life Sciences Symposium 2021)



### iTraXS (intra-Tracheal multipleXed Sensing) - an optical fibre sensing endotracheal tube

The University of Nottingham, Department of Electrical and Electronic Engineering  
Brett Gadsby, Ricardo Correia, Sergiy Korposh, Andrew M. Norris, Barrie R. Hayes-Gill, Rishie Sinha, Jonathan G. Hardman, David S. Gardner, Simon Talbot, Daniel Harvey, Julian Mcglashan, and Stephen P. Morgan



#### 1. Abstract

A smart endotracheal tube (ETT) has been developed containing integrated optical fibre sensors (OFS) to determine pressure at the cuff-trachea interface and blood perfusion to the tracheal mucosa.

This system reduces trachea damage and helps to avoid ventilator associated pneumonia (VAP).

#### 2. Introduction

- ETTs are routinely used globally in 290M operations per year (1.1M in NHS).
- Endotracheal tube cuff forms a seal in the trachea.
- Ideal cuff inflation pressures vary due to trachea size & medical complications.
- Cuff under-inflation causes loss of effective ventilation leading to increased rates of ventilator associated pneumonia (VAP).
- Cuff over-inflation causes tracheal ischemia and tracheal stenosis due to pressure on the trachea.

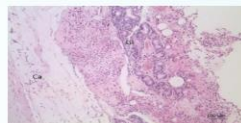
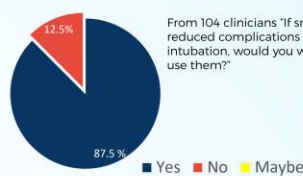


Fig.1. Uninflated animal tracheal section. Minimal numbers of lymphocytes are present within lamina propria & submucosa. 10x. Hematoxylin & Eosin. Ca = cartilage; Ep = epithelium; Cl = submucosal glands.

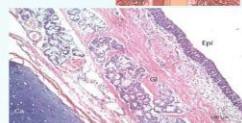


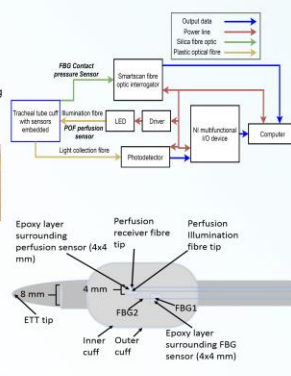
Fig.2. Inflated animal tracheal section. Visible diffuse ulceration of tracheal mucosa and abundant neutrophils admixed with pale extracellular eosinophilic material (edema) within lamina propria & submucosa. 10x. Hematoxylin & Eosin. Ca = cartilage; Cl = submucosal glands.

#### 3. iTraXS Design & System

- An opto-electronic system controls & interprets data from OFSs.
- The system fits inside a small control box, with tablet screen displaying information allowing setting changes.



- Fibres embedded into a small epoxy layer - then integrated into cuff of standard ETT.
- Sensors held in intimate contact with trachea, allowing measurement of core vital signs, ensuring ideal cuff inflation.



#### 4. Perfusion

- Photoplethysmography (PPG) used to non-invasively measure blood volume change of microvascular tissues.
- PPG measured/detected using two plastic optical fibres.
- Core PPG more desirable than peripheral PPG.
- Additional optical fibres allows SpO<sub>2</sub> measurement and identification of accidental oesophageal intubation (AOI).

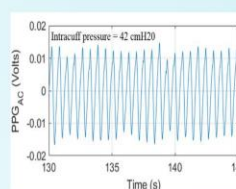


Fig.3. Tracheal PPG at intracuff pressure of 42 cmH<sub>2</sub>O, measured with iTraXS in porcine model.

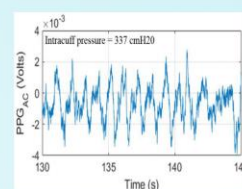


Fig.4. Tracheal PPG at intracuff pressure of 337 cmH<sub>2</sub>O, measured with iTraXS in porcine model. NOTE: Artificially large intracuff pressure highlights PPG amplitude and perfusion index (PI) decrease.

#### 5. Cuff-Trachea Contact Pressure

- Fibre Bragg grating embedded in small epoxy layer used to measure cuff-trachea contact pressure.
- Intracuff pressure is currently used as surrogate for true contact pressure.
- However, iTraXS continuously measures the actual cuff pressure exerted on trachea.

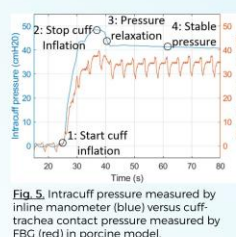


Fig.5. Intracuff pressure measured by inline manometer (blue) versus cuff-trachea contact pressure measured by FBG (red) in porcine model.

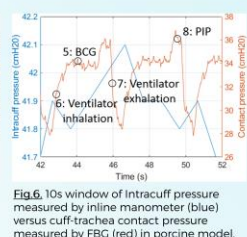


Fig.6. 10s window of intracuff pressure measured by inline manometer (blue) versus cuff-trachea contact pressure measured by FBG (red) in porcine model. NOTE: 5: BCG is 'ballistocardiograph response'. 8: PIP is 'peak inspiratory pressure'.

#### 6. Acknowledgements and Contact

- National Institute for Health Research (II-LA-0813-20008)
- Medical Research Council (MR/T025638/1)
- The University of Nottingham - PhD funding EPSRC
- Contact: Brett Gadsby email: brett.gadsby@nottingham.ac.uk; 07588731146

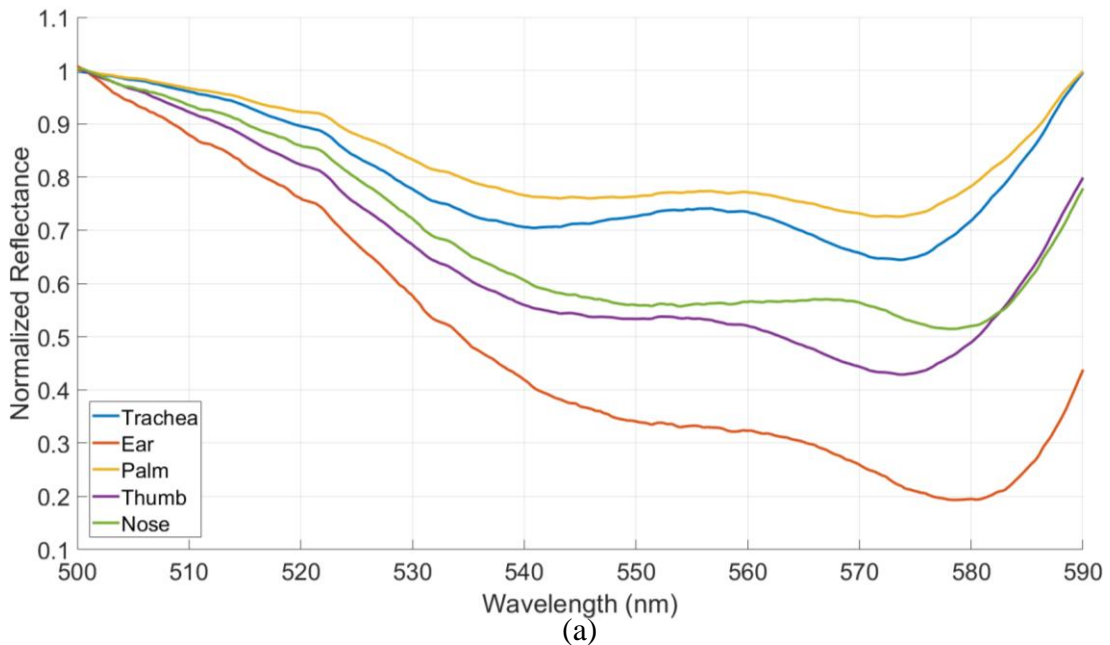
Brett Gadsby - PhD Researcher at the University of Nottingham



# Appendix F

## Characterisation of the Human Body

Measurements on an *in-vivo* human model were performed with the reflection probe to determine the presence of this characteristic as well as its variation. The reflection probe was placed on the surface of various body parts and 10 spectra were stored for each position by lifting the probe up and then placing it back on the surface of the body, the resulting spectra were then normalized with a white reference standard and averaged. The single wavelength normalization at 500 nm was then performed. The integration time was set to 500 ms, and a dark and white reference was taken by turning off the LED and covering the probe with a non-transparent felt and by placing the sensor against the white reflection standard, respectively. For comparison, a porcine tracheal sample was once again acquired, and the probe was placed against the inside wall of firstly the trachea and then the oesophagus.





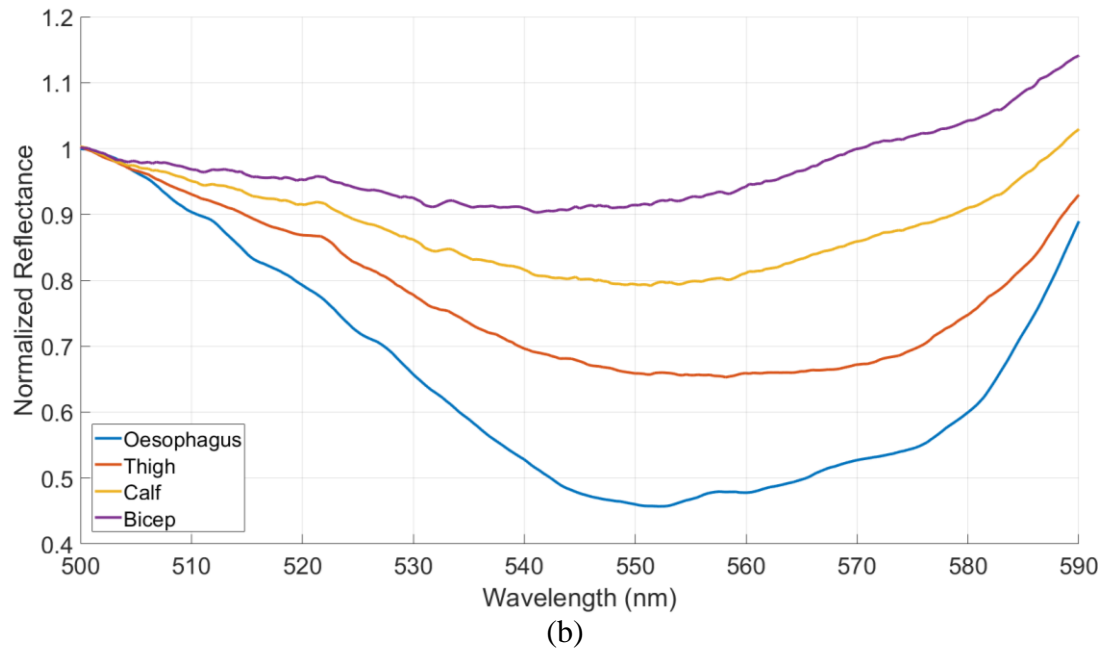
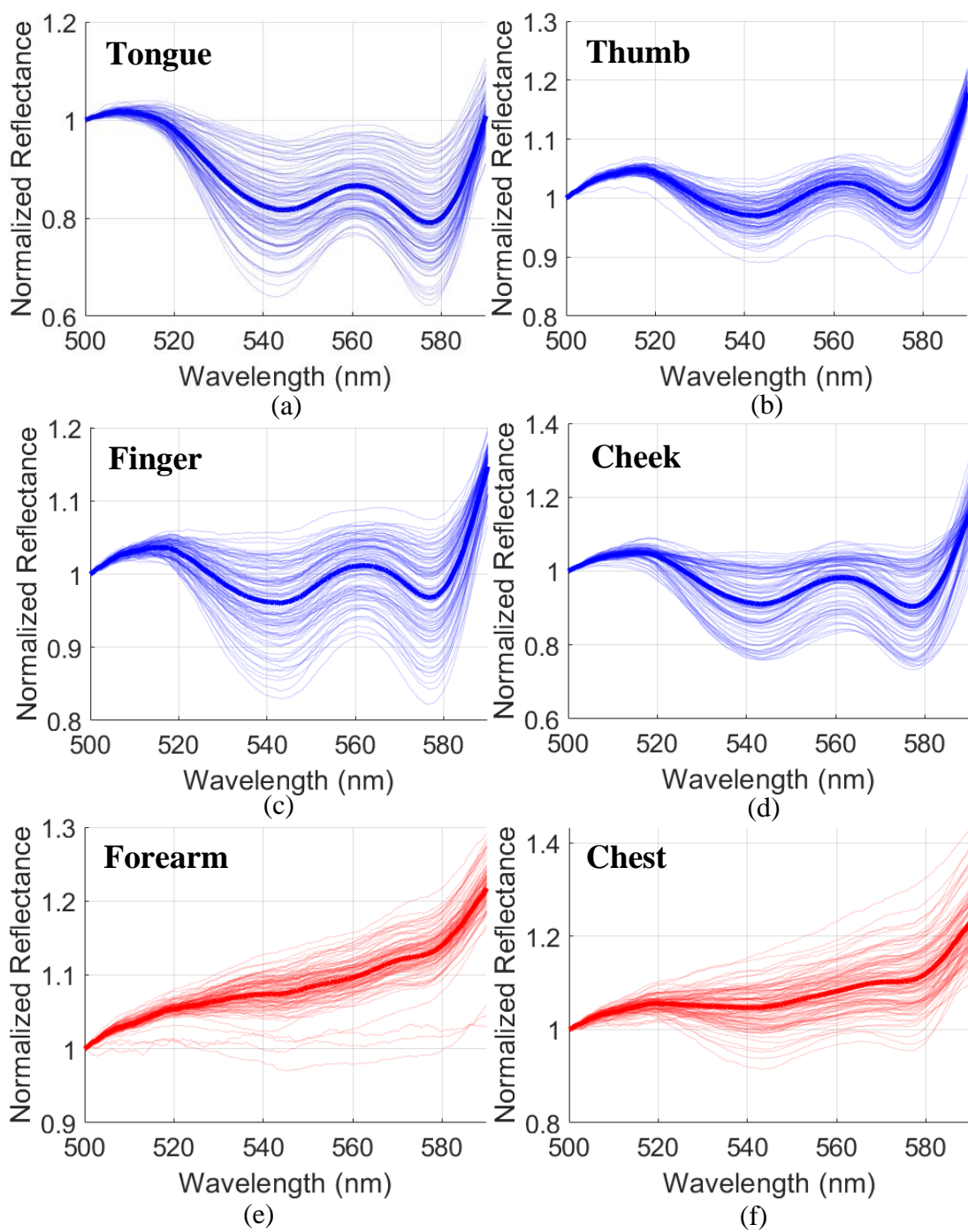


Fig. F1: Reflection spectra measured with a bifurcated probe placed on an (a) *ex-vivo* porcine trachea as well as an *in-vivo* human volunteer's ear, palm, thumb, and nose, as well as a (b) *ex-vivo* porcine oesophagus and an *in-vivo* human volunteer's thigh, calf, and bicep.

The body parts have been grouped by whether their spectra present the trough-peak-trough absorption characteristic in the 530 - 590 nm wavelength range. From the body parts measured, those that are 'connective' i.e. being flexible or on the periphery of the body. These parts tend to have a thinner mucosa with little muscle under it and exhibit absorption characteristics (Fig. F1a). Whereas, those that are more muscular and centralised in the body and contain more fat with a thicker mucosa tend not to show this characteristic (Fig. F1b). This is physiologically reasonable as the light can less easily interact with OHb in muscular tissues as the thicker less transparent mucosa absorbs the more light, similar to the mucosal differences in the trachea and oesophagus. This can be observed in some people in the connective and peripheral body parts. For example, the fingertips can be a reddish hue as the mucosa close to the surface of the skin is thin and more transparent and is well perfused with oxygenated blood allowing the reddish hue to be seen with the naked eye. However, it should be noted only a single volunteer was used, and these results require a broader more representative sample of the human population

Measurements of the diffuse reflectance of another set of body parts were then performed using the same methodology, namely: spectrometer; light source; and commercial probe. However, the integration time was decreased from 500 ms to 300 ms, as the spectrometer was saturating with the higher integration time on some body parts. The number of measurements was also increased from 10 to 100.



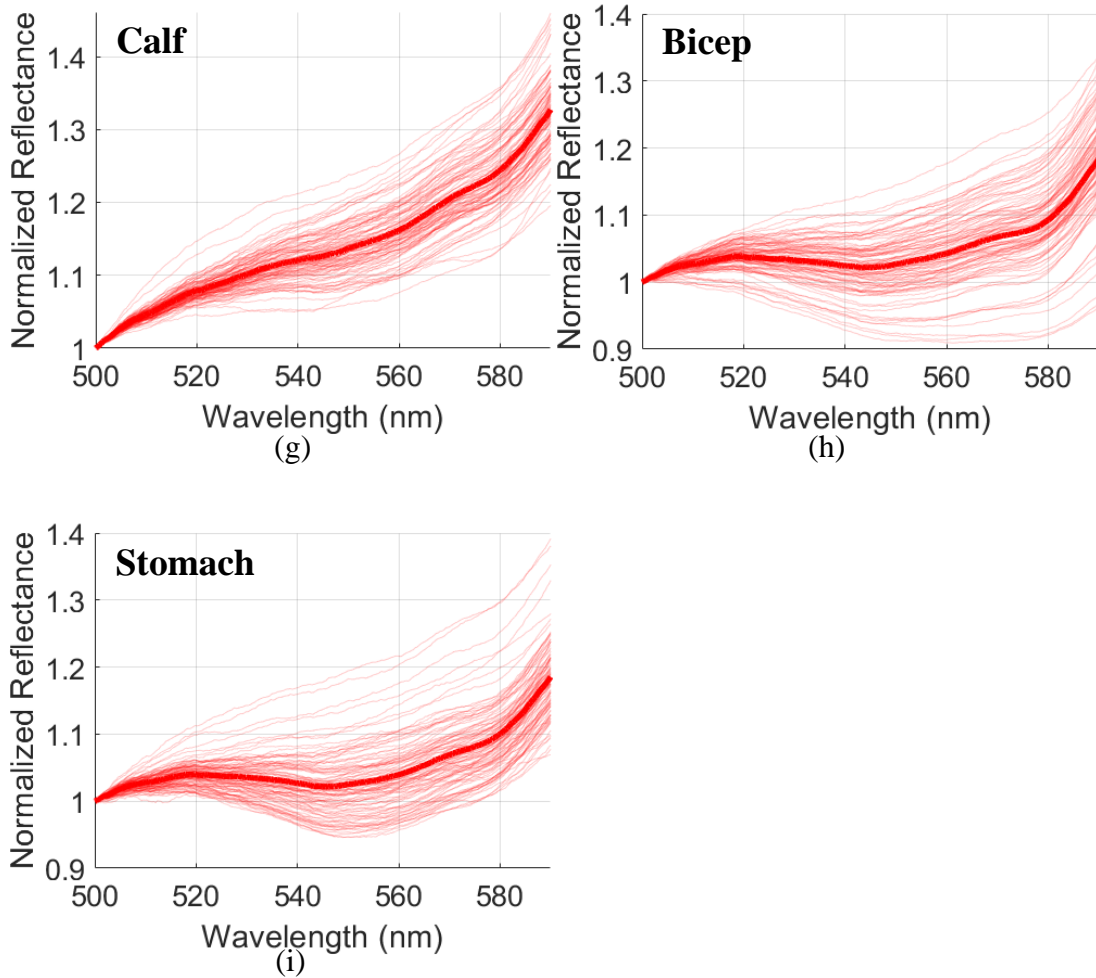


Fig. F2: Reflection spectra measured with a bifurcated probe placed on an *in-vivo* human volunteer's (a) tongue, (b) thumb, (c) finger, and (d) cheek, as well as the (e) forearm, (f) chest, (g) calf, (h) bicep, and (i) stomach. Each repeat is shown by a lighter and thinner line, with the mean of all the repeats shown in a darker and thicker line. The blue spectra demonstrate the trough-peak-trough characteristic.

The colour blue was used to highlight body parts where the trough-peak-trough characteristic is visible (Fig.F2a-d) and the colour red was chosen to highlight those where this characteristic was not visible (Fig.F2e-i). The finger and thumb are both connective and peripheral parts of the body as discussed previously in this section. However, muscle also presents the feature, as can be seen on the outside of the oesophagus during dissection experiments.

Therefore, it is not surprising that the tongue spectra have this characteristic, due to it consisting of mostly muscle with a thin mucosa. Furthermore, the cheeks are thin and connective with a good blood supply close to the surface and consequently exhibit this feature. The forearm, chest, bicep, calf, and stomach are mostly absent of the OHb absorption trough-peak-trough, and show only an increased absorption in this region, as is typical of the inside of the oesophagus. The fingertips and inner arm are useful models for the trachea and oesophagus due to their resemblance to the spectral characteristics in the 530 - 590 nm wavelength range. Furthermore, they are easily accessible parts of the body making *in-vivo* measurements easier. Measurements were made on a single volunteer, with evidence from literature suggesting that skin tone may play a large role when detecting the feature.



## Appendix G

### Tissue-Sensor Separation

Depending on how the ETT placement sensor will eventually be integrated into the ETT, the sensor may be separated from the tissue by a few millimetres. For example, if the sensor is attached inside or outside the lumen of the ETT, or if it presses directly into the tissue when the sensor is attached to the cuff. Therefore, an experiment was designed to determine what was the optimal range of separation distances between the probe and the tissue. with the spectrometer integration time set to 300 ms and with scan averaging set to 10 this time. Therefore, the spectrometer averaged 10 individual scans, generating 1 scan every 3 s.

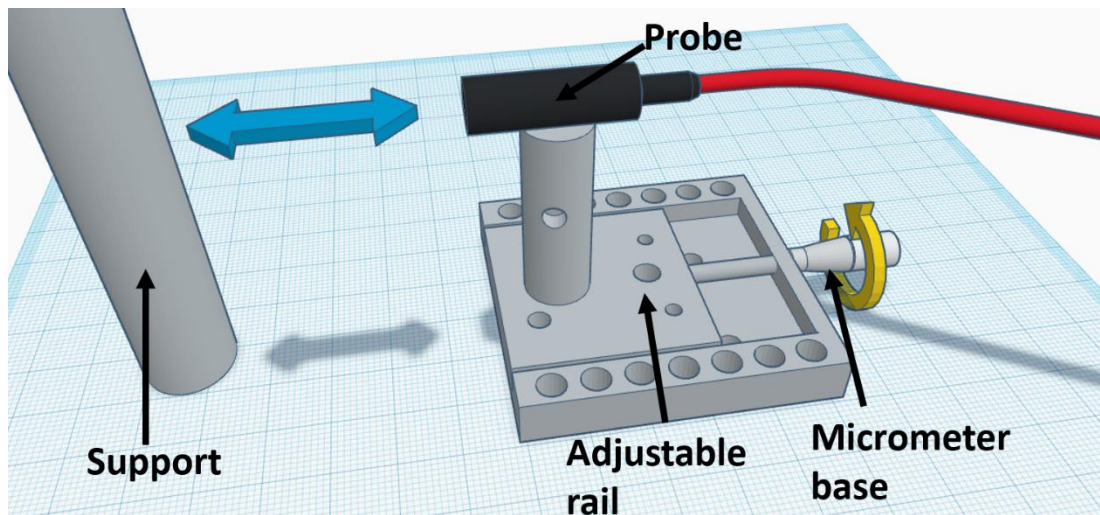
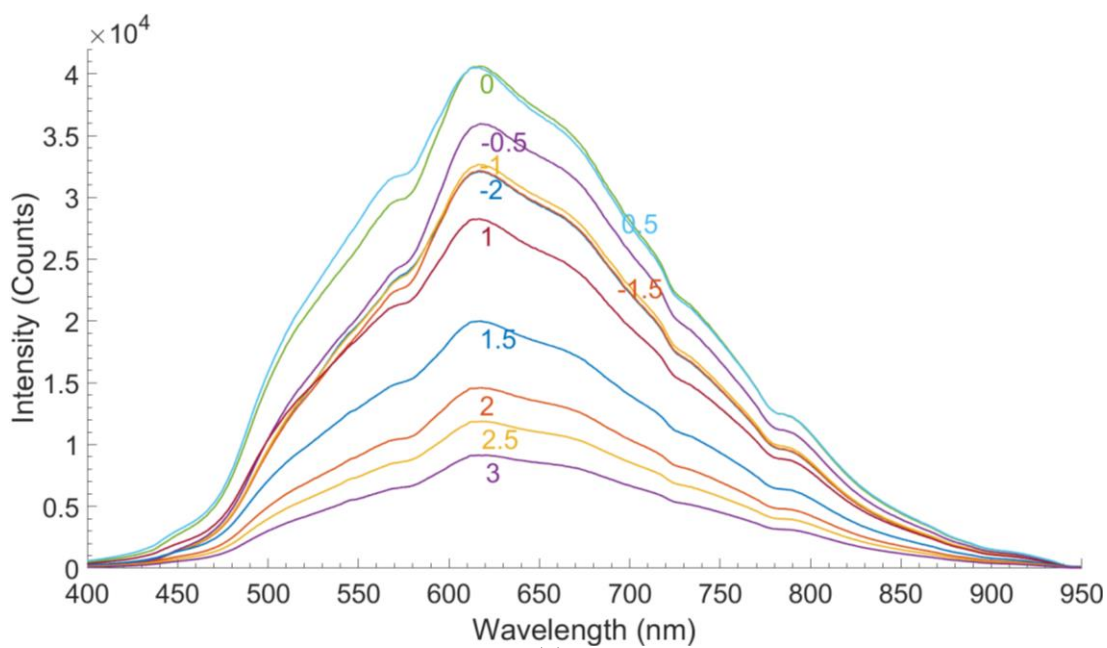
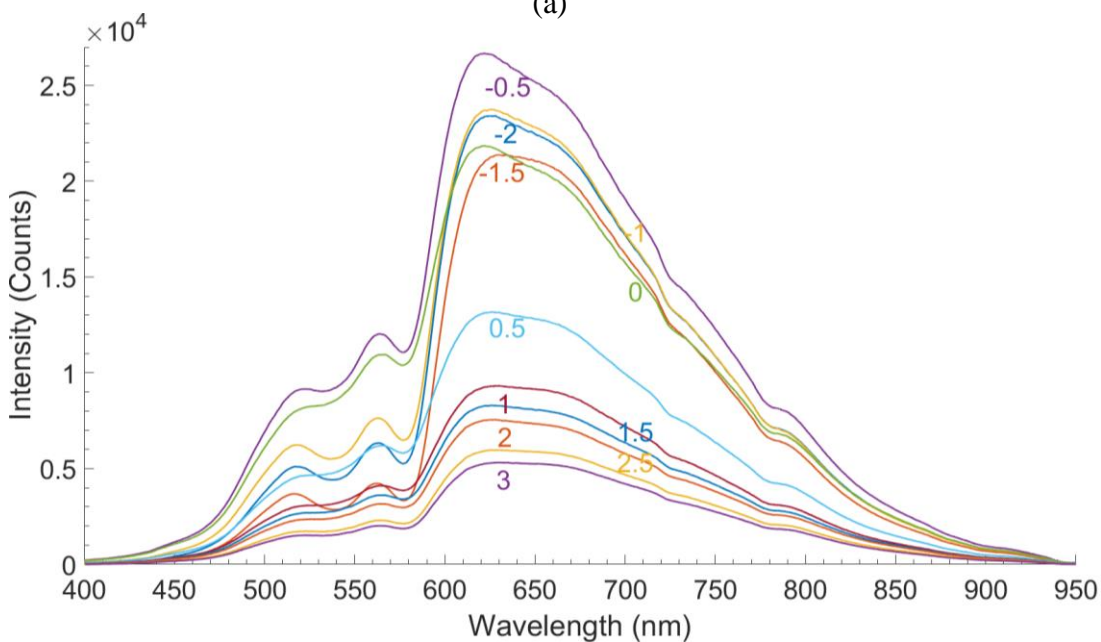


Fig. G1: 3D rendering of the reflection probe mounted adjustable rail.

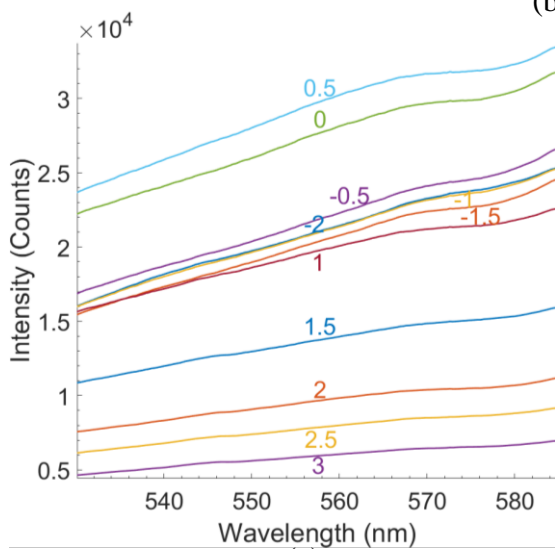
Fig. G1 shows a custom set-up consisting of a micrometer-controlled rail which was used to move an attached reflection probe. The volunteer's arm was placed between the support and the probe. A support beam behind the arm stops it from moving backwards away from the probe. The rail was adjusted in increments of  $0.500 \pm 0.001 \text{ mm}$  and the probe was initially touching the surface of the skin and then moved inwards 2 mm so that the probe was lightly pressed into the skin, where measurements began at -2 mm until the probe was +3 mm above the surface of the skin, giving 11 total increments. Measurements were made on a single volunteer's forearm and middle of thumb.



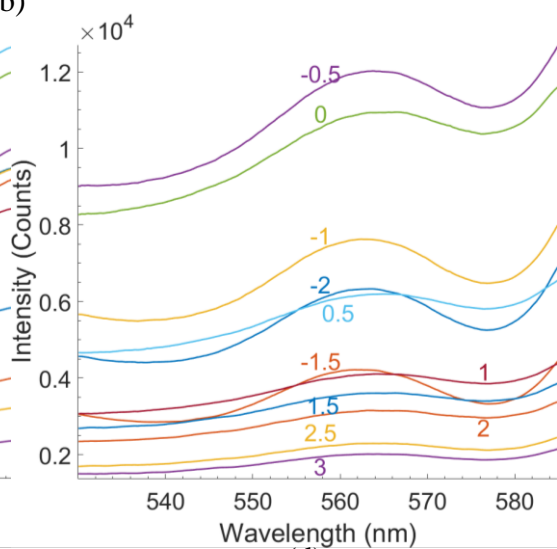
(a)



(b)



(c)



(d)

Fig. G2: Spectra measured by a diffuse reflectance probe at varying distances from the skin for (a) forearm and (b) thumb, with the labels denoting the distance from the tissue in mm. (c) and (d) shows a close-up of the spectra in the characteristic wavelength region (530 - 590 nm) for the arm and thumb, respectively.

The spectrometer has a varying quantum efficiency with wavelength and so the absolute optical power could not be found. However, the spectrometer does have the same quantum efficiency at wavelengths between measurements, so relative comparisons between spectra can be found by calculating the area under each of the spectra. The resulting data was then normalized so that the largest optical power was assigned a value of 1 for a direct comparison.

Table G1: Relative normalized power change calculated from the diffuse reflectance of a human volunteer's arm and thumb. Calculated from the data in Fig G2.

<b>Distance from the surface of skin <math>\pm 0.001 \text{ mm}</math></b>	<b>Relative total power (arm) <math>\pm 0.001</math></b>	<b>Relative total power (thumb) <math>\pm 0.002</math></b>	<b>Relative power 530 - 590 nm (arm) <math>\pm 0.001</math></b>	<b>Relative power 530 - 590 nm (thumb) <math>\pm 0.002</math></b>
-2	0.753	0.799	0.719	0.500
-1.5	0.748	0.704	0.691	0.326
-1	0.764	0.832	0.716	0.612
-0.5	0.839	1.000	0.746	1.000
0	0.982	0.845	0.935	0.924
0.5	1.000	0.509	1.000	0.520
1	0.690	0.509	0.667	0.344
1.5	0.488	0.318	0.467	0.303
2	0.355	0.288	0.326	0.264
2.5	0.29	0.226	0.266	0.191
3	0.224	0.200	0.202	0.168



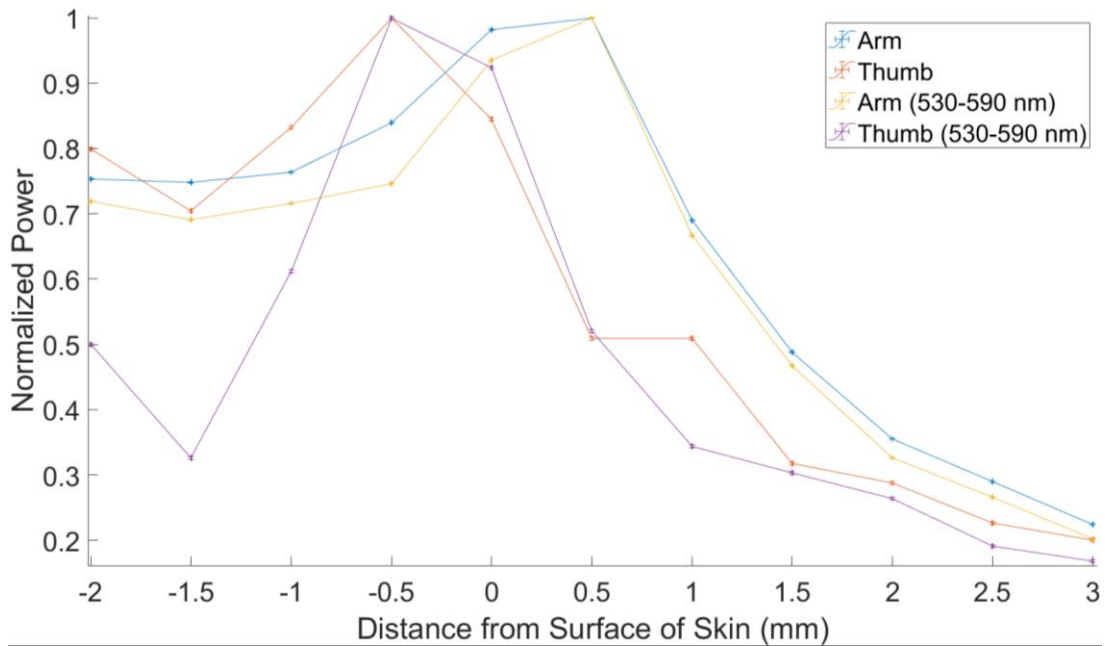


Fig. G3: Normalized optical power of the full spectrum for diffuse reflectance measurements on the arm (blue) and thumb (red), as well as the 530 - 590 nm wavelength region for the arm (yellow) and thumb (purple).

A shift in the peak normalized optical power between the arm and thumb can be seen in Fig. G3. The peak power reflected from the Arm occurs at 0.5 mm above the surface of the skin, whereas the peak power from the thumb occurs at -0.5 mm (pressed into the skin 0.5 mm), although relatively large increments mean that the peak power can only be estimated to  $\pm 0.25$  mm. Multiple factors could affect the distance at which the peak power is obtained. The arm may be more reflective on its surface tissues, the skin, and mucosa. Therefore, the peak reflectance is obtained when the sensor is positioned just above the surface of the skin, while the thumb may reflect more light deeper into the tissue from cartilage and ligaments. Furthermore, blood may be occluded from the tissues causing blanching. This causes the reflectance to increase as there is less blood to absorb light in the relevant regions, which has been documented in literature previously. However, it is also possible that due to the arm's larger size, there is more area for light to be reflected from as the probe is pulled away from the surface of the skin, although visibly the outer circle of the light remained well within the thumb during measurements, so only a negligible amount of light is expected to have missed the thumb. The normalized optical power also falls off much more rapidly in the OHb double trough wavelength region (530 - 590 nm), implying that blood is being occluded. Furthermore, the optical power falls off even more rapidly for the thumb, implying that more blood is being occluded in the thumb than the arm, which is consistent with there being more blood accessible closer to the surface of the skin of 'connective' tissues such as the thumb.

For measurements in the 530 - 590 nm wavelength region, the optimal separation distance between the sensor and the tissue should be -0.5 mm (pressed into the skin 0.5 mm). However, the acceptable distances will be dependent on the: sensor and opto-electronic units; the diameter of fibres; the number of fibres; the optical power of the light source; and the sensitivity of the spectrometer. Although if this, or a comparable

system is used, between -2 and +2 mm separation distance equates to approximately 30% of the peak optical power being detected in the 530 - 590 nm wavelength region. Furthermore, from Fig. G2, the trough-peak-trough characteristic remains clear between -2 and +3 mm separation distance. Finally, a relatively robust range of acceptable tissue-sensor separation distances was found to be between -2 and +2 mm from the surface of the skin. However, this will be dependent on the optical power measured and the separation distances between the fibres.